UNIVERSITÀ
degli STUDI
di CATANIA

Experimental and theoretical multi-channel study of direct nuclear reactions: a tool to provide data driven information on neutrino-less double-beta decay

A DISSERTATION PRESENTED
BY
ALESSANDRO SPATAFORA
TO
THE DEPARTMENT OF PHYSICS "ETTORE MAJORANA"

IN PARTIAL FULFILLMENT OF THE REQUIREMENTS
FOR THE DEGREE OF
DOCTOR OF PHILOSOPHY
IN THE SUBJECT OF
PHYSICS

UNIVERSITÁ DEGLI STUDI DI CATANIA
CATANIA, ITALIA
APRIL 2022

Thesis tutors:
Prof. Francesco Cappuzzello
Ph. D. Diana Carbone
Ph. D. Manuela Cavallaro

Alessandro Spatafora

Experimental and theoretical multi-channel study of direct nuclear reactions: a tool to provide data driven information on neutrino-less double-beta decay

Abstract

The search for neutrino-less double beta ($0\nu\beta\beta$) decay has attracted much interest in the last years due to the extraordinary consequences that could derive from its observation. The NUMEN project aims to provide experimental information on the nuclear matrix elements involved in the expression of $0\nu\beta\beta$-decay half-life by measuring the cross-section of double charge exchange nuclear reactions. The experimental set-up to measure the zero-degrees double charge exchange nuclear reaction cross-section, including the K800 superconducting cyclotron and the MAGNEX magnetic spectrometer at the INFN - Laboratori Nazionali del Sud, in Catania, are described in the present thesis. The data-reduction and theoretical analysis performed during the PhD period are detailed in the present thesis. They involve the cases of the ^{18}O + ^{12}C, ^{18}O + ^{76}Se and ^{20}Ne + ^{76}Ge networks of quasi-elastic nuclear reactions at 15.3 AMeV incident energy. The advantages of the newly proposed multi-channel approach are applied to the NUMEN nuclear reaction data analysis. Regarding the ^{18}O+^{12}C data analysis, a unique comprehensive and coherent theoretical calculation able to describe the whole network of direct reactions using state-of-the-art nuclear structure and reaction theories is performed for the first time in this work. This *holistic* approach, applied both to the experimental and theoretical analysis, is the main feature and novelty of the work here presented. The experimental and theoretical analysis for the ^{76}Ge $\leftrightarrow$ ^{76}Se network of direct nuclear reactions, with a special attention to the elastic and inelastic scattering, single and double charge exchange reaction channels, is also carried out and described in detail.

Contents

List of Figures

Acknowledgments

Introduction

The understanding of heavy-ion direct nuclear reaction mechanisms, such as the ones involved in single and double charge-exchange reactions, is the main purpose of the present work. This task demands and inspires, at the same time, the deep understanding of the nature of atomic nuclei. The experimental and theoretical study of direct nuclear reactions induced by ^{18}O and ^{20}Ne beams at 15.3 AMeV incident energy on ^{12}C, ^{76}Se and ^{76}Ge targets performed at the INFN-Laboratori Nazionali del Sud is the main focus of the research presented in this thesis. The data-reduction and theoretical analysis on these systems, entirely performed during the PhD period, are the main topic of the present volume.

The scientific background and motivation of this work are common to that of the NUMEN [1] (Nuclear Matrix Elements for neutrino-less double-beta decay) project aiming to extract information about the Nuclear Matrix Elements (NMEs) of interest in the context of neutrino-less double beta decay ($0\nu\beta\beta$) research. This process is considered the *experimentum crucis* to reveal the Majorana nature of neutrinos and the lepton-number violation, being a link between the current and next-generation physics beyond the standard model [2–4]. The role of NMEs in $0\nu\beta\beta$ research is crucial to design the next-generation experiments and to access the neutrino effective mass, if the process will be actually observed. For such reasons, the large discrepancies between the NMEs calculated among different nuclear structure theories [5] need to be overcome and the NUMEN project suggests the possibility to constrain such calculations using a new data-driven approach. This scientific background is presented in Chapter 1.

Direct nuclear reactions are a good source of information on nuclear structure since their cross-sections depend on the overlap between the initial and final many-body nuclear wave functions. The study of double charge-exchange (DCE) nuclear reaction cross-sections is particularly relevant for the $0\nu\beta\beta$ decay physics since the NMEs for DCE and $0\nu\beta\beta$ decay transitions share the same initial and final nuclear states [1].

Although the theoretical connection between DCE measured cross-sections and the $0\nu\beta\beta$ NMEs is the most interesting and debated aspect, a crucial point in this context is also the capability of state-of-the-art nuclear theories to give the clearest and the most complete description of the DCE reaction mechanism. A brief introduction of the main aspects and the most widespread methodologies adopted for the analysis of the heavy-ion nuclear reactions are proposed in Chapter 2.

The complete DCE mechanism is a competition of three possible contributions: *i)* the direct process, called Majorana DCE [6], in analogy to the direct $0\nu\beta\beta$ Majorana process; *ii)* the double Single Charge-Exchange (double-SCE) process, consisting of two direct-SCE steps, in analogy to the $2\nu\beta\beta$-decay; *iii)* the multi-nucleon transfer process involving all the possible one- and two-nucleon successive transfers connecting the same initial and final DCE partitions. Recent studies are excluding a relevant role of the multi-nucleon transfers in the DCE reaction mechanism [7, 8], whereas the role of the double-SCE is to date far from being considered negligible. In that case the double-SCE contribution to the total DCE can be estimated considering a folding of two SCE reaction amplitudes [9].

The theoretical ingredients required to perform this study are both from nuclear structure and reaction physics. The response of nuclei to the first- and second-order isospin and spin-isospin operators, and the single-particle or correlation features coming from the mean-field or residual interaction, respectively, are the relevant nuclear structure information. On the other side, the introduction of an average interacting potential to describe the relative motion of the colliding nuclei, the proper description of the residual interaction and the dynamical effects responsible to couple states of the same or different partitions, are the main nuclear reaction theory aspects needed to be addressed. From the experimental side, a good understanding of such properties implies the necessity to study a wide network of nuclear reactions including the elastic and inelastic scattering, the one and two-nucleon transfer, the SCE and DCE nuclear reactions. Furthermore, the NUMEN project wants to study the (^{18}O,^{18}Ne) DCE reaction as a probe for the $\beta^+\beta^+$ transitions and the (^{20}Ne,^{20}O) one for the $\beta^-\beta^-$, with the aim to explore the DCE mechanism in both directions [1]. Since NMEs are *time invariant* quantities, they are common to a DCE and to its inverse, so the contextual measurements of both directions in the DCE represent a useful test of the procedure to extract NME from the measured DCE cross-section.

The ^{18}O and the ^{20}Ne beams accelerated by the K800 Superconducting Cyclotron [10] and the MAGNEX large acceptance magnetic spectrometer [11] installed at the Labo-

ratori Nazionali del Sud (INFN-LNS) in Catania are the main experimental tools used to perform the NUMEN experimental campaign. MAGNEX is the ideal instrument to study such kinds of reactions, since it conjugates good energy, mass and angular resolutions with a large acceptance both in solid angle and momentum. All these features are relevant to perform the advanced zero-degrees DCE measurements on the $\beta\beta$-candidate nuclear targets, which are very suppressed processes characterized by very small cross-section. The relevant aspects of the experimental set-up are presented in Chapter 3.

The extraction of excitation energy spectra and cross-section angular distributions are the main experimental results. These are accessed thanks to a complex data reduction procedure involving the calibration of the relevant parameters measured by the MAGNEX focal plane detector, the identification in atomic number, mass number and charge state of the ejectiles produced in the nuclear reactions of interest, the trajectory reconstruction of the ions in the MAGNEX spectrometer and the cross-section extraction after an appropriate normalization. The details of the data reduction are presented in Chapter 4.

The main feature and novelty of the work proposed in this thesis concern both experimental and theoretical aspects. From the experimental side, the idea is to produce new data of the angular distributions and energy spectra differential cross-sections measured in the same experiment for a broad network of nuclear reactions. From the theoretical side, the purpose is to analyse the experimental data using state-of-art nuclear structure and reaction theories in a unique full-comprehensive and coherent calculation. This approach has been applied to the study of many nuclear reaction channels involving the ^{18}O + ^{12}C system at 15.3 AMeV incident energy. Although they are not $\beta\beta$-decay candidates, the choice of such projectile and target was driven by the available accurate information on the involved nuclear low-lying states in this mass region from experimental results and large scale shell-model calculations, making this system an ideal benchmark for the proposed multi-channel constrained technique. The results and analysis of this study are discussed in Chapter 5.

The new multi-channel experimental and theoretical approach, once tested, can be further applied to the study of the $\beta\beta$-decay candidates both in the $\beta^+\beta^+$ and in the $\beta^-\beta^-$ transition directions through the (^{18}O,^{18}Ne) and the (^{20}Ne,^{20}O) DCE nuclear reactions. In the present work, new experimental data and the relative theoretical analysis are presented for the networks of nuclear reactions involving the ^{76}Ge $\leftrightarrow$ ^{76}Se $\beta\beta$-decay partners. In particular, the elastic and inelastic scattering, the SCE and the DCE nuclear reaction channels are detailed in Chapter 6.

Introduction References

[1] F. Cappuzzello et al. "The NUMEN project: NUclear Matrix Elements for Neutrinoless double beta decay". In: *European Physical Journal A* 54.5 (2018). cited By 106. DOI: 10.1140/epja/i2018-12509-3.

[2] H. Ejiri, J. Suhonen, and K. Zuber. "Neutrino–nuclear responses for astro-neutrinos, single beta decays and double beta decays". In: *Physics Reports* 797 (2019). Neutrino-nuclear responses for astro-neutrinos, single beta decays and double beta decays, pp. 1–102. DOI: 10.1016/j.physrep.2018.12.001.

[3] S. Dell'Oro et al. "Neutrinoless Double Beta Decay: 2015 Review". In: *Advances in High Energy Physics* 2016.2162659 (2016), p. 37. DOI: 10.1155/2016/2162659.

[4] M. J. Dolinski, A. W.P. Poon, and W. Rodejohann. "Neutrinoless Double-Beta Decay: Status and Prospects". In: *Annual Review of Nuclear and Particle Science* 69.1 (2019), pp. 219–251. DOI: 10.1146/annurev-nucl-101918-023407.

[5] J. Engel and J. Menéndez. "Status and future of nuclear matrix elements for neutrinoless double-beta decay: a review". In: *Reports on Progress in Physics* 80.4 (2017), p. 046301.

[6] H. Lenske et al. "Heavy ion charge exchange reactions as probes for nuclear β-decay". In: *Progress in Particle and Nuclear Physics* 109 (2019), p. 103716. ISSN: 0146-6410. DOI: 10.1016/j.ppnp.2019.103716.

[7] D. Carbone et al. “Analysis of two-nucleon transfer reactions in the ^{20}Ne + ^{116}Cd system at 306 MeV”. In: *Physical Review C* 102.4 (2020). cited By 6. DOI: 10.1103/PhysRevC.102.044606.

[8] J. L. Ferreira et al. “Multinucleon transfer in the ^{116}Cd(^{20}Ne,^{20}O)^{116}Sn double charge exchange reaction at 306 MeV incident energy”. In: *Phys. Rev. C* 105 (1 Jan. 2022), p. 014630. DOI: 10.1103/PhysRevC.105.014630.

[9] J. I. Bellone et al. “Two-step description of heavy ion double charge exchange reactions”. In: *Physics Letters B* 807 (2020), p. 135528. ISSN: 0370-2693. DOI: 10.1016/j.physletb.2020.135528.

[10] D. Rifuggiato, L. Calabretta, and G. Cuttone. “Cyclotrons and their applications. Proceedings, 17th International Conference, Cyclotrons 2004”. In: *Part. Accel. Soc. Japan (2004) 541 p* (2004). Ed. by Akira Goto.

[11] F. Cappuzzello et al. “The MAGNEX spectrometer: results and perspectives”. In: *Eur. Phys. J.* A52.6 (2016), p. 167. DOI: 10.1140/epja/i2016-16167-1.

Soltanto i vivi intelligenti possono scomparire senza lasciar traccia.

L. Sciascia, La scomparsa di Majorana

1

Nuclear matrix elements for neutrino-less double-beta decay

Contents

The observation of neutrino oscillations [12] stimulated the interest of physicists towards a new physics beyond the Standard Model. Many aspects of neutrino properties need to be better understood, such as the mass-generation mechanism, the absolute mass scale, the CP-transformation properties and Majorana or Dirac nature of such fermions [13]. A full understanding of these questions would have implications not only on the underlying symmetries governing leptons but also on the baryogenesis and the Universe evolution.

One of the most promising way to access the physics beyond the Standard Model is the neutrino-less double-beta ($0\nu\beta\beta$) research. This process is considered the *experimentum crucis* to reveal the Majorana nature of neutrinos and the lepton-number violation. Without assuming any particular driving decay mechanism, the $0\nu\beta\beta$ decay physics is devoted to test the lepton-number symmetry violation whose observation would demonstrate the breaking of a global conservation law of the Standard Model. The information obtained from such observation could turn out crucial for opening to the next scientific era. These are the motivations for the worldwide scientific interest devoted to $0\nu\beta\beta$ studies from both the experimental and theoretical sides.

In this context, the role of nuclear physics is central [3, 14] since it is involved in $0\nu\beta\beta$ decay research, helping to choose the best $\beta\beta$-unstable isotope and the right amount of it needed to achieve the desired sensitivity and also to access the neutrino effective mass, if the decay rate will be actually observed. This role is explained in the following chapter in which the Nuclear Matrix Elements (NMEs) for the $0\nu\beta\beta$ decay are introduced. NMEs are not physical observables, as the decay rates, and can be only accessed by calculations. The results of such calculations are deeply dependent on the unavoidable truncations performed by the state-of-art nuclear structure models. The possibility to constrain such calculations using the data-driven approach proposed by the NUMEN project is finally presented.

1.1 The neutrino-less double-beta decay

The double-beta decays ($\beta^+\beta^+$ and $\beta^-\beta^-$) are isobaric transitions from a parent (A, Z) to a daughter (A, Z $\pm$ 2) nucleus. In the two-neutrino double-beta ($2\nu\beta\beta$) decay the energy $Q_{\beta\beta}$ is released when two electrons (positrons) and two electron-type antineutrinos

(neutrinos) are involved during the transition :

$$(A, Z) \rightarrow (A, Z+2) + 2e^- + 2\bar{\nu}_e \tag{1.1}$$

$$(A, Z) \rightarrow (A, Z-2) + 2e^+ + 2\nu_e \tag{1.2}$$

The two rows indicate the SM-allowed second-order weak *double beta disintegration* processes predicted by Goeppert-Meyer in 1935 [15]. This decay mode, whose typical half-lives are greater than 10^{19} years, was first observed both in radiochemical experiments and in real time on several nuclei since the 1950s [16, 17]. In 1937 Majorana [13] proposed his relativistic quantum field theory of neutral fermions where a single Majorana quantum field characterizes the situation in which particles and antiparticles coincide, in analogy to the photon case. Two years later, Furry [18] studied within this scenario a new process similar to the Goeppert-Mayer one, the SM-forbidden neutrinoless double beta ($0\nu\beta\beta$) decay:

$$(A, Z) \rightarrow (A, Z+2) + 2e^- \tag{1.3}$$

$$(A, Z) \rightarrow (A, Z-2) + 2e^+ \tag{1.4}$$

in which the lepton number is violated by two units since a pair of leptons is expected to be created. This process is nowadays still not observed. The experimental search is extremely challenging and the best current half-life limits is 1.8×10^{26} years [19].

The $0\nu\beta\beta$ decay is first of all a nuclear process and needs to be described properly, taking into account all the relevant aspects of nuclear structure and dynamics. It is a second-order nuclear-weak process and the (A, Z) nucleus can decay to its (A, Z+2) isobar if the mass difference is enough to allow the creation of two electrons. If the nucleus can also decay by single beta decay in the (A, Z+1) nucleus, the branching ratio for the $0\nu\beta\beta$ would be too small to make the process measurable due to the huge background rate from the first order weak decay, as sketched in Figure 1.1 (b). The (A,Z) isotopes, candidate to the $0\nu\beta\beta$ decay, are even-even 0^+ nuclei that, due to the nuclear pairing force, are lighter than their (A,Z+1) odd-odd isobars making the single beta decay kinematically forbidden (see Figure 1.1 (a)).

The theoretical expression of the half-life of the $0\nu\beta\beta$ process, if we assume that it is mediated by the exchange of light Majorana neutrinos and the Standard Model weak

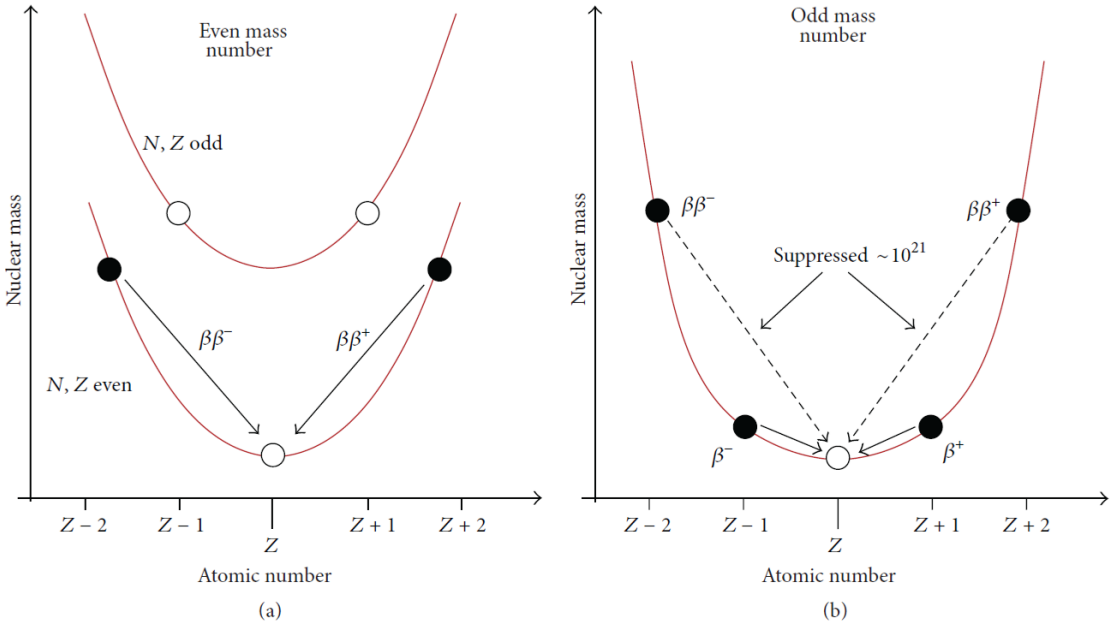

Figure 1.1: Nuclear mass A as a function of the atomic number Z in the case of an isobar candidate with A even (a) and A odd (b). Figure from Ref. [3].

interaction, can be factorized [20] as follows:

$$\left[T_{0\nu}^{1/2}\right]^{-1} = G_{0\nu} \left|\mathcal{M}_{0\nu}\right|^2 m_{\beta\beta}^2 \tag{1.5}$$

where $G_{0\nu}$ comes from the phase-space integral, $m_{\beta\beta}$ is the effective neutrino mass and $\mathcal{M}_{0\nu}$ is the nuclear matrix element. $\mathcal{M}_{0\nu}$ is of larger interest for the purposes of this work and will be deeper treated in the next section.

The $G_{0\nu}$ factor calculations are nowadays very advanced and accurate. The key ingredient are the scattering electron wave functions taking into account relativistic corrections, the nuclear size and the atomic screening effect on the emitted electrons. State-of-art calculations of the $G_{0\nu}$ factor can be found in Refs. [21, 22].

The effective neutrino mass $m_{\beta\beta}$ is defined by the following expression

$$m_{\beta\beta} = \left| m_1 \left|U_{e1}\right|^2 + m_2 \left|U_{e2}\right|^2 e^{i(\alpha_2 - \alpha_1)} + m_3 \left|U_{e3}\right|^2 e^{i(-\alpha_1 - 2\delta)} \right| \tag{1.6}$$

where m_k (k = 1, 2, 3) are the three neutrino mass eigenvalues, U_{ek} are the three electric components of the Pontecorvo–Maki–Nakagawa–Sakata (PMNS) matrix containing the three mixing angles, δ is the so-called Dirac phase and α_j are the two Majorana phases

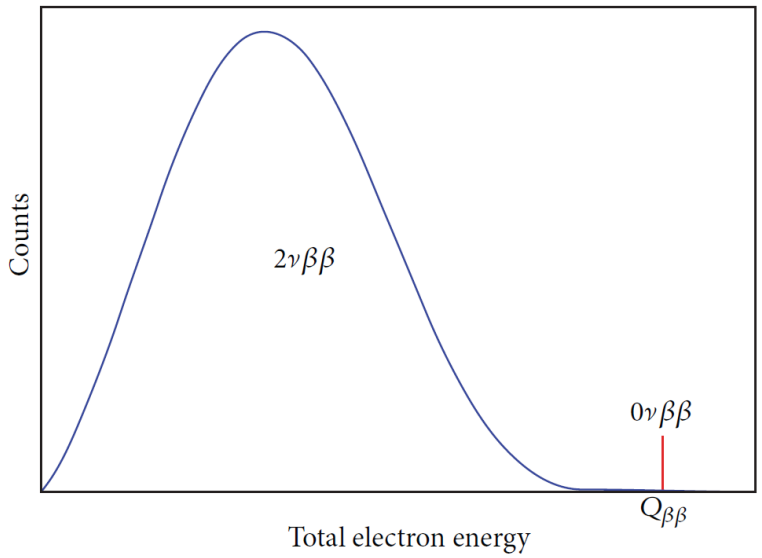

Figure 1.2: Schematic view of the $2\nu\beta\beta$- and the $0\nu\beta\beta$-decay spectra.

(vanishing if neutrinos are Dirac particles). In Ref. [3] it is explained how not only the light neutrino exchange (the one described in the Equation 1.5) can contribute to the $0\nu\beta\beta$ decay. Indeed, once the weak operator violates the lepton number symmetry, some other lepton-number violating mechanisms could be present or even dominate the process, i.e. exchange of sterile neutrinos via left-handed currents or production of Majorons. This would imply that the detection of $0\nu\beta\beta$ decay would not give the information about the absolute neutrino mass but could be used as a low-energy gateway of new physics that would complement high-energy searches using accelerators such as the Large Hadron Collider.

1.1.1 The $T_{0\nu}^{1/2}$ measurement

The observables of interest in the $0\nu\beta\beta$ experiments are the kinematic parameters of the two emitted electrons. Their total energy is detected and sometimes the individual electron paths are reconstructed to reject backgrounds through algorithms based on topology. The signature of $0\nu\beta\beta$ decay is a mono-energetic peak (see red line in Figure 1.2) at $Q_{\beta\beta}$ searched in a very narrow region-of-interest (ROI) selected on the basis of the energy resolution of the detector.

The most important parameter in the design of a $0\nu\beta\beta$ decay experiment is the

sensitivity $S^{0\nu}$. In case of a background free experiment or with some background sources, the two following expressions can be introduced:

$$S^{0\nu} \propto \begin{cases} aM\epsilon t & \text{background free} \\ a\epsilon\sqrt{\frac{Mt}{B\Delta E}} & \text{with background} \end{cases} \tag{1.7}$$

where a is the isotopic abundance of the parent isotope, M is the mass of isotope, ϵ is the detection efficiency in the ROI region, t is the measurement time, ΔE is the detector energy resolution and B is the background index, normalized to the width of the ROI, source mass and measurement time (in units of (keV·kg·year)$^{-1}$). The comparison between the two expressions clarifies the advantages to perform a background-free experiment, since the $S^{0\nu}$ scales with t or $\sqrt{(}t)$ in the case of experiments without or with background, respectively.

The complete list of the 35 $0\nu\beta\beta$ decay candidate isotopes can be found in Ref. [23], although not all of them are suitable as candidate isotopes for the research activity. Following Equation 1.7, the ideal isotope should have an high isotopic abundance, could be procured in large quantity, used as high resolution detector and under low background conditions. In this framework, the experiments should be organized in order to make the best design choices in order to optimize these parameters.

The detection efficiency and energy resolution can be optimized if the source material is integrated as the detector medium. When the source material is external to the detector, the escape probability of one or two electrons increases due to self-absorption, although in this external-source configuration it is possible to perform superior tracking and effective background rejection techniques.

Another important constraint in the experiments design is the isotope enrichment cost. To reduce it, the material should be readily available in its natural form and the candidate isotope should have an high natural abundance. The isotope enrichment is typically more expensive depending on the isotopic abundance of the starting material: the higher the natural abundance, the lower the cost. A summary of the most used isotopes and relative abundances and $Q_{\beta\beta}$ values for the $0\nu\beta\beta$ decay candidates is reported in Table 1.1.

The most critical aspects of the experimental design is related to the background sources. The electrons coming from the $2\nu\beta\beta$ decay reaching the ROI are an irreducible source since they are indistinguishable from those coming from the $0\nu\beta\beta$ decay mode (see Figure 1.2). Other sources are related to the U and Th decay chains, intrinsically

Table 1.1: Isotopic abundance and $Q_{\beta\beta}$ for the known $2\nu\beta\beta$ emitters and $0\nu\beta\beta$ decay candidates from Ref. [24].

Isotope	Isotopic abundance(%)	$Q_{\beta\beta}$ (MeV)
^{48}Ca	0.187	4.263
^{76}Ge	7.8	2.093
^{82}Se	9.2	2.998
^{96}Zr	2.8	3.348
^{100}Mo	9.6	3.305
^{116}Cd	7.6	2.813
^{130}Te	34.08	2.527
^{136}Xe	8.9	2.459
^{150}Nd	5.6	3.371

present in the materials used for the detectors construction. The detailed description of these aspects can be found in Refs. [3, 4, 24].

1.2 The $0\nu\beta\beta$ Nuclear Matrix Elements

The NME $\mathcal{M}_{0\nu}$ introduced in Equation 1.5 plays a central role being the link between the experimental measurement of the $0\nu\beta\beta$ decay half-lives and effective neutrino masses. $\mathcal{M}_{0\nu}$ is the transition amplitude from the initial ϕ_i to the final ϕ_f nuclear state of the $0\nu\beta\beta$ process through the $\hat{O}^{0\nu\beta\beta}$ operator:

$$\mathcal{M}_{0\nu} = \langle \phi_f | \hat{O}^{0\nu\beta\beta} | \phi_i \rangle \tag{1.8}$$

The NME is decomposed as follows:

$$\mathcal{M}_{0\nu} = \mathcal{M}_{0\nu}^{GT} + \frac{g_V^2}{g_A^2}\mathcal{M}_{0\nu}^{F} + \mathcal{M}_{0\nu}^{T} \tag{1.9}$$

with $\mathcal{M}^{GT}_{0\nu}$, $\mathcal{M}^{F}_{0\nu}$ and $\mathcal{M}^{T}_{0\nu}$, Gamow-Teller, Fermi and rank-two Tensor components, respectively. They are defined as follows:

$$\mathcal{M}^{GT}_{0\nu} = \frac{2R}{\pi g_A^2} \int_0^{+\infty} |\mathbf{q}|\, d\,|\mathbf{q}|\, \langle f| \sum_{a,b} \frac{j_0(|\mathbf{q}|\, r_{ab}) h_{GT}(|\mathbf{q}|) \boldsymbol{\sigma}_a \cdot \boldsymbol{\sigma}_b}{|\mathbf{q}| + \bar{E} - (E_i + E_f)/2} \tau_a^+ \tau_b^+ |i\rangle \tag{1.10}$$

$$\mathcal{M}^{F}_{0\nu} = \frac{2R}{\pi g_A^2} \int_0^{+\infty} |\mathbf{q}|\, d\,|\mathbf{q}|\, \langle f| \sum_{a,b} \frac{j_0(|\mathbf{q}|\, r_{ab}) h_{F}(|\mathbf{q}|)}{|\mathbf{q}| + \bar{E} - (E_i + E_f)/2} \tau_a^+ \tau_b^+ |i\rangle \tag{1.11}$$

$$\mathcal{M}^{T}_{0\nu} = \frac{2R}{\pi g_A^2} \int_0^{+\infty} |\mathbf{q}|\, d\,|\mathbf{q}|\, \langle f| \sum_{a,b} \frac{j_2(|\mathbf{q}|\, r_{ab}) h_{T}(|\mathbf{q}|) \left[3\boldsymbol{\sigma}_j \cdot \hat{r}_{ab} \boldsymbol{\sigma}_k \cdot \hat{r}_{ab} - \boldsymbol{\sigma}_a \cdot \boldsymbol{\sigma}_b\right]}{|\mathbf{q}| + \bar{E} - (E_i + E_f)/2} \tau_a^+ \tau_b^+ |i\rangle \tag{1.12}$$

The nucleon coordinates are operators acting on the nuclear final $|f\rangle$ and initial $|i\rangle$ states. The nuclear radius R is inserted by convention to make the matrix element dimensionless with a compensating factor in $G_{0\nu}$ in Equation 1.5. For that reason, we need to be careful in comparing the NMEs competing to different nuclei. As an example, in Figure 1.3, the ^{48}Ca NMEs, obtained by Eq. 1.10 definition for different model assumptions, are smaller than the others. This is not only due to the different nuclear structure properties of ^{48}Ca but also because its radius is the smallest among the other considered nuclei. r_{ab} is the magnitude of the inter-nucleon position vector and $\hat{r}_{ab}$ is the corresponding unit vector. j_0 and j_2 denote spherical Bessel functions and the h parameters, called neutrino potentials, are defined in momentum space as follows:

$$h_{GT}(|\mathbf{q}|) = g_A^2 - \frac{g_A(\mathbf{q}^2) g_P(\mathbf{q}^2) \mathbf{q}^2}{3m_N} + \frac{g_P^2(\mathbf{q}^2)\mathbf{q}^4}{12m_N^2} + \frac{g_M^2(\mathbf{q}^2)\mathbf{q}^2}{6m_N^2} \tag{1.13}$$

$$h_{F}(|\mathbf{q}|) = \frac{g_V^2(\mathbf{q}^2)}{g_A^2(\mathbf{q}^2)} \tag{1.14}$$

$$h_{T}(|\mathbf{q}|) = \frac{g_A(\mathbf{q}^2) g_P(\mathbf{q}^2) \mathbf{q}^2}{3m_N} - \frac{g_P^2(\mathbf{q}^2)\mathbf{q}^4}{12m_N^2} + \frac{g_M^2(\mathbf{q}^2)\mathbf{q}^2}{12m_N^2} \tag{1.15}$$

where the higher order terms in $1/m_N$ (m_N nucleon mass) of the nuclear current operators have been neglected. Sometimes the operators inside the matrix elements of Equation 1.10 are multiplied by a radial function $f(r_{ab})$, designed to take into account short-range correlations that are omitted by Hilbert-space truncation in most many-body calculations [5].

At this point we want to underline that there are two main approximations adopted in the previous definitions. Neutrino potentials in Equation 1.13 have been introduced

applying the *impulse approximation*, in which the effects due to the in-medium interaction are neglected and the current operator for a collection of *free nucleons* is adopted. The second used approximation is known as *closure approximation*. It begins with the observation that the average momentum $\langle \delta q \rangle$ available in the virtual intermediate channel is of the order of 100 MeV/c. This value is deduced by the Heisenberg relation $\langle \delta q \rangle \langle \delta r \rangle \approx \hbar c/c$ where $\langle \delta r \rangle \approx 2$ fm is the average spacing between the nucleons confined in the nucleus and exchanging the virtual neutrino, and $\hbar c$ is approximated to 200 MeV $\cdot$ fm. Being the neutrino mass negligible compared to the virtual momentum, the available neutrino energy is $E \approx \langle \delta q \rangle c \approx 100$ MeV and, consequently, this is the range of nuclear intermediate states excitation energies involved in the decay. The closure approximation consists in neglecting the intermediate-state-dependence that, summing on a very large excitation energy range, is treated as an unitary operator. In such approach, the state-dependent energy entering in the operators used to describe the propagation among the virtual intermediate states is fixed to an average value $\bar{E}$ and the contributions of the intermediate states is summed implicitly. This approximation avoids the explicit calculation of all the excited states of the intermediate odd-odd nucleus up to very high energies making the nuclear structure calculation computationally less involved considering only the initial and final state in the decay. In the case of the $2\nu\beta\beta$ decay the momentum transfer is limited by the Q-value of the reaction and the closure approximation cannot be applied.

1.2.1 Relevance of NME

The $0\nu\beta\beta$ decay lifetime depends on the square of the NME through the relation of Equation 1.5. Since the next generation experiments will be characterised by a higher sensitivity, compatible with the 10 meV $m_{\beta\beta}$ effective mass region[4], it will be necessary to perform accurate calculations of the NMEs due to several reasons.

Firstly, the amount of material needed to set the experimental sensitivity to any particular value of $m_{\beta\beta}$ in a given exposure time is proportional to the inverse square of the NME. An uncertainty of a factor of about three in the NME corresponds to an order of magnitude uncertainty in the amount of material required to achieve the same sensitivity level, in the case of a background free experiment, and even larger if the experiment is background-limited (see Equation 1.7). More accurate NME are thus needed to take an informed decision about how much material to use in the next generation (expensive) experiments.

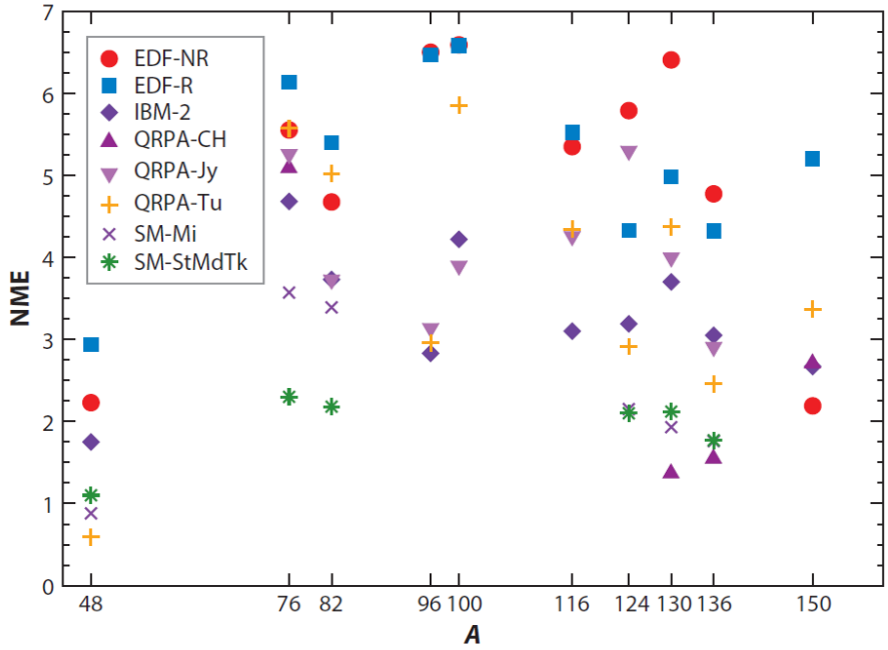

Figure 1.3: Nuclear matrix elements calculations for different isotopes (see Ref. [5] for details). Abbreviations: EDF, energy-density functional; IBM, interacting boson model; QRPA, quasi-particle random phase approximation, SM, shell-model. Figure from Ref. [4]

Furthermore, the NMEs values may constrain the choice of the material to be used in future $0\nu\beta\beta$ decay experiments. In Figure 1.3, the NMEs calculated in different approaches are shown and, because of the spread of the results, we can only conclude that the matrix element of ^{48}Ca is smaller than those of the other $0\nu\beta\beta$ decay candidates while better calculations would make it easier to select an optimal isotope.

Finally, we want to remark the most obvious reason why we need to calculate high accuracy NMEs, so that to obtain information about the $m_{\beta\beta}$ once a $0\nu\beta\beta$ decay lifetime will be measured.

1.2.2 The models for nuclear structure calculations

The difficulties in calculating the NMEs are related to the initial and final state many-body nuclear wave functions problem not allowing for any exact solution. Several approaches to that problem exist and have been summarized in the reviews of Refs. [2–5].

Here we only want to show the main aspects, limits and approximations of such nuclear structure methods in order to clarify why the results shown in Figure 1.3 are so much heterogeneous changing the adopted theoretical framework.

Each of the adopted nuclear structure model has proper features and makes some assumptions in terms of configuration and/or correlation truncations:

- In the energy-density functional (EDF) models, the generator coordinate method (GCM) starts from the minimization of the energy functional in order to find the ground states properties. A large number of single particle configurations and the collective motions of nucleons are taken into account but only few selected correlations are used, leading to a possible overestimation of the NMEs. The Projected Hartree-Fock-Bogoliubov Method (PHFB) is a related approach.

- In the nuclear shell-model (NSM), the truncation of the Hilbert space of the nucleon states is the most relevant approximation and the valence space is constructed including levels near the Fermi surface. The number of interacting and acting nucleons is limited and the shells are constructed in an harmonic oscillator potential leading to a proper description and representation of the low-lying states. The effects of pairing correlations cannot be fully included and this lead to an underestimation of the NME.

- In the interacting boson model (IBM), nucleon pairs are represented as interacting-bosons. The reduction of the number of interacting objects opens the possibility to include more shells than in the NSM, although with fewer correlations. The description is typically more phenomenological than the other methods and relies more on adjusting the model parameters to match the observables.

- The quasi-particle random-phase approximation (QRPA) contains few correlations but a large number of single-particle orbits. The proton–neutron interaction and the particle–hole coupling parameters are fitted to reproduce the measured $2\nu\beta\beta$-decay half-lives.

- In the ab-initio methods all nucleons are taken as degrees of freedom, and interactions are fitted from the data involving nucleons or small nucleon systems. The main limitation is the availability of computing power.

All the approaches propose different truncation schemes of the unsolvable full nuclear many-body problem into a solvable one, limited to a model space. A naive hypothesis

is that the lack of configurations and correlations lead to the NMEs underestimation and overestimation, respectively, and this behaviour seems to be confirmed by the results shown in Figure 1.3. There is hope that the calculations could converge once their disagreements will be overcome. Indeed, indirect hints of the reliability of model calculations could come from their relative convergence to common values, even if this condition would not exclude that common unverified assumptions are still present in all the models.

Uncertainties in the NMEs evaluations are hard to be quantified and identified also because some of them, common to the different competing calculations, would shift all the matrix elements causing unknown overall systematic uncertainties. The use of quenched coupling constants within the nuclei, for the weak and strong interactions in the spin-isospin sector, is strongly debated in the last years [25]. In 2019, an important step forward was made by P. Gysbers and co-workers in the field of the single β-decay. In Ref. [26] the authors solved the 50 years old puzzle about the apparent quenching of the fundamental coupling constant by a factor of about 0.75. They demonstrated that, in the case of β-decay, the quenching of g_A arises to a large extent from the coupling of the weak force to two nucleons as well as from strong correlations in the nucleus. From the strong interaction side, a similar result has been recently presented in Ref. [27] by D. Gambacurta and co-workers. In their model, without *ad hoc* quenching factors, the inclusion of two-particle-two-hole configurations revealed to be very effective and has an impact on the integrated strengths which is comparable to (and even stronger than) the one produced by the inclusion of two-body currents in *ab initio* results. In the case of the $\beta\beta$-decays, preliminary encouraging results of controlled and small quenching correction factors were achieved. However, they have been recently questioned by a more comprehensive analysis of the leading order effects of two-body weak currents from chiral effective field theory (χEFT) [28]. In this case, two-body effects become divergent and must be renormalized by a contact operator, the coefficient of which is completely undetermined by χEFT at present. Lattice QCD calculations could, in principle, overcome this problem, but they are missing at the present time.

1.3 The NUMEN project

The future nuclear structure calculations purpose is to enlarge the adopted model-spaces in order to include all the relevant degrees of freedom and allow a complete description of the (A, Z) $\rightarrow$ (A, Z$\pm$2) nuclear transition mediated by the $0\nu\beta\beta$ weak operator.

The relevance of some model-space components is not *a priori* known and need to be checked, i. e. searching the support of experimental data.

First information have been searched through the study of single-charge exchange nuclear reactions [29–31] with the aim to extract the Gamow-Teller strength and consequently the nuclear response of the $0\nu\beta\beta$ candidates to nuclear first-order spin-isospin excitations. Furthermore, the occupancies of valence single-particle orbitals have been constrained from nucleon transfer reaction experimental data [32, 33] in order to improve the reliability of the NME calculations. However, despite these attempts, the ambiguities remained almost unchanged since the constraints were too loose to provide accurate values of the NMEs. In the $0\nu\beta\beta$ nuclear transition many single-particle and many-body nuclear properties are involved, even at the same time, and studying only one of these at a time proved to be insufficient.

In this scenario, the experimental study of double-charge exchange reactions, in analogy to the $\beta\beta$-decay, has revealed as the most promising approach. Pion-induced double charge exchange reactions [34–36] were performed but then abandoned due to the large differences in the structure of the operators. Double Charge Exchange (DCE) reactions induced by heavy-nuclei were also studied but, due the lack of zero-degree data and the poor yields in the measured energy spectra and angular distributions (cross sections ranging from about 5-40 nb/sr to 10 μb/sr [37–39]), were not conclusive. The additional complication of the possible contributions of multi-nucleon transfer reactions leading to the same final states complicated the interpretation of the data, nowadays not yet been deeply discussed.

The use of modern high resolution and large acceptance spectrometers has been proven to be effective in overcoming the main experimental challenges to perform zero-degree measurements and to extract reliable quantitative information from DCE reactions. The measurement of DCE high-resolution energy spectra and accurate absolute cross sections at very forward angles is essential to identify the transitions of interest. From the theoretical point of view, the concurrent measurement of all the relevant reaction channels is mandatory to untangle the nuclear structure from the nuclear reaction effects.

Thanks to the progress in both experimental and theoretical physics, nowadays most of the limits of the heavy-ion DCE of the 1980s could be overcome. The NUMEN (NUclear Matrix Elements for Neutrinoless double beta decay) project, proposed in 2015, has the main goal to investigate the nuclear response to SCE and DCE reactions induced by heavy projectiles at energies above the Coulomb barrier for all the isotopes

explored by present and future studies of $0\nu\beta\beta$ decay [1]. The main tools used to perform such experimental measurements are the K800 Superconducting Cyclotron [10] and the MAGNEX large acceptance magnetic spectrometer [11] installed at INFN-LNS. Several aspects of the project are requiring the development of innovative techniques, for both experimental set-up and theoretical analysis of the collected data. The work presented in this thesis has been developed among the purposes and methods of the NUMEN project that will be presented in the next paragraphs.

1.3.1 DCE reactions and $0\nu\beta\beta$ decays

The DCE and $0\nu\beta\beta$ decay are different processes mediated by the strong and weak interactions, respectively. In DCE, unlike in $0\nu\beta\beta$, also the projectile involved in the nuclear reaction plays an important role both from the nuclear structure and reaction dynamics side and sequential multi-nucleon transfer mechanisms can be involved as well. However, there are also a variety of important similarities among the two processes [1]:

- The initial and final many-body states involved are the same in both the $0\nu\beta\beta$ decay and in the DCE reaction;
- Both the $0\nu\beta\beta$ and the DCE operators have a short-range Fermi, a Gamow–Teller and rank-2 tensor components, even if with different relative weights, depending on the incident energy in the reaction case.
- A large linear momentum (≈ 100 MeV/c) is available in the virtual intermediate channel. It is worth to underline that other processes such as single β decay, $2\nu\beta\beta$ decay, SCE reactions induced by light ions are characterized by small momentum transfer, so they cannot probe this feature while the μ-capture experiments [40] could represent interesting developments in this context;
- Both processes require non-local operators acting on the same pairs of nucleons;
- Both transitions take place in the same nuclear medium. Since effects due to the presence of the nuclear medium are expected in both cases, DCE experimental data could give a helpful constraint on the theoretical determination of quenching phenomena in $0\nu\beta\beta$;
- In both cases there is an off-shell propagation through virtual intermediate nuclear states. Since the virtual states do not represent asymptotic channels, their energies are not well defined as those (measurable) at stationary conditions.

A simple relation between DCE cross sections and the $0\nu\beta\beta$ decay NMEs is not trivial and needs to be explored. The first step is to correctly describe the DCE reaction mechanism, in all direct (more than one!) and sequential components.

Again, the possibility to perform DCE nuclear reactions at very forward angles and measure the cross-sections and the development of new theories to analyse such experimental data, still leave open the question of how these results can be profitably used toward the experimental access to $0\nu\beta\beta$ decay NMEs. NMEs from DCE reactions and $0\nu\beta\beta$ decay require the same degree of complexity for the nuclear structure model, with the advantage for DCE to be accessible in the laboratory under controlled conditions.

The NUMEN project is as ambitious as it is complex both from the experimental and theoretical side. In the following the goals, the methods and the phases will be better clarified.

1.3.2 The goal(s)

The extraction of data-driven information on NME for all systems candidates to the $0\nu\beta\beta$ decay is the main goal of the NUMEN project. This implies an accurate description and a complete study of the reaction mechanism in both its reaction dynamics and nuclear structure parts. The latter can be factorized in a projectile and target components. The development of a consistent and coherent microscopic description of the DCE reaction and the nuclear structure part is essential to explore this opportunity and need to be explored for the different target systems at different bombarding energies [1].

The measurement of the DCE absolute cross sections could have a crucial impact in tuning the nuclear structure theories of $0\nu\beta\beta$ decay NMEs. As already said, the NMEs for DCE and $0\nu\beta\beta$ decay transitions share the same initial and final wave functions by operators with similar structure. Consequently, the measured DCE absolute cross sections allow to test the validity of the assumptions done for the truncation of the many-body wave functions. The reaction part needs to be precisely controlled to this purpose, a result that NUMEN aims to pursue within a fully quantum scattering framework. Once the nuclear wave functions have been constrained against DCE cross sections, the same can be used for $0\nu\beta\beta$ decay NMEs.

Another goal is to provide relative NME information on the different candidate isotopes of interest for the $0\nu\beta\beta$ decay. The ratio of the measured cross sections can give a model independent way to compare the sensitivity of different half-life experiments.

This result can be achieved even in presence of sizeable systematic errors in the measured cross sections and in the extraction of DCE matrix elements, as they are largely reduced in the ratio. Performing these comparative analyses could have strong impact in the future developments of the field, especially in a scenario where fundamental choices for the best isotope candidates for $0\nu\beta\beta$ decay need to be made.

1.3.3 The phases

Once fixed the goals, the NUMEN project was conceived in 2015 as a long-range time plan involving an intense experimental activity, a renewal of the INFN-LNS research infrastructure, a specific R&D activity on detectors, materials and instrumentations and a state-of-art development of new theoretical reaction formalisms for the DCE data analysis. NUMEN is divided into the four phases the are presented in the following and nowadays the project is in its phase 3.

1.3.3.1 Phase 1: Pilot experiment

In 2013 the $^{18}O + ^{40}Ca$ collision at 275 MeV incident energy was performed at the INFN-LNS exploring the $-1.2° < \theta_{lab} < 8°$ angular range, where θ_{lab} is the scattering angle in the laboratory frame. The $^{40}Ca(^{18}O,^{18}Ne)^{40}Ar$ DCE, the $^{40}Ca(^{18}O,^{18}F)^{40}K$ SCE, the $^{40}Ca(^{18}O,^{20}Ne)^{38}Ar$ two-proton transfer and the $^{40}Ca(^{18}O,^{16}O)^{42}Ca$ two-neutron transfer cross-sections were measured during the experiment. The experimental set-up and the data-reduction methods are described in Ref. [41].

The work showed for the first time high resolution and statistically significant experimental data of DCE reactions in a wide range of transferred momenta and scattering angles, including 0°. The measured differential cross-section for the ground-to-ground state transition in the $^{40}Ca(^{18}O,^{18}Ne)^{40}Ar$ DCE showed a clear oscillating pattern compatible with an L = 0 Bessel function and a suppression of the multi-nucleon transfer routes was found. Preliminary DCE matrix elements were extracted under the hypothesis of the dominance of the two-step double charge exchange reaction mechanism and, despite the large uncertainties of ±50% due to the simplified analysis scheme, the obtained results are compatible with the values from literature signalling that the gross of the physic content is been kept. Further studies have been performed to deeply analyse the experimental data in the DCE [9], SCE [42] and two-proton transfer [43] nuclear reaction channels. New experimental data have been acquired in further experiments for

the same system and have been recently published for the elastic and inelastic scattering [42], one-proton and one-neutron transfer reaction channels[44].

To prove the experimental feasibility of the NUMEN project was the main goal of the phase 1 pilot experiment and it has been completely achieved. The results obtained for the DCE makes the (^{18}O,^{18}Ne) reaction very interesting to investigate the DCE response of the nuclei involved in $0\nu\beta\beta$ research.

1.3.3.2 Phase 2: Preliminary experiments and R&D

Although the Phase 1 results indicated the experimental feasibility of the 0° measurements of DCE reactions and the possibility to extract information relevant for the $0\nu\beta\beta$ reaction, the experimental set-up used to perform those measurements was not appropriate to extend the research also to the cases of interest for $\beta\beta$-decay, due to the very low cross-sections involved [1]. This was confirmed also by the preliminary DCE cross-sections measurements performed during the Phase 2 that corresponds to tens of nbarn for the ground-to-ground state DCE transition. Although the very long experimental runs (3 to 4 weeks), the number of counts collected was often not enough to achieve sufficient statistical significance [45].

Preliminary experimental campaign The Phase 2 experiments were performed with integrated charge of tens of mC. The data taking required several weeks for each reaction, since thin targets are mandatory in order to achieve enough energy and angular resolution. The attention was focused on a few candidate cases for $\beta\beta$-decay with the goal to achieve conclusive results for them and more deeply understand the main features limiting the experimental sensitivity, resolution and systematic errors. During the Phase 2, the data reduction strategy was optimized through the development of more advanced algorithms.

Table 1.2 shows the systems studied during the NUMEN Phase 2. For each of the collisions a wide network of nuclear reactions have been studied under the same experimental conditions. The network of nuclear reactions included: elastic and inelastic scattering, one-nucleon and two-nucleon transfer, single and double charge exchange. We studied the (^{18}O,^{18}Ne) reaction as a probe for the $\beta^+\beta^+$ transitions and the (^{20}Ne,^{20}O) one for the $\beta^+\beta^+$. More details of the methods adopted to perform the experimental studies are discussed in Section 1.3.4.

The choice of the target isotopes was the result of a compromise between the $\beta\beta$-decay

Table 1.2: Nuclear systems studied during the Phase 2 of the NUMEN project.

Collision	Beam energy(AMeV)	References
^{18}O + ^{116}Sn	15.3	[46]
^{20}Ne + ^{116}Cd	15.3	[7, 47, 48]
^{20}Ne + ^{130}Te	15.3	[45, 46, 49]
^{20}Ne + ^{76}Ge	15.3	[50]
^{18}O + ^{76}Se	15.3	[51]
^{18}O + ^{12}C	15.3	[52]
^{18}O + ^{48}Ti	15.3	[53]
^{18}O + ^{12}C	22.0	-

interest of the scientific community to specific isotopes and related technical issues. The possibility to separate ground-to-ground state transition in the DCE measured energy spectra and the availability of thin uniform targets of isotopically enriched material was one of the more stringent constraint.

The experimental activity of NUMEN Phase 2 and the analysis of the results is the main aspect of the NURE project [116] recently awarded by the European Reseach Council. The synergy between the two projects is an added value which significantly enhance the discovery potential already achieved in NUMEN Phase 2.

Important theoretical progresses have been done during the NUMEN Phase 2 by developing new formalisms and performing numerical calculations. New reaction mechanisms have been formalised for SCE and DCE including important advances in nuclear reactions and nuclear structure [8, 9, 54–57].

Research and development activity The measurement of very small cross-sections implied the necessity to increase the beam current for the DCE experiments. This goal can be achieved by a substantial change in all the experimental set-up technologies.

In two recent publications [58, 59], the details of the experimental set-up upgrading are extensively described and all the results achieved and decisions taken during the R&D NUMEN Phase 2 are deeply discussed. The main novelties of the new experimental apparatus regard the Cyclotron beam extraction and transport, the development of a radiation tolerant cooling system for the targets used during the measurements, the introduction of a new γ-detectors array, the increase of the maximum accepted magnetic

rigidity of the MAGNEX spectrometer, the replacement of the wire-based gas tracker with a new micro pattern gas detector, the replacement of the wall of silicon pad stop detectors with a dedicated array of smaller size telescopes based on the SiC + CsI technology and the development of new electronics chains and data acquisition systems for high rate measurements.

1.3.3.3 Phase 3: Facility upgrade

Once all the building blocks for the upgrade of the whole facility were prepared, the NUMEN Phase 3 started in June 2020. At the same time the INFN-LNS initiated the disassembling of the old set-up and re-assembling of the new one. After one year from the beginning of the upgrade, the end of these operations and restarting of the experimental activity is expected to be in 2023.

During this period, the data analysis of the Phase 2 experiments (see Table 1.2) continued and nowadays all of them are completed or in a very advanced status. Tests of the new detectors and selected experiments will be performed in other laboratories (i. e. Institute of Physics of the University of Sao Paulo in Brazil, INFN-Laboratori Nazionali di Legnaro in Italy, iThemba in South Africa, Institute of Nuclear Physics of Orsay in France) in order to provide possible pieces of still missing information in the explored reactions network.

1.3.3.4 Phase 4: The high-intensity beam experiments

The NUMEN Phase 4 will consist of a series of experimental campaigns at high beam intensities (some pμA) and integrated charge of hundreds of mC up to C, for the experiments in which γ-coincidence measurements are required, spanning all the variety of $0\nu\beta\beta$ decay candidate isotopes of interest, like: ^{48}Ca, ^{76}Ge, ^{82}Se, ^{96}Zr, ^{100}Mo, ^{106}Cd, ^{110}Pd, ^{116}Cd, ^{110}Sn, ^{124}Sn, ^{128}Te, ^{130}Te, ^{136}Xe, ^{148}Nd, ^{150}Nd, ^{154}Sm, ^{160}Gd, ^{198}Pt. Based on the know-how gained during the experimental activity of Phase 2, the Phase 4 will be devoted to determine the absolute DCE cross sections and their uncertainties. Hopefully, the use of upgraded theoretical analyses will give access to the challenging NMEs $0\nu\beta\beta$ decay which is the most ambitious goal of the project.

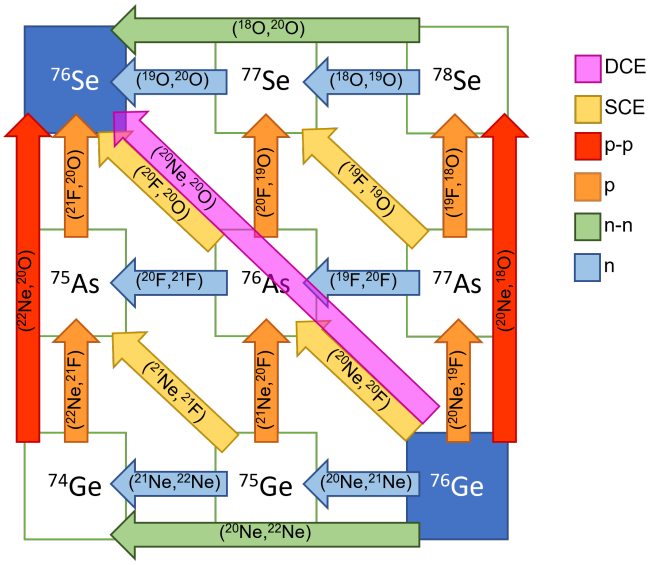

Figure 1.4: Cartoon of the nuclear transitions involved in the routes connecting the initial partition to the final DCE one in a typical NUMEN experiment with $^{20}Ne^{10+}$ ion beam. Here the cases of the ^{76}Ge target.

1.3.4 The method: a full-comprehensive experimental and theoretical multi-channel study

The heavy-ion collisions are performed at the INFN-LNS in Catania where the K800 Superconducting Cyclotron provides the ^{20}Ne and ^{18}O beams. The ejectiles, emerging from the heavy-ion direct nuclear reactions, are analysed in momentum by the MAGNEX spectrometer at forward angles including 0° in the case of the DCE measurements (see Chapter 3). The main experimental results are the excitation energy spectra and the absolute cross-sections. They are obtained thanks to a data-reduction procedure described in Chapter 4.

The use of the quantum approach and the Distorted Wave Born Approximation (DWBA), coupled channel (CC) or Coupled Reaction Channel (CRC) formalisms with form factors from state-of-art nuclear structure calculations is the suitable framework in which the theoretical description of all the nuclear reactions needs to be developed. The main features of these approaches, applied to the study of heavy-ion direct nuclear reactions, are described in Chapter 2 together with a brief summary of state-of-art nuclear theories for SCE and DCE reactions.

The complete set of routes connecting the initial to the final DCE partition is shown in Figure 1.4 for the ^{20}Ne + ^{76}Ge collision. The figure shows as the whole DCE reaction

comes from the competition of many different mechanisms. In order to shed light in the theoretical connection between measured cross sections of DCE nuclear reactions and the $0\nu\beta\beta$ NMEs, the most crucial aspect is the capability of nuclear theories to give the clearest and the most complete description of the DCE reaction mechanism. The direct DCE, called Majorana DCE (MDCE) [6] in analogy to the direct $0\nu\beta\beta$ Majorana process, indicated by the magenta arrow in Figure 1.4, is only a part of the complete DCE mechanism.

A wide network of nuclear reactions needs to be studied. Indeed, many features of the dynamical process and the structure of the colliding nuclei need to be understood through the study of nuclear reactions in order to disentangle the many DCE contributions:

- The initial and final state interactions, such as the ones competing to the intermediate partitions, are responsible for the distortion of the incoming and outgoing wave functions involved in nuclear reactions and play a central role in all the reaction mechanisms. Studies of *elastic and inelastic scattering* are mandatory to investigate nucleus-nucleus potential and nuclear deformations, respectively. These aspects are relevant to describe the mean field interaction among the nuclei and the role of the couplings with the first low-lying excited states.

- The occupation probabilities of valence orbits active in the decay and reaction dynamics is one of the most relevant features of the nuclear wave functions. In this framework, the study of *one-nucleon transfer reactions* is an irreplaceable tool to access the single-particle configurations in nuclear states.

- Many-body properties of nuclei, such as the pairing interaction, play a crucial role in the nuclear structure of the $\beta\beta$-candidates nuclei. *Two-nucleon transfer reactions* are very sensitive to those nuclear features and their study is one the most powerful tool to investigate them.

- Although recent studies are excluding a relevant role of the multi-nucleon transfers [7, 8], the role of the double-SCE is to date far from being considered negligible. In that case the double-SCE contribution to the total DCE can be estimated considering a folding of two SCE reaction amplitudes [9]. For that reason, it is particularly important to improve the description of the *single charge-exchange* process with the special purpose of factorizing the corresponding cross section into reaction and structure parts.

All the studies present in literature on heavy-ion induced direct reactions are focused on few (often one) reaction channels at the time. In this way the information extracted from data analysis cannot be fully constrained and important parameters need to be taken either from other experimental studies performed in similar conditions, or by model calculations. A comprehensive study of a wide ensemble of reaction channels explored in the same experimental conditions and consistently described by a unique theoretical framework would be desirable to make significant step forwards in the field. For that reason, the multi-channel approach, presented here for the first time, to the ^{18}O + ^{12}C, ^{18}O + ^{76}Se and ^{20}Ne + ^{76}Ge heavy-ion collisions at 15.3 AMeV is an important result.

This new approach needs to be tested and, for that reason, it has first been applied to the analysis of the ^{18}O + ^{12}C collisions at 275 MeV incident energy (see Chapter 5). The low density of states of all the nuclei involved in the explored partitions and the well known nuclear properties of such nuclei justify the choice of the target, despite it is typically far from the $\beta\beta$-decay research interests. In this study the focus is on the consistent approach to all the scrutinized channels of the colliding systems, with the aim to use then the same strategy for the exploration of isotopes of interest for $0\nu\beta\beta$ decay.

As already discussed, the NUMEN project wants to study the DCE mechanism in both directions through the (^{18}O,^{18}Ne) and the (^{20}Ne,^{20}O) reactions. Since NMEs are *time invariant* quantities, they are common to a DCE and to its inverse, so the contextual measurement of both directions in the DCE represents a useful test bench of the procedure to extract NME from the measured DCE cross section. The application of this approach to the ^{76}Ge-^{76}Se nuclear system, candidate for $0\nu\beta\beta$ decay, is reported in Chapter 6 in which the initial state interaction, the SCE and the DCE reaction channels are discussed.

Chapter References

[1] F. Cappuzzello et al. “The NUMEN project: NUclear Matrix Elements for Neutrinoless double beta decay”. In: *European Physical Journal A* 54.5 (2018). cited By 106. DOI: 10.1140/epja/i2018-12509-3.

[2] H. Ejiri, J. Suhonen, and K. Zuber. “Neutrino–nuclear responses for astro-neutrinos, single beta decays and double beta decays”. In: *Physics Reports* 797 (2019). Neutrino-nuclear responses for astro-neutrinos, single beta decays and double beta decays, pp. 1–102. DOI: 10.1016/j.physrep.2018.12.001.

[3] S. Dell’Oro et al. “Neutrinoless Double Beta Decay: 2015 Review”. In: *Advances in High Energy Physics* 2016.2162659 (2016), p. 37. DOI: 10.1155/2016/2162659.

[4] M. J. Dolinski, A. W.P. Poon, and W. Rodejohann. “Neutrinoless Double-Beta Decay: Status and Prospects”. In: *Annual Review of Nuclear and Particle Science* 69.1 (2019), pp. 219–251. DOI: 10.1146/annurev-nucl-101918-023407.

[5] J. Engel and J. Menéndez. “Status and future of nuclear matrix elements for neutrinoless double-beta decay: a review”. In: *Reports on Progress in Physics* 80.4 (2017), p. 046301.

[6] H. Lenske et al. “Heavy ion charge exchange reactions as probes for nuclear β-decay”. In: *Progress in Particle and Nuclear Physics* 109 (2019), p. 103716. ISSN: 0146-6410. DOI: 10.1016/j.ppnp.2019.103716.

[7] D. Carbone et al. “Analysis of two-nucleon transfer reactions in the ^{20}Ne + ^{116}Cd system at 306 MeV”. In: *Physical Review C* 102.4 (2020). cited By 6. DOI: 10.1103/PhysRevC.102.044606.

[8] J. L. Ferreira et al. “Multinucleon transfer in the ^{116}Cd(^{20}Ne,^{20} O)^{116}Sn double charge exchange reaction at 306 MeV incident energy”. In: *Phys. Rev. C* 105 (1 Jan. 2022), p. 014630. DOI: 10.1103/PhysRevC.105.014630.

[9] J. I. Bellone et al. “Two-step description of heavy ion double charge exchange reactions”. In: *Physics Letters B* 807 (2020), p. 135528. ISSN: 0370-2693. DOI: 10.1016/j.physletb.2020.135528.

[10] D. Rifuggiato, L. Calabretta, and G. Cuttone. “Cyclotrons and their applications. Proceedings, 17th International Conference, Cyclotrons 2004”. In: *Part. Accel. Soc. Japan (2004) 541 p* (2004). Ed. by Akira Goto.

[11] F. Cappuzzello et al. “The MAGNEX spectrometer: results and perspectives”. In: *Eur. Phys. J.* A52.6 (2016), p. 167. DOI: 10.1140/epja/i2016-16167-1.

[12] A. B. McDonald. “Nobel Lecture: The Sudbury Neutrino Observatory: Observation of flavor change for solar neutrinos”. In: *Rev. Mod. Phys.* 88 (3 July 2016), p. 030502. DOI: 10.1103/RevModPhys.88.030502.

[13] E. Majorana. “Teoria simmetrica dell’elettrone e del positrone”. In: *Il Nuovo Cimento (1924-1942)* 14 (1937), pp. 171–184.

[14] J. Menéndez *et al.* “Is it possible to study neutrinoless $\beta\beta$ decay by measuring double Gamow-Teller transitions?” In: *J. Phys.: Conf. Ser.* 1056, 012037 (July 2018), p. 012037. DOI: 10.1088/1742-6596/1056/1/012037.

[15] M. Goeppert-Mayer. “Double Beta-Disintegration”. In: *Phys. Rev.* 48 (6 Sept. 1935), pp. 512–516. DOI: 10.1103/PhysRev.48.512.

[16] M. G. Inghram and J. H. Reynolds. “Double Beta-Decay of ^{130}Te”. In: *Phys. Rev.* 78 (6 June 1950), pp. 822–823. DOI: 10.1103/PhysRev.78.822.2.

[17] S. R. Elliott, A. A. Hahn, and M. K. Moe. “Direct evidence for two-neutrino double-beta decay in ^{82}Se”. In: *Phys. Rev. Lett.* 59 (18 Nov. 1987), pp. 2020–2023. DOI: 10.1103/PhysRevLett.59.2020.

[18] W. H. Furry. “On Transition Probabilities in Double Beta-Disintegration”. In: *Phys. Rev.* 56 (12 Dec. 1939), pp. 1184–1193. DOI: 10.1103/PhysRev.56.1184.

[19] M. Agostini et al. “Final Results of GERDA on the Search for Neutrinoless Double-β Decay”. In: *Phys. Rev. Lett.* 125 (25 Dec. 2020), p. 252502. DOI: 10.1103/PhysRevLett.125.252502.

[20] F. T. Avignone, S. R. Elliott, and J. Engel. “Double beta decay, Majorana neutrinos, and neutrino mass”. In: *Rev. Mod. Phys.* 80 (2 Apr. 2008), pp. 481–516. DOI: 10.1103/RevModPhys.80.481.

[21] S. Stoica and M. Mirea. “New calculations for phase space factors involved in double-β decay”. In: *Phys. Rev. C* 88 (3 Sept. 2013), p. 037303. DOI: 10.1103/PhysRevC.88.037303.

[22] Du šan Štefánik et al. “Reexamining the light neutrino exchange mechanism of the $0\nu\beta\beta$ decay with left- and right-handed leptonic and hadronic currents”. In: *Phys. Rev. C* 92 (5 Nov. 2015), p. 055502. DOI: 10.1103/PhysRevC.92.055502.

[23] V. I. Tretyak and Y. G. Zdesenko. “Tables of double beta decay data - an update”. In: *Atomic Data and Nuclear Data Tables* 80.1 (2002), pp. 83–116. ISSN: 0092-640X. DOI: https://doi.org/10.1006/adnd.2001.0873.

[24] R. Saakyan. “Two-Neutrino Double-Beta Decay”. In: *Annual Review of Nuclear and Particle Science* 63.1 (2013), pp. 503–529. DOI: 10.1146/annurev-nucl-102711-094904.

[25] F. Cappuzzello and M. Cavallaro. “Nuclear Response to Second-Order Isospin Probes in Connection to Double Beta Decay”. In: *Universe* 6.11 (2020). ISSN: 2218-1997. DOI: 10.3390/universe6110217.

[26] P. Gysbers et al. “Discrepancy between experimental and theoretical β-decay rates resolved from first principles”. In: *Nat. Phys.* 15.1 (2019), pp. 428–431. DOI: 10.1038/s41567-019-0450-7.

[27] D. Gambacurta, M. Grasso, and J. Engel. "Gamow-Teller Strength in ^{48}Ca and ^{78}Ni with the Charge-Exchange Subtracted Second Random-Phase Approximation". In: *Phys. Rev. Lett.* 125 (21 Nov. 2020), p. 212501. DOI: 10.1103/PhysRevLett.125.212501.

[28] L.-J. Wang, J. Engel, and J. M. Yao. "Quenching of nuclear matrix elements for $0\nu\beta\beta$ decay by chiral two-body currents". In: *Phys. Rev. C* 98 (3 Sept. 2018), p. 031301. DOI: 10.1103/PhysRevC.98.031301.

[29] H. Akimune et al. "GT strengths studied by (^{3}He, t) reactions and nuclear matrix elements for double beta decays". In: *Physics Letters B* 394.1 (1997), pp. 23–28. ISSN: 0370-2693. DOI: https://doi.org/10.1016/S0370-2693(96)01659-0.

[30] D. Frekers. "Nuclear reactions and the double beta decay". In: *Progress in Particle and Nuclear Physics* 64.2 (2010). Neutrinos in Cosmology, in Astro, Particle and Nuclear Physics, pp. 281–284. ISSN: 0146-6410. DOI: https://doi.org/10.1016/j.ppnp.2009.12.029.

[31] C. J. Guess et al. "The ^{150}Nd(^{3}He,t) and ^{150}Sm(t,^{3}He) reactions with applications to $\beta\beta$ decay of ^{150}Nd". In: *Phys. Rev. C* 83 (6 June 2011), p. 064318. DOI: 10.1103/PhysRevC.83.064318.

[32] J. P. Schiffer et al. "Nuclear Structure Relevant to Neutrinoless Double β Decay: ^{76}Ge and ^{76}Se". In: *Phys. Rev. Lett.* 100 (11 Mar. 2008), p. 112501. DOI: 10.1103/PhysRevLett.100.112501.

[33] S. J. Freeman and J. P. Schiffer. "Constraining the $0\nu\beta\beta$ matrix elements by nuclear structure observables". In: *Journal of Physics G: Nuclear and Particle Physics* 39.12 (Nov. 2012), p. 124004. DOI: 10.1088/0954-3899/39/12/124004.

[34] J. D. Vergados. "Pion-double-charge-exchange contribution to neutrinoless double-β decay". In: *Phys. Rev. D* 25 (3 Feb. 1982), pp. 914–917. DOI: 10.1103/PhysRevD.25.914.

[35] A. Fazely and L. C. Liu. "Neutrinoless Double-β Decay and Its Relation to Pion Double Charge Exchange". In: *Phys. Rev. Lett.* 57 (8 Aug. 1986), pp. 968–971. DOI: 10.1103/PhysRevLett.57.968.

[36] S. Mordechai et al. “Pion Double Charge Exchange to the Double Dipole Resonance”. In: *Phys. Rev. Lett.* 61 (5 Aug. 1988), pp. 531–534. DOI: 10.1103/PhysRevLett.61.531.

[37] J. Blomgren et al. “Search for double Gamow-Teller strength by heavy-ion double charge exchange”. In: *Physics Letters B* 362.1 (1995), pp. 34–38. ISSN: 0370-2693. DOI: https://doi.org/10.1016/0370-2693(95)01190-2.

[38] F. Naulin et al. “Mass of ^{18}C from the double-charge-exchange reaction ^{48}Ca(^{18}O, ^{18}C) ^{48}Ti”. In: *Phys. Rev. C* 25 (2 Feb. 1982), pp. 1074–1075. DOI: 10.1103/PhysRevC.25.1074.

[39] D. M. Drake et al. “Exotic Heavy-Ion Reactions on ^{40}Ca: (^{14}C, ^{14}O) Double Charge Exchange and (^{14}C, ^{15}O) Rearrangement Transfer”. In: *Phys. Rev. Lett.* 45 (22 Dec. 1980), pp. 1765–1769. DOI: 10.1103/PhysRevLett.45.1765.

[40] L. Jokiniemi et al. “Pinning down the strength function for ordinary muon capture on ^{100}Mo”. In: *Physics Letters B* 794 (2019), pp. 143–147. ISSN: 0370-2693. DOI: https://doi.org/10.1016/j.physletb.2019.05.037.

[41] F. Cappuzzello et al. “Heavy-ion double charge exchange reactions: A tool toward $0\nu\beta\beta$ nuclear matrix elements”. In: *Eur. Phys. J.* A51.11 (2015), p. 145. DOI: 10.1140/epja/i2015-15145-5.

[42] M. Cavallaro et al. “A Constrained Analysis of the ^{40}Ca(^{18}O,^{18}F)^{40}K Direct Charge Exchange Reaction Mechanism at 275 MeV”. In: *Frontiers in Astronomy and Space Sciences* 8 (2021), p. 61. DOI: 10.3389/fspas.2021.659815.

[43] J.L. Ferreira et al. “Analysis of two-proton transfer in the ^{40}Ca (^{18}O, ^{20}Ne) ^{38}Ar reaction at 270 MeV incident energy”. In: *Physical Review C* 103.5 (2021). cited By 0. DOI: 10.1103/PhysRevC.103.054604.

[44] S. Calabrese et al. “^{18}O-induced single-nucleon transfer reactions on ^{40}Ca at 15.3A MeV within a multichannel analysis”. In: *Phys. Rev. C* 104 (6 Dec. 2021), p. 064609. DOI: 10.1103/PhysRevC.104.064609.

[45] V. Soukeras et al. “Measurement of the double charge exchange reaction for the ^{20}Ne + ^{130}Te system at 306 MeV”. In: *Results in Physics* 28 (2021), p. 104691. ISSN: 2211-3797. DOI: https://doi.org/10.1016/j.rinp.2021.104691.

[46] D. Carbone et al. “Initial state interaction for the ^{20}Ne + ^{130}Te and ^{18}O + ^{116}Sn systems at 15.3 AMeV from elastic and inelastic scattering measurements”. In: *Universe* 7.3 (2021). cited By 1. DOI: 10.3390/universe7030058.

[47] S. Calabrese et al. “Analysis of the background on cross section measurements with the MAGNEX spectrometer: The (20Ne, 20O) Double Charge Exchange case”. In: *Nuclear Instruments and Methods in Physics Research, Section A: Accelerators, Spectrometers, Detectors and Associated Equipment* 980 (2020). cited By 0. DOI: 10.1016/j.nima.2020.164500.

[48] S. Burrello et al. “Multichannel experimental and theoretical constraints for the ^{116}Cd(^{20}Ne,^{20} F)^{116}In charge exchange reaction at 306 MeV”. In: *Phys. Rev. C* 105 (2 Feb. 2022), p. 024616. DOI: 10.1103/PhysRevC.105.024616.

[49] M. Cavallaro et al. “Charge-state distributions of ^{20}Ne ions emerging from thin foils”. In: *Res. in Phys.* 13 (2019), p. 102191. ISSN: 2211-3797. DOI: https://doi.org/10.1016/j.rinp.2019.102191.

[50] A. Spatafora et al. “^{20}Ne+^{76}Ge elastic and inelastic scattering at 306 MeV”. In: *Phys. Rev. C* 100 (3 Sept. 2019), p. 034620. DOI: 10.1103/PhysRevC.100.034620.

[51] L. La Fauci et al. “^{18}O +^{76} Se elastic and inelastic scattering at 275 MeV”. In: *Phys. Rev. C* 104 (5 Nov. 2021), p. 054610. DOI: 10.1103/PhysRevC.104.054610.

[52] F. Cappuzzello et al. “Confirmation of Giant Pairing Vibration evidence in ^{12,13}C(^{18}O,^{16}O) ^{14,15}C reactions at 275 MeV”. In: *European Physical Journal A* 57.1 (2021). cited By 1. DOI: 10.1140/epja/s10050-021-00345-7.

[53] O. Sgouros et al. “One-proton transfer reaction for the ^{18}O +^{48} Ti system at 275 MeV”. In: *Phys. Rev. C* 104 (3 Sept. 2021), p. 034617. DOI: 10.1103/PhysRevC.104.034617.

[54] H. Lenske et al. “Theory of Single Charge Exchange Heavy Ion Reactions”. In: *Phys. Rev.* C98.4 (2018), p. 044620. DOI: 10.1103/PhysRevC.98.044620.

[55] H. Lenske. “Probing Double Beta-Decay by Heavy Ion Charge Exchange Reactions”. In: *J. Phys.: Conf. Ser.* 1056 (July 2018), p. 012030. DOI: 10.1088/1742-6596/1056/1/012030.

[56] J. A. Lay et al. “Double charge-exchange reactions and the effect of transfer”. In: *Journal of Physics: Conference Series* 1056 (July 2018), p. 012029. DOI: 10.1088/1742-6596/1056/1/012029.

[57] E. Santopinto et al. “Heavy-ion double-charge-exchange and its relation to neutrinoless double-β decay”. In: *Phys. Rev. C* 98 (6 Dec. 2018), p. 061601. DOI: 10.1103/PhysRevC.98.061601.

[58] P. Finocchiaro et al. “The NUMEN Heavy Ion Multidetector for a Complementary Approach to the Neutrinoless Double Beta Decay”. In: *Universe* 6.9 (2020). ISSN: 2218-1997. DOI: 10.3390/universe6090129.

[59] F. Cappuzzello et al. “The NUMEN Technical Design Report”. In: *International Journal of Modern Physics A* 0.0 (0), p. 2130018. DOI: 10.1142/S0217751X21300180.

La filosofia è scritta in questo grandissimo libro che continuamente ci sta aperto innanzi a gli occhi (io dico l'universo), ma non si può intendere se prima non s'impara a intender la lingua, e conoscer i caratteri, ne' quali è scritto. Egli è scritto in lingua matematica, e i caratteri son triangoli, cerchi, ed altre figure geometriche, senza i quali mezzi è impossibile a intenderne umanamente parola; senza questi è un aggirarsi vanamente per un oscuro laberinto.

G. Galilei, Il saggiatore, 1624

2

Heavy-ion direct nuclear reactions

Contents

The direct-nuclear reactions are the main subject of the work presented in this thesis. For this reason, I thought to be appropriate to insert a brief review of the scattering theory basic concepts useful to introduce the analysis of the experimental data described in the Chapters 5 and 6. However, «The question of defining direct reactions is one to which no all-embracing answer can be given» said G. R. Satchler in the first chapter of its most famous book (see Ref. [60]) that is nowadays the user manual for the direct nuclear reaction theory. Qualitatively, if the overlap between the incoming and outgoing wave-functions of the nuclei involved in the reaction is large, the collision may quickly occur with a minimum rearrangement of the constituent nucleons and it may be called *direct*. In order to have a more quantitative approach it appears appropriate to clarify *where* and *when* (or better to say *in which time*) the direct nuclear reactions occur.

To answer to the question of *where* the direct nuclear reactions occur, we may underline that the projectile can interact with just one or few nucleons of the target or can just stimulate simple modes of nuclear motion if they meet in their surface region. However, the picture of direct reaction being strictly localized in the surface is oversimplified [60]. One exception is the elastic scattering of low-energy nucleons for which there is a finite probability to pass through the target nucleus without being absorbed. Despite this nuclear transparency phenomenology, most non-elastic direct nuclear reactions occurs in the surface region.

On *when* the direct nuclear reactions happen, they are completed in a time of the order of the transit time of the projectile across the target, which is comparable to the time it takes a target nucleon to complete one orbit. The most interesting consequence of this property is that if the reaction happens quickly, it will vary slowly with the changing in bombarding energy. Indeed, a rapid variation with energy, such resonances or fluctuating cross-sections, implies a long reaction time compared to the passage time and hence the formation of an intermediate system with a relatively long life (compound nucleus).

The direct nuclear reactions attract attentions as they are a good source of information on nuclear structure. Since they proceed through a single step, or at least only few steps are relevant to describe the processes up to very high order, the reaction amplitudes depend on the overlap of the initial and final states. This overlaps is generally introduced in terms of the *spectroscopic amplitudes* and *response functions* in the case of nucleon-transfer and single charge exchange direct nuclear reactions, respectively.

The most obvious example of direct nuclear reaction is the elastic scattering, where the initial and final wave-functions are exactly the same. Elastic scattering dominates

in terms of flux intensity over all of the direct nuclear reaction channels and for that reason it makes sense to write

$$V(\mathbf{r}_i, x_i) = U(\mathbf{r}_i) + V_{res}(\mathbf{r}_i, x_i) \tag{2.1}$$

where the complete interaction $V(\mathbf{r}_i, x_i)$, depending on the internal variables x_i of the nuclei and on their distances $\mathbf{r}_i$, is divided into two pieces. The $U(\mathbf{r}_i)$ component is the optical potential, mainly depending on the distance between the two nuclei, that describes the nucleus-nucleus average interaction. The $V_{res}(\mathbf{r}_i, x_i)$ term, depending on the internal variables x_i, describes the residual part of the interaction.

The $U(\mathbf{r}_i)$ of Equation 2.1 is often treated in the optical model framework in which, same as in the optical physics, the potential is only responsible to deflect the interacting nuclei trajectories so to describe the most part of the direct nuclear reaction. Furthermore, the potential U must be complex [60] because of the possibility of flux absorption into compound nucleus even at bombarding energies below the lowest non-elastic threshold or into any reaction channel not explicitly introduced in the coupling scheme. The U potential is non-local due to the Pauli principle that implies the presence of an exchange term in the treatment of many-body average potential. This non local component is often treated in local-equivalent momentum dependent approaches [61, 62].

The V_{res} term is very small in comparison to the optical potential. This fact justifies the use of a perburbative treatment of V_{res} responsible for the less intense but much more interesting reaction channels such as the transfer of nucleons or the single and double charge exchange. In the following section we are going to introduce the main features of the quantum many-body scattering theory used in describing direct nuclear reactions. A review of single and double charge exchange as nuclear response to first and second-order isospin probes has been recently published by Cappuzzello et al. in Ref. [25]. A brief summary of the main aspects, relevant for the purposes of this thesis, is also presented in the following sections.

2.1 Quantum scattering theory for direct nuclear reactions

Nuclear quantum scattering theory is complicated due to the many-body nature characterizing the nuclear systems. In fact, for elementary particles the elastic scattering can be treated as the scattering of a particle with reduced mass in a potential with a

fixed centre. Nuclear many-body colliding systems, on the other hand, are treated only as a first approximation as objects imperturbable in their internal degrees of freedom, even if the initial and final states of the particles are absolutely identical.

Quantum scattering task is to solve the time dependent Schrödinger equation

$$i\hbar\frac{d}{dt}\left|\psi\right\rangle = \hat{H}\left|\psi\right\rangle \tag{2.2}$$

where $\hat{H} = \hat{H}_0 + \hat{V}$ is the time-dependent complete Hamiltonian. The Lippmann-Schwinger (LS) equation

$$\left|\psi\right\rangle = \left|\phi\right\rangle + \hat{G}_0\hat{V}\left|\psi\right\rangle \tag{2.3}$$

is a formal solution of the Schrödinger problem in Equation 2.2 and it is made by a decomposition of $\left|\psi\right\rangle$ in the plane wave $\left|\phi\right\rangle$ and the perturbed $\hat{G}_0\hat{V}\left|\psi\right\rangle$ terms. $\hat{G}_0$ is the propagation operator of the system governed by the unperturbed $\hat{H}_0$ Hamiltonian. This solution has the advantage to provide a recursive approach in which one can truncate the expansion at a given term corresponding to a given degree of approximation

$$\left|\psi\right\rangle = \left|\phi\right\rangle + \hat{G}_0\hat{V}\left|\phi\right\rangle + \hat{G}_0\hat{V}\hat{G}_0\hat{V}\left|\phi\right\rangle + \hat{G}_0\hat{V}\hat{G}_0\hat{V}\hat{G}_0\hat{V}\left|\phi\right\rangle + \dots \tag{2.4}$$

It is also useful, in this framework, to introduce the T-matrix operator

$$\hat{T}\left|\phi\right\rangle = \hat{V}\left|\psi\right\rangle \tag{2.5}$$

that has the property of representing the full effect on $\left|\psi\right\rangle$ of the potential $\hat{V}$ but in the case in which it was applied to the plane wave $\left|\phi\right\rangle$. Inserting the Equation 2.4 in the 2.5 one can obtain the following recursive definition

$$\hat{T} = \hat{V} + \hat{V}\hat{G}_0\hat{V} + \hat{V}\hat{G}_0\hat{V}\hat{G}_0\hat{V} + \hat{V}\hat{G}_0\hat{V}\hat{G}_0\hat{V}\hat{G}_0\hat{V} + \dots \tag{2.6}$$

useful to better understand many approximations that will be presented in the following.

2.1.1 Cross-section definition and approximations

The LS equation (2.3) in coordinate space and in case of a $\hat{V}$ local potential, can be rewritten as follows

$$\psi(\mathbf{x}) \simeq e^{i\mathbf{k}\cdot\mathbf{x}} + f(\theta)\frac{e^{ikx}}{x} \tag{2.7}$$

where the scattering amplitude $f(\theta)$ is

$$f(\theta) = -\frac{\mu}{2\pi\hbar^2} \int dx' e^{-i\mathbf{k}'\cdot\mathbf{x}'} \hat{V}(x')\psi(x') \tag{2.8}$$

The scattering amplitude is the key ingredient in the study of direct nuclear reactions because of its close relation with the angular distribution of differential cross-section

$$\frac{d\sigma}{d\Omega}(\theta) = |f(\theta)|^2$$

The simplest way to evaluate the scattering amplitude is to consider a plane wave inside the integral of Equation 2.8. This approximation consists in stopping the sums in Equations 2.4 and 2.6 to the first order and is called ordinary Born Approximation or Plane Wave Born Approximation (PWBA).

The Distorted Wave Born Approximation (DWBA) consists in reformulate the LS problem defining a new $\hat{H}_1$ operator which includes not only the $\hat{H}_0$ term but also the main treatable average component $U(\mathbf{r}_i)$ of the potential introduced in Equation 2.1. The $U(\mathbf{r}_i)$ can be treated, for example, in the optical model framework, as already said, and the solution of the operator $\hat{H}_1 = \hat{H}_0 + U_{OM}$ can be easily evaluated. We distinguish two solutions: one consisting of a plane wave plus an outgoing scattered wave and the other consisting of the plane wave and an ingoing scattered wave denoted by the $\chi^{(+)}(\mathbf{k},\mathbf{x})$ and $\chi^{(-)}(\mathbf{k},\mathbf{x})$ symbols, respectively. The two are related by the $\chi^{(+)}(\mathbf{k},\mathbf{x}) = \left(\chi^{(+)}(-\mathbf{k},\mathbf{x})\right)^*$ since the one is the time-inverse of the other. These are the *distorted waves*.

In analogy to the plane wave approximation, the DWBA consists in doing the approximation $\psi(\mathbf{x}) \simeq \chi^{(+)}(\mathbf{k},\mathbf{x})$ and use it in Equation 2.3. The new scattering amplitude, resulting from this approximation, is

$$\begin{aligned} &f_{DWBA}(\theta) = f_1(\theta) + f_{res}(\theta) = \\ &\quad = -\frac{\mu}{2\pi\hbar^2}\left[\int dx' e^{-i\mathbf{k}'\cdot\mathbf{x}'}\hat{U}\chi^{(+)}(\mathbf{k},\mathbf{x}') + \int dx' \left(\chi^{(-)}(\mathbf{k}',\mathbf{x}')\right)^* \hat{V}_{res}\chi^{(+)}(\mathbf{k},\mathbf{x}')\right] \end{aligned} \tag{2.9}$$

that is the sum of the contribution associated with the potential U (exactly solved) and the one associated to the $\hat{V}_{res}$ component of the complete interaction potential.

2.1.2 Coupled channels method

The coupled channels approaches, namely coupled-channel (CC), coupled-channel Born approximation (CCBA) and coupled reaction channel (CRC), are methods in which a set of coupled equations is defined in a restricted model space and exactly solved. The model space contains a selection of the infinite many-body possible configurations. The use of such approaches is necessary to clarify if the loss or excess of flux in a specific reaction channel is due to the couplings with specific partitions or states in the same partition. They also have effects on the distortion of the incoming and outgoing spherical waves defined in the previous paragraphs and consequently can directly influence all of the other reaction channels results. A complete description of these approaches is present in Ref. [60] and in the following the main relevant aspects and differences among them will be introduced.

The reduced portion of the complete set of many-body configurations is called model space and the operators acting within this space are effective operators. The minimal space only includes the entrance α and exit β partitions in which the involved nuclei are in their ground state. The model space can be extended including some excited bound or continuum states of the already included partitions or other γ or δ intermediate partitions. Let us consider the minimal space and define the model space wave function as

$$\Psi_{model} = u_\alpha(\alpha)\psi_\alpha(x_\alpha) + u_\beta(\beta)\psi_\beta(x_\beta) \tag{2.10}$$

where $u_\alpha(\alpha)$ and $\psi_\alpha(x_\alpha)$ describe the relative motion of the a and A (projectile and target nuclei) and the internal state configuration of the α partition. The same is also assumed for β. Let us introduce now these two equivalent forms of the effective Hamiltonian operator

$$H = H_\alpha + K_\alpha + V_\alpha = H_\beta + K_\beta + V_\beta \tag{2.11}$$

and project the model Schrödinger equation $(E - H)\Psi_{model} = 0$ in each of the defined partitions. The following coupled equations are:

$$\begin{aligned} \left[(E - \epsilon_\alpha) - K_\alpha - (\alpha|V_\alpha|\alpha)\right] u_\alpha(\mathbf{r}_\alpha) &= u_\beta(\psi_\alpha|H - E|\psi_\beta) \\ \left[(E - \epsilon_\beta) - K_\beta - (\beta|V_\beta|\beta)\right] u_\beta(\mathbf{r}_\beta) &= u_\alpha(\psi_\beta|H - E|\psi_\alpha) \end{aligned} \tag{2.12}$$

This example regards the two channel case. In general, the number of coupled equations is equal to the number of configurations considered in the model space.

Let us consider now the case of the elastic and inelastic scattering. In such case the final β partition is the same as the initial α and we can introduce in the model space only one excitation for the projectile or for the target nuclei. The coupled equations in such a case are the following:

$$\begin{aligned}[E - \epsilon_\alpha - K_\alpha - U_{\alpha\alpha}]\, u_\alpha(\mathbf{r}) &= U_{\alpha\alpha'} u_{\alpha'}(\mathbf{r}) \\ [E - \epsilon_{\alpha'} - K_{\alpha'} - U_{\alpha'\alpha'}]\, u_{\alpha'}(\mathbf{r}) &= U_{\alpha'\alpha} u_\alpha(\mathbf{r})\end{aligned} \tag{2.13}$$

where the U potentials are coupling potentials. $U_{\alpha\alpha'}$ promotes the transition from the ground state α to the only introduced α' excited state. An example of such coupling potential in the case of inelastic scattering will be presented in Sec. 5.2.1 in terms of deformed potentials. Although nucleon-transfer or single charge exchange coupling potentials have more complicated features that will be discussed in the next section, once the model space and proper coupling potentials are defined, the problem can always be reduced to a set of coupled equations similar to the ones in Equations 2.12 or 2.13.

The solution of coupling equations proceeds recursively. In the first step the set of coupled equations is simplified as follows

$$\begin{aligned}[E - \epsilon_\alpha - K_\alpha - U_{\alpha\alpha}]\, u_\alpha(\mathbf{r}) &\simeq 0 \\ [E - \epsilon_{\alpha'} - K_{\alpha'} - U_{\alpha'\alpha'}]\, u_{\alpha'}(\mathbf{r}) &= U_{\alpha'\alpha} u_{\alpha'}(\mathbf{r})\end{aligned} \tag{2.14}$$

and the $u_\alpha(\mathbf{r})$ solution is determined. Such approximation is justified since $u_\alpha(\mathbf{r})$ represents the elastic scattering large component while $u_{\alpha'}(\mathbf{r})$ is the inelastic small one. The $u_\alpha(\mathbf{r})$ is now inserted in the second of Equation 2.14 to evaluate the solution also for the $u_{\alpha'}(\mathbf{r})$ inelastic component. This approach, up to now, is completely equivalent to the DWBA approximation introduced in the previous paragraphs. This is a good approximation of the final solution if the $u_{\alpha'}(\mathbf{r})$ component is small compared to $u_\alpha(\mathbf{r})$ in all the energy and angular ranges considered. In the CC approach $u_{\alpha'}(\mathbf{r})$ is again inserted in the first equation of 2.13 to determine the changes in $u_\alpha(\mathbf{r})$ due to the $U_{\alpha\alpha'} u_{\alpha'}(\mathbf{r})$ coupling finding a new second-step DWBA solution, and so on.

The CC and CRC methods are the infinite iterations limit for this recursive approach in case of states competing to the same partition and to different partitions, respectively. Sometimes it is useful to treat in the full infinite order the coupling among the same initial or final partition and to adopt the first order DWBA approximation for the coupling between different partitions. This approach is called CCBA.

2.2 Single charge exchange reactions

In SCE nuclear reactions, a neutron (proton) of the target transforms into a proton (neutron) while the opposite transition simultaneously occurs in the projectile. Using the isospin degree of freedom, SCE reactions are the isovector excitations induced by a combination of the isospin rising and lowering $\tau_{a\pm}\tau_{A\mp}$ operators acting on a nucleon in the a projectile and A the target, respectively. The monopole response $\Delta L = 0$ is particularly interesting since the associated $\sigma\tau$ operator is formally analogous to the Gamow–Teller (GT) one acting in the β-decay.

Important reviews are found in the reports by Alford and Spicer [63], for the experimental aspects of SCE induced by light projectiles, and by Osterfeld [64] for a description of the theoretical aspects. Another relevant paper was published by Taddeucci et al. [65], proposing a useful factorization of the (p,n) and (n,p) cross-section into a reaction factor, named unit cross-section, and a matrix element connected to the nuclear structure overlap. More recently, the attention has been pointed out to SCE reactions induced by heavy projectiles, mainly discussed in the recent review from Lenske et al. [6].

2.2.1 Analogy with beta decay

The strong interaction is responsible for the SCE nuclear reaction in which isovector mesons are exchanged. At low momentum transfer compared to the π mass, the lightest meson, the SCE is weakly influenced by the meson form factors and a simplified description in terms of smoothly energy-dependent coupling factors is allowed. This approach is the same as the one adopted for the weak interaction, where constant coupling factors g_V and g_A control the isospin and spin-isospin operators. As a consequence, SCE reactions are complementary to β-decay.

An interesting exploration of such complementarity regards the investigation of the GT nuclear transitions by SCE reactions. Indeed, the study of the isovector monopole response ($\Delta J^\pi = 1^+$, $\Delta L = 0$; $\Delta\sigma = 1$; $\Delta\tau = 1$) by β-decay is possible only within a reduced accessible energy window, but this is not the case for SCE reactions. The GT strength, measured by SCE transitions, is broadly fragmented over many states corresponding to different excitation energies in the region of the Gamow–Teller Resonance (GTR) [66, 67]. This is due to the fact that the $\sigma\tau$ operator is not a symmetry for the nuclear systems and, as a consequence, the GT strength distribution is a fingerprint of the nucleus, reflecting in detail its peculiar many-body nature. Therefore, the nuclear

physics community has continuously put efforts into the exploration of GT strength.

Particular care should be paid to keep the momentum transfer as small as possible in order to filter out the $\Delta L \neq 0$ components in the collision or easily unfold them in the data analysis. Such condition is typically matched at incident energy above 100 AMeV and very forward scattering angles. In the years, GT studies have been performed via SCE reactions induced by (n,p), (d,^{2}He), (t,^{3}He), (^{7}Li,^{7}Be), (^{12}C,^{12}N), (^{18}O,^{18}F) for the β^+-like target transitions or the (p,n), (^{3}He,t), (^{12}C,^{12}B) for the β^--like class. Among them, the campaign of measurements of (^{3}He,t) reactions mainly conducted at the Grand Raiden magnetic spectrometer of Research Center for Nuclear Physics of Osaka University (RCNP) laboratories [68] at 140 AMeV incident energy has led to state-of-art results mainly thanks to the zero-degree mode for the spectrometer and the high energy resolution achieved (typical full-width-half-maximum ≈25 keV) from the application of the powerful dispersion matching technique [69]. For the transitions of β^+-type, remarkable results have been obtained by the (d,^{2}He) studies at KVI-Center for Advanced Radiation Technology, University of Groningen and RIKEN facilities [70–73]. The detection of the two protons decaying from ^{2}He with high efficiency has guaranteed an overall energy resolution of about 100 keV in the missing mass spectra.

An interesting application of high-resolution (^{3}He,t) and (d,^{2}He) studies is to map the GT response of specific nuclei, which represent the intermediate systems in $2\nu\beta\beta$ decay. The GT response of the even-even parent and daughter nucleus populating the odd-odd intermediate system is separately explored. The 1^+ states of the intermediate system, which are significantly populated in both SCE reactions, are inferred to give the main contribution to the $2\nu\beta\beta$. A drawback is that the experiments access only the transition probabilities to individual 1^+ states, while the $2\nu\beta\beta$ calculations require the amplitudes with the proper phase since their coherent sum is needed to determine the decay rate. The easiest case is when a single 1^+ intermediate state is dominant (*single-state dominance approximation*), as this prevents any coherent sum of amplitudes. An example of this application to the case of the ^{76}Ge → ^{76}As ← ^{76}Se system is more deeply discussed in Chapter 6.

2.2.2 Heavy-ion single charge-exchange

The complex many-body nature of nuclear systems is expected to play a role when heavy projectiles are used as probes to study SCE reactions [54]. The projectile-target nucleus-nucleus potential needs to be accurately modelled both in the entrance (initial

state interaction, ISI) and exit (final state interaction, FSI) channel. SCE is a direct nuclear reaction which implies a pronounced localization for such process in the nuclear surfaces of the colliding systems and the possibility to treat the reaction process as a perturbation of the direct elastic scattering flux. As a consequence, the accurate study of the ISI and FSI is mandatory. Accurate results are obtained when measurements of elastic scattering cross-sections of the projectile-target system at the same incident energy of the SCE reaction are available to constrain the calculations.

In a projectile-target nuclear collision, other quasi-elastic mechanisms are allowed. Multi-nucleon transfer reactions, featuring nucleon exchange among the colliding partners, could contribute to the observed SCE cross-section [56]. In particular, the transfer of a neutron/proton from the target to the projectile (pick-up) followed by the transfer of a proton/neutron from the projectile to the target (stripping) is a composite two-step mechanism feeding the SCE outgoing channel. Since this process is indistinguishable from the direct one-step SCE mechanism mediated by two-body nucleon-nucleon interaction, the interference between the mechanisms is expected in the reaction observables. The two-step SCE mechanism is sensitive to the nucleon-nucleus mean field potential and does not probe the nucleon-nucleon interactions. It is an unwanted complication that should be accounted for in the data analysis. An updated view of the present status of this research field is reported in reference [6]. The study of this direct vs sequential interference is one of the purposes of the theoretical analysis presented in Chapter 5.

In heavy-ion-induced SCE reactions, a large amount of linear and angular momentum is typically available and transferred to the final asymptotic state, even at small scattering angles. This property turns out to be useful when the goal is to probe the nuclear response to the *higher multipolarities* of the isospin and spin-isospin operators, not accessible neither by β-decay nor by many of the light ions-induced SCE reactions. Nowadays, growing attention is paid to such nuclear structure features thanks to their implications in $0\nu\beta\beta$ decay NMEs [74], where high-order multipoles are expected to give a large contribution [75].

2.2.3 SCE reaction mechanism and formalism

An exhaustive review of both reaction and structure state-of-art single charge exchange nuclear theories has been recently published by H. Lenske et al. in Ref. [6]. In the following we will refer to that review paper to introduce SCE basic elements. A SCE

nuclear reaction can be considered according to the scheme:

$$ {}^{a}_{z}a + {}^{A}_{Z}A \rightarrow {}^{a}_{z\pm1}b + {}^{A}_{Z\pm1}B \tag{2.15} $$

which maintains the distribution of masses but changes the charge partition by a balanced redistribution of protons and neutrons. For such a process, the cross-section is defined as:

$$ d^2\sigma_{\alpha\beta} = \frac{m_\alpha m_\beta}{(2\pi\hbar^2)^2}\frac{k_\beta}{k_\alpha}\frac{1}{(2J_a+1)(2J_A+1)}\sum_{M_a,M_A\in\alpha;M_b,M_B\in\beta}|\mathcal{M}_{\alpha\beta}(\mathbf{k}_\alpha,\mathbf{k}_\beta)|^2\,d\Omega \tag{2.16} $$

where $\mathbf{k}_\alpha$ ($\mathbf{k}_\beta$) and m_α (m_β) denote the relative 3-momentum and reduced mass in the entrance (exit) $\alpha = a, A$ ($\beta = b, B$) channels. As already discussed, heavy ion single charge exchange reactions can proceed through two different paths consisting in the sequential two-step transfer of nucleons and in a direct one step process, mediated by the isovector parts of the nucleon-nucleon interaction. The full SCE amplitude is expressed by the coherent sum of the two types of reaction amplitudes

$$ \mathcal{M}_{\alpha\beta}(\mathbf{k}_\alpha,\mathbf{k}_\beta) = M^D_{\alpha\beta}(\mathbf{k}_\alpha,\mathbf{k}_\beta) + M^S_{\alpha\beta}(\mathbf{k}_\alpha,\mathbf{k}_\beta) \tag{2.17} $$

because the same final state is reached by the one-step route and two step branches. Both $M^D_{\alpha\beta}(\mathbf{k}_\alpha,\mathbf{k}_\beta)$ and $M^S_{\alpha\beta}(\mathbf{k}_\alpha,\mathbf{k}_\beta)$, direct and sequential reaction amplitudes, are complex quantities.

The direct SCE reaction amplitude is given by the following DWBA matrix element

$$ M^D_{\alpha\beta}(\mathbf{k}_\alpha,\mathbf{k}_\beta) = \langle\chi^{(-)}_\beta, bB|T_{NN}|aA,\chi^{(+)}_\alpha\rangle \tag{2.18} $$

The distorted waves $\chi^{(\pm)}_{\alpha,\beta}$ are the asymptotic outgoing and incoming spherical waves, depend on the channel momenta $\mathbf{k}_{\alpha,\beta}$ and are solutions of the equations derived from the complex-valued optical potential scattering problem. The weakness of the SCE coupling allows to treat the charge exchange interactions in the isovector nucleon-nucleon (NN) T-matrix interaction T_{NN} by perturbative methods, justifying the use of the DWBA approach.

The same arguments apply to the two step transfer SCE processes. In such a case, second order DWBA methods leading to reaction amplitudes of the kind

$$ M^S_{\alpha\beta}(\mathbf{k}_\alpha,\mathbf{k}_\beta) = \sum_\gamma \langle\chi^{(-)}_\beta, bB|U_{\beta\gamma}G_\gamma U_{\gamma\alpha}|aA,\chi^{(+)}_\alpha\rangle \tag{2.19} $$

where G_γ is the full many-body propagator of the intermediate single-nucleon transfer channels γ.

2.2.4 SCE as direct meson-exchange reaction mechanism

The short range nature of the strong nuclear interaction has allowed to use the DWBA and the zero range approximation in the formalism introduced by Taddeucci et al. in Ref. [65] for the (p,n) charge exchange reaction that has been extended to the case of heavy ion single charge exchange by Bellone *et al.* (see Ref. [54, 76]). In these cases the direct transition matrix element, already introduced in Equation 2.18, can be written as follows:

$$M^D_{\alpha\beta}(\mathbf{k}_\alpha, \mathbf{k}_\beta) = \sum_{ST} \int d^3p K^{(ST)}_{\alpha\beta}(\mathbf{p}) N^D(\mathbf{p}) \tag{2.20}$$

expressed in the momentum space which allows the separation of the projectile and ejectile coordinates. In this last equation

$$N^D(\mathbf{p}) = \int \frac{d^3r}{(2\pi)^3} \chi^*_{\mathbf{k}_\beta}(\mathbf{r}) \chi_{\mathbf{k}_\alpha}(\mathbf{r}) e^{-i\mathbf{r}\cdot\mathbf{p}} \tag{2.21}$$

is the Fourier transform of the distorted waves product in the initial and final partitions accounting for the reaction dynamics of the process. This has been introduced by Taddeucci and it is also called distortion factor. The dependence of the final cross-section from such a factor is very important and justifies the thorough analysis performed on the elastic and inelastic scattering channel and described in Sec. 5.2.1.

The structure of the $K^{(ST)}_{\alpha\beta}(\mathbf{p})$ is shown in coordinate space:

$$K^{(ST)}_{\alpha\beta}(\mathbf{r}, \omega) = \int \frac{d^3q}{(2\pi)^3} \rho^{ST}_{a\to b}(\mathbf{q}, \omega) V^{ST}(\mathbf{q}, \omega) \rho^{ST}_{A\to B}(\mathbf{q}, \omega) e^{i\mathbf{q}\cdot\mathbf{r}} \tag{2.22}$$

where $V^{ST}(\mathbf{q}, \omega)$ is the Fourier transform of the local effective nucleus-nucleus interaction potential and

$$\rho^{ST}_{a\to b}(\mathbf{q}, \omega) = \langle \phi_b | \sum_{j=1}^{A} \hat{O} e^{i\mathbf{q}\cdot\mathbf{r_j}} | \phi_a \rangle \tag{2.23}$$

is the probability amplitude that the initial nucleus a transforms by means of the $\hat{O^{ST}}$ operator into the final nucleus b. $\hat{O}^{ST}$ is the spin isospin transition operator and ω is the total excitation energy of the considered system.

2.2.4.1 QRPA transition densities

QRPA transition densities are calculated according to the Green function method through the following expression

$$\rho^{ST}_{a\to b}(\mathbf{q},\omega) = \frac{1}{\pi}\,\mathrm{Im}\,\frac{\int dr' G_{RPA}(r,r',\omega) M^*_\lambda(r')}{\sqrt{\int d\omega R(\omega,P_\lambda)}} \tag{2.24}$$

where $\lambda = (S,T)$, $G_{RPA}(r,r',\omega)$ is the many body green function, $R(\omega,P_\lambda)$ is the nuclear response function associated to the operator P_λ and $M^*_\lambda(r')$ is an auxiliary external field used for computational reasons. The response function is calculated according to the expression

$$R(\omega,P_\lambda) = \frac{1}{\pi}\,\mathrm{Im}\,\langle 0|P^\dagger_\lambda G_{RPA} P_\lambda|0\rangle \tag{2.25}$$

so that the poles of the RPA Green function lead to peaks in the response function, thus identifying resonances and other excited nuclear states populated by the transition. The many-body problem it is now confined to the proper treatment of the many-body Green function problem. This is solved in the Dyson equation approach and in the Random Phase Approximation:

$$G_{RPA}(\omega) = G_0(\omega) + G_0(\omega) V_{res} G_{RPA}(\omega) \tag{2.26}$$

involving the G_0 Green function and the V_{res} potential, already introduced in Equation 2.1. For excitation energies near the excited nuclear states the G_{RPA} Green function is approximates by a Lorentzian distribution, with a finite width due to the imaginary part of quasi-particle self energy, accounting for the lifetime quasiparticle. Dyson equation is solved recursively once the free propagator G_0 is calculated. To evaluate the latter it is necessary to know nucleon single particle wave functions. These are obtained separately for protons and neutrons.

More details of this approach are described in Chapter 5 where it is applied in the theoretical analysis of the direct meson-exchange component of the ^{12}C(^{18}O,^{18}F)^{12}B SCE reaction.

2.3 Double charge exchange reactions

DCE reactions are nuclear processes induced by a projectile on a target in which two neutrons (protons) of the target are converted into two protons (neutrons) with the op-

posite transition simultaneously occurring in the projectile and leaving the mass number of projectile and target unchanged. DCE reactions can be used as a probe for selective investigation of the response of nuclear states to two-neutron/two-proton symmetry and can be seen as double isovector excitations generated by a combination of the isospin rising and lowering operators $\tau_{a\pm}\tau_{a\pm}\tau_{A\mp}\tau_{A\mp}$ acting on two nucleons in the projectile and the target, respectively. Furthermore, double beta ($\beta\beta$) decay processes induce the same transition in the parent nucleus, although allowed only for positive Q-value. As for SCE, DCE reactions probe nuclear response to the isospin degree of freedom, despite DCE selects second-order effects.

In $2\nu\beta\beta$ decay the GT operator acts in two independent steps, each time exchanging with the nuclear states a vanishing amount of momentum. On the other hand, the $0\nu\beta\beta$ decay is connected to the nuclear response to two-body isospin operators, which carry a sizeable amount of momentum, broadly distributed around 100 MeV/c, and consequently excite virtual states up to high multipolarities [75]. Therefore, despite $2\nu\beta\beta$ and $0\nu\beta\beta$ decays are both weak processes, connecting the same states in the parent and daughter nuclei, they map different regions of the involved nuclear wave functions in the momentum space.

Other second-order processes of interest are the (π^+,π^-) or (π^-, π^+) pion-induced DCE reactions, in which the isospin components of the strong interaction act twice in the sequential interaction of two independent nucleons with the π fields. Extensive explorations of (π^+,π^-) reactions have been performed leading to the discovery of second-order collective excitations as the double isobaric analog state (DIAS) and the isobaric analog state built on the top of the giant dipole resonance (GDR-IAS). The Double Gamow–Teller (DGT) was instead missed in the energy spectra. This fact was attributed to the spin-less nature of pions, making spin-isospin nuclear responses not directly accessible and thus difficult to be observed in pion-induced reactions. Recently, Lenske et al. [6] have pointed out that correlation-driven processes are not specific for pion-induced DCE and can also manifest in other hadronic reactions. In addition, since nucleon-nucleon correlations influence $0\nu\beta\beta$ dynamics, the study of such correlations in DCE reactions may provide key information.

However, the effect of such correlations can only be observed if rank-2 isotensor processes are allowed, thus excluding processes involving isolated nucleons. Since two-proton and two-neutron systems are unbound, the projectiles for DCE must have at least a mass number equal to three; thus, the lightest allowed ones are tritons or ^{3}He. However, in this case, the reactions of interest, the (t,3p) or (^{3}He,3n), are very challeng-

ing from the experimental point of view since one should detect with high efficiency the three emitted protons or neutrons in coincidence in order to reconstruct the DCE ejectile momentum. When heavier projectiles are considered, the experiments are still rather demanding. If one requires that the final ejectile is in a bound state, in order to easily identify the DCE channel in the experiments, no light nucleus can be practically used as a projectile and ^{12}C, ^{18}O, ^{20}Ne or heavier projectiles are needed. Pioneering explorations of the heavy-ion-induced DCE were performed at Berkeley, Institut de Physique Nucléaire d'Orsay, Australian National University-Pelletron, National Superconducting Cyclotron Laboratory—Michigan State University, Los Alamos laboratories [37, 38, 77, 78]. These studies focused on the (^{14}C,^{14}O), (^{18}O,^{18}Ne) and (^{18}O,^{18}C) reactions at energies above the Coulomb barrier, often with the main purpose of measuring the mass of neutron-rich isotopes by reaction Q-value measurements. However, these experiments were not conclusive for spectroscopic purposes, mainly because of the poor statistical significance of the few DCE collected events; thus, no further DCE measurement was performed for a long time. Furthermore, the development of theories to investigate the DCE reaction mechanism [79, 80] soon slowed down, and the field was almost abandoned for many years.

DCE studies have raised an increasing interest, also because of their possible connection to double beta decay issues. New reactions have been explored at RIKEN and RCNP at energies between 80 and 200 AMeV. The (^{8}He,^{8}Be) reaction was adopted to search for the tetra-neutron (4n) resonances by the ^{4}He(^{8}He,^{8}Be)4n at 186 AMeV [81]. The (^{11}B,^{11}Li) and the (^{12}C,^{12}Be) were investigated to search for the Double Gamow–Teller Giant Resonance (DGTGR) and provide quantitative information about the DGT sum-rule, of interest for modern nuclear structure theories.

The proposal of the NUMEN project, introduced in Chapter 1, fits into the historical and scientific context so far described. From the theoretical side, it has to be noticed that a complete approach to the full DCE reaction mechanism did not exist before the start of the NUMEN experimental activity. Today this theoretical study is in progress [6, 8, 9, 55, 57, 82]. Going deeper into these theoretical issues is beyond the purposes of the present work, while the experimental aspects of the NUMEN proposal to the DCE measurements will constitute the central topic of all the next Chapters.

Chapter References

[6] H. Lenske et al. “Heavy ion charge exchange reactions as probes for nuclear β-decay”. In: *Progress in Particle and Nuclear Physics* 109 (2019), p. 103716. ISSN: 0146-6410. DOI: 10.1016/j.ppnp.2019.103716.

[8] J. L. Ferreira et al. “Multinucleon transfer in the ^{116}Cd(^{20}Ne,^{20} O)^{116}Sn double charge exchange reaction at 306 MeV incident energy”. In: *Phys. Rev. C* 105 (1 Jan. 2022), p. 014630. DOI: 10.1103/PhysRevC.105.014630.

[9] J. I. Bellone et al. “Two-step description of heavy ion double charge exchange reactions”. In: *Physics Letters B* 807 (2020), p. 135528. ISSN: 0370-2693. DOI: 10.1016/j.physletb.2020.135528.

[25] F. Cappuzzello and M. Cavallaro. “Nuclear Response to Second-Order Isospin Probes in Connection to Double Beta Decay”. In: *Universe* 6.11 (2020). ISSN: 2218-1997. DOI: 10.3390/universe6110217.

[37] J. Blomgren et al. “Search for double Gamow-Teller strength by heavy-ion double charge exchange”. In: *Physics Letters B* 362.1 (1995), pp. 34–38. ISSN: 0370-2693. DOI: https://doi.org/10.1016/0370-2693(95)01190-2.

[38] F. Naulin et al. “Mass of ^{18}C from the double-charge-exchange reaction ^{48}Ca(^{18}O, ^{18}C) ^{48}Ti”. In: *Phys. Rev. C* 25 (2 Feb. 1982), pp. 1074–1075. DOI: 10.1103/PhysRevC.25.1074.

[54] H. Lenske et al. “Theory of Single Charge Exchange Heavy Ion Reactions”. In: *Phys. Rev.* C98.4 (2018), p. 044620. DOI: 10.1103/PhysRevC.98.044620.

[55] H. Lenske. “Probing Double Beta-Decay by Heavy Ion Charge Exchange Reactions”. In: *J. Phys.: Conf. Ser.* 1056 (July 2018), p. 012030. DOI: 10.1088/1742-6596/1056/1/012030.

[56] J. A. Lay et al. “Double charge-exchange reactions and the effect of transfer”. In: *Journal of Physics: Conference Series* 1056 (July 2018), p. 012029. DOI: 10.1088/1742-6596/1056/1/012029.

[57] E. Santopinto et al. “Heavy-ion double-charge-exchange and its relation to neutrinoless double-β decay”. In: *Phys. Rev. C* 98 (6 Dec. 2018), p. 061601. DOI: 10.1103/PhysRevC.98.061601.

[60] G. R. Satchler. *Direct nuclear reactions*. Vol. 68. Int. series of monographs on physics. Oxford, UK: Clarendon Press, 1983. ISBN: 9780198512691.

[61] F. Hofmann and H. Lenske. “Hartree-Fock calculations in the density matrix expansion approach”. In: *Phys. Rev. C* 57 (5 May 1998), pp. 2281–2293. DOI: 10.1103/PhysRevC.57.2281.

[62] L. C. Chamon et al. “Toward a global description of the nucleus-nucleus interaction”. In: *Phys. Rev.* C66 (2002), p. 014610. DOI: 10.1103/PhysRevC.66.014610.

[63] W. P. Alford and B. M. Spicer. “Nucleon charge-exchange reactions at intermediate energy”. In: *Advances in Nuclear Physics* (2002), pp. 1–82.

[64] F. Osterfeld. “Nuclear spin and isospin excitations”. In: *Rev. Mod. Phys.* 64 (2 Apr. 1992), pp. 491–557. DOI: 10.1103/RevModPhys.64.491.

[65] T. N. Taddeucci et al. “The (p, n) reaction as a probe of beta decay strength”. In: *Nuclear Physics A* 469.1 (1987), pp. 125–172. ISSN: 0375-9474. DOI: https://doi.org/10.1016/0375-9474(87)90089-3.

[66] K. Ikeda, S. Fujii, and J.I. Fujita. “The (p,n) reactions and beta decays”. In: *Physics Letters* 3.6 (1963), pp. 271–272. ISSN: 0031-9163. DOI: https://doi.org/10.1016/0031-9163(63)90255-5.

[67] D. E. Bainum et al. “Observation of Giant Particle-Hole Resonances in $^{90}\mathrm{Zr}(p,n)^{90}\mathrm{Nb}$”. In: *Phys. Rev. Lett.* 44 (26 June 1980), pp. 1751–1754. DOI: 10.1103/PhysRevLett.44.1751.

[68] Y. Fujita, B. Rubio, and W. Gelletly. "Spin–isospin excitations probed by strong, weak and electro-magnetic interactions". In: *Progress in Particle and Nuclear Physics* 66.3 (2011), pp. 549–606. ISSN: 0146-6410. DOI: https://doi.org/10.1016/j.ppnp.2011.01.056.

[69] Y. Fujita et al. "Matching of a beam line and a spectrometer New beam line project at RCNP". In: *Nuclear Instruments and Methods in Physics Research Section B: Beam Interactions with Materials and Atoms* 126.1 (1997). International Conference on Electromagnetic Isotope Separators and Techniques Related to Their Applications, pp. 274–278. ISSN: 0168-583X. DOI: https://doi.org/10.1016/S0168-583X(96)01008-7.

[70] H. Okamura et al. "Tensor analyzing power of the (d, ^{2}He) reaction at 270 MeV". In: *Physics Letters B* 345.1 (1995), pp. 1–5. ISSN: 0370-2693. DOI: https://doi.org/10.1016/0370-2693(94)01607-E.

[71] S. Rakers et al. "Measuring the (d,^{2}He) reaction with the focal-plane detection system of the BBS magnetic spectrometer at AGOR". In: *Nuclear Instruments and Methods in Physics Research Section A: Accelerators, Spectrometers, Detectors and Associated Equipment* 481.1 (2002), pp. 253–261. ISSN: 0168-9002. DOI: https://doi.org/10.1016/S0168-9002(01)01365-1.

[72] E. W. Grewe et al. "The $(d, ^2\mathrm{He})$ reaction on ^{76}Se and the double-β-decay matrix elements for $A = 76$". In: *Phys. Rev. C* 78 (4 Oct. 2008), p. 044301. DOI: 10.1103/PhysRevC.78.044301.

[73] D. Frekers. "Facets of charge-exchange reactions — from astrophysics to double beta decay". In: *Progress in Particle and Nuclear Physics* 57.1 (2006). International Workshop of Nuclear Physics 27th course, pp. 217–225. ISSN: 0146-6410. DOI: https://doi.org/10.1016/j.ppnp.2005.11.019.

[74] H. Ejiri, N. Soukouti, and J. Suhonen. "Spin-dipole nuclear matrix elements for double beta decays and astro-neutrinos". In: *Physics Letters B* 729 (2014), pp. 27–32. ISSN: 0370-2693. DOI: https://doi.org/10.1016/j.physletb.2013.12.051.

[75] J. Suhonen and O. Civitarese. “Weak-interaction and nuclear-structure aspects of nuclear double beta decay”. In: *Physics Reports* 300.3 (1998), pp. 123–214. DOI: https://doi.org/10.1016/S0370-1573(97)00087-2.

[76] J. I. Bellone. “Determination of the link between heavy-ion charge-exchange reactions and single and double beta decay matrix elements”. PhD thesis. Università degli studi di Catania, 2018.

[77] L. K. Fifield et al. “The mass of 18C from a heavy ion double-charge-exchange reaction”. In: *Nuclear Physics A* 385.3 (1982), pp. 505–515. ISSN: 0375-9474. DOI: https://doi.org/10.1016/0375-9474(82)90100-2.

[78] D. M. Drake et al. “Exotic Heavy-Ion Reactions on ^{40}Ca: (^{14}C, ^{14}O) Double Charge Exchange and (^{14}C, ^{15}O) Rearrangement Transfer”. In: *Phys. Rev. Lett.* 45 (22 Dec. 1980), pp. 1765–1769. DOI: 10.1103/PhysRevLett.45.1765.

[79] D. R. Bes, O. Dragún, and E. E. Maqueda. “The (14C, 14O) reaction considered as simultaneous pair-exchange or double-charge-exchange processes”. In: *Nuclear Physics A* 405.2 (1983), pp. 313–347. ISSN: 0375-9474. DOI: https://doi.org/10.1016/0375-9474(83)90575-4.

[80] C. H. Dasso and A. Vitturi. “Mechanism for double-charge exchange in heavy ion reactions”. In: *Phys. Rev. C* 34 (2 Aug. 1986), pp. 743–745. DOI: 10.1103/PhysRevC.34.743.

[81] K. Kisamori et al. “Candidate Resonant Tetraneutron State Populated by the ^{4}He(^{8}He,^{8} Be) Reaction”. In: *Phys. Rev. Lett.* 116 (5 Feb. 2016), p. 052501. DOI: 10.1103/PhysRevLett.116.052501.

[82] H. Lenske et al. “Nuclear Matrix Elements for Heavy Ion Sequential Double Charge Exchange Reactions”. In: *Universe* 7.4 (2021). ISSN: 2218-1997. DOI: 10.3390/universe7040098.

Singuli singula novit et cetera taceat.

Valerio Aprea

3 The Experiment

Contents

The study of heavy-ions direct nuclear reactions, and especially the study of DCE, has been proposed by the NUMEN project as a powerful tool to provide data-driven information on $0\nu\beta\beta$ decay. The following chapter is devoted to describe tools and techniques used to experimentally access the absolute cross-sections for such reactions. The main experimental activity of the project has been carried out in the last ten years in Catania, at the Laboratori Nazionali del Sud of the Istituto Nazionale di Fisica Nucleare (LNS-INFN). Indeed, the coexistence therein of the K800 Superconducting Cyclotron and the MAGNEX large-acceptance magnetic spectrometer constitutes the key research infrastructure allowing zero-degree DCE nuclear reactions to be investigated with state-of-the-art sensitivity at the LNS-INFN.

The NUMEN experimental activity concerns two main classes of experiments in which the two directions of isospin transfer $\tau^-\tau^-$ and $\tau^+\tau^+$, corresponding to the $\beta^-\beta^-$ and $\beta^+\beta^+$ decays, are under study. In particular, the $\beta^+\beta^+$ direction in the target is investigated using the $^{18}O^{8+}$ beam and measuring the (^{18}O,^{18}Ne) DCE transition while the $\beta^-\beta^-$ direction is instead explored through the (^{20}Ne,^{20}O) nuclear reaction using the $^{20}Ne^{10+}$ beam. Together with the DCE, a large network of reaction channels, involving the same beam and target, is studied to set additional information on the initial and final state interaction, the single particle and the collective components of the many-body wave functions and the interplay of different components in the reaction mechanisms populating the same final states. In the just appointed network, the involved reaction channels concern the elastic and inelastic scattering, the one- and two-nucleon transfer and the single and double charge exchange. During my PhD course both the $\tau^-\tau^-$ and $\tau^+\tau^+$ experiments have been performed and they are described in the following.

The ^{18}O and the ^{20}Ne beams used to perform the experiments are both accelerated by the K800 Superconducting Cyclotron (CS). The ions are accelerated at energies ranging from 10 AMeV to 80 AMeV and fully stripped by a thin carbon foil along the beam line. High energy resolution of 1/1000 and low emittance of $\approx 2\pi$ mm mr of the CS beams are the fundamental features for the purposes of the NUMEN project because of their connection to the energy and angular resolution reachable in the final experimental data. The maximum CS beam power ($\approx$ 100 W) is a limiting property for the measurement of nb cross-sections, although more stringent limitations come, nowadays, from the maximum rate tolerable by the present detectors [58].

The main topic of this thesis is the description of the results obtained about the networks of nuclear reactions populated in the ^{18}O + ^{76}Se and ^{18}O + ^{12}C collisions at

275 MeV incident energy and therefore in this chapter the focus is on the description of the details of this two experiments performed in November 2018 in Catania. The tools and the experimental techniques here described are similar for all the NUMEN experiments, with some differences when the ^{20}Ne is used.

3.1 The zero-degree measurement

The feasibility of the ^{76}Se(^{18}O, ^{18}Ne)^{76}Se DCE nuclear reaction strongly depends on the following constraints:

- Energy and angular resolution of the ion beams;
- Efficiency in the identification of the medium-heavy quasi-projectiles involved in the nuclear reactions of interest;
- Energy and angular resolution of the MAGNEX magnetic spectrometer;
- Accuracy in the cross-sections measurements down to the nb range with high sensitivity at very forward angles, including zero degrees.

The practicability of such conditions depends not only on the availability of adequate experimental equipment but also on the ability to tune it appropriately.

One of the main experimental challenges is the measurement of the DCE and two-proton transfer (2p-transfer) nuclear reactions at very forward angles, including zero-degree, and this task is accomplished thanks to the large momentum acceptance of the MAGNEX spectrometer. The measurements are performed by fixing the θ_{opt} angle between the beam direction and the spectrometer optical axis at +3°. In these zero-degree measurements, the MAGNEX quadrupole and dipole magnetic fields are set in order to transport the incident $^{18}O^{8+}$ beam in a region which is besides the MAGNEX focal plane detector but external to it, where a specifically designed Faraday Cup (FC) is located. The FC allows to stop the beam and collect the total beam charge incident on the target necessary for the measurement of absolute cross-sections. Figure 3.1 shows a sketched layout of the MAGNEX spectrometer and the beam trajectories for the zero-degree measurements. In the $\beta^+\beta^+$ case, the $^{18}O^{8+}$ beam (see the red trajectory in Figure 3.1) has a magnetic rigidity ($B\rho$) higher than the $^{18}Ne^{10+}$ and $^{20}Ne^{10+}$ ejectiles corresponding to the DCE and 2p-transfer reaction channels, respectively. Therefore, the FC has to be located in the high-rigidity region of the spectrometer in order to stop the beam. Differently, in the case of $\beta^-\beta^-$ experiments, the $^{20}Ne^{10+}$ beam has a

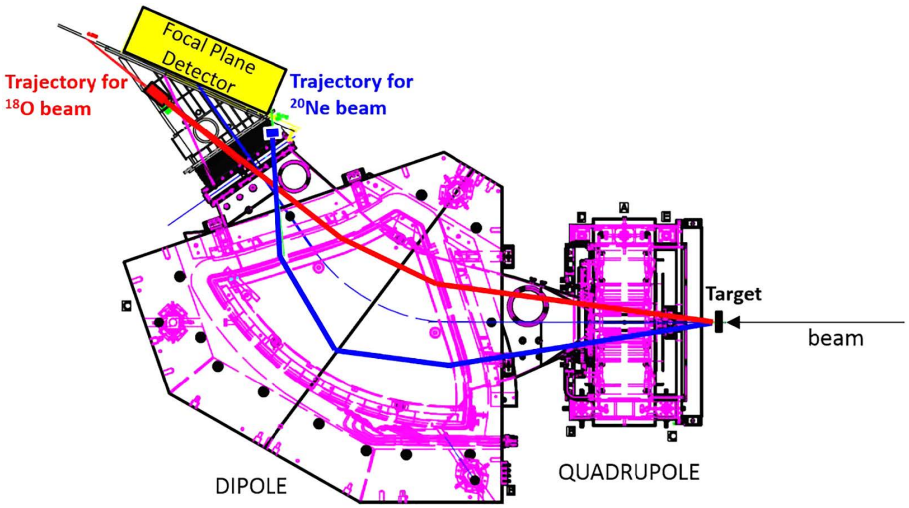

Figure 3.1: Sketch of the layout of the MAGNEX spectrometer in the zero-degree measurements. The blue and red lines represent schematic trajectories of the $^{20}Ne^{10+}$ and $^{18}O^{8+}$ beams passing through the spectrometer and reaching the zero degree Faraday cups located next to the Focal Plane Detector entrance window.

$B\rho$ lower than the ones of the $^{20}O^{8+}$ and $^{18}O^{8+}$ ejectiles (see the blue curve in Figure 3.1) of interest to measure the DCE and 2p-transfer channels, respectively, and the FC has to be located in the low-rigidity region of the spectrometer. High-order ion-optics simulations, including the tracking of the ion trajectories inside the magnetic field and the complete geometry of the spectrometer, are performed before each experiment. The simulations allow to describe the actual motion of the beam coming out of the target and of the ejectiles along the spectrometer towards the focal plane detector (FPD) region and, consequently, allow to properly locate the FC and set the quadrupole and dipole magnetic fields.

A peculiarity of the $^{20}Ne^{10+}$ beam experiments is the treatment of the different charge states emerging from the target. $^{20}Ne^{9+}$ and $^{20}Ne^{8+}$ ions are produced by the interaction of the fully-stripped beam ions with the target electrons. These ions have a Bρ higher than the $^{20}Ne^{10+}$ main beam, which make them entering in the FPD acceptance and conditioning the maximum accessible beam current compatible with the rate tolerable by the detectors. A study of the intensities for such secondary charge-state beams has been recently published in Ref. [49]. It was observed that adding a low Z material post-stripper foil located downstream of the main target is particularly effective to shift the charge state distributions towards fully stripped conditions. However, the

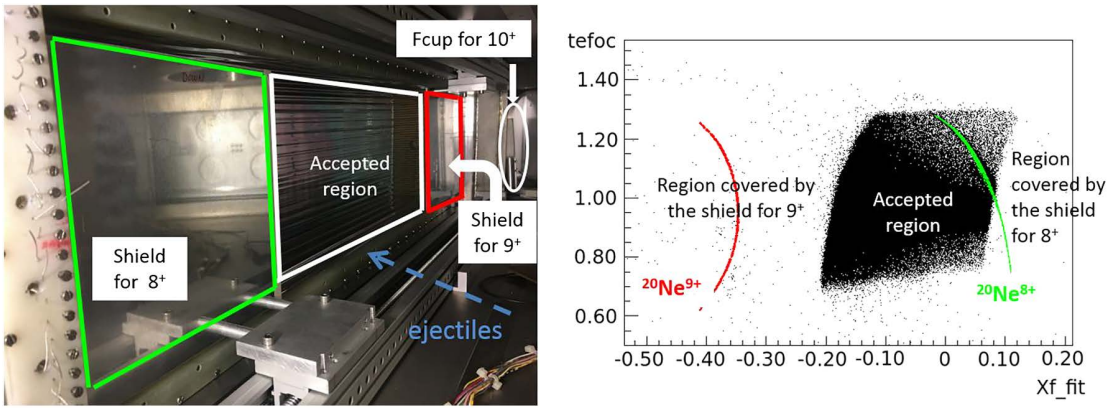

Figure 3.2: (left) Picture of the focal plane region of the MAGNEX spectrometer showing the two shields and the Faraday cup used for the $^{20}Ne^{10+}$ induced reactions. (right) Plot of the horizontal angle ($tefoc$) in rad units versus the horizontal position (xf_fit) in m units measured at the focal plane. The black points are the unidentified experimental data, the red and green lines are the simulated data for the $^{20}Ne^{10+}$ and $^{18}O^{8+}$ beams, respectively. Figure from Ref. [49]

emerging $^{20}Ne^{9+}$ and $^{20}Ne^{8+}$ fluxes are not negligible ($I(^{20}Ne^{9+})/I(^{20}Ne^{10+}) \approx 10^{-3}$ and $I(^{20}Ne^{8+})/I(^{20}Ne^{10+}) \approx 10^{-5}$) for nuclear physics experiments which use magnetic spectrometers. This means that, for a typical beam current of 10 enA, the amount of $^{20}Ne^{9+}$ and $^{20}Ne^{8+}$ components at the focal plane is of the order of 10^7 and 10^5 pps, respectively. This is beyond the acceptable rate of the FPD. In addition, the elastic scattering on the target at forward angles of $^{20}Ne^{9+}$ and $^{20}Ne^{8+}$ beams also produces high counting rate at the focal plane. In order to stop these unwanted background sources, two aluminium shields are mounted upstream the sensitive region of the focal plane detector, as shown in Figure 3.2. The shields act on a limited phase space region which stops the $^{20}Ne^{9+}$ and $^{20}Ne^{8+}$ beams and the elastic scattering at very forward angles, but not the other reaction channels populated by the nuclear reactions of the $^{20}Ne^{10+}$ ion beams impinging on the target.

The $^{18}O^{8+}$ beam experiments are completely free of such low-charge state contaminations and limitations. Indeed the $^{18}O^{8+}$ beam joins the low-Bρ region of the spectrometer and the lower charge-state components of the beam, generated during the atomic interaction with the target material, have even lower magnetic rigidity resulting to be completely off from the region covered by the FPD. For such reason, during the $^{18}O^{8+}$ beam experiments no post-stripper is used and shield is mounted in front of the FPD, allowing to cover the full momentum acceptance of the spectrometer.

3.2 The MAGNEX scattering chamber

The $^{18}O^{8+}$ ions are transported through the magnetic elements of INFN-LNS beam line up to the MAGNEX scattering chamber located inside the MAGNEX experimental hall. The origin of the laboratory reference frame, where the kinematic variables (e. g. the scattering angle) are expressed, is set on the *object point* of the MAGNEX spectrometer. It is defined by the intersection between the symmetry plane and the rotational axis of the spectrometer. The $\hat{y}$ and $\hat{z}$ directions are fixed by the rotational axis and the beam direction, respectively, and, consequently, the $\hat{x}$ is fixed by them.

A very important step in the setting of the experimental apparatus is related to the positioning of all the experimental objects in the laboratory reference frame. The targets, the FC and the monitor detector have to be placed inside the scattering chamber while the gas tracker, the zero degree Faraday cup and the aluminium shields have to be placed in the FPD region. All these alignment operations have to be performed within 0.1 mm to ensure a good accuracy in the measurement of the kinematic variables. These operations are performed using accurate optical instruments (e.g. theodolites and bubble-levels) to fix the origin of the reference frame and the distances between the objects. Theodolite, located along the beam line, is used to fix the symmetry plane and the axis of the MAGNEX spectrometer thanks to some references and alignment tips located inside the experimental hall and around the MAGNEX spectrometer that have been provided by the manufacturer itself. The positioning and handling of all the objects are managed by appropriate slow control systems.

3.2.1 The targets

Figure 3.3(a) shows a picture of the target ladder used during the ^{18}O + ^{76}Se and ^{18}O + ^{12}C experiments at 275 MeV incident energy. The ^{76}Se target has been made by the thin-films laboratory at LNS. It is a ^{76}Se isotopically enriched (purity 99.8 ± 0.1%) film, 280 ± 14 $\mu g/cm^2$ thick, evaporated onto a natural carbon layer 80 ± 4 $\mu g/cm^2$ thick. A second self-supporting natural carbon layer 400 ± 20 $\mu g/cm^2$ thick was used to perform independent measurements and to subtract the background due to the natural carbon backing of the ^{76}Se target. Supplementary runs have been performed using a ^{12}C target 60 ± 3 $\mu g/cm^2$ thick. The thickness values are obtained by energy-loss measurements performed using an α-radioactive source and the uncertainties are about ±5%. The slow control system, moving the target ladder, ensures a sub millimetre accuracy on the positioning of the target in the object point of the spectrometer.

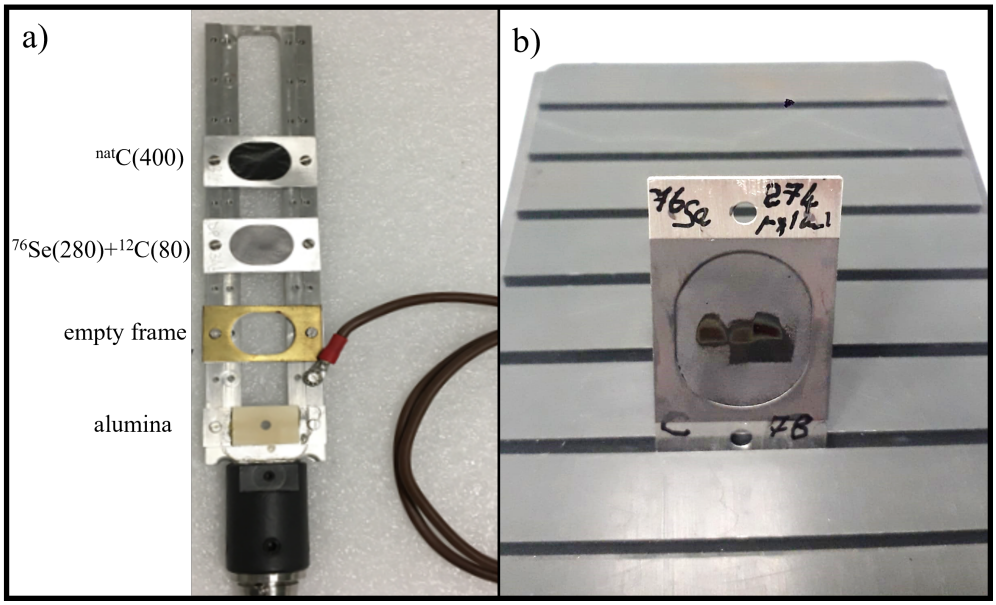

Figure 3.3: (a) Target ladder: the thicknesses of the natural ^{nat}C and ^{76}Se targets are expressed in μg/cm^2. (b) Zoomed view of the selenium target: the three marks left by the beam, corresponding to the three irradiation loci, are clearly visible.

The target ladder also holds an empty frame and an alumina. Both of them are used during the initial phases of the experiment, to set-up the beam and magnetic fields conditions. The empty frame is used to monitor the dimensions of beam spot and its halo. Indeed, during the one-month long experiment, the presence of background events coming from the scattering of the beam ions onto the target frame was often monitored. Alumina, that emits visible light under the beam irradiation, is a perforated quartz and the hole (ϕ = 3 mm) is aligned to the optical axis of the spectrometer. During the initial beam set-up, the LNS beam operators, using a proper CCD camera to see inside of the scattering chamber, could set the magnetic elements along the beam line to minimize the dimensions of the beam shape and to centre it with respect to the hole in the alumina.

The tuning of beam properties could be affected by misalignments both in the horizontal position and incident angle. Although such misalignments may be kept under control using more sophisticated collimation systems just before the target point inside the MAGNEX scattering chamber [11], these are excluded for zero degree measurements due to the huge background that would be generated by the energy degraded beam ions passing through the spectrometer. For that reason, together with the centring of the

beam on the alumina and properly setting of the magnetic fields of the spectrometer, small changes on the beam directions are made in order to maximize the beam current read by the zero degree Faraday cup.

A special issue of the ^{18}O + ^{76}Se experiment was the low melting temperature of the ^{76}Se film (220°C from Ref. [83]). A copper cable was connected to the target ladder (visible in Figure 3.3 (a)) and to the floor of the scattering chamber to increase heat conduction during the beam irradiation and further the thermal dissipation. To avoid the possibility that the melting and evaporation of the ^{76}Se film in localised region could compromise the validity of the experiment, the target was irradiated in different positions. Furthermore, a monitor detector was mounted inside the scattering chamber (see next paragraphs) to check the target thickness in each experimental run by measuring the elastic scattering count rate. A picture of the target after the experiment is shown in Figure 3.3 (b) in which the burns due to the different beam irradiation positions are clearly visible. Measurements of the thickness were performed also after the data taking and they excluded the possibility of any significant evaporation or melting of the ^{76}Se isotope material.

3.2.1.1 Energy resolution: Role of the target thickness

In order to separate the ground-to-ground state transition from that to the first excited state of the residual nucleus, sufficient energy resolution in the measured excitation energy spectra is required. This resolution mainly depends on three factors, namely the intrinsic energy resolution of the MAGNEX spectrometer ($\delta E_{MAGNEX} \approx 1/1000$), the energy spreading of the cyclotron accelerated beam ($\delta E_{CS} \approx 1/1000$) and a contribution due to the straggling and energy loss of the beam and ejectiles in the target film (δE_{TARGET}). A contribution due to the kinematic effect should also be considered in principle but for quasi-elastic reactions at forward angles, including DCE, it is very small.

δE_{TARGET} depends, for a given beam, on the target film material and thickness and on its uniformity. Thus, the request on resolution of the measured energy spectra implies stringent requests on the target characteristics. To this purpose, the target thickness for each experiment is chosen in order to be small enough to guarantee a sufficient δE_{TARGET} to separate the transition to the ground state from the transition to the first 2^+ excited state. In this respect, isotopes with corresponding high E_x (2^+) in the residual nucleus allow to produce targets with larger thickness, which is advantageous

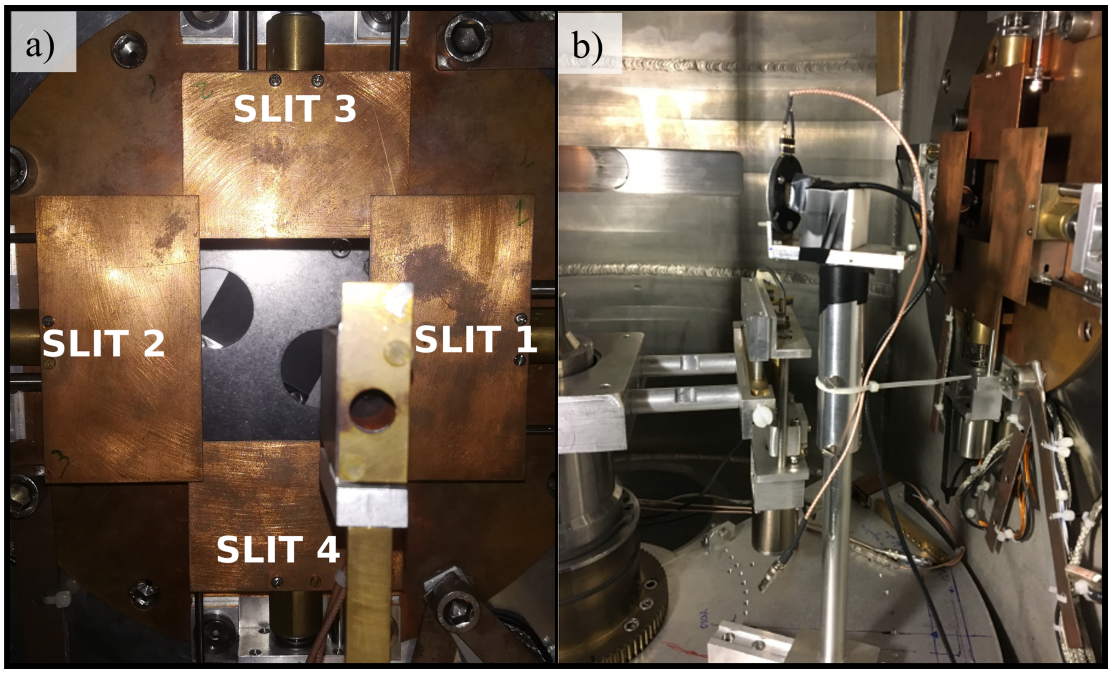

Figure 3.4: Insight of the scattering chamber: (a) beam direction point of view (b) lateral view.

in studies of rare processes to increase the count rate.

The average thickness of the target foils is determined by direct weighting the foils and by measuring the energy loss of α particles from a ^{241}Am source traversing them. A crucial requirement of the target construction is the uniformity. A non-uniform target causes, in fact, a spreading in the energy loss of the ion traversing the target. Specific studies on the target uniformities produced by the evaporation procedure are in progress (see Ref. [59]) in order to find the best conditions for each atomic species.

3.2.2 The Faraday cups

The scattering chamber FC is an 8 mm diameter copper cup positioned 15 cm downstream the target ladder, along the incident beam direction. The electrons suppressor was polarized at -200 V preventing from a significant loss of electrons back-scattered in the atomic interaction between the beam ions and the copper material and increasing the accuracy in the charge collection measurement. The interior of the scattering chamber is shown in Figure 3.4(a) from the incident beam point of view: the FC is clearly visible, in front of four copper slits. The accurate positioning and alignment

of the slits ensure a precise definition of the MAGNEX entrance window and angular acceptance [84].

The zero degree FC is located in the FPD vacuum chamber, as already explained in the previous section. Since the beam spot at the focal plane is $\approx 30 \times 30$ mm^2, as resulting from the simulations of the beam transport inside the spectrometer, the zero degree FC is a large aluminium cup 80 mm wide, 55 mm high and 100 mm deep. No electron suppressor was mounted in front of it at the time the experiment was done. In the next NUMEN experiments also the zero degree FC was equipped with a suppression ring.

The beam current measured by the Faraday cups is integrated by a low noise circuit including a digital integrator [85] with an intrinsic accuracy better than 0.5% [11]. The integrated charge is stored in the memory of a Latching Scaler [86] for each run in two different logic circuits (see Figure A.2 in Appendix A): independently from the not-busy signal of the acquisition module (Q_{raw}) and in coincidence with it (Q_{live}). The ratio between these two charges gives the live time (t_{live}=Q_{live}/Q_{raw}) of each measurement run.

3.2.3 The monitor detector

The monitor detector (see Figure 3.4(b)) is an ancillary ΔE-E telescope mounted inside the scattering chamber to check the target thickness in each experimental run by measuring the elastic scattering count rate. The ΔE stage is constituted by a 50 μm thick silicon (Si) detector polarized at +10 V that measures the energy loss by the incident ions. The E stage is constituted by a Thallium doped cesium iodide crystal (CsI(Tl)) $15 \times 15 \times 5$ mm that stops the ion and produce a number of photons proportional to the residual energy. The photons are collected by a silicon photomultiplier (SiPM) polarized at -70 V. The complete electronic scheme is shown in Figure A.4 of Appendix A. The telescope was positioned in the symmetry plane of the spectrometer, at the same altitude of the object point. The covered solid angle was defined by the presence of a small rectangular collimator (3×3 mm) used to limit the rate of ions incident on the telescope. It was fixed to the rotating floor of the scattering chamber at $\theta_{lab} = 15°$, within 0.1°.

3.3 The MAGNEX magnetic elements

MAGNEX is a large-acceptance magnetic spectrometer, an high-performance device merging the advantages of traditional magnetic spectrometry with those of a large an-

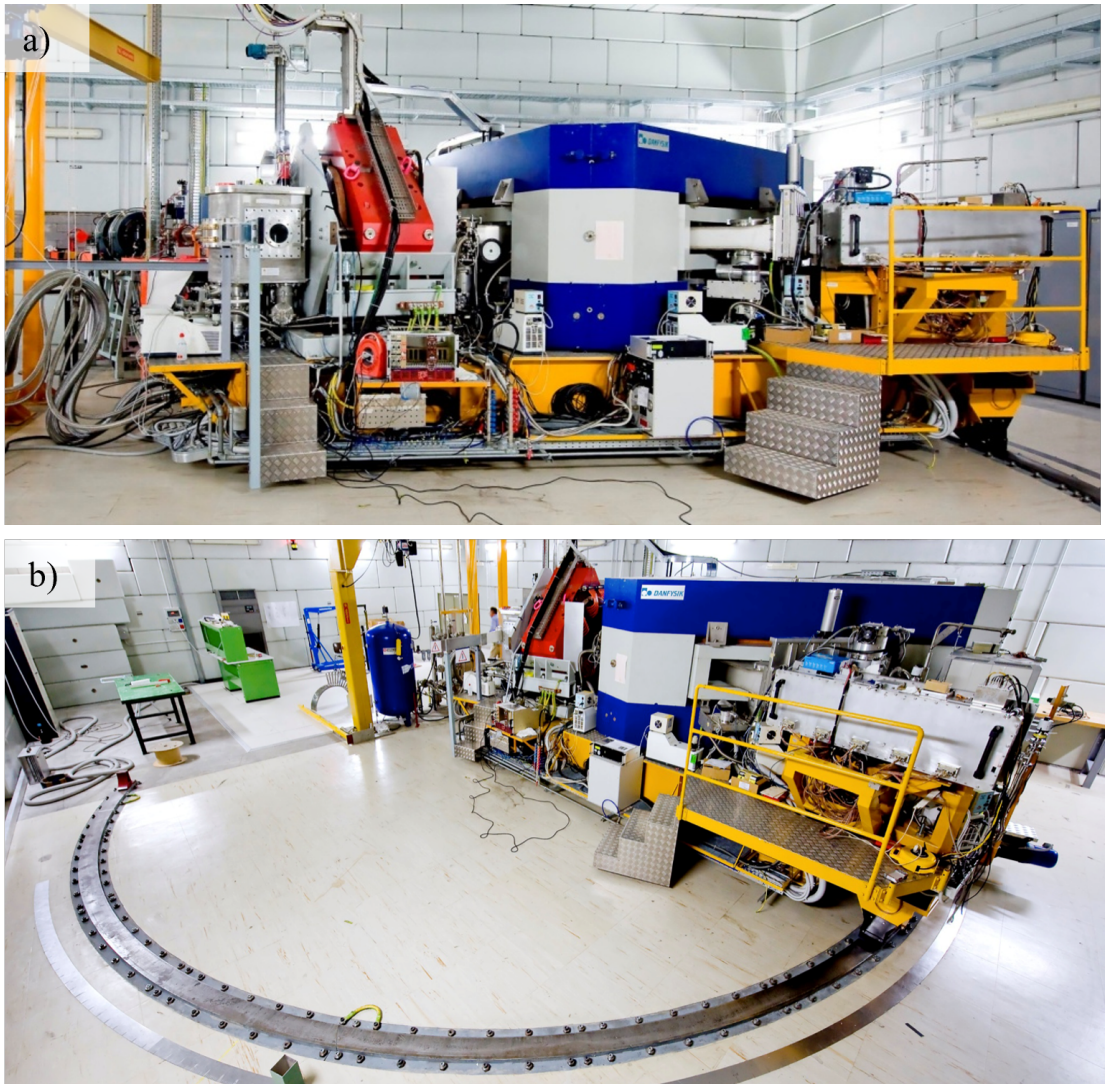

Figure 3.5: MAGNEX at the INFN-LNS. (a) From the left to the right: the scattering chamber, the quadrupole (red) magnet, the dipole (blue) magnet and the FPD chamber. (b) Panoramic view of the experimental hall. The rail that allows the spectrometer rotation is visible.

gular and momentum acceptance detector [11]. A picture of the MAGNEX experimental hall at the LNS-INFN in Catania is shown in Figure 3.5. The spectrometer is a Quadrupole-Dipole (QD) device composed of two large aperture magnets: the quadrupole [87] and the 55° dipole [88] (see Figure 3.5(a)). An overall sketch of the spectrometer layout in the zero degree measurements is shown in Figure 3.1.

3.3.1 Design and set-up

The quadrupole magnet (Q) is responsible for the focusing in the vertical non dispersive direction while the dipole magnet (D) provides the dispersion along the symmetry plane of the spectrometer and horizontal focusing. Two sets of surface coils, generating tunable quadrupole and sextuple strength, are mounted between the dipole poles and the vacuum vessel to optimize the focusing conditions. Nevertheless, during the here described experiment the two coils were not used. Table 3.1 shows the main optical and magnetic properties of the spectrometer and its elements.

The spectrometer optical axis can be set in the range of scattering angles θ_{opt} between $-15°$ and $70°$ by moving the spectrometer on a rail around its object point (see Figure 3.5(b)). During the experiment θ_{opt} was set at different values depending on the studied reaction. For each case a specific configuration of the angular acceptance was adopted by setting the horizontal and vertical slits located at the entrance window of the spectrometer (see Figure 3.4). These information are listed in Tables 5.1 and 6.1 for the ^{18}O + ^{12}C and the ^{18}O + ^{76}Se collisions, respectively.

MAGNEX allows the identification of heavy ions with quite high mass (ΔA/A $\approx$ 1/300)[89–91], angular ($\Delta\theta/\theta \approx 0.2°$) and energy resolution (ΔE/E $\approx$ 1/1000). High-resolution measurements for quasi-elastic processes, characterized by differential cross-sections falling down to tens of nb/sr, were already performed by this setup [92]. A crucial feature is the implementation of the trajectory reconstruction, based on differential algebraic methods, which makes possible the solving of the equation of motion of each detected particle up to the 10$^{\text{th}}$ order. In the next paragraphs this technique will be detailed.

Table 3.1: Main optical properties and parameters of the MAGNEX spectrometer from Ref. [11].

		Actual value
Optical properties	Maximum magnetic rigidity (Tm)	1.8
	Solid angle (msr)	50
	Horizontal angular acceptance (mrad)	-90, +110
	Vertical angular acceptance (mrad)	-123, +123
	Momentum acceptance (%)	-14, +10
	Central path length (cm)	596
	Momentum dispersion (cm/%)	3.68
	First order momentum resolution	5400
	Focal plane rotation angle (deg)	59.2
	Focal plane length (cm)	92
	Focal plane height (cm)	20
Dipole parameters	Maximum Field (T)	1.15
	Bending angle (deg)	55
	Bending radius ρ (m)	1.60
	$\rho_{\min}$,$\rho_{\max}$ (m)	0.95, 2.35
	Pole gap (cm)	18
	Entrance and exit pole face rotation (deg)	-18
Surface coils	Maximum value for α (at 1.15T)	0.03
	Maximum value for β (at 1.15T)	0.03
Quadrupole	Maximum field strength (T/m)	5
	Radius of aperture (cm)	20
	Effective length (cm)	58

3.3.2 Trajectory reconstruction

The motion of charged ions produced in the nuclear reactions and moving along the spectrometer can be formally described by the following formula

$$F : P_i \rightarrow P_f \tag{3.1}$$

that is a phase space mapping connecting the $P_f \equiv (x_f, \theta_f, y_f, \phi_f, l_f, \delta_f)$ final phase space vectors to the $P_i \equiv (x_i, \theta_i, y_i, \phi_i, l_i, \delta_i)$ initial one. x, θ, y, ϕ are the horizontal and vertical coordinates and angles, respectively, at the impact point of the ion trajectory with a plane normal to the spectrometer axis. l is the trajectory length and $\delta = (p - p_0)/p_0$ is the fractional momentum of the actual p momentum with respect to the p_0 reference one.

In Equation 3.1 the mapping F depends on the three-dimensional spatial distribution of the magnetic fields of the actual optical system. It can be written more explicitly in terms of measured observables:

$$\begin{aligned} x_f &= F_1(x_i, \theta_i, y_i, \phi_i, l_i, \delta_i) \\ \theta_f &= F_2(x_i, \theta_i, y_i, \phi_i, l_i, \delta_i) \\ y_f &= F_3(x_i, \theta_i, y_i, \phi_i, l_i, \delta_i) \\ \phi_f &= F_4(x_i, \theta_i, y_i, \phi_i, l_i, \delta_i) \\ l_f &= F_5(x_i, \theta_i, y_i, \phi_i, l_i, \delta_i) \\ \delta_f &= \delta_i \end{aligned} \tag{3.2}$$

The l_i parameter, initial position along the optical axis of the transported particle, is practically constant in case of thin targets while the last equation expresses the conservation of the momentum modulus for static magnetic fields in case of no-energy-degrading material.

The trajectory reconstruction consists of determining the momentum vector at the target position from tge measured phase space parameters at the focal plane. These operations can be formally written as follows

$$F^{-1} : P_f \rightarrow P_i \tag{3.3}$$

The measured quantity in case of our experiments is the $Q_f \equiv (x_f, \theta_f, y_f, \phi_f, x_i)$ vector while the reconstructed one is $Q_i \equiv (\theta_i, x_i, y_i, l_f, \delta)$. The set of parameters can be

further reduced neglecting the x_i interval in the case of a beam horizontally focused on the target, and renouncing to the reconstruction of l_f. Indeed, as already discussed, the horizontal dimension of the beam spot at the target point is expected to be $\lesssim 3$ mm and often neglected in the trajectory reconstruction. The new reduced vectors $Q'_f \equiv (x_f, \theta_f, y_f, \phi_f)$ and $Q'_i \equiv (\theta_i, y_i, \phi_i, \delta)$ are now related by the new formal inverted equation:

$$G^{-1} : Q'_f \rightarrow Q'_i \tag{3.4}$$

The main task in the trajectory reconstruction is to define the G operator and, consequently, the G_i transport equations analogues to the ones in 3.2. The capability to find a stable and accurate solution of the discussed equations strongly depends on the device acceptance because, far from the optical axis and far from the reference magnetic rigidity, high-order terms in the Taylor expansion of the transport operators are not negligible (see Refs. [93]). This is the reason why the advanced COSY INFINITY algorithm [94], developed at the Michigan State University, uses the differential algebra formalism to calculate the high-order transport matrices. In this approach, the following recurrence formula is used:

$$M_n =_n (A_1^{-1} \otimes (\mathbb{1} - A_n^* \otimes M_{n-1})) \tag{3.5}$$

where the symbol $=_n$ means that the product is truncated to the n-th order, while A_n and M_n are the direct and inverse n-th order matrices.

The application of these advanced techniques requires the detailed description of the magnetic fields crossed by the ions [87, 88, 95, 96], the exact knowledge of the geometry and optics of the spectrometer [93] and the accurate measurement of the phase space vector Q'_f at the focal plane. The accuracy required for the determination of the field is also needed for the position of the beam spot at the target, of the magnets and the FPD. This is achieved by the lengthy and accurate measurements and alignments of all the elements within decimals of millimetre, as already described in the previous section. This is a fundamental point since the measured vectors Q'_f must be defined in the same reference frame of the transport matrices (G or G').

3.4 The MAGNEX focal plane detector

The properties of MAGNEX large-acceptance magnetic spectrometer described so far require a Focal Plane Detector (FPD) that has to provide not only an unambiguous

particle identification, but also an accurate three-dimensional tracking of the ions trajectory at the focal plane. In this section the MAGNEX FPD described in Ref. [90] is presented. It is the upgraded version of the FPD of previous Refs. [11, 89] and it has been recently developed with the aim to improve the tracking and the identification performances.

3.4.1 Design and set-up

The MAGNEX FPD consists of two main sections: a gas tracker, sensitive to the energy loss of the ions, and a stopping wall for the measurements of the residual energy. The gas tracker is a proportional drift chamber with a total active volume of 1360 $\times$ 200 $\times$ 90 mm^3. It is divided in six sections that are six independent position-sensitive proportional counters. The stopping wall, placed behind the gas tracker, is made of 57 silicon pad detectors covering an area of 1360 $\times$ 200 mm^2. A sketch of the MAGNEX FPD is shown in Figure 3.6.

3.4.1.1 The gas tracker

The gas tracker is contained in the vacuum chamber already shown in Figure 3.5, where it appears in its external view. It is $\pm$0.08 m movable along the optical axis of the spectrometer to allow to translate the focal plane according to different focus conditions [11]. The FPD is rotated by an angle $\theta_{tilt} = 59.2°$ with respect to a plane normal to the optical axis in order to reduce the effect of chromatic aberrations [93]. The gas vacuum chamber and the high-vacuum region inside the spectrometer are separated by a large Mylar® window 2.5 μm thick (see Figure 3.7(a)) mechanically supported by a grid made of twenty metallic wires mounted in front of it. This grid is also used to perform the calibration of vertical measured positions, as it will described in Section 4.1. The gas tracker region is filled with N35 isobutane at the pressure of 14.5 mbar fluxed and continually renewed to guarantee a fast drift velocity of the electrons and good operational stability.

By the sectional sketch shown in Figure 3.6(a), it is clear how the gas tracker is made by three different regions: drift, multiplication and induction region.

- The *drift region* is constituted by the cathode aluminium plate at -1200 V and a Frisch grid made of ten gold-plated tungsten wires ($\phi = 50$ μm) at 300 V placed at a distance of 5 mm from each other. The active area of the tracker is surrounded by a double partition grid consisting of 41 couples of rings made of gold-plated

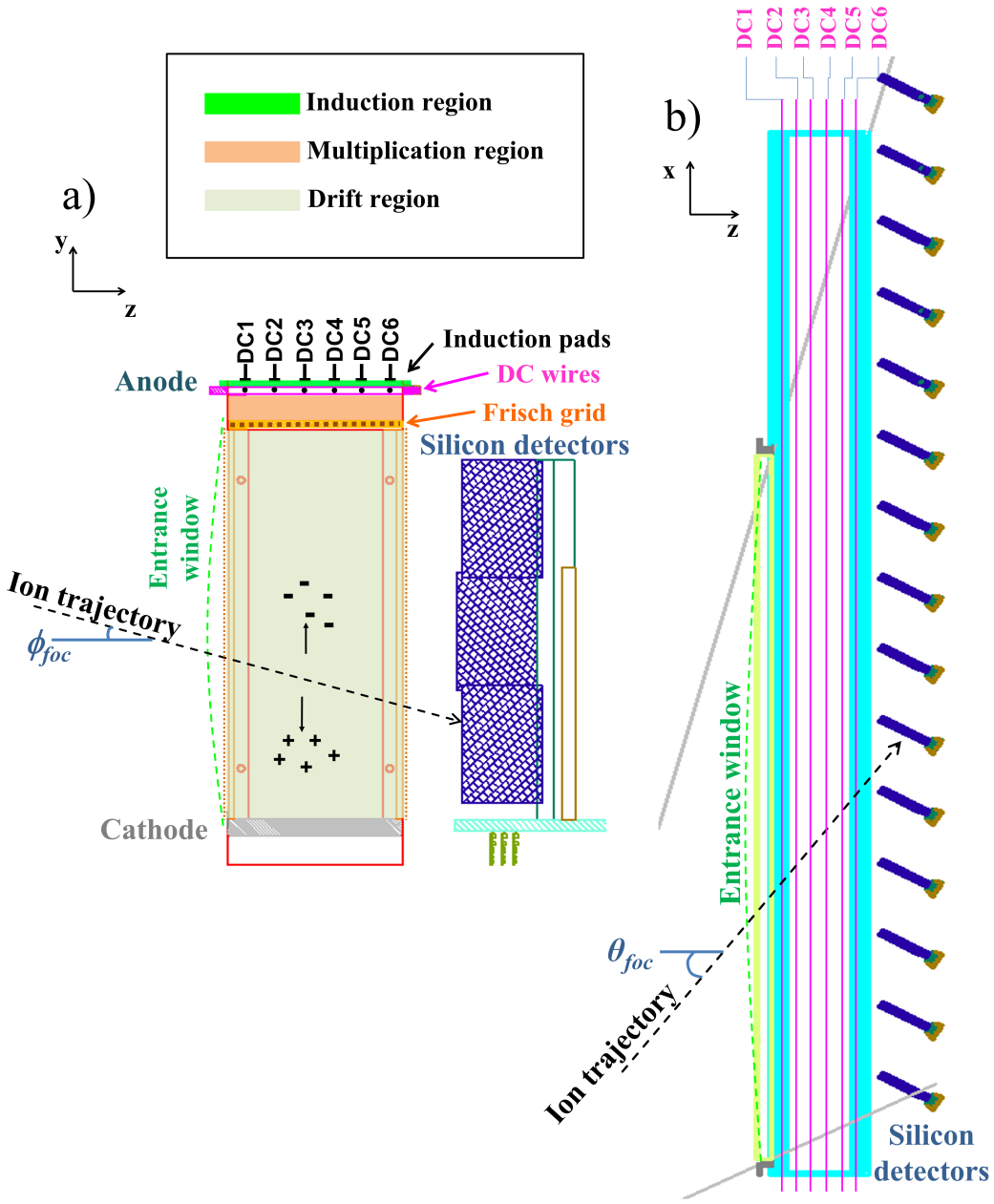

Figure 3.6: Scale drawing of the MAGNEX FPD in its gas tracker and silicon stopping wall parts. (a) Sectional view (y-z plane) (b) Top view (z-x plane). Typical ion trajectories are also included.

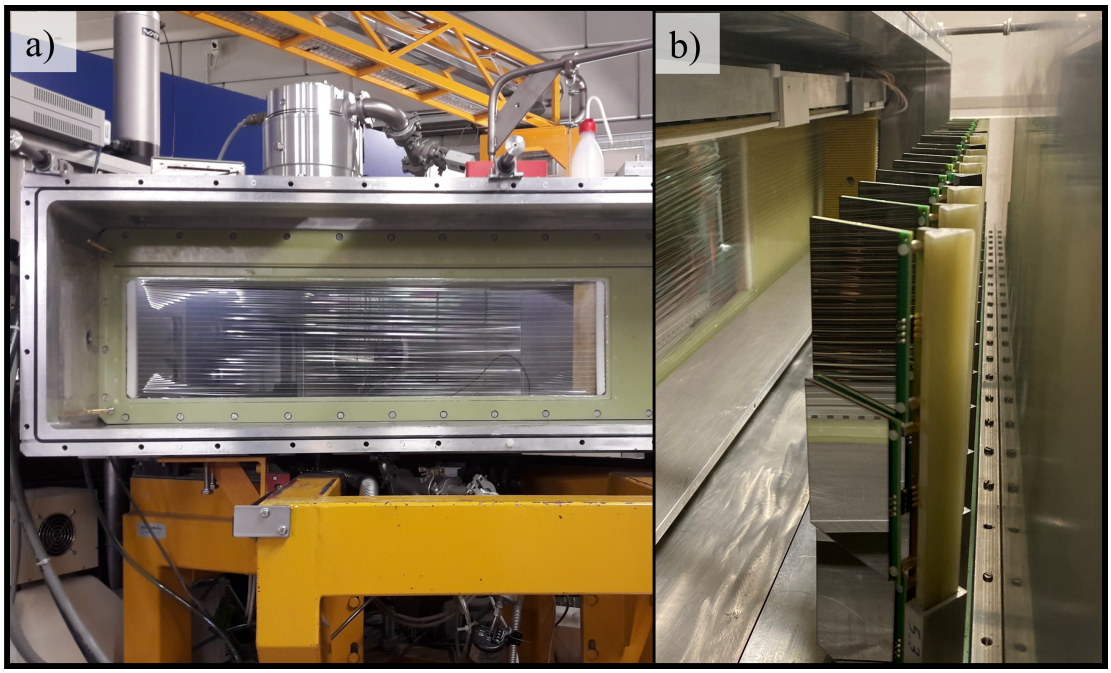

Figure 3.7: Photos of FPD elements. (a) Mylar® window. (b) Silicon columns inside the FPD.

wires. This allows to make as uniform as possible the electric field of the drift region and to shield it from external fields, namely from the high voltages applied to the silicon detectors of the stopping wall.

- The *multiplication region* is the 20 mm high volume between the Frisch grid and the plane where ten proportional gold-plated tungsten wires (ϕ = 50 μm) are located. The proportional wires are biased at +650 V by a common power supply and are shared among the six Drift Chambers DC_i i = 1, ..., 6 as shown in the sketch of Figure 3.8 where a bottom scale drawing of a part of the segmented anode board is shown. An additional partition grid is positioned on the border of the multiplication region to reduce the effects due to the non-uniformity of the electric field.

- The *induction region* is limited by the 10 proportional wires plane and the anode. The latter (see Figure 3.8) consists of a segmented read-out plane divided in six longitudinal strips, one for each DC, 8 mm (DC2 and DC5) and 16 mm (DC1, DC3, DC4 and DC6) wide. Each strip is segmented in almost 220 pads oriented along the spectrometer optical axis, with an angle equal to θ_{tilt}.

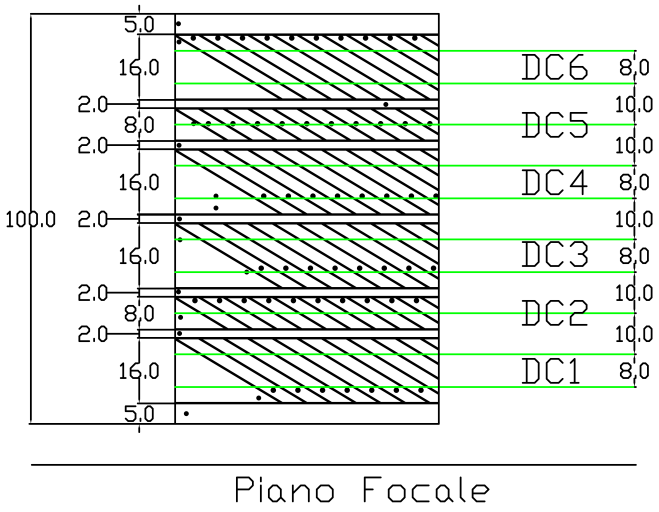

Figure 3.8: Scale drawing of a portion of the segmented anode (bottom view). In the drawing the six strips of the anode that corresponds to the six drift chambers DCs are shown. Each strip is further segmented in pads (in gray) that are tilted of $\theta_{tilt} = 59.2°$. In green the positions of the proportional wires are shown. All the sizes are expressed in mm. Figure from Ref. [90]

3.4.1.2 The silicon stopping wall

The silicon stopping wall is embedded in the gas filling the tracker to avoid further dead layers. It is made of 57 Micron Semiconductor Ltd. silicon detectors (model SX35) arranged in 19 columns (see Figure 3.7). They have rectangular shape, an active area of 50 $\times$ 70 mm^2 and a thickness of 500 μm able to completely stop the incident ions. They are mounted orthogonally to the optical axis of MAGNEX in order to minimize the effective dead layer. The closest distance of the silicon detector from the active area of the tracker is 15 mm, enough to avoid interferences with the electric field of the drift region of the tracker.

3.4.2 Principle of operation and read-out

The nuclear reaction ejectiles, crossing the entrance Mylar® window and moving through the gas tracker drift region, ionize the highly pure isobutane gas, generating a track made of ions and electrons. The uniform drift electric field ($\approx$ 50 V/cm) makes the ions drift towards the cathode and the electrons towards the Frisch grid (v $\approx$ 5 cm/μs) [97] at almost constant velocity. The primary electrons, entering the multiplication region, are

accelerated by the strong electric field generated by the proportional wires and multiplicate. The number of electrons produced close to the wires is proportional to the number of electrons primarily originated, thus generating a signal on the wires proportional to the ion energy loss [97]. Six independent measurements of the energy loss, one for each DC_i, are available and these signals, shaped and amplified by 200 mV/MeV (silicon equivalent) charge-sensitive preamplifiers, are sent to 16-channel MEGAMP modules designed at INFN-Milano [98]. The signals are then sent to peak-sensing Analog to Digital Converters (ADC) to provide the energy loss (ΔE_{DC_i}) by the ions crossing the gas, used for identification purposes. The MEGAMP module is made so that each channel is split and sent to a shaping amplifier for the spectroscopic output for the energy-loss determination and a Constant Fraction Discriminator (CFD) to produce a logic output used as a stop signal for the drift time measurement.

In addition, the electron avalanche generated close to the wires induces a charge in a given number of pads of the segmented anode just above the wires. Such induced charge signals, preamplified and shaped by an analog multiplexed read-out system based on GASSIPLEX chips [99], are readout and digitally converted by a 100 MS/s Digitizer (CAEN model V1724) [100] controlled by a general purpose VME board (CAEN model V1495) [101]. The centre of gravity of the charge distribution of the pads corresponding to a given DC is extracted and finally the six centres of gravity are converted in horizontal position providing six independent measurements x_i with i= 1,..., 6. From them, the position of the crossing point between the ion track and the focal plane x_f as well as the horizontal angle of the track θ_f is obtained (see next chapter).

After crossing the gas tracker the ions hit the silicon detector stopping wall. Charge pre-amplifiers similar to those used for the wire signals, but with lower sensitivities (typically ranging from 5 mV/MeV) are used. The outputs are sent to MEGAMP modules providing spectroscopic and CFD outputs. The spectroscopic signals, similarly to the ΔE_{DC_i}, are sent to peak-sensing Analog to Digital Converters (ADC) to provide the residual energy (E_{resid}) of the ions after crossing the gas, mainly used for identification purposes. The CFD output gives multipurpose timing signals of MAGNEX. Its logic OR is used as START signal for the electron drift times measurements (as explained below), to trigger the data acquisition and to generate the gate windows for the ADCs. Thanks to the very small dead layer, almost entirely due to the Mylar® window, the energy threshold for the detection of charged particles crossing the FPD could be very small down to about 0.5 AMeV with the thinnest Mylar® window of 1.5 μm.

The vertical position is extracted by measuring the arrival time of the electron

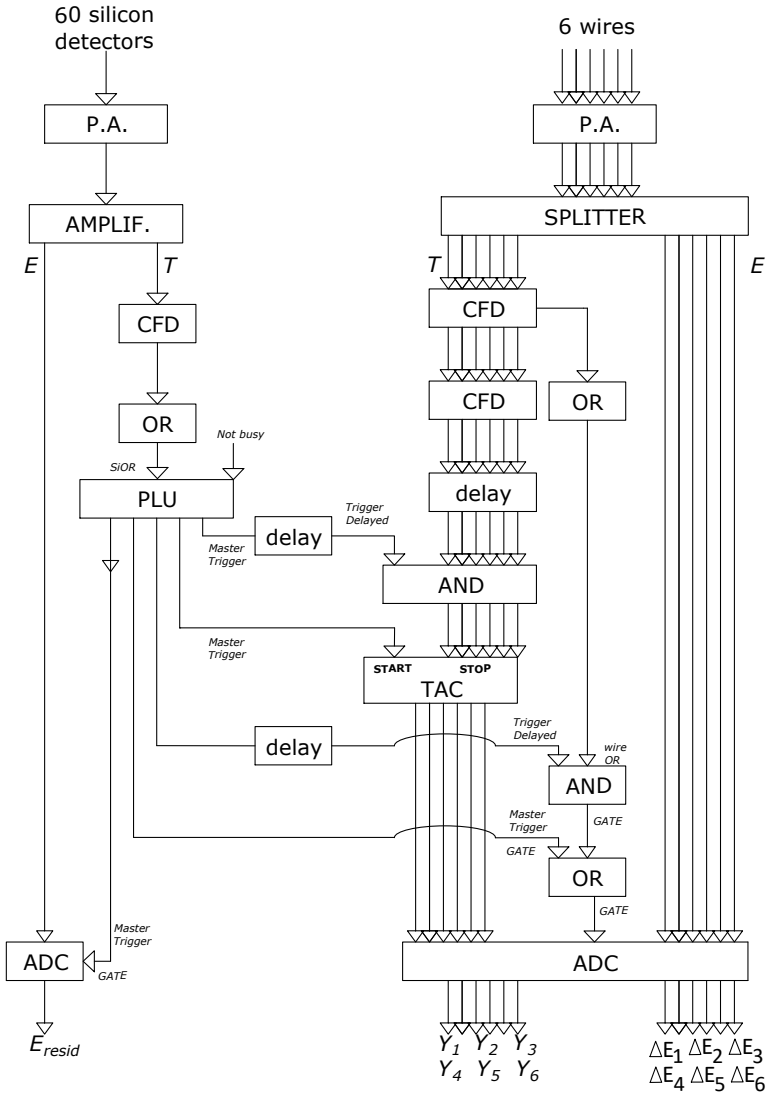

Figure 3.9: Schematic diagram of the electronics and read-out of the detectors signals at the MAGNEX FPD.

avalanches in the wires taking advantage of the fact that the tracker works in a regime where the drift velocity is almost constant in the whole volume of the detector. Six vertical positions are extracted measuring the drift time of the primary electrons along in the drift region by six standard Time to Amplitude Converter (TAC) plus ADC electronic chains. The six vertical positions y_i with i = 1,..., 6 are used to obtain the vertical position y_f on the focal plane detector and the vertical angle ϕ_f of the ion track.

As described above, the MAGNEX FPD produces several signals that have to be properly treated to get the analog and digital information of interest. A simplified schematic diagram of the electronics and read-out of the detector signals is shown in Figure 3.9. The detailed electronic circuits are rather complicated and during the PhD period appropriate schematic models have been produced to summarize and describe the main features and the involved modules. Examples of these models for the detector signal processing are shown in Appendix A. Their usefulness is being tested in these days when the FPD, after being dismantled by the LNS-INFN, is being reassembled at the iThemba labs (in Cape Town) for the forthcoming NUMEN experimental campaigns.

Chapter References

[11] F. Cappuzzello et al. "The MAGNEX spectrometer: results and perspectives". In: *Eur. Phys. J.* A52.6 (2016), p. 167. DOI: 10.1140/epja/i2016-16167-1.

[49] M. Cavallaro et al. "Charge-state distributions of ^{20}Ne ions emerging from thin foils". In: *Res. in Phys.* 13 (2019), p. 102191. ISSN: 2211-3797. DOI: https://doi.org/10.1016/j.rinp.2019.102191.

[58] P. Finocchiaro et al. "The NUMEN Heavy Ion Multidetector for a Complementary Approach to the Neutrinoless Double Beta Decay". In: *Universe* 6.9 (2020). ISSN: 2218-1997. DOI: 10.3390/universe6090129.

[59] F. Cappuzzello et al. "The NUMEN Technical Design Report". In: *International Journal of Modern Physics A* 0.0 (0), p. 2130018. DOI: 10.1142/S0217751X21300180.

[83] W. M. Haynes. *CRC Handbook of Chemistry and Physics*. 95th Edition, Internet Version 2015. Boca Raton, FL: CRC Press/Taylor and Francis, 1983.

[84] M. Cavallaro et al. "Transport efficiency in large acceptance spectrometers". In: *Nucl. Instrum. Meth. A* 637 (May 2011), pp. 77–87. DOI: 10.1016/j.nima.2011.01.078.

[85] USA ORTEC. *Digital Current Integrator mod. 439*. https://www.ortec-online.com/products/electronics/digital-current-integrator/439. 2021.

[86] Italy CAEN Viareggio. *32 channel Latching Scaler mod. v820*. https://www.caen.it/products/v830/. 2021.

[87] A. Lazzaro et al. "Field measurement for large quadrupole magnets". In: *Nuclear Instruments and Methods in Physics Research Section A: Accelerators, Spectrometers, Detectors and Associated Equipment* 591.2 (2008), pp. 394–405. ISSN: 0168-9002. DOI: https://doi.org/10.1016/j.nima.2008.02.103.

[88] A. Lazzaro et al. "Field measurement for large bending magnets". In: *Nuclear Instruments and Methods in Physics Research Section A: Accelerators, Spectrometers, Detectors and Associated Equipment* 585.3 (2008), pp. 136–145. ISSN: 0168-9002. DOI: https://doi.org/10.1016/j.nima.2007.10.046.

[89] M. Cavallaro et al. "The low-pressure focal plane detector of the MAGNEX spectrometer". In: *The European Physical Journal A* 48.5 (May 2012), p. 59. ISSN: 1434-601X. DOI: 10.1140/epja/i2012-12059-8.

[90] D. Torresi et al. "An upgraded focal plane detector for the MAGNEX spectrometer". In: *Nuclear Instruments and Methods in Physics Research Section A: Accelerators, Spectrometers, Detectors and Associated Equipment* 989 (2021), p. 164918. ISSN: 0168-9002. DOI: https://doi.org/10.1016/j.nima.2020.164918.

[91] A. Badalà et al. "Trends in particle and nuclei identification techniques in nuclear physics experiments - *Nuovo Cimento accepted*". In: *Nuovo Cimento C* (2022). DOI: 10.1007/s40766-021-00028-5.

[92] D. Pereira et al. "Nuclear rainbow in the 16O+27AL system: The role of couplings at energies far above the barrier". In: *Phys. Lett. B* 710.3 (2012), pp. 426–429. ISSN: 0370-2693. DOI: https://doi.org/10.1016/j.physletb.2012.03.032.

[93] A. Cunsolo et al. "Ion optics for large-acceptance magnetic spectrometers: application to the MAGNEX spectrometer". In: *Nuclear Instruments and Methods in Physics Research Section A: Accelerators, Spectrometers, De-*

tectors and Associated Equipment 484.1 (2002), pp. 56–83. ISSN: 0168-9002. DOI: https://doi.org/10.1016/S0168-9002(01)02004-6.

[94] K. Makino and M. Berz. "COSY INFINITY version 8". In: *Nuclear Instruments and Methods in Physics Research Section A: Accelerators, Spectrometers, Detectors and Associated Equipment* 427.1 (1999), pp. 338–343. ISSN: 0168-9002. DOI: https://doi.org/10.1016/S0168-9002(98)01554-X.

[95] A. Lazzaro et al. "Field simulations for large dipole magnets". In: *Nuclear Instruments and Methods in Physics Research Section A: Accelerators, Spectrometers, Detectors and Associated Equipment* 570.1 (2007), pp. 192–204. ISSN: 0168-9002. DOI: https://doi.org/10.1016/j.nima.2006.10.055.

[96] A. Lazzaro et al. "Field reconstruction in large aperture quadrupole magnets". In: *Nuclear Instruments and Methods in Physics Research Section A: Accelerators, Spectrometers, Detectors and Associated Equipment* 602.2 (2009), pp. 494–500. ISSN: 0168-9002. DOI: https://doi.org/10.1016/j.nima.2009.01.019.

[97] W.R. Leo. *Techniques for Nuclear and Particle Physics Experiments: A How-to Approach*. Springer, 1994. ISBN: 978-3-642-57920-2.

[98] C. Boiano, A. Guglielmetti, and S. Riboldi. "A 16 channels multi detector pulse shape amplifier with serialized readout". In: *2012 IEEE Nuclear Science Symposium and Medical Imaging Conference Record (NSS/MIC)*. 2012, pp. 865–867. DOI: 10.1109/NSSMIC.2012.6551228.

[99] M. Bordessoule et al. "A simplified read out for high-resolution linear gas detector". In: *Nuclear Instruments and Methods in Physics Research Section A: Accelerators, Spectrometers, Detectors and Associated Equipment* 390.1 (1997), pp. 79–85. ISSN: 0168-9002. DOI: https://doi.org/10.1016/S0168-9002(97)00352-5.

[100] Italy CAEN Viareggio. *8 Channel 14 bit 100 MS/s Digitizer mod. V1724*. https://www.caen.it/products/v1724/. 2021.

[101] Italy CAEN Viareggio. *General purpose vme board mod. v1495*. https://www.caen.it/products/v1495/. 2021.

μὴ εἶναι βασιλικὴν ἀτραπόν ἐπὶ γεωμετρίαν

Proclus, Commentary on the First Book of Euclid's Elements

4

Data reduction

Contents

Important observables coming out from the experimental study of a reaction are the excitation energy spectra of the residual nuclei and the absolute cross-sections. The following Chapter is devoted to explain how the experimental data reduction is performed in a typical NUMEN experiment using the MAGNEX spectrometer.

The data reduction is made up of several phases. First, an accurate calibration of the positions, measured for the ejectile of the performed nuclear reactions, at the MAGNEX focal plane is mandatory, since these parameters are used as input for the ray-reconstruction procedure. Second, the particle identification, which consists of two different phases: the atomic number (Z) and the $\sqrt{m}/\mathrm{q}$ identification. These two techniques allow an unambiguous selection of the reaction channels of interest, although a third approach, performed for the first time during the experiment and data reduction here described, is presented in the following. The final phase space, spanned by all the reaction channels of interest, is measured and compared with the simulations of random events transported inside the spectrometer. The high-order transport matrix is fine tuned and inverted to finally access the momentum vector at the target point for each of the analysed events. Finally, the excitation energy spectra and the absolute cross-sections are extracted after a proper normalization of the measured yields. In the following the details of the data reductions performed for the ^{18}O + ^{12}C and ^{18}O + ^{76}Se collisions at 275 MeV incident energy are presented.

4.1 Calibration

The angular and energy resolutions achievable in a typical MAGNEX experiment strongly depends on the tracking capability of the FPD. Accurate calibrations of the measured vertical and horizontal positions are crucial since they constitute the main link between the FPD measurements and the laboratory reference frame where the G and G' transport operators are defined.

4.1.1 Horizontal positions and angles

The measurement of six horizontal positions inside the FPD depends on the relative calibration of the induction pads response for each DC detector. Four pulses of different amplitudes (2, 5, 8 and 10 V) are generated by a pulse generator and sent onto the wires of a given DC. Thus, the same charge is generated in front of each segmented anode pad for each of the DC volume and pulse amplitude. The histograms containing the

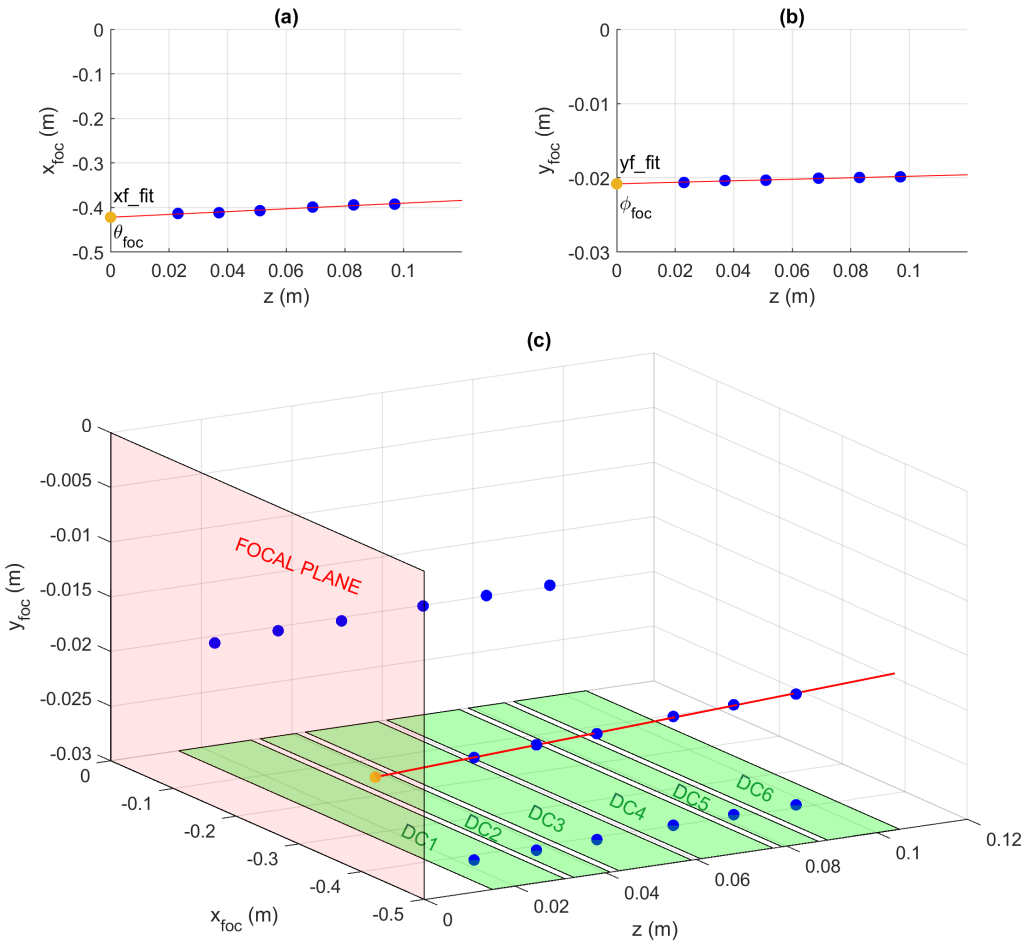

Figure 4.1: Ion track through the FPD. Blue and orange dots are the experimentally measured and the extrapolated positions of the ion, respectively. Red line is the implemented linear fit. (a) x_{foc}-z projection (b) y_{foc}-z projection (c) 3D representation.

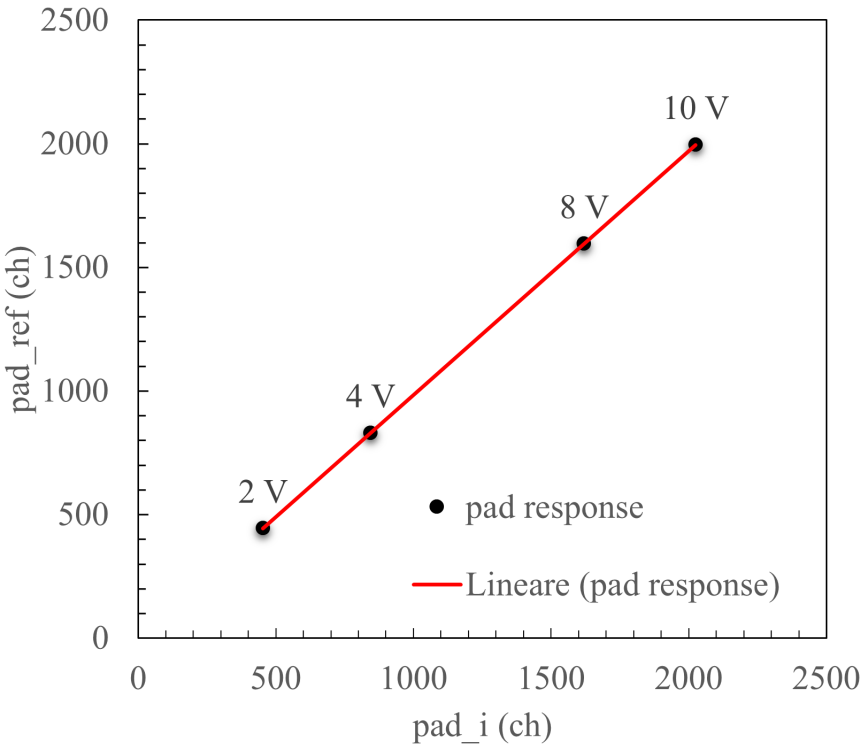

Figure 4.2: Linear correlation between the response of a pad (pad_i) with the response of a reference one (pad_ref). Each point corresponds to the pads response to the signal (2, 5, 8 and 10 V) generated by a pulse generator and sent onto the wires in the case of DC3.

induced charge on each pad are built and a linear fit, correlating the signals amplitude of each pad with that of a reference one, is performed (see Figure 4.2). This procedure leads to a relative calibration of the different electronic channels of the pads induction electrode.

4.1.1.1 Center of gravity algorithm

The centre of gravity (COG) algorithm [102] is used to extract the centroid of the charge distributions induced on the pads by the electronic clouds generated in the multiplication region. The centroid $\bar{n}$ is calculated by weighting each pad n_j with its charge q_j

$$\bar{n} = \frac{\sum_j (q_j - b) n_j}{\tilde{Q}} \tag{4.1}$$

where

$$\tilde{Q} = \sum_{\{q_j > b\}} (q_j - b)$$

is the total induced charge, above the threshold b (bias). A careful choice of b is the key aspect of the COG algorithm and leads to improve the quality and stability of the measurement. The best value for b has been found to be proportional to the total charge $Q = \sum_j q_j$, induced and measured in the overall strip,

$$b = kQ \tag{4.2}$$

where k can vary between 0.005 and 0.025.

To analyse the charge distribution and test the quality of the chosen thresholds and the calculated centroids, the standard deviation σ of the distributions is defined and studied:

$$\sigma = \sqrt{\frac{\sum_j (n_j - \bar{n})^2 (q_j - b)}{\tilde{Q}}} \tag{4.3}$$

If the threshold is properly set, σ should range from 1 to 5 corresponding to the cases of 3 to 20 pads above the threshold, respectively. In the technique described in Ref. [102], the σ is taken as a control parameter and a recursive algorithm increases the bias level of a small quantity in each iteration, controlled by the i index

$$b_i = (k + 0.002i)Q \tag{4.4}$$

The iterations are repeated until the σ value becomes less than 5. Typically a number of iterations smaller than 40 is enough to obtain the correct bias level. The technique allows to get an high efficiency in the number of centroids correctly determined and restoring 40% of the bad reconstructed events with the standard COG algorithm. This is an important result especially in case of low signal-to-noise ratio data.

The present data reduction has been performed using a revised version of the described algorithm. The initial b_0 was set using the same Equation 4.2 with $k = 0.018$. This quantity was subtracted to the charge distribution, at each iteration i in which $\sigma > 5$, so that

$$q_{ij} = q_{i-1j} - b_{i-1} \tag{4.5}$$

being $b_i = kQ_i$ and $Q_i = \sum_j q_{ij}$. Although the new efficiencies are similar to those of Ref. [102], the new algorithm has the advantage to perform a finer search of b_i, being

smaller at each step and depending on a constant fraction of Q_i.

Figure 4.3 illustrates three examples of charge distributions. The charge distribution of a signal over a low background level is shown in panel (a). The initial b_i and the one optimized by the recursive algorithm are also indicated in green and red, respectively. The main effect due to the threshold increasing is a better evaluation of the centroid and consequently the improvement of resolution in the position measurement. Two other examples of charge distributions are presented in panel (b) and (c). The first one, characterized by an high background level, can be recovered by the proper choice of b_i whereas the second one, corresponding to the piling up of two charge distributions of different ions, will have $\sigma > 5$ for any b_i value and will be rejected.

The selection of the good measured events was performed looking at the σ_i vs σ_{i+1} correlations, corresponding to the charge distributions of adjacent DC_i. These correlations are shown in Figure 4.4 for the events collected during the $^{18}O + ^{76}Se$ measurement and identified as ^{18}F ejectiles (see Section 4.2). The main coloured central region holds more than the 98% of the total identified events.

Once the centroids of the electronic avalanche were determined, the six x_{foc_i}, horizontal measurements of the track ion at the focal plane, were obtained by the following formula

$$x_{foc_i} = \tilde{n}_i d + h_i \tag{4.6}$$

where d is the horizontal size of each pad (6 mm within 0.01 mm) and h_i is the horizontal position of the crossing-point between the optical axis of the spectrometer and the symmetry plane of each DC_i, accurately determined by optical sights.

The x_{foc_i} parameters were used to access the x-z projection of the linear ion track passing through the gas detector. Longitudinal positions z_i of the symmetry planes of the DC_i are very accurately defined by mechanical construction (within 0.1 mm) while the positioning of the overall tracker detector was fixed during the alignment phases. The z_i positions are measured with respect to the z= 0 locus corresponding to the MAGNEX focal plane. An example of correlation between the $\{x_{foc_i}\}$ and the $\{z_i\}$ values is shown in Figure 4.1(a). A linear fit for each event was performed to extract the xf_fit and θ_{foc} parameters corresponding to the x position at $z = 0$ and to the incident angle with respect to the z-axis, respectively. Both the xf_fit and θ_{foc} were used as input parameters for the ray-reconstruction described in Sections 3.3.2 and 4.3.

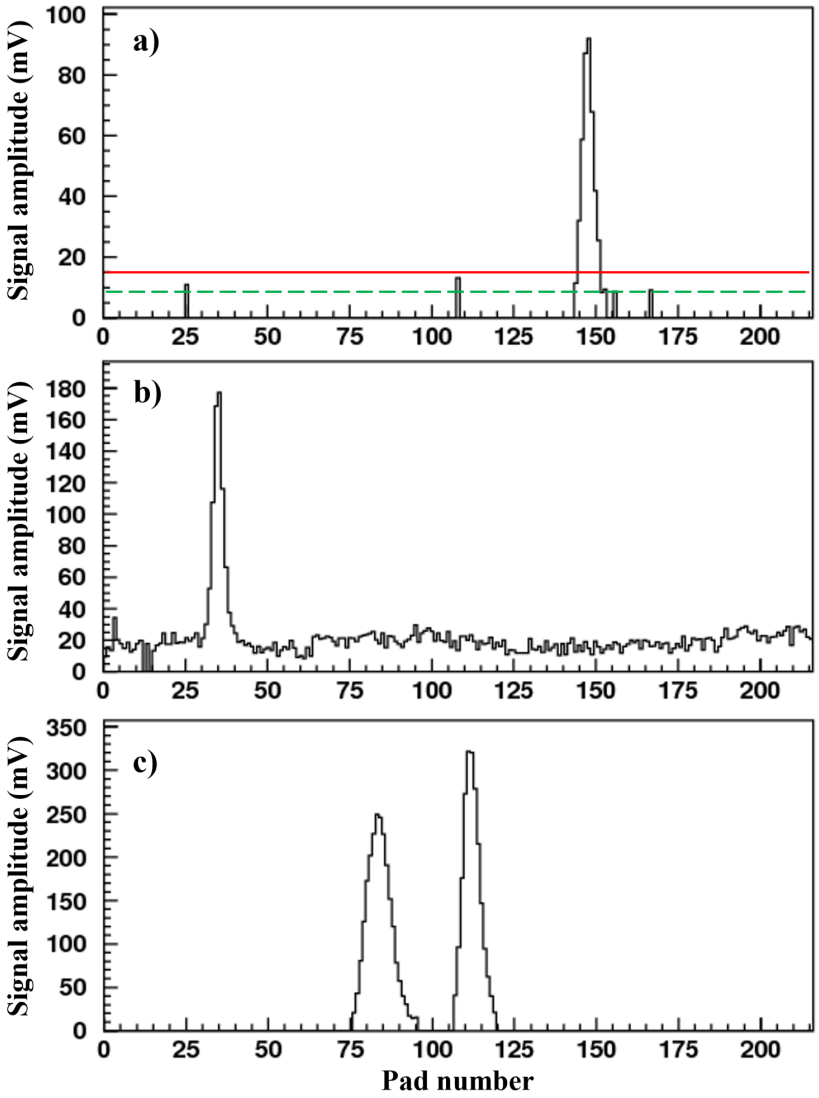

Figure 4.3: Examples of charge distributions on DC1: a) presence of spurious signals distant from the main avalanche. Threshold values obtained using the standard COG method and the optimized algorithm (green dashed and red solid line, respectively); b) time variation of the pedestal level above the stored values; c) two ions trajectories piling-up in the multiplexer. Figure from Ref. [102].

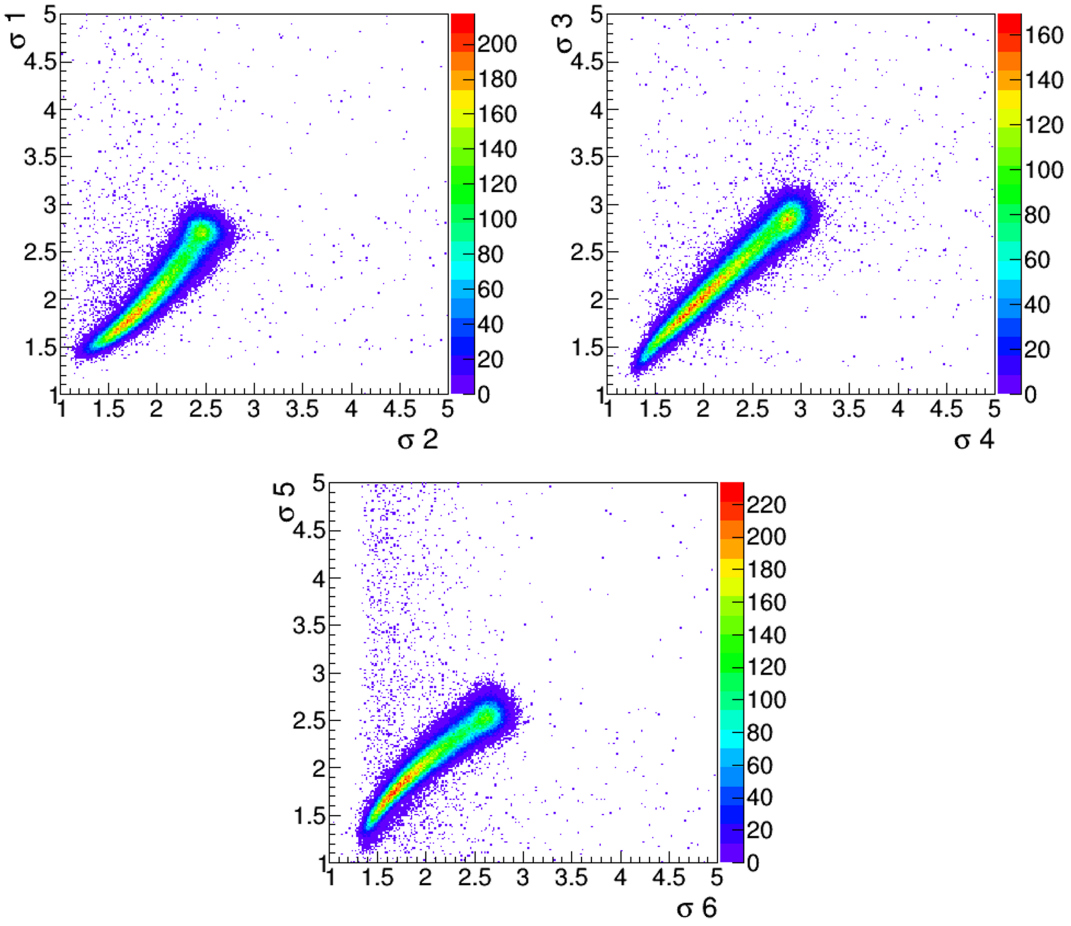

Figure 4.4: Sigma correlations of adjacent DC_i charge distributions obtained using the COG algorithm (see text).

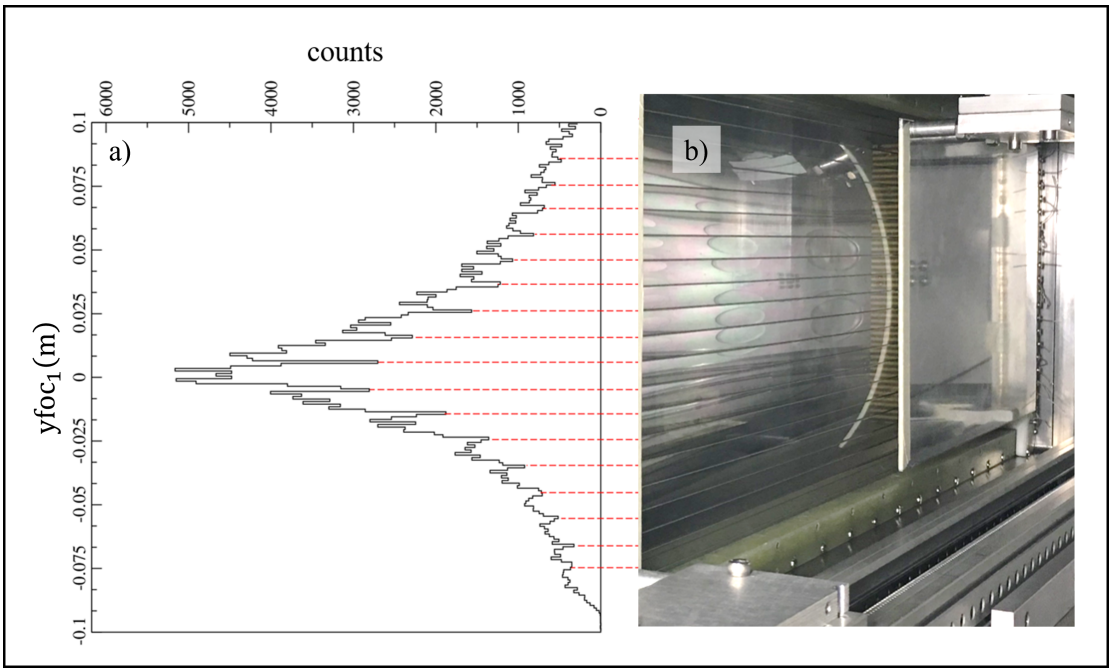

Figure 4.5: (a) y_{foc_1} distribution of unidentified events. The minima, indicated by the red dashed lines, correspond to the mechanical wires (see text) shown in panel (b).

4.1.2 Vertical positions and angles

The vertical position of the track (see Figure 4.1 (c)) is determined inside each of the six DC_i by measuring the drift time of the primary electrons moving towards the wires. Mechanical constraints are used to calibrate the vertical y_{foc_i} measured parameters. The y_{foc_i} distribution of unidentified events collected by the FPD is shown in Figure 4.5. The 17 minima, clearly visible in the acquired spectrum, are due to the lack of ions intercepting the metallic wires, mentioned in Section 3.4, that are used to mechanically support the thin Mylar® entrance window of the FPD.

The distance between two adjacent wires is fixed (10 mm) and their altitude in the laboratory reference frame was measured in the alignment operations. The correlation between the position of the minima (in channels) and the position of the wires in the laboratory reference frame (see Figure 4.5) was used to perform the calibration of the vertical y_{foc_i} variables. The gain and offset of such calibration was obtained from a linear fit of the defined correlation.

The y_{foc_i} parameters were used for the reconstruction of the projection of the linear ion track passing through the detector on the y-z plane. An example of correlation between the $\{y_{foc_i}\}$ and the $\{z_i\}$ values is shown in Figure 4.1(b), where the linear fit is performed to extract the yf_fit and ϕ_{foc} parameters corresponding to the y position at $z = 0$ and to the vertical incident angle, respectively. The yf_fit and ϕ_{foc}, together with the already discussed xf_fit and θ_{foc}, completed the set of parameters required for the ray-reconstruction.

4.2 Particle Identification

The second step of the data reduction corresponds to the particle identification. This procedure is needed to correctly isolate the reaction channel of interest among all the ejectiles produced in the nuclear collision. In this work, we are interested in the study of the reaction channels listed in Table 4.1 and thus the particle identification of ^{18}O, ^{17}O, ^{19}F, ^{16}O, ^{18}F and ^{18}Ne ions were performed as described in the following paragraphs.

4.2.1 Atomic number identification

The ΔE-E correlation allows to perform the identification of the atomic number (Z) based on the Bethe-Bloch formula ($\Delta E \propto mZ^2/E$) [103]. A typical MAGNEX ΔE-E plot, correlating the total energy lost by the ejectiles in the gas tracker ΔE_{TOT} and the

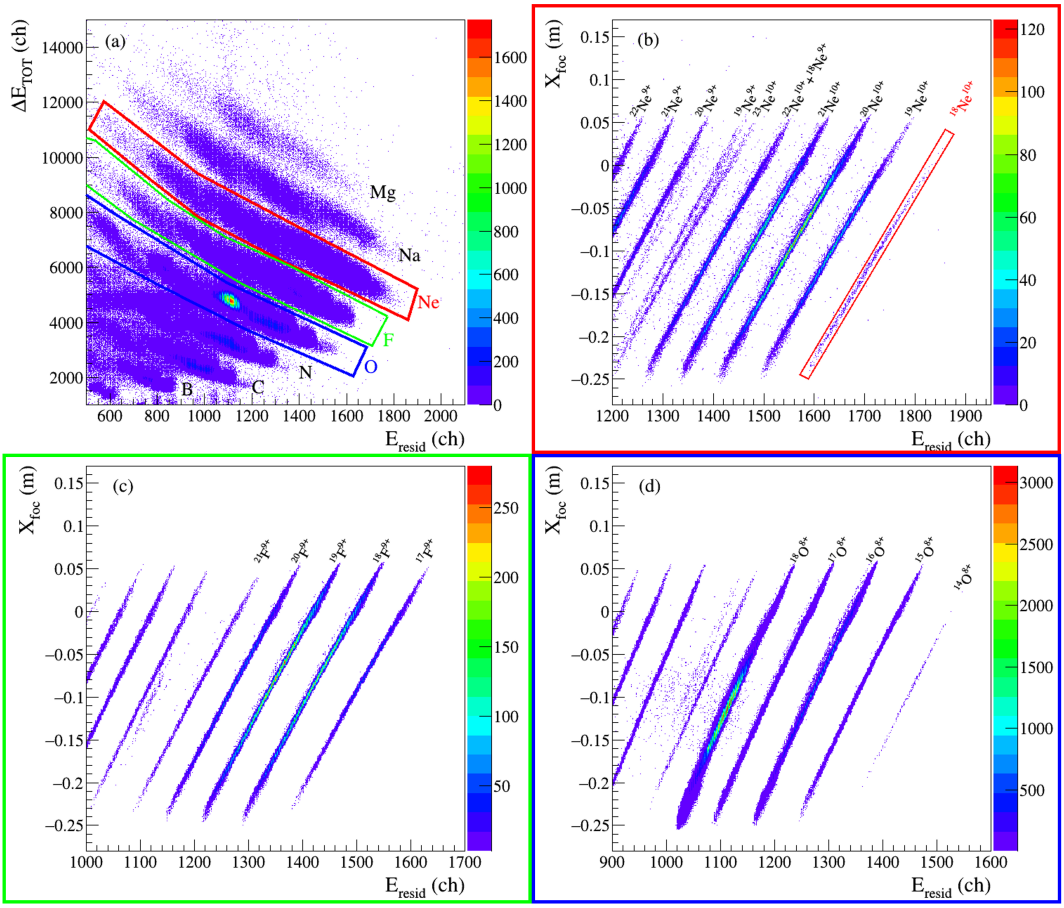

Figure 4.6: Particle identification spectra for the ^{18}O + ^{76}Se collision at 275 MeV incident energy performed with the MAGNEX spectrometer. (a) Ions energy loss inside the gas tracker, ΔE, as a function of the residual energy E_{resid}, measured by one silicon detector of the FPD. The blue, green and red graphical contours select the oxygen, fluorine and neon ion events. (b)(c)(d) The horizontal position X_{foc} at the MAGNEX focal plane as a function of the residual energy for the selected oxygen, fluorine and neon ions of panel (a). The loci correspond to ions with a different ratio $\sqrt{m}/q$. Graphical selections on the ^{18}O, ^{17}O, ^{19}F, ^{16}O, ^{18}F and ^{18}Ne events are shown by solid coloured lines.

Table 4.1: Nuclear reactions analysed in the present work for the ^{18}O + ^{12}C and ^{18}O + ^{76}Se collisions at 275 MeV incident energy.

Target	Nuclear reaction		ejectile
^{12}C	el. & in. scattering	^{12}C(^{18}O,^{18}O)^{12}C	^{18}O
	one-neutron addition	^{12}C(^{18}O,^{17}O)^{13}C	^{17}O
	one-proton removal	^{12}C(^{18}O,^{19}F)^{11}B	^{19}F
	two-neutron addition	^{12}C(^{18}O,^{16}O)^{14}C	^{16}O
	single charge exchange	^{12}C(^{18}O,^{18}F)^{12}B	^{18}F
^{76}Se	single charge exchange	^{76}Se(^{18}O,^{18}F)^{76}As	^{18}F
	double charge exchange	^{76}Se(^{18}O,^{18}Ne)^{76}Ge	^{18}Ne

residual energy E_{resid} measured by one silicon detector, is shown in Figure 4.6(a). The ΔE_{TOT} is the sum of the $\Delta E^{corr}_{DC_i}$ measured by each DC$_i$ and corrected for the angle of the detected ions measured in the gas tracker. Such angle correction takes into account the different ion path lengths in the gas, as consequence of the different incident angle θ_{foc}. The correction, which takes into account also the rotation of the FPD (θ_{tilt}), is expressed in the following formula:

$$\Delta E^{corr}_{DC_i} = \Delta E_{DC_i} \frac{\cos\theta_{tilt}}{\cos\theta_{foc}} \tag{4.7}$$

The absolute calibration of E_{resid} and ΔE_{TOT} is not performed since both variables are used just for particle identification purposes. As a reference, the absolute identification of the ^{18}O ions is achieved studying appropriate data at very forward angles, where the measured yields is dominated by elastic scattering events. In these experimental runs the FPD is set at the same gas pressure and electric field conditions used for the actual experiment.

4.2.2 Mass and charge state identification

The ΔE-E technique is not enough to clearly identify ions with the same Z and different mass and charge state. An innovative particle identification technique, introduced in Ref. [104], is based on the Lorentz force determining the trajectory of a q-charged particle in a magnetic field B normal to its momentum p:

$$B\rho = \frac{p}{q} \tag{4.8}$$

with ρ radius of the curved trajectory. p is related to the kinetic energy E that, in low-pressure conditions of the gas tracker, can be approximated with the residual energy E_{resid} measured by the silicon detectors, by the non-relativistic relation $p \approx \sqrt{2mE_{resid}}$, where m is the ion mass. Since ρ is related to the positions x_{foc_i} measured by the FPD, we can rewrite Equation 4.8 as:

$$x^2_{foc_i} \propto \frac{m}{q^2} E_{resid} \tag{4.9}$$

In panels (b), (c) and (d) of Figure 4.6, the x_{foc}-E_{resid} correlations are shown for the Z = 8, 9 and 10 ions selected by the red, green and blue graphical contour of Figure 4.6 (a). Different loci are clearly visible in the x_{foc}-E_{resid} plots, where other graphical contours are indicate to isolate, among specific Z ions, the $\sqrt{m}/q$ ejectile ions listed in Table 4.1. From the analysis of the present experimental data we extracted a mass resolution of $\Delta A/A \approx 1/300$ [91], better than the value reported in previous Refs. [89, 90, 104], in which straggling effects on the E_{resid} were more important.

The complete particle identification of the ions of interest, e. g. $^{20}Ne^{10+}$, is made, for the events associated to each silicon detector, by imposing the logic AND of the two graphical conditions in the ΔE_{TOT}-E_{resid} and x_{foc}-E_{resid} correlation plots. The logic OR operation between the selection conditions for each silicon detector guarantees a clean identification of all the detected ejectiles.

Another way to identify the ejectiles in a magnetic spectrometer is to couple the $\Delta E - E$ technique to the measurement of the Time of Flight (TOF) along the instrument. This approach requires the generation of a start signal for the measurement of the TOF using an appropriate start detector close to the target. Such an approach limits the performances of the spectrometer itself introducing a deterioration of the final energy and angular resolutions due to the straggling introduced by the interaction of the ejectiles with the crossed material in the *start detector*. For this reason the x_{foc}-E_{resid} approach is preferred to the latter one. However, in some cases, the x_{foc}-E_{resid} correlation is not enough to separate ions characterized by different masses and charge states but similar $\sqrt{m}/q$ ratio. It is the case of $^{22}Ne^{10+}$ and $^{18}Ne^{9+}$ ($\sqrt{m}/q = 0.469$ and 0.471, respectively), lying in the same locus of the $xfoc - E_{\text{resid}}$ plot of Figure 4.6 (c) selected through the magenta graphical contour. A new technique, based on the TOF approach, is presented in Ref. [49]. This technique has been developed for the first time during the experiment described in this thesis and the published experimental data compete to the same analysis described in the present chapter. In this approach, the time dif-

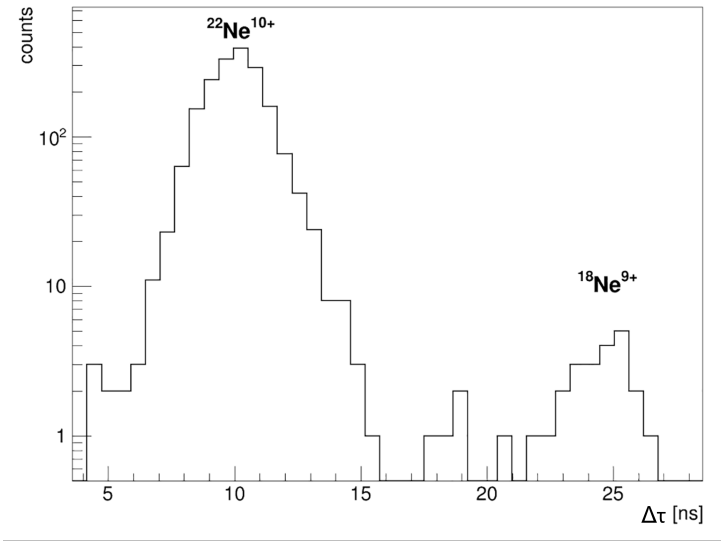

Figure 4.7: Typical $\Delta\tau$ spectrum, corresponding to the RF delay in ns, for the events gated by the graphical red and magenta contours shown in Figures 4.6(a) and (d), respectively. The peaks correspond to the $^{22}Ne^{10+}$ and the $^{18}Ne^{9+}$ events.

ference between the superconductive cyclotron radio-frequency (RF) is used as periodic STOP signal for a time to amplitude converter (TAC) module, while the START signal is provided by the timing of the silicon detectors of the MAGNEX FPD. The calibrated TAC parameter distribution measured for the events entering in the magenta gate of Figure 4.6(d) is shown in Figure 4.7. A clear separation between two peaks at different time is evident, corresponding to the $^{22}Ne^{10+}$ and $^{18}Ne^{9+}$ ejectiles. The discussed quantity, TAC (ns), is not the time of flight of the ions inside the spectrometer but the difference in time between the ion START signal and the STOP signal given by the RF radio-frequency. For that reason, the TAC parameter has a relative meaning and it is good to see how the observed time difference between the two ions with the same magnetic rigidity is compatible with the different path time ($\approx$ 13 ns) of the two ions in the spectrometer. In Figure 4.7 it is relevant to notice that the number of detected $^{18}Ne^{9+}$ is not negligible, although the very small DCE cross-section and further charge state reduction. This is due to the fact that the $^{22}Ne^{10+}$ and $^{18}Ne^{9+}$ ejectiles identified in Figure 4.7 correspond to a region of the focal plane compatible with 57 and 47 MeV of excitation energies of the final α-transfer and DCE partition, respectively. At these excitation energies the spectra are practically continue and the cross-sections are much larger than those typically measured in the bound-state region.

4.3 Trajectory reconstruction: application to the data

The trajectory reconstruction formalism of Section 3.3.2 has then applied to the $^{18}F^{8+}$ identified events, as an example to describe in detail the adopted procedure. As already discussed, the technique consists in solving the Equation 3.4 where the $Q'_f \equiv (x_f, \theta_f, y_f, \phi_f)$ vector is measured for each ion, $Q_i \equiv (\theta_i, y_i, \phi_i, \delta)$ is the trajectory reconstruction goal and G^{-1} is the inverted transport matrix. In case of the MAGNEX, G operator and its inverse G' are calculated up to the 10^{th} order using the COSY INFINITY program [94].

In the COSY INFINITY input, the spectrometer geometry and the magnetic elements and FPD positions are set. The dipole and quadruple magnetic strengths are other fundamental input parameters together with the Effective Field Boundaries (EFB) of the dipole magnet. The latter are mathematically represented as 5^{th} order polynomials in the COSY INFINITY language: there is a weak dependence of the shape of the entrance and exit EFB on the magnetic strength and therefore they are carefully optimized for each magnetic set looking at the resulting transport simulations.

The practical way to tune the trajectory reconstruction to a physics case is to compare the measured final phase space parameters with the simulated ones, which represent a model of the spectrometer response to the selected reaction: the closer the simulated description is to the measured one the better is the model of the transport operator.

4.3.1 Final phase space parameters

The analysis of the final phase space parameters for the events competing to the identified reaction channel provides information about the achieved horizontal/vertical focusing and aberrations. As an example, the final phase space populated in the (^{18}O, ^{18}F) SCE nuclear reactions at 275 MeV incident energy and $\theta_{opt} = 8°$ involving the Selenium target previously introduced is shown in Figure 4.8. The plot correlating the $^{18}F^{9+}$ horizontal angle θ_{foc} and position xf_fit is shown in panel (a). The ^{18}F ions are ejectiles of the ^{12}C(^{18}O,^{18}F)^{12}B and ^{76}Se(^{18}O,^{18}F)^{76}As single charge exchange nuclear reactions. The measured θ_{foc} values are distributed around the θ_{tilt} angle. The distribution is almost flat for xf_fit between -0.25 m and -0.10 m due to the high level density of the ^{76}As residual nucleus. The -0.35 m to -0.25 m xf_fit region is characterized by curved vertical intense loci corresponding to the populations of ^{12}C(^{18}O,^{18}F)^{12}B bound states. The deviation of such loci from vertical lines is essentially due both to the kinematic effect, i. e. the kinematic dependence of the kinetic energy on the scattering angle

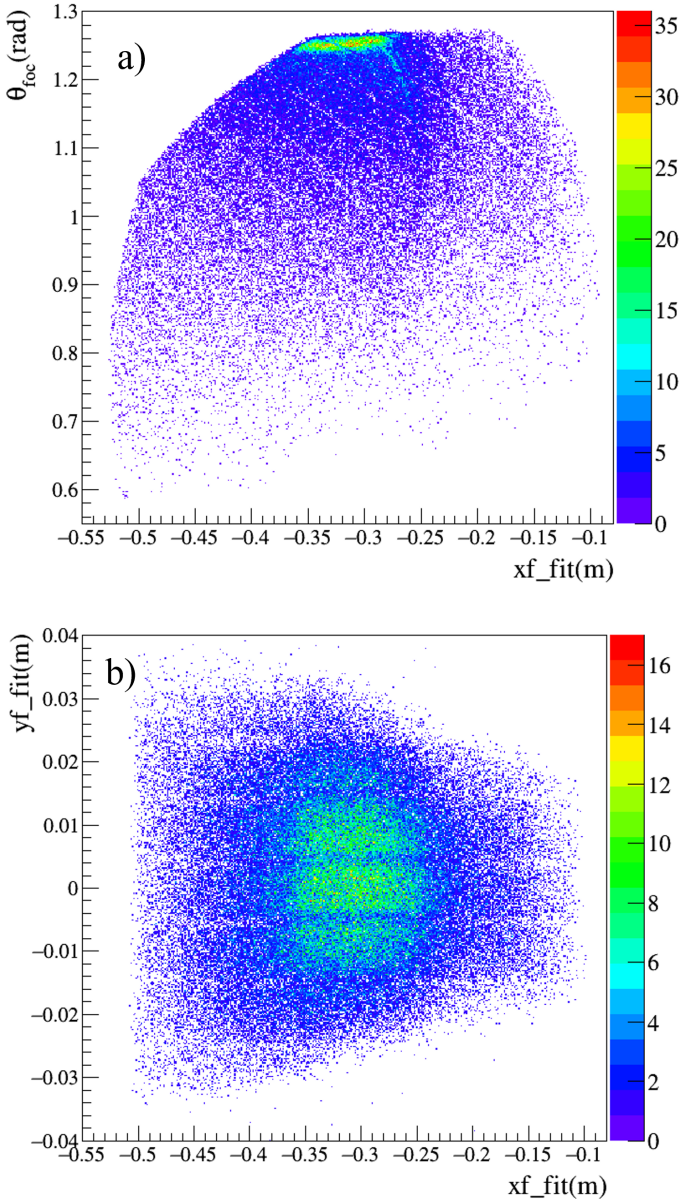

Figure 4.8: Final phase space parameters for the selected $^{18}F^{9+}$ events belonging to the (^{18}O, ^{18}F) single charge exchange reactions at 275 MeV incident energy and $\theta_{opt} = 8°$ for the Selenium target described in Section 3.2.1. (a) and (b) are the θ_{foc}-xf_fit and yf_fit-xf_fit correlations, respectively.

in a binary collision, and to high order aberrations in the horizontal phase space. A very intense bump characterizes the $\theta_{foc} > 1.25$ region corresponding to the smallest scattering angles explorable in the actual experimental set-up. It is due to the high cross-section of the (p,n) reaction p(^{18}O,^{18}F)n, occurring because of the presence of hydrogen contamination in the target.

Figure 4.8(b) shows the yf_fit-xf_fit correlation for the same $^{18}F^{9+}$ identified ejectiles. The $yf\_fit - xf\_fit$ correlations in a QD spectrometer like MAGNEX are expected to be characterized by the typical *butterfly* shape (see Refs. [105]) indicating how the ion trajectories were vertically focused only for certain value of the ion momenta. This *butterfly* shape is only half visible in the present data. The chosen quadruple field is such as to focus the ^{18}F ejectiles with magnetic rigidity larger than the one corresponding to the ^{76}Se(^{18}O, ^{18}F)^{76}As ground-to-ground state transition. No discrete structure is visible in the correlation plot.

4.3.2 Simulations

The practical way to apply the trajectory reconstruction to real data is to compare the measured observables at the focal plane with the simulated ones, which represent a model of the spectrometer response. Small adjustments ($\approx 10^{-3}$ of the field integral) are allowed in the simulations, in particular in the fringe field regions of the magnetic elements. This accounts for residual discrepancies between the real spectrometer and its model, as the known variation of the magnetic field geometry as a function of its strength, or the effect of slight misalignments of the real elements compared to the simulated ones. The closer is the simulated description of the phase space at the focal plane to the measured one the better is the model of the transport operator and consequently of its inverse.

A set of events corresponding to the (^{18}O, ^{18}F) nuclear reaction on various target nuclei, was generated using a Monte Carlo simulator tool. The ^{18}O beam energy value is an important parameter required to perform the simulations. This differs from the nominal beam energy (275.4 MeV) because of the energy loss in the target by both the ^{18}O projectile and ^{18}F ejectile before entering the spectrometer. In Figure 4.9 a sketch of the ^{76}Se target sectional view is shown. Assuming that on average the reaction occurs in the middle of the target, the energies E_i of ^{18}O/^{18}F ions before, during and after the interactions with the target material were estimated by the LISE++ [106] energy loss and the CATKIN relativistic kinematic calculations [107] and are indicated

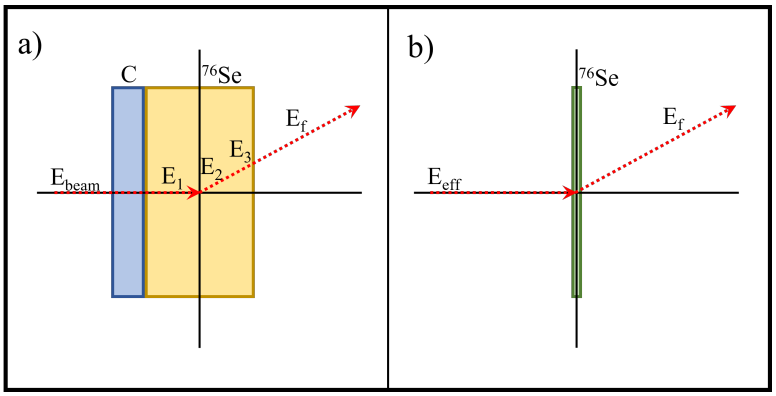

Figure 4.9: Sketches of the target and the projectile/ejectile energies involved in the nuclear reactions from the ^{18}O + ^{76}Se collision at 275 MeV of incident energy. Panels (a) and (b) indicate the true scale geometry and the zero thickness hypothesis described in the text, respectively.

in Figure 4.9 (a). The ^{76}Se target was mounted so that the beam passes first through the natural carbon backing and then through the ^{76}Se film. This choice reduces the path and minimizes the difference in energy loss for all the ejectiles coming from the nuclear reactions. In Figure 4.9 (b) the zero thickness hypothesis, used in performing the simulations that are going to be described, is sketched. The effective ^{18}O beam energy E_{eff}, used as input in the simulations, is determined as that necessary to obtain a ^{18}F ejectile at E_f energy without any energy loss in the target.

The comparison of coloured simulations and black experimental data is shown in Figure 4.10. Three nuclear reactions were simulated: ^{76}Se(^{18}O,^{18}F)^{76}As, ^{12}C(^{18}O,^{18}F)^{12}B and p(^{18}O,^{18}F)n SCE corresponding to the red, green and cyan points, respectively. For the ^{76}Se(^{18}O,^{18}F)^{76}As case only the ground-to-ground state transition has been simulated (red points)since no clear structure is visible in the experimental data competing to the charge exchange reaction on this target.

The presence of hydrogen in the target contaminates the charge exchange spectrum at very forward angles since the p(^{18}O, ^{18}F)n component dominates the $\theta_{foc} > 1.25$ rad and $xf\_fit <$ -0.28 m region of the θ_{foc}-xf_fit phase space. As already mentioned, the deviation of such loci from vertical lines is also due to the kinematic relation between the kinetic energy and the scattering angle of the ions emerging from the target. This correlation justifies the different shapes in the θ_{foc}-xf_fit representation of the loci competing to the nuclear reactions on the three target nuclei. Indeed, in the p(^{18}O, ^{18}F)n case the extreme inverse kinematics results in a very small maximum scattering

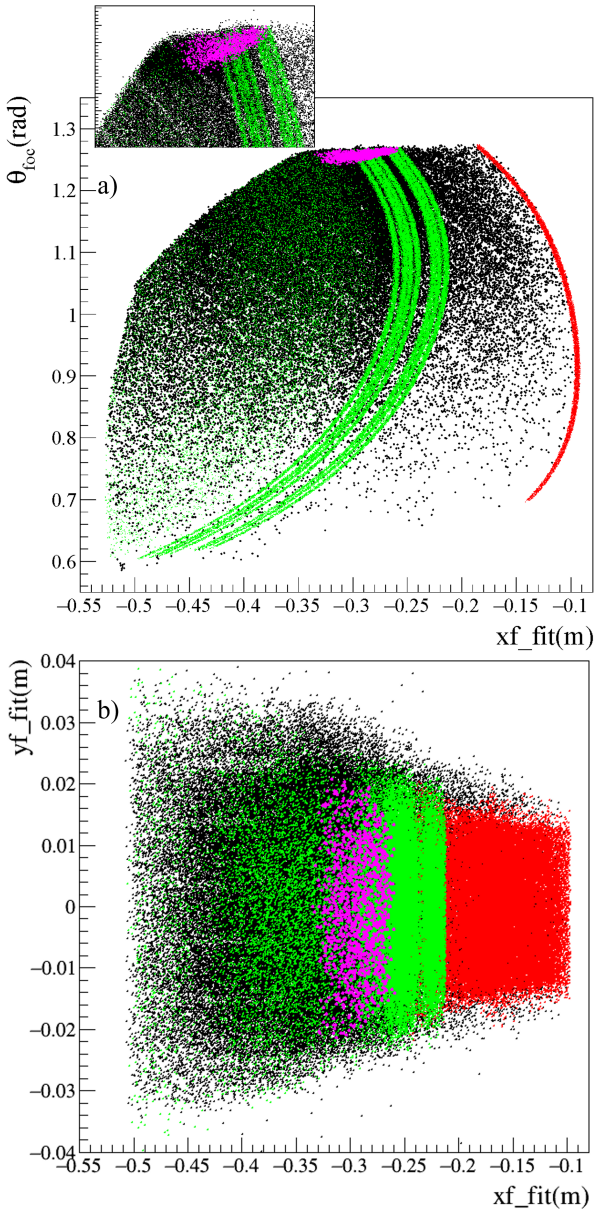

Figure 4.10: Comparison between the experimental (black points) and the simulated data: red, green and magenta points refer to the ^{76}Se(^{18}O,^{18}F)^{76}As, ^{12}C(^{18}O,^{18}F)^{12}B and p(^{18}O,^{18}F)n, reactions, respectively (see text). Panels (a) and (b) refer to the θ_{foc}-xf_fit and yf_fit-xf_fit, respectively. The inset in panel (a) is a zoomed view of the θ_{foc}-xf_fit plot ($\theta_{foc} > 1.22$) in the region dominated by the p(^{18}O,^{18}F)n contamination.

angle ($\theta_{lab} = 3.1°$) and in a very inclined kinematic locus.

The comparison of simulated and measured events was also checked in the yf_fit-xf_fit representation to test the capability of the direct transport matrix to describe the vertical components of the final phase space. This comparison is shown in the lower panel of Figure 4.10 in which many broad artificial excited states are simulated for the ^{76}Se(^{18}O, ^{18}F)^{76}As nuclear reaction up to 10 MeV of excitation energy. Looking at Figure 4.10, we can conclude that the simulated events give a rather faithful representation of the experimental ones in both the θ_{foc}-xf_fit and yf_fit-xf_fit plots.

4.3.3 Initial phase space parameters

The COSY INFINITY program makes it possible to invert the direct transport map, the one used to perform the simulations discussed before, in order to define the inverse transport equations and get the initial coordinates Q_i from the measured final ones Q_f. This procedure, already described in the previous Chapter, is the trajectory reconstruction that allows to access the momentum vector $Q_i \equiv (\theta_i, y_i, \phi_i, \delta)$ at the target point [108].

A plot of the initial vertical versus horizontal angle (ϕ_i-θ_i) is shown in Figure 4.11. The angular acceptance was defined by the positioning of the copper slits at the entrance of the MAGNEX quadrupole ($|\phi_i| < \pm 2°$ and $-5.16° < \theta_i < 6.3°$).

The laboratory scattering angle θ_{lab} and the excitation energy E_x of the ejectiles are two of the quantities of interest. The first one is related to the initial horizontal, vertical and optical angles by the following relation:

$$\theta_{lab} = \arccos \frac{\cos\theta_{opt} - \sin\theta_{opt}\tan\theta_i}{\sqrt{1 + \tan^2\theta_i + \tan^2\phi_i}} \tag{4.10}$$

From the reconstructed relative momentum δ, the kinetic energy of the ejectile is deduced and, consequently, the corresponding Q-values or, equivalently, the excitation energy E_x. The latter comes out from missing mass calculations based on relativistic energy and momentum conservation laws for binary reactions:

$$E_x = Q_0 - Q = Q_0 - K\left(1 + \frac{M_e}{M_r}\right) + E_{beam}\left(1 - \frac{M_b}{M_r}\right) + 2\frac{\sqrt{M_b M_e}}{M_r}\sqrt{E_{beam}K}\cos\theta_{lab} \tag{4.11}$$

where M_e, M_r, M_b are the ejectile, residual and beam nuclei masses, respectively. K

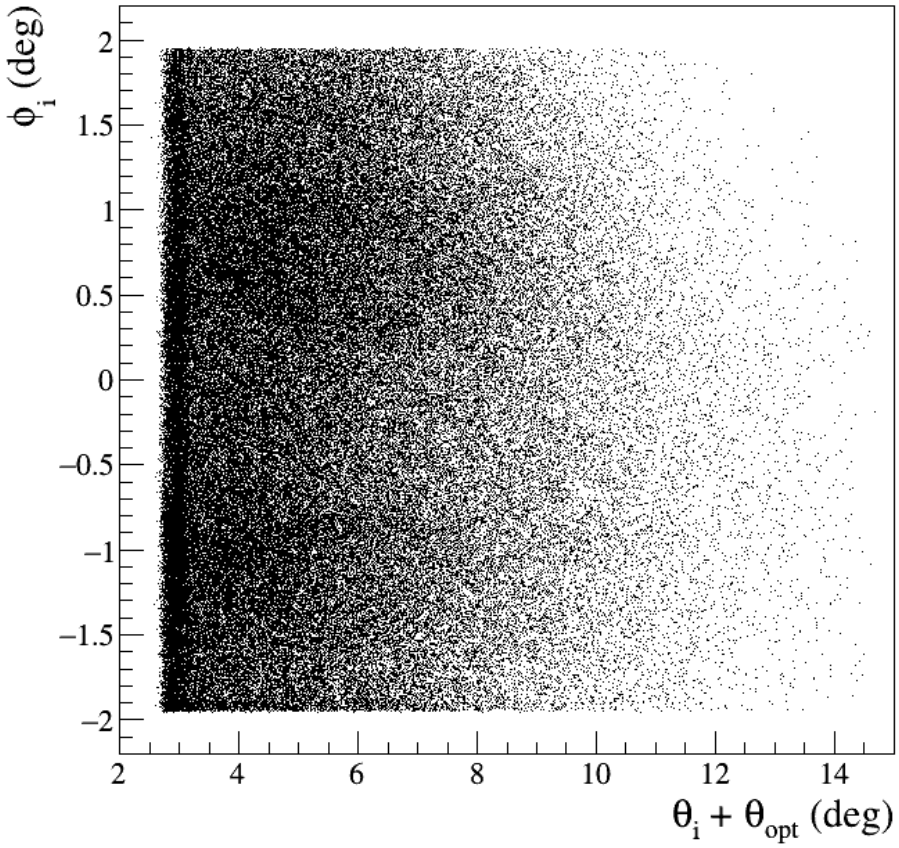

Figure 4.11: ϕ_i-θ_i+θ_{opt} plot of reconstructed variables for the selected $^{18}F^{9+}$ events belonging to the $^{76}Se(^{18}O, ^{18}F)^{76}As$ single charge exchange reaction at 275 MeV incident energy and $\theta_{opt} = 8°$. The sharp edges of the locus are due to the entrance slits of the spectrometer.

is the kinetic energy of the ejectile (related to the δ parameter) and Q_0 is the ground-to-ground state Q-value for the considered nuclear reaction. In case of the ^{76}Se(^{18}O, ^{18}F)^{76}As nuclear reaction Q_0 = -4.618 MeV and the θ_{lab}-E_x plot is shown in Figure 4.12. Due to the very high level-density of the ^{76}As residual nucleus, the θ_{lab}-E_x distribution of events is structureless. The efficiency loss, above 30 MeV excitation energy, is due to the limited acceptance of the spectrometer [84].

4.4 Cross-sections

Cross-sections are the main link between the experimental and theoretical study of nuclear reactions. Methods and formulae used to evaluate the differential and integrated absolute cross-sections, in the case of the reconstructed MAGNEX data, will be described in the following section. Particularly relevant is the technique used for the solid angle evaluation.

4.4.1 Cross-section energy and angular distribution

The energy and angular distribution of double differential cross-section is often used to perform the multipole decomposition analysis (MDA) [63]. It is experimentally defined by the following formula:

$$\frac{d^2\sigma}{dE_{lab}d\Omega_{lab}} = \frac{N(\theta_{lab}, E_x)}{N_t N_{beam}\epsilon(\theta_{lab})\Delta E_{lab}\Delta\Omega_{lab}} \tag{4.12}$$

where $N(\theta_{lab}, E_x)$ is the number of counts acquired in the energy interval ΔE_{lab} centred on E_x and in the angular interval $\Delta\theta_{lab}$ centred on θ_{lab}; N_t, N_{beam} and $\epsilon(\theta_{lab})$ are the number of scattering centre in the target (in atoms/cm^2), the number of incident ^{18}O beam ions and the total detection and reconstruction efficiency at θ_{lab}, respectively; $\Delta\Omega_{lab}$ is the solid angle covered by the MAGNEX spectrometer for the $\Delta\theta_{lab}$ interval centred on θ_{lab}. The $\epsilon(\theta_{lab})$ was estimated taking into account the FPD detection efficiency ($\approx$ 95%) and the loss of events due to bad ray-reconstruction, calculated making the ratio between the well reconstructed events and the total identified events at the focal plane for each considered transition and angle. The $\Delta\Omega_{lab}$ solid angle will be described in detail in Section 4.4.2. The centre-of-mass reference frame is often used to compare the measured cross sections with the theoretical calculations. The formula

$$\left.\frac{d^2\sigma}{dE_{lab}d\Omega_{lab}}\right|_{lab} = J \left.\frac{d^2\sigma}{dE_{cm}d\Omega_{cm}}\right|_{cm} \tag{4.13}$$

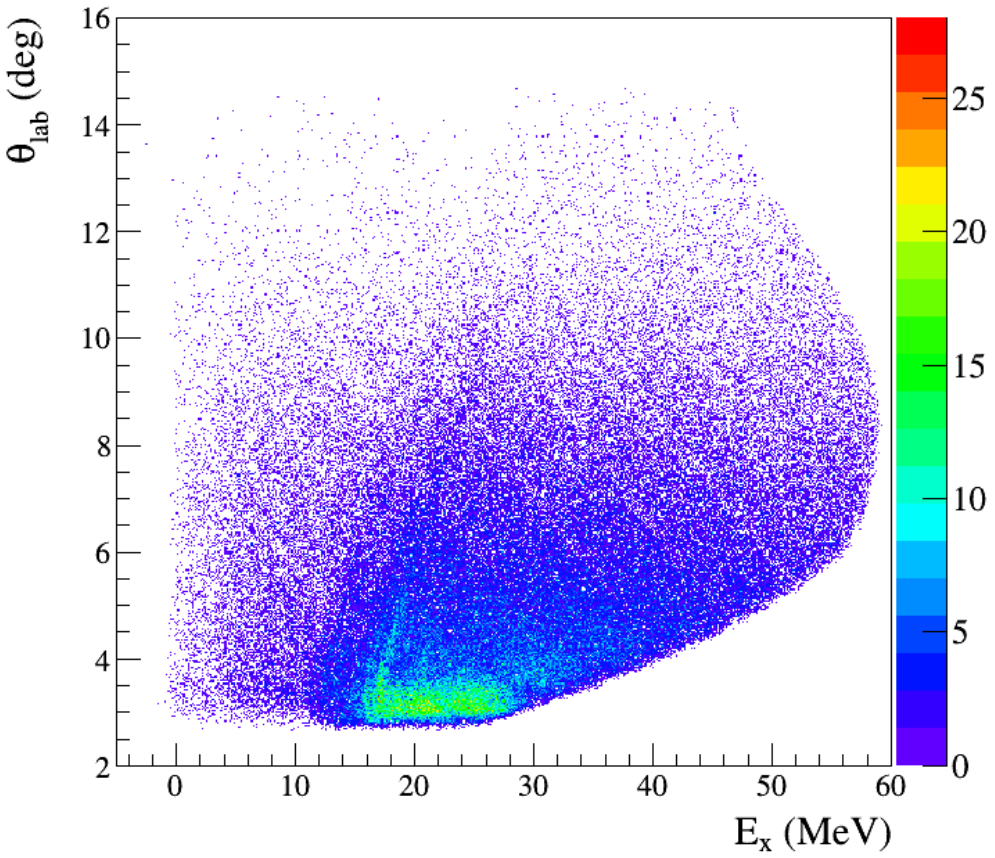

Figure 4.12: Plot of the reconstructed θ_{lab} against E_x for the selected $^{18}F^{9+}$ events belonging to the $^{76}Se(^{18}O, ^{18}F)^{76}As$ single charge exchange reaction at 275 MeV incident energy and $\theta_{opt} = 8°$.

is useful to convert the Equation 4.12 from laboratory to centre of mass reference frame. The J quantity is Jacobian operator defined by the ratio $\frac{dE_{lab}d\Omega_{lab}}{dE_{cm}d\Omega_{cm}}$ (see Ref. [109]).

The energy distribution of differential cross-section $\frac{d\sigma}{dE}(E_x)$ can be obtained just angle integrating the Equation 4.12 in $\theta_a < \theta_{lab} < \theta_b$. It is defined in the laboratory reference frame by the following formula

$$\begin{aligned}\left.\frac{d\sigma}{dE}\right|_{lab}(E_x) &= \int_{\theta_a}^{\theta_b} \frac{d^2\sigma}{dE_{lab}d\Omega_{lab}} d\Omega_{lab} = \\ &= \sum_{\theta_{lab}\in[\theta_a,\theta_b]} \frac{N(\theta_{lab}, E_x)}{N_t N_{beam}\epsilon(\theta_{lab})\Delta E_{lab}\Delta\Omega_{lab}} 2\pi \sin\theta_{lab}\Delta\theta_{lab}\end{aligned} \tag{4.14}$$

while the *lab to cm* transformation can be written using again the relation

$$\left.\frac{d\sigma}{dE}\right|_{cm} = \frac{\Delta E_{lab}}{\Delta E_{cm}} \left.\frac{d\sigma}{dE}\right|_{lab} \tag{4.15}$$

The angular distribution of differential cross-section $\frac{d\sigma}{d\Omega}(\theta_{lab})$ competing to a particular state can be obtained just integrating the 4.12 in the energy range $E_a < E_x < E_b$. It is defined in the laboratory reference frame by the following formula

$$\left.\frac{d\sigma}{d\Omega}\right|_{lab}(\theta_{lab}) = \int_{E_a}^{E_b} \frac{d^2\sigma}{dE_{lab}d\Omega_{lab}} dE_{lab} = \sum_{E_x\in[E_a,E_b]} \frac{N(\theta_{lab}, E_x)}{N_t N_{beam}\epsilon(\theta_{lab})\Delta\Omega_{lab}} \tag{4.16}$$

while the *lab to cm* transformation can be written using the relation

$$\left.\frac{d\sigma}{d\Omega}\right|_{cm} = J \left.\frac{d\sigma}{d\Omega}\right|_{lab} \tag{4.17}$$

4.4.2 Solid angle evaluation

One of the crucial aspects of the cross-section evaluation is the solid angle $\Delta\Omega_{lab}$. The spectrometer solid angle acceptance is defined by the already described copper slits visible in Figure 3.4, located 260 mm downstream of the target point. A sketch of all the relevant geometry involved in the solid angle evaluation is shown in Figure 4.13. In particular, the object point of the spectrometer, the beam direction, the scattering chamber Faraday cup, the optical axis of the spectrometer at $\theta_{opt} = 8°$ and the four copper slits are sketched. Black circles indicate the loci corresponding to the angles in the laboratory reference frame from 0° to 15°. Different views are proposed to better

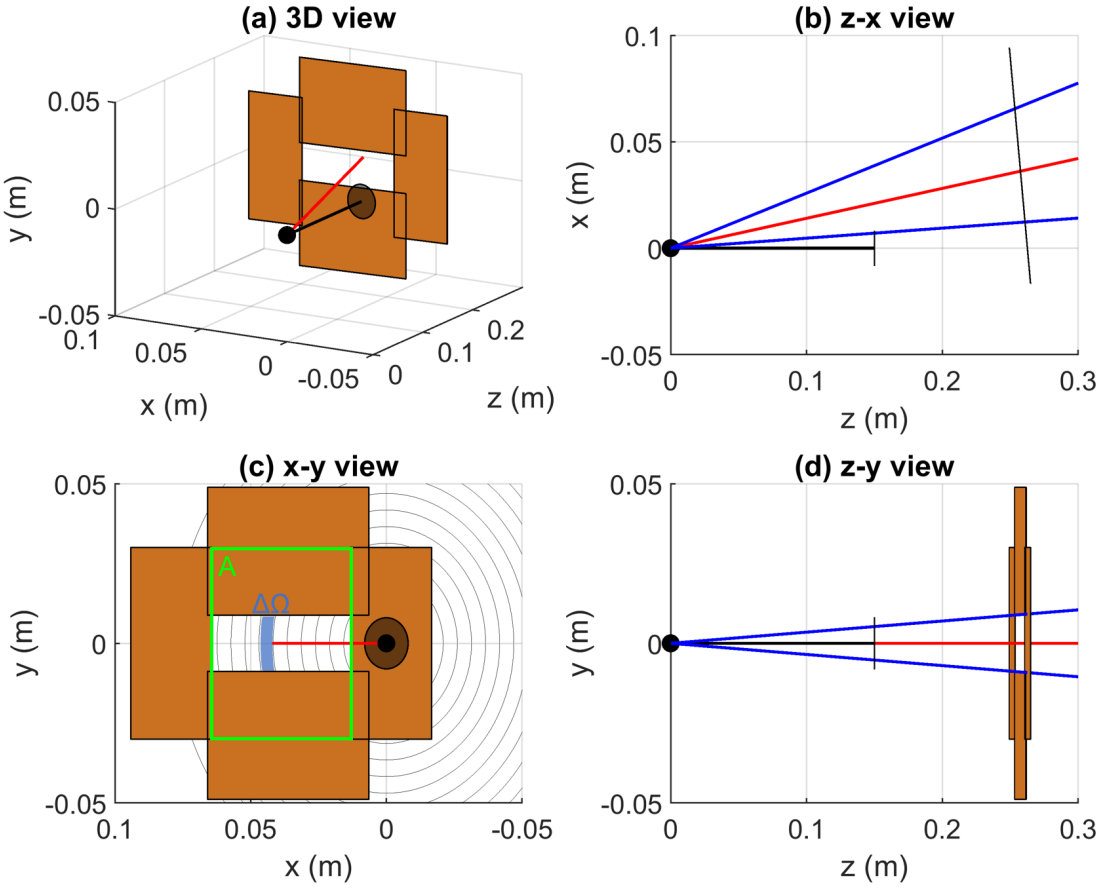

Figure 4.13: Views of the insight of the scattering chamber: target point (black dot), beam axis (black line), Faraday cup (dark-grey circle), MAGNEX optical axis (red line), MAGNEX entrance slits (brown rectangles) are sketched. Blue lines correspond to the maximum and minimum vertical and horizontal angles accepted by the MAGNEX spectrometer.

clarify the geometry.

The actual solid angle acceptance is deduced taking the contour of the θ_i-ϕ_i distribution of reconstructed events (already shown in Figure 4.11). In the reduced vertical acceptance configuration, here analysed, it is exactly coincident with the position of copper slits inner edges. The x-y view in Figure 4.13 (c) shows the blue coloured area corresponding to the $8° < \theta_{lab} < 9°$ solid angle. $\Delta\Omega$ has been deduced using a Monte Carlo tool, useful in the case of the full solid angle acceptance set-up in which the overall efficiency losses in the spectrometer correspond to an effective reduction of the solid angle, as demonstrated in Ref. [84]. In the Monte Carlo approach the following formula was used:

$$\Delta\Omega = \lim_{N \to +\infty} \frac{N_{in}}{N} A \tag{4.18}$$

where N is the number of points uniformly extracted in the A area while N_{in} is the number of points counted inside the blue delimited region. The N number is typically large enough to ensure the statistical convergence.

Chapter References

[49] M. Cavallaro et al. "Charge-state distributions of ^{20}Ne ions emerging from thin foils". In: *Res. in Phys.* 13 (2019), p. 102191. ISSN: 2211-3797. DOI: https://doi.org/10.1016/j.rinp.2019.102191.

[63] W. P. Alford and B. M. Spicer. "Nucleon charge-exchange reactions at intermediate energy". In: *Advances in Nuclear Physics* (2002), pp. 1–82.

[84] M. Cavallaro et al. "Transport efficiency in large acceptance spectrometers". In: *Nucl. Instrum. Meth. A* 637 (May 2011), pp. 77–87. DOI: 10.1016/j.nima.2011.01.078.

[89] M. Cavallaro et al. "The low-pressure focal plane detector of the MAGNEX spectrometer". In: *The European Physical Journal A* 48.5 (May 2012), p. 59. ISSN: 1434-601X. DOI: 10.1140/epja/i2012-12059-8.

[90] D. Torresi et al. "An upgraded focal plane detector for the MAGNEX spectrometer". In: *Nuclear Instruments and Methods in Physics Research Section A: Accelerators, Spectrometers, Detectors and Associated Equipment* 989 (2021), p. 164918. ISSN: 0168-9002. DOI: https://doi.org/10.1016/j.nima.2020.164918.

[91] A. Badalà et al. "Trends in particle and nuclei identification techniques in nuclear physics experiments - *Nuovo Cimento accepted*". In: *Nuovo Cimento C* (2022). DOI: 10.1007/s40766-021-00028-5.

[94] K. Makino and M. Berz. "COSY INFINITY version 8". In: *Nuclear Instruments and Methods in Physics Research Section A: Accelerators, Spectrometers, Detectors and Associated Equipment* 427.1 (1999), pp. 338–343. ISSN: 0168-9002. DOI: https://doi.org/10.1016/S0168-9002(98)01554-X.

[102] D. Carbone, F. Cappuzzello, and M. Cavallaro. "Universal algorithm for the analysis of charge distributions in segmented electrodes of gas detectors". In: *The European Physical Journal A* 48.5 (May 2012), p. 60. ISSN: 1434-601X. DOI: 10.1140/epja/i2012-12060-3.

[103] E. Segrè. *Experimental Nuclear Physics*. Experimental Nuclear Physics v. 1. Wiley, 1953.

[104] F. Cappuzzello et al. "A particle identification technique for large acceptance spectrometers". In: *Nucl. Instrum. Meth.* A621.1-3 (2010), pp. 419–423. DOI: 10.1016/j.nima.2010.05.027.

[105] D. Carbone. "Signals of the Giant Pairing Vibration in ^{14}C and ^{15}C nuclei populated by (^{18}O,^{16}O) two-neutron transfer reactions". In: *The European Physical Journal Plus* 130.7 (July 2015), p. 143. ISSN: 2190-5444. DOI: 10.1140/epjp/i2015-15143-0.

[106] O.B. Tarasov and D. Bazin. "LISE++: Radioactive beam production with in-flight separators". In: *Nuclear Instruments and Methods in Physics Research Section B: Beam Interactions with Materials and Atoms* 266.19 (2008). Proceedings of the XVth International Conference on Electromagnetic Isotope Separators and Techniques Related to their Applications, pp. 4657–4664. ISSN: 0168-583X. DOI: https://doi.org/10.1016/j.nimb.2008.05.110.

[107] W.N. Catford. "CATKIN". In: *University of Surrey* (2005).

[108] F. Cappuzzello, D. Carbone, and M. Cavallaro. "Measuring the ions momentum vector with a large acceptance magnetic spectrometer". In: *Nucl. Instrum. Methods Phys. Res. A* 638.1 (2011), pp. 74–82. ISSN: 0168-9002. DOI: https://doi.org/10.1016/j.nima.2011.02.045.

[109] Gary L. Catchen, Javed Husain, and Richard N. Zare. "Scattering kinematics: Transformation of differential cross sections between two moving frames". In: *The Journal of Chemical Physics* 69.4 (1978), pp. 1737–1741. DOI: 10.1063/1.436749.

holistic, adj.: dealing with or treating the whole of something or someone and not just a part.

Cambridge English Dictionary©

5

Multi-channel experimental and theoretical study of the $^{12}C(^{18}O,^{18}F)^{12}B$ single charge exchange reaction

Contents

The holistic approach is the main feature and novelty of the work here presented. It was applied both to the experimental and the theoretical analysis and justifies the interest of the NUMEN collaboration for the study of the ^{18}O + ^{12}C collisions. The first goal of this work is to produce new experimental data of the angular distributions and energy spectra differential cross-sections measured in the same experiment at the INFN-LNS for a broad network of quasi-elastic nuclear reactions induced by the ^{18}O + ^{12}C collisions at 275 MeV incident energy. A second goal is to analyse the experimental data using state-of-art nuclear structure and reaction theories in a unique full-comprehensive and coherent calculation. The choice of projectile and target was driven by available accurate information on the involved nuclear low-lying states in this mass region from experimental results and large scale shell-model, making this collision an ideal benchmark for the proposed multi-channel constrained technique.

5.1 Main experimental results

In the previous chapters the methods and the main properties of the nuclei involved in a typical NUMEN experiment were introduced. Here, the focus is on the experimental and theoretical results obtained in the case of the multi-channel study of the ^{18}O + ^{12}C network of nuclear reactions at 275 MeV. In Figure 5.1 a cartoon shows a zoomed view of the chart of nuclides near the A = 12 region. The coloured arrows indicate the studied reactions whose results will be shown in the following. The study of other

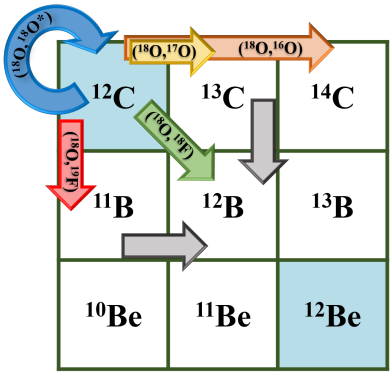

Figure 5.1: Cartoon of the nuclear reaction channels analysed in the ^{12}C + ^{18}O NUMEN experiment at 275.3 MeV described Chapter 5.

reaction channels, such as the (^{18}O, ^{20}Ne) two-proton removal and the double charge exchange, is still in a preliminary stage and will not be presented in the present work.

Target thicknesses, covered angular ranges, spectrometer optical angles and solid angles are given in Table 5.1 for each studied reaction channel. The magnetic fields of the dipole and quadrupole magnets were set in order to transport the ^{18}F^{9+}, ^{19}F^{9+}, ^{17}O^{8+} and ^{16}O^{8+} ions, corresponding to the ejectiles of the nuclear reactions of interest, in the active region of the FPD. Thanks to the large momentum acceptance of MAGNEX, a unique magnetic setting was enough to explore the relevant low-lying bound states populated in SCE, one-neutron pick-up, one- and two-proton stripping reactions. Differently, for the study of elastic and inelastic scattering a different magnetic setting was necessary to intercept the ^{18}O^{8+} ejectiles emerging from such processes.

5.1.1 The ^{12}C(^{18}O,^{18}O)^{12}C elastic and inelastic scattering

The energy spectrum of the ^{12}C(^{18}O,^{18}O)^{12}C elastic and inelastic scattering at angles between 5° and 6° in the laboratory frame is shown in Figure 5.2. The energy resolution is $\delta E_x \approx 0.6$ MeV in full-width at half maximum (FWHM). This resolution, together with the low level density in the involved nuclei, made it possible to identify from the observed peaks the transitions to individual states that are listed in Table 5.2.

The bound-state region of the spectrum is dominated by the transition to ground and to the collective 2_1^+ states at 1.982 MeV and 4.440 MeV of projectile and target, respectively, whereas their simultaneous excitation is visible in the structure at $E_x \approx 6.42$ MeV. The two-phonon triplet of the ^{18}O (4_1^+ at 3.555 MeV, 0_2^+ at 3.634 MeV

Table 5.1: Experimental set-up of each explored reaction channels: the target thickness, the range of scattering angles $[\theta_{lab}^{min}; \theta_{lab}^{max}]$, the central angle θ_{opt}, the Bρ magnetic rigidity, the BQ quadrupole magnetic field and the solid angle of the MAGNEX spectrometer are given.

	target thickness (μg/cm^2)	$[\theta_{lab}^{min}; \theta_{lab}^{max}]$ (deg)	θ_{opt} (deg)	Bρ (Tm)	BQ (T)	solid angle (msr)
^{12}C(^{18}O,^{18}O)^{12}C	60 ± 3	[3.5; 14.2]	7.5	1.1767	-0.657	49.2
	400 ± 20		9.0	1.2134	-0.661	13.6
	60 ± 3		13.5	1.1767	-0.657	49.2
^{12}C(^{18}O,^{17}O)^{13}C	200 ± 10	[3.1; 17.5]	8.0	1.1494	-0.622	13.6
	60 ± 3		13.5	1.1260	-0.629	49.2
^{12}C(^{18}O,^{16}O)^{14}C	60 ± 3	[3.0; 19.0]	7.5	1.1260	-0.632	49.2
	60 ± 3		13.5	1.1260	-0.632	49.2
^{12}C(^{18}O,^{19}F)^{11}B	60 ± 3	[3.6; 16.1]	7.5	1.1260	-0.629	49.2
	200 ± 10		8.0	1.1494	-0.622	13.6
	60 ± 3		13.5	1.1260	-0.624	49.2
^{12}C(^{18}O,^{18}F)^{12}B	60 ± 3	[3.2; 14.3]	7.5	1.1260	-0.629	49.2
	200 ± 10		8.0	1.1494	-0.622	13.6
	60 ± 3		13.5	1.1260	-0.629	49.2

Table 5.2: Excitation energies (E_x) in MeV, total angular momentum and parity (J^π) of the populated states and transferred orbital angular momenta (L) in the ^{12}C(^{18}O,^{18}O)^{12}C elastic and inelastic scattering at 275 MeV. The energies in the first column correspond to those listed in the legend of Figure 5.2. The dimensionless quality factors (QFs) defined by the Equation 5.6 are listed for the DWBA, CCBA and CRC performed calculations.

	E_x (MeV)		L	QF		
	^{18}O (J^π)[110]	^{12}C (J^π)[111]		DWBA	CCBA	CRC
0.00	0.000 (0^+)	0.000 (0^+)	0	0.63	0.78	0.80
1.98	1.982 (2^+)	0.000 (0^+)	2	0.52	0.64	0.65
	3.554 (4^+)	0.000 (0^+)	4			
3.60	3.633 (0^+)	0.000 (0^+)	0	-	-	-
	3.920 (2^+)	0.000 (0^+)	2			
4.44	0.000 (0^+)	4.440 (2^+)	2	0.71	0.65	0.60
5.10	5.097 (3^-)	0.000 (0^+)	3	0.71	0.71	0.68
6.42	1.982 (2^+)	4.440 (2^+)	2⊕2	-	0.71	0.72
7.65	0.000 (0^+)	7.654 (0^+)	0	-	-	-
9.64	0.000 (0^+)	9.641 (3^-)	3	0.58	0.68	0.68

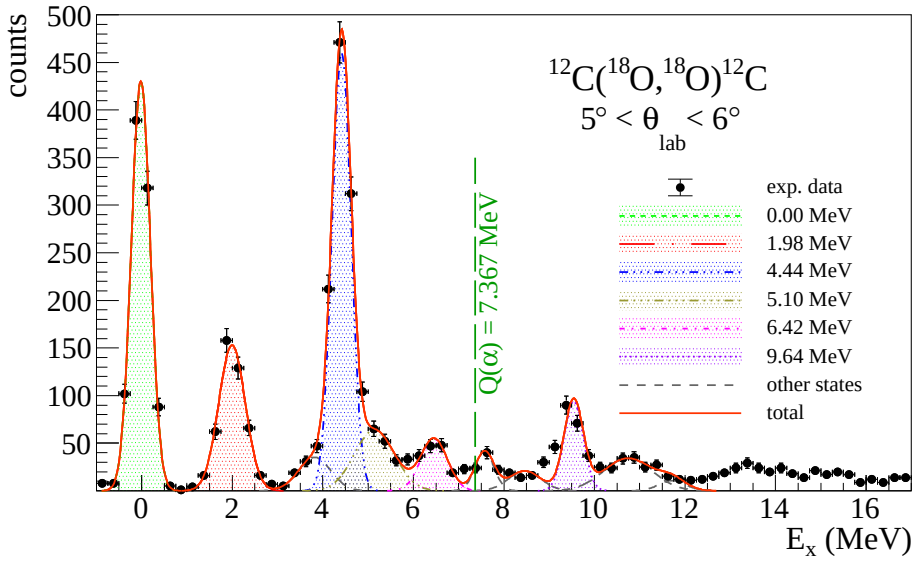

Figure 5.2: ^{12}C(^{18}O,^{18}O)^{12}C elastic and inelastic scattering energy spectrum at 5° $< \theta_{lab} <$ 6°. Lines, obtained from best-fit procedure, identify peaks corresponding to the superposition of the projectile and target states, as labelled in the legend.

and 2_2^+ at 3.920 MeV) is not resolved in the spectra and corresponds to a structure centred at 3.6 MeV, very close to the strong peak at $E_x \approx 4.44$ MeV. The two peaks at $E_x \approx 5.10$ MeV and $E_x \approx 9.64$ MeV in Figure 5.2 were attributed to the collective 3_1^- states of ^{18}O and ^{12}C, respectively. The 7.654 MeV peak corresponding to the ^{12}C 0_2^+ Hoyle state was identified in the spectrum, although the collected statistics is not enough to extract the angular distribution.

The excitation energy region of the ^{12}C around 10 MeV was extensively studied in recent years searching for the 2_2^+ state, considered the first excited state of the Hoyle rotational band, predicted by the α-cluster model [112, 113]. In the study of M. Itoh *et al.* a 2^+ state was observed at $E_x = 9.84$ MeV with a FWHM of about 1 MeV, submerged by the broad 0^+ state at $E_x = 9.93$ MeV and width of 2.7 MeV. Indeed, the peak at 9.64 MeV observed in our spectra could also contain contributions from these states. The comparison with the theoretical calculations will help in clarifying the interpretation of the peak as due to the population of the 3_1^- state of ^{12}C.

The multiple-fit procedure, shown in Figure 5.2, was performed to extract the number of counts in the explored angular range, disentangling the contributions coming from

the different transitions lying on the same excitation energy region. The width of each Gaussian function in the multiple-fit procedure was set according to the experimental energy resolution, including the recoil energy broadening due to the in-flight decay of the ejectile for the transitions in which it was in a bound excited state.

The angular distributions of differential cross-section were extracted for the ground-state, the 1.98 MeV, the 4.44 MeV, the 5.10 MeV, the 6.42 MeV and the 9.64 MeV peaks. These angular distributions are shown in Figures 5.3 and 5.4. The explored angular range was spanned in three independent measurements performed at different, but partially overlapping, MAGNEX central angles as already mentioned and listed in Table 5.1. The three cross-section measurements were found to be in good agreement each other without the need of any re-normalization factor. The experimental points in Figures 5.3 and 5.4 were obtained, in the overlap region, by a weighted average of the measured values at the different angular sets. The error bars include uncertainties coming from the statistical contribution, solid angle estimation and fitting procedure. An overall uncertainty of about 10%, due to the determination of charge collection and target thickness, is common to all data points in the angular distributions and it is not included in the error bars. The angular resolution is $\delta\theta_{cm} \approx 0.5°$ allowing for a clear observation of the diffracting oscillation pattern in the angular distributions. The excitation energy and spin-parity of the states involved in the measured angular distribution, together with the transferred angular momentum L^*, are given in Table 5.2.

5.1.2 The ^{12}C(^{18}O,^{17}O)^{13}C one-neutron addition reaction

The energy spectrum of the ^{12}C(^{18}O,^{17}O)^{13}C one-neutron stripping reaction is shown in Figure 5.5 for $3.8° < \theta_{lab} < 3.9°$. The obtained energy resolution is $\delta E_{\rm x} = 0.6$ MeV FWHM. The correspondence between the peaks observed in the spectrum and populated states of projectile and target is indicated in Table 5.3.

The spectrum resembles the one reported of Ref. [114], measured at 84 MeV incident energy. In both spectra the strength is concentrated in the low excitation energy region ($E_{\rm x} < 5$ MeV). This is a result of the similar Q-value matching conditions [115] which give the optimal excitation energies E_x^{opt}(84 MeV) = 1.6 MeV and E_x^{opt}(275 MeV) = -7.3 MeV†, and the angular momenta L^{opt}(84 MeV) = 1.5 and L^{opt}(275 MeV) = 1.

*Throughout the present work, the transferred angular momentum L is expressed in $\hbar$ units.

†One should notice that a negative value for the E_x^{opt} is unphysical. Here we only mean that the best energy matching is expected for transitions close to that condition, namely those to low lying states.

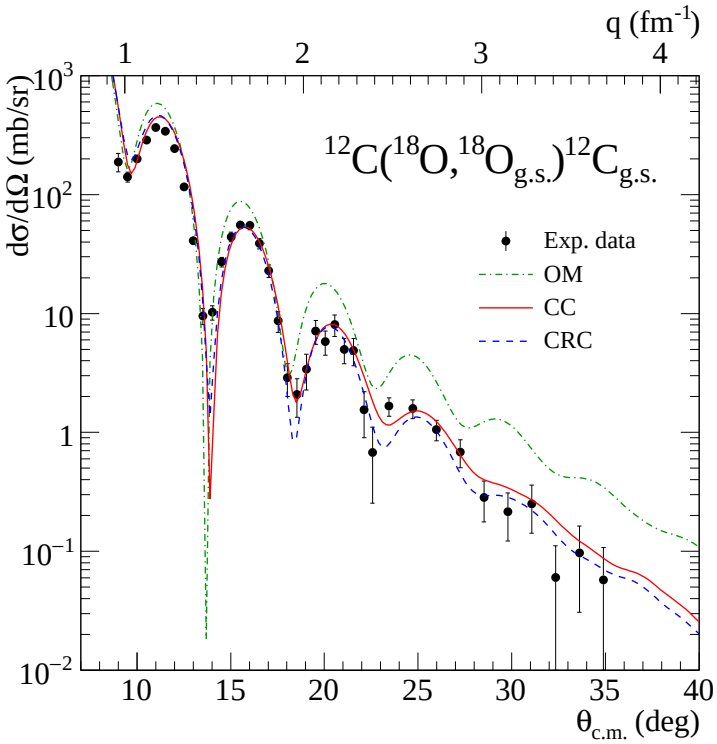

Figure 5.3: Experimental cross-section angular distribution of the ^{12}C(^{18}O,^{18}O)^{12}C elastic scattering at 275 MeV incident energy. Theoretical calculations for the elastic transition in OM, CC and CRC approaches are shown with the green dot-dashed, continuous red and blue dashed lines, respectively.

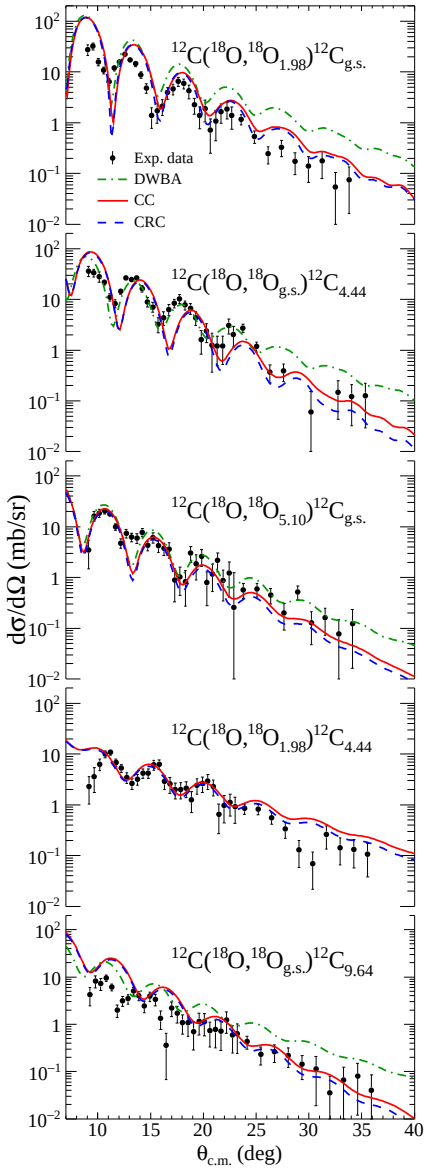

Figure 5.4: Experimental cross-section angular distribution of the $^{12}C(^{18}O,^{18}O)^{12}C$ inelastic scattering at 275 MeV incident energy associated with the peaks at 1.98, 4.44, 5.10, 6.42 and 9.64 MeV indicated in Figure 5.2 and Table 5.2. Theoretical calculations for the inelastic transitions in DWBA, CC and CRC approaches are shown with the green dot-dashed, continuous red and blue dashed lines, respectively.

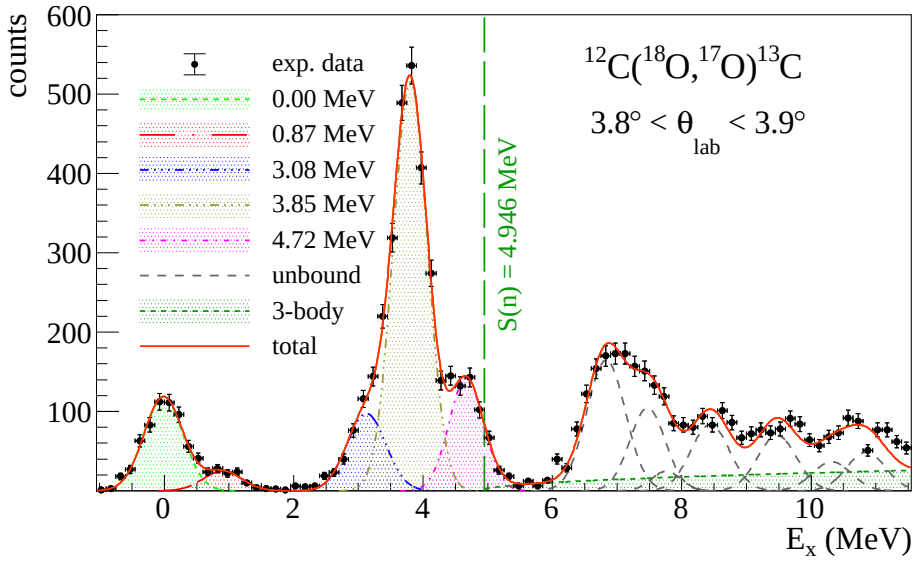

Figure 5.5: ^{12}C(^{18}O,^{17}O)^{13}C one-neutron addition energy spectrum at $3.8° < \theta_{lab} < 3.9°$. Lines, obtained from best-fit procedure, identify peaks corresponding to the superposition of the projectile and target states, as labelled in the legend.

As already noticed from the data at 84 MeV [114], the transitions to well-known single-particle states of ^{13}C products and ^{17}O ejectiles are dominant. The same scenario was found in the study of the ^{12}C(d,p)^{13}C reaction reported in Ref. [116], in which the weak population of states with more complex configurations indicates that the direct transfer of one neutron is the leading mechanism.

A multiple-fit procedure, similar to that discussed for the elastic and inelastic scattering spectrum (see Figure 5.2), was applied to the one-neutron transfer case and an example is shown in Figure 5.5. A list of the different transitions lying underneath the same peak is detailed in Table 5.3.

The cross-section angular distributions were extracted for the peaks at $E_x = 0.00$, 0.87, 3.08, 3.85 and 4.64 MeV and are shown in Figure 5.6. These correspond to the superposition of transitions to bound states of ^{13}C (below the one-neutron separation energy $S_n = 4.946$ MeV) and/or of ^{17}O ($S_n = 4.143$ MeV). Resembling the elastic scattering case, the explored angular range was covered by two independent measurements (see Table 5.1). The measured cross-sections in the overlapping angular regions do not need any re-normalization factor witnessing a small systematic error in this procedure.

The error bars include the same contributions discussed for the elastic and inelastic scattering angular distributions.

5.1.3 The ^{12}C(^{18}O,^{16}O)^{14}C two-neutron addition reaction

The excitation energy spectrum for the ^{12}C(^{18}O,^{16}O)^{14}C two-neutron addition nuclear reaction is shown in Figure 5.7. An energy resolution of $\approx$ 500 keV FWHM is estimated from fit of the experimental peaks with gaussian functions. Several narrow peaks corresponding to ^{14}C low-lying bound and resonant states are observed.

The correspondence between labels in Figure 5.7 and the ^{14}C states is listed in Table 5.4. Most of them were previously observed in the ^{12}C(^{18}O,^{16}O)^{14}C experiment at 84 MeV incident energy [119]. A broad bump is visible at the excitation energy E_{x} = 17.1 $\pm$ 0.2 MeV, with FWHM = 1.1 $\pm$ 0.2 MeV superimposed to a flat background. These values agree with the energy (E_{x} = 16.9 $\pm$ 0.1 MeV) and width (FWHM = 1.2 $\pm$ 0.3 MeV) of the Giant Pairing Vibration (GPV) resonance measured at 84 MeV, thus confirming the first GPV evidence of Ref. [119]. Matching the present results with those of Ref. [119], the weighted average for the centroid and width of the ^{14}C GPV was calculated as E_{x} = 16.94 $\pm$ 0.09 MeV and FWHM = 1.1 $\pm$ 0.2 MeV, respectively.

Some differences are evident between the spectra measured at 84 and 275 MeV bombarding energies. Above the two-neutron emission threshold (S_{2n} = 13.122 MeV) a much larger background is observed in the present higher energy case. This is a consequence of the widening of the phase space at increasing incident energy and of the different kinematical matching conditions. An estimate of the optimal excitation energy for the analysed reaction, based on the semi-classical formalism of Ref. [115], gives E_x^{opt}(84 MeV) = 10.3 MeV and E_x^{opt}(275 MeV) = 31 MeV, in agreement with the data. Another effect of the higher incident energy is to favour the population of high spin states. The optimal angular momentum transfer, calculated according to Ref. [115], is L^{opt}(84 MeV) = 3 and L^{opt}(275 MeV) = 5.5. Indeed, in the present ^{14}C spectrum, the most intense structure includes the 4^+ state at 10.736 MeV. The high spin states at 12.963 MeV and 14.868 MeV, not observed at 84 MeV, are now well visible, while the 0^+ ground state is strongly suppressed.

The ^{12}C(^{18}O,^{16}O)^{14}C cross-section angular distributions of some populated states are presented in Figure 5.8. For each transition the number of counts collected at each angle was determined through a fit procedure similar to that described in the previous paragraphs. An analytical shape is adopted for the three-body phase space for the ^{16}O

Table 5.3: Excitation energies (E_x), total angular momentum and parity (J^π) of the populated states and transferred orbital angular momenta (L) in the ^{12}C(^{18}O,^{17}O)^{13}C one-neutron addition at 275 MeV. Together with the cross-sections $\sigma_{theo.}$ integrated in the angular domain between 0 and 180°, quality factors QF are calculated using Equation 5.6 for each of the angular distributions shown in Figures 5.6. The energies in the first column correspond to those listed in the legend of Figure 5.5.

	E_x (MeV)		DWBA		CCBA		CRC	
	^{17}O (J^π)[117]	^{13}C (J^π)[118]	$\sigma_{theo.}$ (μb)	QF	$\sigma_{theo.}$ (μb)	QF	$\sigma_{theo.}$ (μb)	QF
0.00	0.000 ($5/2^+$)	0.000 ($1/2^-$)	2031	0.75	1865	0.72	1742	0.69
0.87	0.871 ($1/2^+$)	0.000 ($1/2^-$)	689	0.76	666	0.74	622	0.73
3.08	3.055 ($1/2^-$)	0.000 ($1/2^-$)	118	0.46	112	0.56	109	0.49
	0.000 ($5/2^+$)	3.089 ($1/2^+$)	633		412		397	
3.85	0.000 ($5/2^+$)	3.684 ($3/2^-$)	567	0.74	606	0.72	566	0.77
	0.000 ($5/2^+$)	3.854 ($5/2^+$)	12640		11525		10732	
	0.871 ($1/2^+$)	3.089 ($1/2^+$)	262		193		191	
4.64	0.871 ($1/2^+$)	3.684 ($3/2^-$)	221	0.63	232	0.75	220	0.78
	0.871 ($1/2^+$)	3.854 ($5/2^+$)	4617		3469		3307	
6.88	3.055 ($1/2^-$)	3.684 ($3/2^-$)						
	0.000 ($5/2^+$)	6.864 ($5/2^+$)	-	-	-	-	-	-
	3.055 ($1/2^-$)	3.854 ($5/2^+$)						
7.52	0.000 ($5/2^+$)	7.492 ($7/2^+$)	-	-	-	-	-	-
	0.000 ($5/2^+$)	7.547 ($5/2^-$)						
7.71	0.000 ($5/2^+$)	7.686 ($3/2^+$)	-	-	-	-	-	-
	0.871 ($1/2^+$)	6.864 ($5/2^+$)						
8.39	0.871 ($1/2^+$)	7.492 ($7/2^+$)	-	-	-	-	-	-
	0.871 ($1/2^+$)	7.547 ($5/2^-$)						
9.50	0.000 ($5/2^+$)	9.500 ($9/2^+$)	-	-	-	-	-	-
10.37	0.871 ($1/2^+$)	9.500 ($9/2^+$)	-	-	-	-	-	-
10.80	0.000 ($5/2^+$)	10.753 ($7/2^-$)						
	0.000 ($5/2^+$)	10.819 ($5/2^-$)	-	-	-	-	-	-
	0.000 ($5/2^+$)	10.996 ($1/2^+$)						

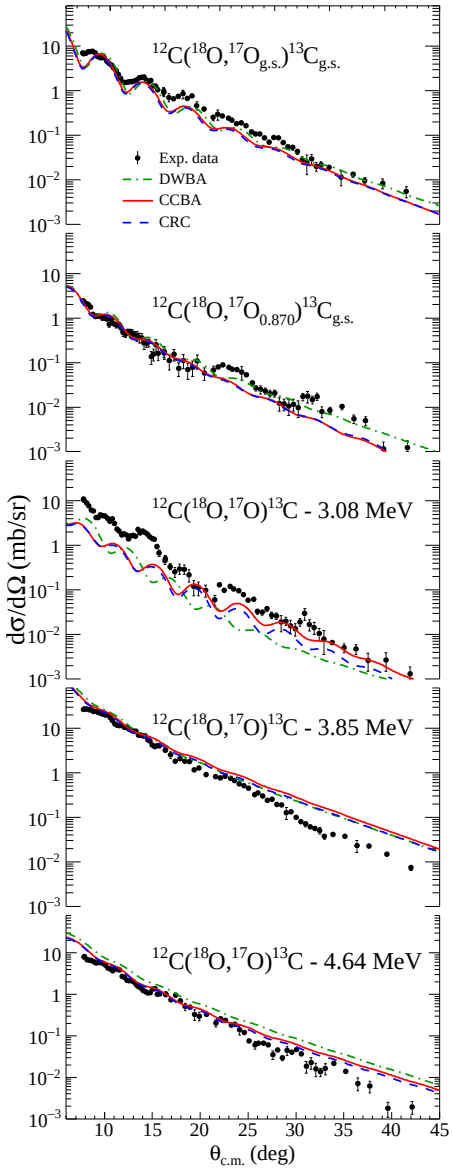

Figure 5.6: Experimental cross-section angular distribution of the ^{12}C(^{18}O,^{17}O)^{13}C one-neutron addition at 275 MeV incident energy associated with the peaks at 0.00, 0.87, 3.08, 3.85 and 4.72 indicated in Figure 5.5 and Table 5.3. Theoretical calculations of the one-neutron addition nuclear reaction in DWBA, CCBA and CRC approaches are shown with the green dot-dashed, continuous red and blue dashed line, respectively.

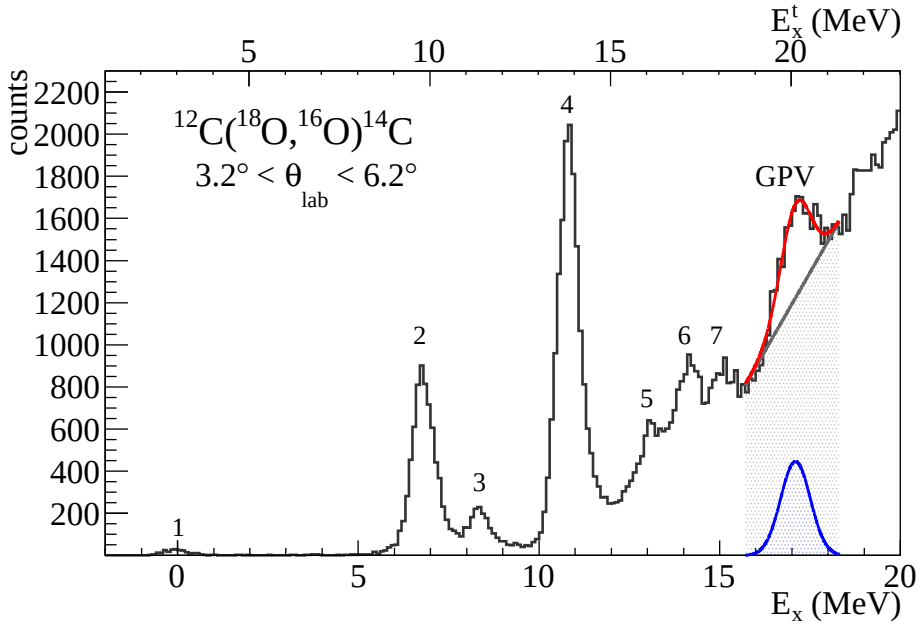

Figure 5.7: ^{12}C(^{18}O,^{16}O)^{14}C two-neutron addition energy spectrum at $3.2° < \theta_{lab} < 6.2°$. Figure from Ref. [52].

Table 5.4: Excitation energies (E_x), total angular momentum and parity (J^π) of the populated states and transferred orbital angular momenta (L) in the ^{12}C(^{18}O,^{16}O)^{14}C two-neutron addition at 275 MeV. The labels in the first column correspond to those shown in the legend of Figure 5.7.

Peak label	^{14}C (from Ref. [118])	
	E_x (MeV)	J^π
1	0.000	0^+
2	6.728	3^-
	7.012	2^+
3	8.318	2^+
4	10.425	2^+
	10.736	4^+
5	12.963	3^-
6	14.05	-
7	14.868	6^+,5^-
GPV	16.94 ± 0.09	0^+

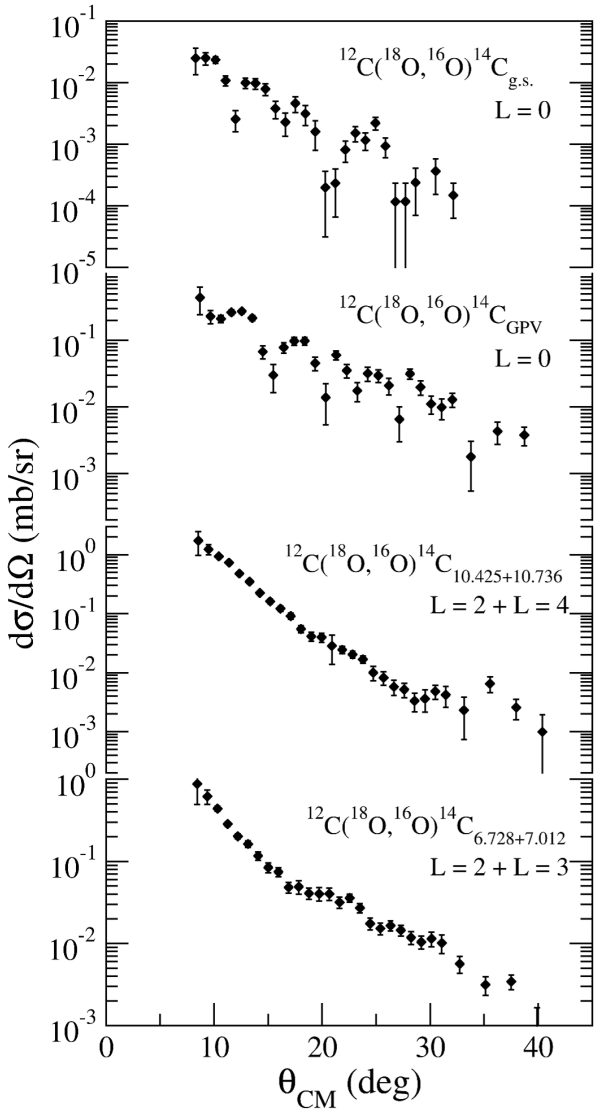

Figure 5.8: Experimental cross-section angular distribution of the $^{12}C(^{18}O,^{16}O)^{14}C$ two-neutron addition at 275 MeV incident energy associated with the peaks labelled in Figure 5.7 and listed in Table 5.4. Data are published in Ref. [52]

+ ^{13}C + n breakup from Ref. [120]. The continuum background at high excitation energy, due to the convolution of not resolved states, is modelled by a linear function in the region of the GPV as represented in Figure 5.7. The statistical error and the uncertainties coming from the peak integration and from the differential solid angle evaluation are included in the error bars. The angular resolution in the centre of mass frame is about 0.5°. Figure 5.8 shows the experimental angular distributions for the transitions to the ^{14}C 0^+ ground state and GPV. The angular distributions show an oscillating pattern, distinctive feature of L= 0 angular momentum transfer as already observed for the same transitions in the previous experiment at 84 MeV. The period of the oscillation is smaller in the present data than Ref. [119] as a consequence of the higher bombarding energy. The angular distributions for higher multipolarity (L= 2, 3, 4), corresponding to the transitions marked by the label 2 of Figure 5.7 and Table 5.4 (unresolved 6.728 MeV and 7.012 MeV) and by the label 4 (unresolved 10.425 MeV and 10.736 MeV), are shown in Figure 5.8. Here we observe structureless patterns, due to the out-of-phase contributions of even and odd components of the angular momentum transfer partial waves, present in $L\neq$ 0 transitions for transfer reactions as discussed in Ref. [121].

5.1.4 The ^{12}C(^{18}O,^{19}F)^{11}B one-proton removal reaction

The excitation energy spectrum measured for the ^{12}C(^{18}O,^{19}F)^{11}B one-proton pick-up reaction at 4.4°$< \theta_{lab} <$4.6° is shown in Figure 5.9. The energy resolution could not be easily extracted from the collected data due to the high level density in the ^{19}F nucleus. We can assume an energy resolution $\delta E_{\mathrm{x}} \approx$ 0.5 MeV, similar to the other reaction channels since the experimental conditions were the same.

As already observed for the one-neutron transfer reaction, the strength is concentrated at energies below the Q(α) = 8.664 MeV threshold. This behaviour is compatible with the optimal matching conditions E_x^{opt} = -3.3 MeV (see footnote † on page 113) and the L^{opt} = 2 calculated according to Ref. [115]. We identified four main peaks (see Figure 5.9) described in terms of the ^{19}F and ^{11}B populated states listed in Table 5.5.

The population of the ^{11}B ($\frac{3}{2}^-$) ground state can be easily explained by the direct removal of one $1\mathrm{p}_{\frac{3}{2}}$ proton from the g.s. of the ^{12}C. The 2.124 MeV ($\frac{1}{2}^-$) and 5.020 MeV ($\frac{3}{2}^-$) states are mainly accessed by the removal of one proton from the $1\mathrm{p}_{\frac{1}{2}}$ and $1\mathrm{p}_{\frac{3}{2}}$ shells, respectively, starting from the ^{12}C g.s. configuration in which two protons are found in the $1\mathrm{p}_{\frac{1}{2}}$ orbital [122, 123].

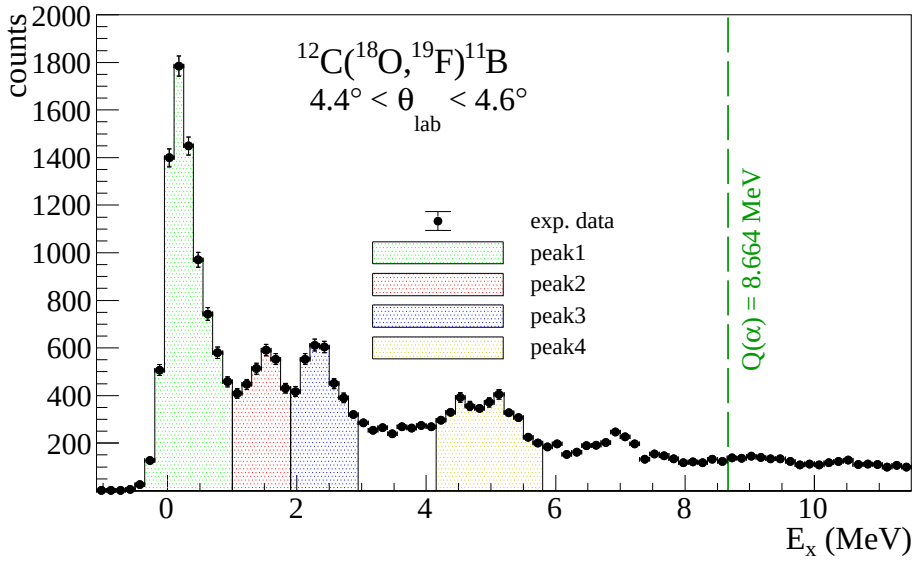

Figure 5.9: ^{12}C(^{18}O,^{19}F)^{11}B one-proton removal energy spectrum at $4.4° < \theta_{lab} < 4.6°$. The hatched areas indicate the regions of interest for the study of the angular distributions as labelled in the legend.

The states at 4.445 MeV ($\frac{5}{2}^-$) and 6.76 MeV ($\frac{7}{2}^-$) have attracted particular interest in the past [122, 124] for the following reasons. In order to be populated by the removal of a proton from the ^{12}C g.s., these states should contain large admixtures of $1f$ orbitals or, alternatively, they should have a significant configuration of a $1p_{\frac{3}{2}}$ proton hole coupled to the 2^+ core excitation of ^{12}C at 4.440 MeV. This second hypothesis corresponds to two different but analogous reaction paths: the excitation of the 2^+ state in the initial partition followed by the removal of the $1p_{\frac{3}{2}}$ proton or the removal of a $1p_{\frac{3}{2}}$ proton followed by the inelastic 2^+ excitation in the final partition. According to that, the proper treatment of such two-step processes requires the explicit inclusion of the couplings with the inelastic states in both the initial and final partitions, demanding for sophisticated reaction calculations.

Similar arguments can be applied to the ^{19}F level structure. The ground ($\frac{1}{2}^+$), 0.197 MeV ($\frac{5}{2}^+$) and 1.554 MeV ($\frac{3}{2}^+$) states are expected to have strong single-particle configurations with a proton in the $2s_{\frac{1}{2}}$, $1d_{\frac{5}{2}}$ and $1d_{\frac{3}{2}}$ orbitals, respectively. The negative parity states 0.110 MeV ($\frac{1}{2}^-$) and 1.458 MeV ($\frac{3}{2}^-$) can have a single particle component in the $1p_{\frac{1}{2}}$ and $1p_{\frac{3}{2}}$ shells. Regarding the 1.345 MeV ($\frac{5}{2}^-$) and 2.780 MeV ($\frac{9}{2}^+$) states

we expect a very small contribution from single particle configurations since they should involve the $1f_{\frac{5}{2}}$ and $1g_{\frac{9}{2}}$ orbitals that are far away from the Fermi level of $^{18}O_{g.s.}$. Thus, also for these states we expect important contributions from core excitation configurations involving the 2^+ and 3^- collective excitation of ^{18}O, as we recently found in other (^{18}O, ^{19}F) one-proton transfer reactions [53].

In this case we considered not safe to extract the counts using the multiple-fit technique described in the previous paragraphs. Instead, for each peak we determines the yield in the regions highlighted with colours in Figure 5.9. The obtained angular distributions are given in Figure 5.10, in which the error bars include only the statistical and solid angle estimation uncertainties. The angular range was covered by three independent measurements performed at the central angles listed in Table 5.1. Once again no re-normalization factor was used for the cross-sections.

5.1.5 The $^{12}C(^{18}O,^{18}F)^{12}B$ single charge exchange reaction

An example of excitation energy spectrum for the $^{12}C(^{18}O,^{18}F)^{12}B$ charge exchange reaction at 275 MeV, measured in the angular region $8° < \theta_{lab} < 10°$, is shown in Figure 5.11. Heavy-ion induced charge exchange reactions populating odd-odd nuclei both in the projectile and target side typically produce energy spectra characterized by high level density [42, 48], where the contribution of transitions to individual states is difficult to be extracted. In the present case, where the light ^{12}C target is used, the final level density is still manageable, allowing to recognize several isolated structures in the populated spectra.

Peaks in Figure 5.11 are described in terms of the states listed in Table 5.6. The achieved energy resolution was enough to isolate, in the first peak, contributions coming only from the ground-to-ground state transition opening to the possibility to study, without any ambiguity, the complete reaction mechanism feeding this state. Angular distributions were extracted in the region of bound and unbound states and are shown in Figures 5.18 and 5.19, respectively. The full angular range was covered by three independent measurements performed at the central angles listed in Table 5.1. Once again no re-normalization factor was used for the cross-sections.

Below the ^{12}B one-neutron emission threshold $S_n = 3.370$ MeV, three peaks are visible. The first one corresponds to the transition to the isolated 1^+ ground state of ^{18}F and ^{11}B. The second peak is due to the unresolved transitions to the ^{18}F 3^+ state at 0.937 MeV, 0^+ at 1.042 MeV and 5^+ at 1.121 MeV, and ^{12}B 2^+ state at 0.953 MeV.

Table 5.5: Excitation energies (E_x), total angular momentum and parity (J^π) of the populated states and transferred orbital angular momenta (L) in the ^{12}C(^{18}O,^{19}F)^{11}B one-proton removal at 275 MeV. Together with the cross-sections $\sigma_{theo.}$ integrated in the angular domain $[0°; 180°]$, quality factors QF are calculated using Equation 5.6 for each of the angular distributions shown in Figure 5.10. The labels in the first column correspond to those listed in the legend of Figure 5.9.

	E_x (MeV)		DWBA		CCBA		CRC	
	^{19}F (J^π)[110]	^{11}B (J^π)[125]	$\sigma_{theo.}$ (μb)	QF	$\sigma_{theo.}$ (μb)	QF	$\sigma_{theo.}$ (μb)	QF
peak1	0.000 ($1/2^+$)	0.000 ($3/2^-$)	900	0.75	653	0.80	621	0.75
	0.110 ($1/2^-$)	0.000 ($3/2^-$)	163		249		236	
	0.197 ($5/2^+$)	0.000 ($3/2^-$)	7193		7178		6749	
peak2	1.345 ($5/2^-$)	0.000 ($3/2^-$)	-	0.77	39	0.77	36	0.78
	1.458 ($3/2^-$)	0.000 ($3/2^-$)	1		36		33	
	1.554 ($3/2^+$)	0.000 ($3/2^-$)	1843		2734		2514	
peak3	0.000 ($1/2^+$)	2.124 ($1/2^-$)	80	0.56	111	0.82	102	0.83
	0.110 ($1/2^-$)	2.124 ($1/2^-$)	17		20		19	
	0.197 ($5/2^+$)	2.124 ($1/2^-$)	844		822		755	
	2.780 ($9/2^+$)	0.000 ($3/2^-$)	-		691		616	
peak4	0.000 ($1/2^+$)	4.445 ($5/2^-$)	-	0.33	27	0.60	24	0.55
	0.110 ($1/2^-$)	4.445 ($5/2^-$)	-		11		11	
	0.197 ($5/2^+$)	4.445 ($5/2^-$)	-		155		143	
	2.780 ($9/2^+$)	2.124 ($1/2^-$)	-		119		104	
	0.000 ($1/2^+$)	5.020 ($3/2^-$)	25		23		22	
	0.110 ($1/2^-$)	5.020 ($3/2^-$)	7		8		8	
	0.197 ($5/2^+$)	5.020 ($3/2^-$)	345		339		321	

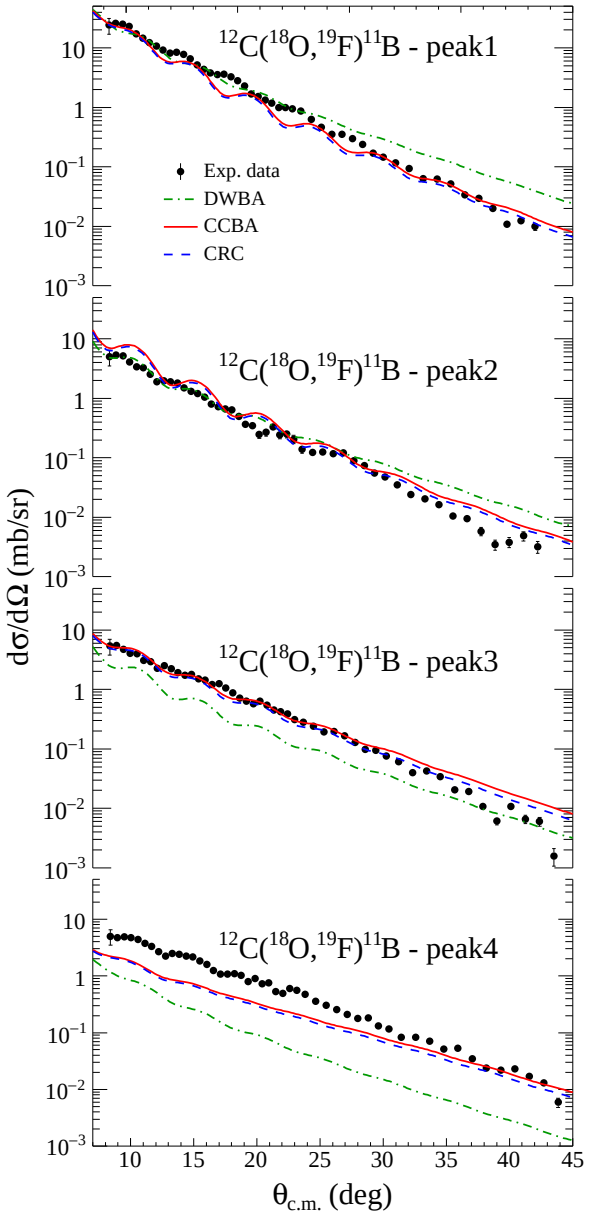

Figure 5.10: Experimental cross-section angular distribution of the ^{12}C(^{18}O,^{19}F)^{11}B one-proton removal at 275 MeV of incident energy associated with the four peaks indicated in Figure 5.9 and Table 5.5. Theoretical calculations of the one-proton removal nuclear reaction for the DWBA, CCBA and CRC approaches are shown with the green dot-dashed, continuous red and blue dashed line, respectively.

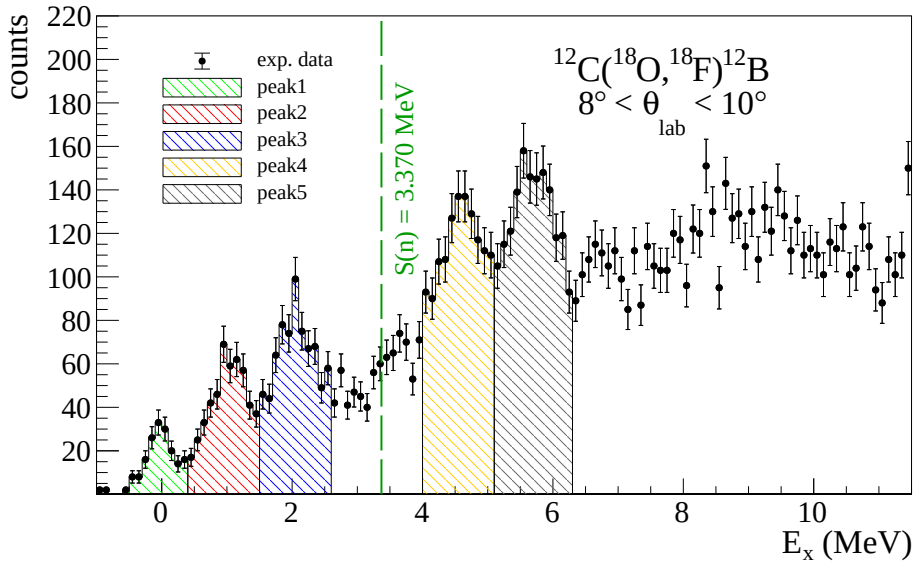

Figure 5.11: ^{12}C(^{18}O,^{18}F)^{12}Be single charge exchange energy spectrum at $8° < \theta_{lab} < 10°$. The hatched areas indicate the regions of interest for the study of the angular distributions as labelled in the legend.

In Ref. [42] it is found that among the ^{18}F states, the dominant one is the 3^+ states at 0.937 MeV. The third peak is mainly due to the double excitation of the ^{12}B (2^+) state at 0.953 MeV leaving the ^{18}F ejectile in its 3^+ state at 0.937 MeV. The transitions to the 2^- state at 1.674 MeV and 1^- at 2.621 MeV of ^{12}B lie in the same region, despite from the shape of the third peak their contribution is found to be small.

Above S_n, the 4^- resonance at 4.523 MeV of ^{12}B is strongly populated as already observed in other charge exchange studies [42, 126, 127]. Once again the transition to a ^{12}B state originates a second peak due to the ^{18}F ejectile excitations visible at ≈ 5.5 MeV.

For a detailed analysis of the measured single charge exchange cross-sections, both the one-step meson exchange and two-step nucleon exchange competitive mechanisms need to be evaluated and coherently added. The study of Nakayama et al. [128] on the ^{12}C(^{7}Li,^{7}Be)^{12}B underlined the relevance of the direct process at very forward angles and the important role of the nucleon exchange mechanisms at larger angles.

Table 5.6: Excitation energies (E_x), total angular momentum and parity (J^π) of the populated states in the ^{12}C(^{18}O,^{18}F)^{12}B single-charge exchange at 275 MeV. Labels in the first column correspond to those listed in the legend of Figure 5.11.

	^{18}F (from Ref. [110])		^{12}B (from Ref. [111])	
	E_x (MeV)	(J^π)	E_x (MeV)	(J^π)
1	0.000	1^+	0.000	1^+
2	0.000	1^+	0.953	2^+
	0.937	3^+	0.000	1^+
	1.042	0^+	0.000	1^+
3	0.000	1^+	1.674	2^-
	0.937	3^+	0.953	2^+
	1.042	0^+	0.953	2^+
4	0.000	1^+	4.37	2^-
	0.000	1^+	4.52	4^-
5	0.937	3^+	4.37	2^-
	0.937	3^+	4.52	4^-
	1.042	0^+	4.37	2^-
	1.042	0^+	4.52	4^-

5.2 Theoretical analysis

The experimental data described in the previous section are analysed in the multi-channel theoretical approach. In this way the information extracted from data analysis can be fully constrained without any need to adjust the relevant parameters from other experimental studies performed in different conditions, or by model calculations. This consistent approach, applied to a broader ensemble of reaction channels explored in the same experimental conditions, lead us to consistently describe them in a unique theoretical framework. The main goal of this work is to test the state-of-art nuclear structure and reaction theories in describing the SCE in a full comprehensive and holistic study of the complete dynamical process.

In addition to that, other specific goals can be achieved through the analysis of each reaction channels. For example, the study of the ^{12}C(^{18}O,^{18}O)^{12}C elastic and inelastic scattering was performed to access the initial state interaction (ISI) responsible for the distortion of the incoming waves. The role of the ISI is crucial to properly describe all the direct nuclear reaction channels. The ^{12}C(^{18}O,^{16}O)^{14}C two-neutron transfer reaction has been already analysed and the results, recently published in Ref. [52], have confirmed the observation of the giant pairing vibration (GPV). From the nuclear reaction side, such observation confirms how the pairing interaction survives after the nuclear reaction, despite the dominance of the mean-field transfer dynamics. From the nuclear structure side, the observation of the GPV shows in the particle-particle sector a behaviour symmetric to the particle-hole one, where Giant Resonances represent the dominant features of the nuclear excitations.

An important and debated aspect in the study of the SCE nuclear reactions is the competition between the direct process, proceeding via the deeply studied meson-exchange [6] and the sequential neutron-proton or proton-neutron transfer processes [129]. The three main paths involved in the SCE nuclear reaction analysis are shown in Figure 5.1. The ^{12}C(^{18}O,^{19}F)^{11}B one-proton knock-out and the ^{12}C(^{18}O,^{17}O)^{13}C one-neutron pick-up reaction channels were therefore analysed to constraint the single particle components of the many-body nuclear wave functions of the involved nuclei.

5.2.1 The initial state interaction

5.2.1.1 Choice of the optical potential

The main ingredient of the initial state interaction (ISI) is the optical potential (OP) $U(r)$ (see Section 2.1). The data analysis was performed using the São Paulo potential (SPP) [62] $\mathrm{V_{SPP}(r)}$ as the real and the imaginary parts of the OP:

$$U(r) = (N_R + iN_I)V_{SPP}(r) \tag{5.1}$$

where N_R and N_I are strength factors for the real and imaginary parts, respectively. The adopted values for N_R and N_I come from a wide application of the SPP to the description of experimental data [7, 46, 50, 84, 130–135]. Although the N_R value is always set to 1, N_I depends on the coupling scheme used in the reaction calculations. Indeed the imaginary part is introduced to effectively account for the absorption to reaction channels and inelastic states not considered in the coupling scheme. In OM, also known as one-channel approximation since the only included channel in the coupling scheme is the elastic one, N_I is typically set to 0.78. The same holds also for the DWBA framework while, if the couplings with the inelastic scattering populating the main low-lying collective states are explicitly taken into account, the N_I value is typically lowered to about 0.6 [136]. The latter configuration was used for all the CC, CCBA and CRC calculations presented in the following section.

The SPP $V_{SPP}(r)$ [62] comes from the double folding of a finite-range folding-type effective nucleon-nucleon interaction with the matter densities of the heavy nuclei involved in the collision. The nucleon-nucleon interaction is quite similar to the M3Y interaction of Refs. [137, 138] in the surface region and contains an additional local-equivalent term given by an energy dependent strength factor to account for the Pauli non locality effects. The double-folding is performed using two-parameter Fermi distributions for the matter density that is assumed to be spherical. The radius and diffuseness of the nuclei matter densities come from the systematic analysis of electron scattering data and Hartree-Fock-Bogoliubov calculations for a wide range of nuclei. Regarding the ^{18}O diffuseness, a value of 0.61 fm (larger than the average 0.56 fm one of the SPP systematic) was used. This choice is well established and account for the effect generated by the two paired valence neutrons bound to the ^{16}O core [42, 43, 51, 139–141].

5.2.1.2 Coupling to the inelastic scattering channels

The OM calculations for the ^{18}O + ^{12}C elastic scattering cross-section at 275 MeV incident energy were performed and are shown in Figure 5.3. The Fraunhofer diffraction pattern ($\eta = 1.9$) is clearly visible in both experimental and theoretical angular distributions and a good agreement is present for transferred momenta up to $q \approx 2$ fm^{-1}. The discrepancy observed at larger q suggests the need to explicitly include the couplings with the first low-lying inelastic transitions, as already observed in similar studies [42, 46, 48, 50, 51, 134]. This task is accomplished assuming a collective or a microscopic model with the proper coupling potentials.

In the adopted approach, the 2^+ and 3^- collective states of both projectile and target are introduced in the coupling scheme, as sketched in Figure 5.12, and treated in terms of quadrupole and octupole excitation of the deformed ^{18}O and ^{12}C nuclei. The coupling potentials are defined in terms of multipole decomposition [60] of the main optical potential. The Coulomb $V_C(r,\lambda)$ and nuclear $V_N(r,\lambda)$ coupling potentials for the λ-component were introduced as follows:

$$V_C(r,\lambda) = M(E\lambda)e^2\frac{\sqrt{4\pi}}{2\lambda+1}r^{-\lambda-1} \tag{5.2a}$$

$$V_N(r,\lambda) = -\frac{\delta_\lambda}{\sqrt{4\pi}}\frac{dU(r)}{dr} \tag{5.2b}$$

The Coulomb component of the deformed potential depends on the parameter $M(E\lambda)$, related to the reduced transition probability $B(E\lambda;\ J \to J')$ for the electric operator Eλ acting between the states J and J', through the relation

$$M(E\lambda) = \pm\sqrt{(2J+1)B(E\lambda; J \to J')} \tag{5.3}$$

The sign is that of the intrinsic quadrupole moment (Q_0), according to ref. [142]. The nuclear component, defined by Eq. 5.2b, is a complex deformed potential depending on the δ_λ deformation length parameter. It is defined as follows:

$$\delta_\lambda = \beta_\lambda R_V = \frac{4\pi}{3Ze}\frac{M(E\lambda)}{R_V^{\lambda-1}} \tag{5.4}$$

where the $B(E\lambda; J \to J')$ and the average radius of the potential R_V are involved. The same definitions for the Coulomb and nuclear deformations were recently applied in [42, 44, 46, 51, 53]. All the adopted values for the mentioned ingredients are listed in

Table 5.7: Average radius R_V of the SPP, reduced transition probability $B(E\lambda; J \rightarrow J')$, reduced matrix element $M(E\lambda)$ and deformation length δ_λ adopted for $\lambda = 2$, 3 for the ^{18}O and ^{12}C nuclei of the entrance partition.

	R_V (fm)	$B(E2; 0^+ \rightarrow 2^+)$ (e^2b^2)	$M(E2)$ (e fm^2)	δ_2 (fm)	$B(E3; 0^+ \rightarrow 3^-)$ (e^2b^3)	$M(E3)$ (e fm^3)	δ_3 (fm)
^{18}O	3.13	0.0043†	+6.56	+1.10	0.000147§	+12.12	+0.65
^{12}C		0.00397†	-6.30	-1.41	0.000257‡	-16.03	-1.14

†from Ref. [143]
§from Ref. [144]
‡from Ref. [113]

Table 5.7. The DWBA and CC calculations were performed for the low-lying inelastic transitions adopting the coupling scheme shown in Figure 5.12. The comparison between experimental data and theoretical calculations is shown in Figure 5.4. The transitions included in the DWBA approach correspond to the green arrows in Figure 5.12. The transition to the $^{18}O(2_1^+) + {}^{12}C(2_1^+)$ states is not allowed due to the lack of higher order terms in DWBA. Such effects, included in the CC approach (orange arrows in Figure 5.12) are responsible for the changes in the slopes observed comparing the DWBA and CC results shown in Figure 5.4. A good description of the experimental data is reached using the CC approach. This is true also for the elastic scattering case (Figure 5.3) in which the CC calculations reproduce very well both the oscillating pattern and the absolute value of the experimental cross-section angular distribution.

5.2.2 Single particle properties of nuclear wave functions

The study of single nucleon transfer processes is a powerful tool to study the single particle properties of nuclear. The main ingredients necessary to perform one-nucleon transfer calculations are the ISI, the final state interaction (FSI), the radial single-particle wave functions and spectroscopic amplitudes. The ISI discussed and defined in the previous section, from the analysis of the elastic and inelastic scattering experimental data, was used. The single-particle wave functions, for the nuclei involved in the one-nucleon transfer reactions, were calculated using the approach already applied in a long series of previous works [8, 43, 44, 53, 114, 130–133, 135, 159]. The transferred particle was considered bound to the core by means of a Woods-Saxon central potential. For

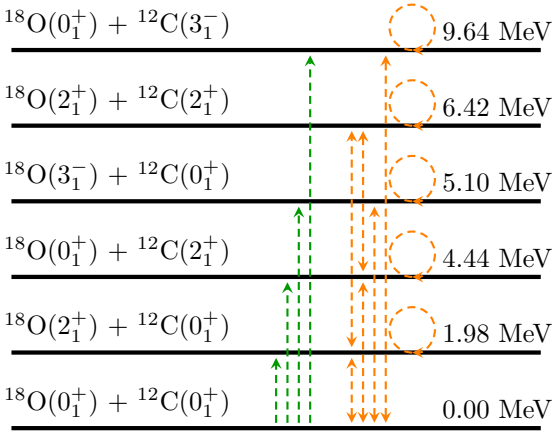

Figure 5.12: Coupling scheme for the ^{18}O + ^{12}C elastic and inelastic scattering. Couplings considered in the DWBA and CC calculations are indicated by the dotted green and orange arrows, respectively. Values on the right are the corresponding excitation energies (in MeV).

the ^{17}O + n and ^{18}O + p cases the adopted reduced radii and diffuseness are 1.26 fm and 0.7 fm, respectively. For the ^{12}C + n and ^{11}B + p the adopted values are 1.25 fm and 0.65 fm, respectively. The depth of the central potential was adjusted to reproduce the separation energy of the transferred particle.

5.2.2.1 Shell-model spectroscopic amplitudes

The reaction calculations are connected to the structure of the involved nuclear states by the corresponding single particle spectroscopic amplitudes. These were computed within a large-scale shell-model formalism implemented in the KSHELL code [145]. The p-sd-mod interaction [146] was used for both the projectile-like (^{18}O, ^{17}O, ^{19}F) and the target-like (^{12}C, ^{13}C, ^{11}B) nuclei. It is a modified version of the PSDWBT interaction [147] involving the full p-sd valence subspace for protons and neutrons, assuming ^{4}He as a closed core and $1p_{\frac{3}{2}}$, $1p_{\frac{1}{2}}$, $1d_{\frac{5}{2}}$, $2s_{\frac{1}{2}}$ and $1d_{\frac{3}{2}}$ valence orbits. In Table B.1 the comparison between the theoretical and experimental excitation energies of the low-lying states for all the involved nuclei is presented. One can see a reasonably good agreement for all the states. In the initial partition the 0^+, 2^+ and 3^- states of both ^{18}O and ^{12}C nuclei were considered. The spectroscopic amplitudes related to the $\langle {}^{18}O|{}^{17}O\rangle$ and $\langle {}^{12}C|{}^{13}C\rangle$ overlaps for the one-neutron transfer case are listed in Tables B.3 and B.2 of Appendix B, respectively. The spectroscopic amplitudes related to the $\langle {}^{18}O|{}^{19}F\rangle$ and $\langle {}^{12}C|{}^{11}B\rangle$ overlaps for the one-proton transfer case are listed in Tables B.5 and B.4

of Appendix B, respectively.

5.2.2.2 The final state interactions

The FSIs, for each of the one nucleon transfer reaction channels, were introduced using again the SPP for the real and imaginary parts of the OPs. The radii and diffusenesses of the matter densities nuclei were taken from the SPP systematic [62]. Regarding the normalization factors, they were set as previously discussed: $N_I = 0.78$ for DWBA calculations and $N_I = 0.6$ for CCBA ones, in which the couplings to the inelastic states also in the final partition were explicitly taken into account. The introduction of such couplings, including the reorientation terms, requires the use of the reduced matrix elements $M(E\lambda)$ and δ_λ. The $M(E\lambda)$ values were extracted from the same shell-model calculations for the $\lambda = 2$ multipole and the δ_2 values were calculated according to Eq. 5.4. The obtained values are listed in Table 5.8 together with the other relevant parameters. The $B(E2; J \rightarrow J')$ values, extracted from shell-model derived $M(E2)$, were compared to the experimental ones, for the transitions in which they are available in literature. A good agreement is which confirms the reliability of our shell-model calculations.

Table 5.8: Reduced matrix element $M(E2)$ and deformation length δ_2 for selected transitions in the final partitions.

	Transition $J^\pi \longleftrightarrow J'^\pi$	Initial state (MeV)	Final state (MeV)	$M(E2)$ (e fm^2)	δ_2 (fm)
^{19}F	$\frac{1}{2}^+ \longleftrightarrow \frac{5}{2}^+$	0.000	0.197	11.24	1.69
	$\frac{1}{2}^+ \longleftrightarrow \frac{3}{2}^+$	0.000	1.554	-9.01	-1.35
	$\frac{5}{2}^+ \longleftrightarrow \frac{5}{2}^+$	0.197	0.197	-12.90	-1.94
	$\frac{5}{2}^+ \longleftrightarrow \frac{3}{2}^+$	0.197	1.554	6.73	1.01
	$\frac{5}{2}^+ \longleftrightarrow \frac{9}{2}^+$	0.197	2.780	15.52	2.33
	$\frac{3}{2}^+ \longleftrightarrow \frac{3}{2}^+$	1.554	1.554	-9.35	-1.40
	$\frac{9}{2}^+ \longleftrightarrow \frac{9}{2}^+$	2.780	2.780	-16.71	-2.51
	$\frac{1}{2}^- \longleftrightarrow \frac{5}{2}^-$	0.110	1.345	-18.90	-2.84
	$\frac{1}{2}^- \longleftrightarrow \frac{3}{2}^-$	0.110	1.458	-16.19	-2.43
	$\frac{5}{2}^- \longleftrightarrow \frac{3}{2}^-$	1.345	1.458	-9.73	-1.46
	$\frac{5}{2}^- \longleftrightarrow \frac{5}{2}^-$	1.345	1.345	-19.16	-2.88
	$\frac{3}{2}^- \longleftrightarrow \frac{3}{2}^-$	1.458	1.458	-15.31	-2.30
^{17}O	$\frac{5}{2}^+ \longleftrightarrow \frac{5}{2}^+$	0.000	0.000	-4.20	-0.71
	$\frac{5}{2}^+ \longleftrightarrow \frac{1}{2}^+$	0.000	0.871	3.56	0.60
^{11}B	$\frac{3}{2}^- \longleftrightarrow \frac{3}{2}^-$	0.000	0.000	5.93	1.60
	$\frac{3}{2}^- \longleftrightarrow \frac{1}{2}^-$	0.000	2.124	3.55	0.96
	$\frac{3}{2}^- \longleftrightarrow \frac{5}{2}^-$	0.000	4.444	8.30	2.24
	$\frac{3}{2}^- \longleftrightarrow \frac{3}{2}^-$	0.000	5.020	-2.37	-0.64
	$\frac{1}{2}^- \longleftrightarrow \frac{5}{2}^-$	2.124	4.444	-5.69	-1.54
	$\frac{1}{2}^- \longleftrightarrow \frac{3}{2}^-$	2.124	5.020	-5.51	-1.49
	$\frac{5}{2}^- \longleftrightarrow \frac{3}{2}^-$	4.444	5.020	5.43	1.47
	$\frac{5}{2}^- \longleftrightarrow \frac{5}{2}^-$	4.444	4.444	0.41	0.11
	$\frac{3}{2}^- \longleftrightarrow \frac{3}{2}^-$	5.020	5.020	-6.19	-1.67

Table 5.8: continued on the next page.

Table 5.8: continued from the previous page.

	Transition $J^\pi \longleftrightarrow J'^\pi$	Initial state (MeV)	Final state (MeV)	$M(E2)$ (e fm^2)	δ_2 (fm)
	$\frac{1}{2}^- \longleftrightarrow \frac{3}{2}^-$	0.000	3.684	5.33	1.21
	$\frac{1}{2}^- \longleftrightarrow \frac{5}{2}^-$	0.000	7.547	6.34	1.44
	$\frac{3}{2}^- \longleftrightarrow \frac{5}{2}^-$	3.684	7.547	-4.13	-0.94
	$\frac{3}{2}^- \longleftrightarrow \frac{3}{2}^-$	3.684	3.684	6.07	1.38
	$\frac{5}{2}^- \longleftrightarrow \frac{5}{2}^-$	7.547	7.547	8.28	1.88
	$\frac{1}{2}^+ \longleftrightarrow \frac{5}{2}^+$	3.089	3.854	4.34	0.98
	$\frac{1}{2}^+ \longleftrightarrow \frac{5}{2}^+$	3.089	6.864	-6.15	-1.39
	$\frac{1}{2}^+ \longleftrightarrow \frac{3}{2}^+$	3.089	7.686	0.91	0.21
^{13}C	$\frac{5}{2}^+ \longleftrightarrow \frac{5}{2}^+$	3.854	3.854	-6.80	-1.54
	$\frac{5}{2}^+ \longleftrightarrow \frac{5}{2}^+$	3.854	6.864	-5.47	-1.24
	$\frac{5}{2}^+ \longleftrightarrow \frac{7}{2}^+$	3.854	7.492	-9.27	-2.10
	$\frac{5}{2}^+ \longleftrightarrow \frac{3}{2}^+$	3.854	7.686	4.35	0.99
	$\frac{5}{2}^+ \longleftrightarrow \frac{5}{2}^+$	6.864	6.864	5.77	1.31
	$\frac{5}{2}^+ \longleftrightarrow \frac{7}{2}^+$	6.864	7.492	-6.63	-1.50
	$\frac{5}{2}^+ \longleftrightarrow \frac{3}{2}^+$	6.864	7.686	-2.98	-0.67
	$\frac{7}{2}^+ \longleftrightarrow \frac{7}{2}^+$	7.492	7.492	-3.39	-0.77
	$\frac{7}{2}^+ \longleftrightarrow \frac{3}{2}^+$	7.492	7.686	1.88	0.43
	$\frac{3}{2}^+ \longleftrightarrow \frac{3}{2}^+$	7.686	7.686	-4.79	-1.09

5.2.2.3 Reaction calculations

All the mentioned ingredients were introduced in a exact finite range, prior, full complex remnant calculation including elastic and inelastic scattering, one-neutron and one-proton transfer and both paths of the sequential single charge exchange reaction (described in the next paragraphs) in which all the cross-sections are simultaneously calculated. The one-nucleon transfer calculations, here described, are the first step for the complete description of the two-step sequential single-charge exchange of the next

section.

The role of couplings with inelastic states in both the initial and final partitions and with the reaction channels were tested comparing the DWBA, CCBA and CRC approaches. The adopted coupling schemes are sketched in Figure 5.13.

In the DWBA calculations only the transitions from the ground state of the initial nuclei are taken into account (green arrows in Figure 5.13) using one-way couplings, i.e. the couplings among different partitions is considered to the first order. The CCBA calculations also include the initial and final state inelastic couplings (orange arrows in Figure 5.13) and thus allow also the transitions from these states of the initial nuclei (blue arrows in Figure 5.13) in a one-way coupling. When the CRC calculations are performed, two-way couplings are introduced, which corresponds to take into account couplings among different partitions to infinite order. The CRC coupling schemes are the same as the CCBA ones shown in Figure 5.13. The resulting theoretical calculations are compared with the experimental angular distributions in Figures 5.6 and 5.10. The integrated theoretical cross-sections are listed in Tables 5.3 and 5.5.

5.2.2.4 Discussion

In general, the theoretical calculations well describe the one-nucleon transfer experimental data (see Figures 5.6 and 5.10). In the one-neutron transfer case, the description is good even in DWBA approach, showing that the role of couplings is not important and the analysed final states are dominated by single-particle configurations. Instead, in the one-proton transfer case, the introduction of the couplings is necessary to describe both the slope and the absolute cross-section. Also, exploratory CCBA calculations in which the couplings were introduced only in the initial partition improved the agreement with respect to the DWBA ones, but were not enough to satisfactory reproduce the data. Thus, in the final CCBA calculations the couplings were introduced in both partitions. The further step to consider couplings among different partitions to infinite order (CRC) did not change the obtained results in both one-neutron and one-proton transfer cases.

To evaluate in a quantitative manner the agreement of the obtained theoretical results with the experimental data, the following quality factor ($qf(\theta_i)$) was analysed:

$$qf(\theta_i) = \frac{1}{1 + \left| \ln \frac{theo(\theta_i)}{exp(\theta_i)} \right|} \tag{5.5}$$

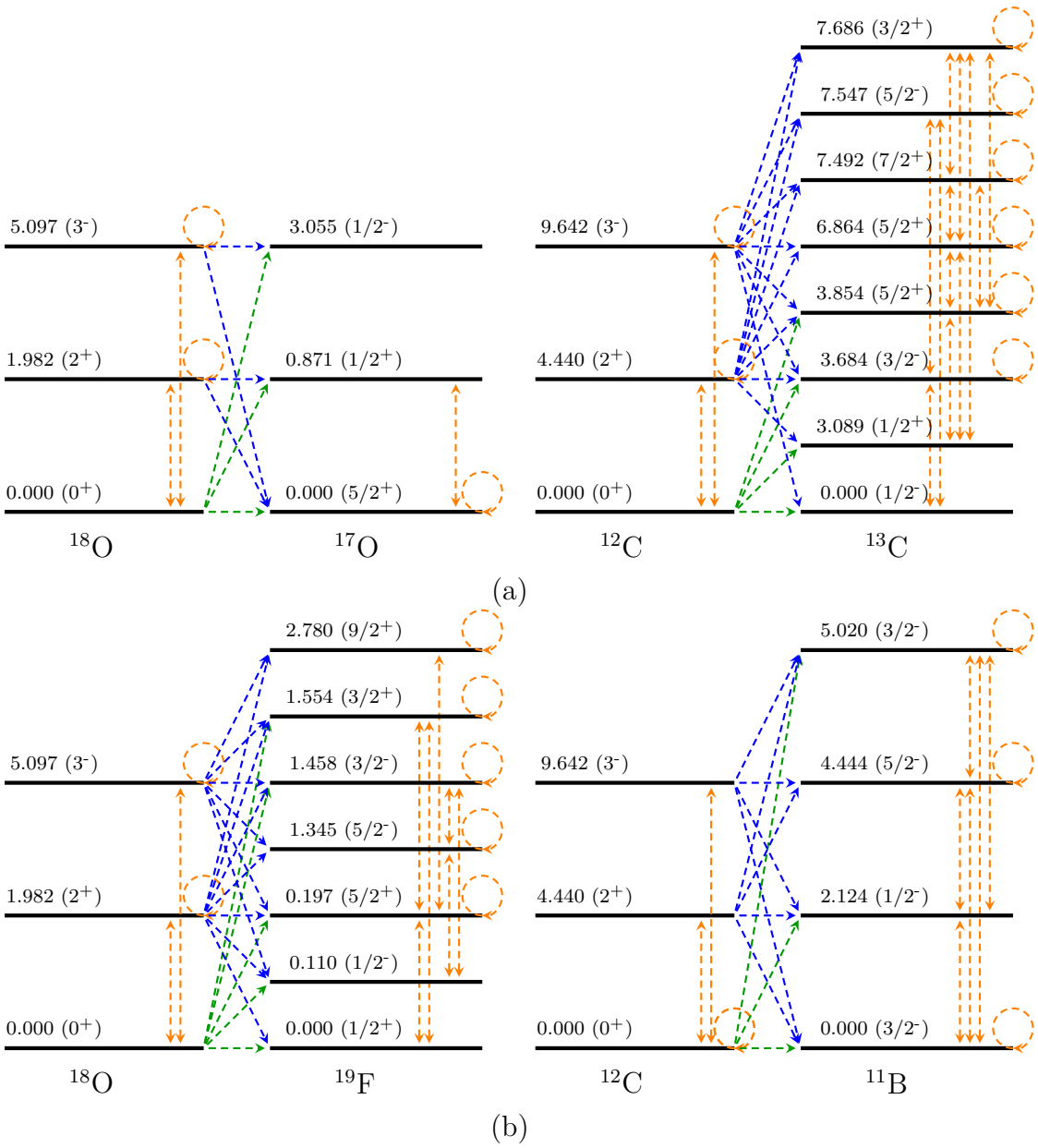

Figure 5.13: Coupling schemes for the performed one-nucleon transfer calculations. Coupling schemes adopted for the one-neutron addition and one-proton removal nuclear reactions are shown in (a) and (b), respectively. Couplings considered in the DWBA, CCBA and CRC calculations are indicated by the dotted green, blue and orange arrows (see text for more information). Excitation energies (in MeV) and J^{π} of each of the involved states are also indicated.

where *exp* and *theo* are the measured and calculated values of the cross-sections for the specific transition at the θ_i scattering angle, respectively. The $qf(\theta_i)$ values range between 0 and 1 corresponding to the worst and best agreement between the calculations and the experimental data, respectively. $qf(\theta_i)$ quantity was calculated for each i point of the experimental angular distributions in comparison to the respective values of each theoretical calculation (DWBA, CCBA and CRC). The quality factors QF were calculated for each analysed angular distribution as an arithmetic average of the N_{points} measurements at different angles:

$$QF = \frac{\sum_i qf(\theta_i)}{N_{points}} \tag{5.6}$$

The obtained results are listed in Tables 5.2, 5.3 and 5.5. The reliability of the defined QF is evident, for example, looking at the results of Table 5.2, in which for the elastic transition we see a clear improvement in the QF value passing from DWBA to CCBA and CRC approaches that reflects what we see in Figure 5.3. Instead, in the case of the inelastic transition to the 4.44 MeV state of ^{12}C the best QF value is obtained in DWBA, since the oscillating pattern of the angular distribution is better described within this approach for this specific transition (see Figure 5.4). Then, to evaluate the global quality of the different approaches, a unique QF was extracted for each analysed reaction channel through an average of the values reported in Tables 5.2, 5.3 and 5.5 and the results are shown in Figure 5.14. In the same figure also a QF value that corresponds to the whole data analysis is reported (total) extracted as an average of the other three. The obtained values highlighted that a significant overall improvement is achieved passing from the DWBA to the CCBA approach, while there is not a significant step forward introducing the computationally challenging CRC one. This confirms that the inclusion of the couplings with the inelastic states in both the initial and final partitions are important in the comprehensive analysis of the ^{18}O + ^{12}C reactions.

5.2.3 Two-step sequential single charge exchange

We want to focus now on the two-step reaction mechanism consisting on a multi-nucleon transfer process ending up in the single charge exchange exit partition, the same also reached in the direct spin-isospin excitation described in the next section. In this process the two nucleons are transferred one-by-one and without any correlation among them, passing through an intermediate partition. Two routes are possible. The first route

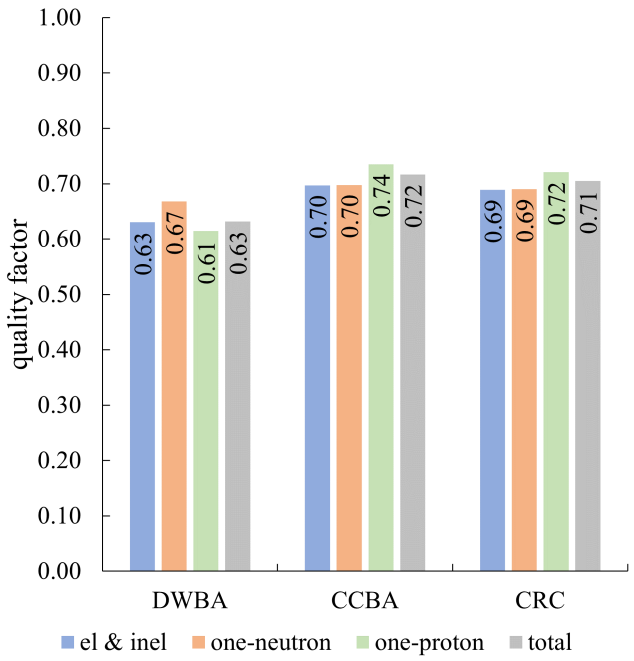

Figure 5.14: Average quality factors extracted according to Eq. 5.6 in the experimentally explored angular range for the three analysed channels (elastic/inelastic, one-neutron transfer and one-proton transfer) and for the three theoretical approaches (DWBA, CCBA and CRC) together with the total value (see text).

consists of a one-neutron addition followed by a one-proton removal in the target. We will refer to it as np-sce path where the involved intermediate partition is the ^{17}O+^{13}C system. The second route, the pn-sce path, consists of a one-proton removal followed by the one-neutron addition reaction. In this case the intermediate partition is the ^{19}F+^{11}B system.

Isospin symmetry would force the two paths to give exactly the same contribution to the complete process if all the bound and continuum states of the intermediate partition would be explicitly included. Indeed, since for both paths the initial and final states are the same, the reaction amplitude could not depend on the basis of intermediate states chosen to perform the expansion, provided that the basis is complete. In such case, one can assume the completeness of the intermediate basis of nuclear states, in order to add them all, get a unity, thus realizing the closure approximation. This approach was not used in the present analysis. A finite model space was defined for the intermediate partitions, basing that choice on the study of the first-step transfer analysis described in the previous paragraphs.

5.2.3.1 Coupling schemes

The spectroscopic amplitudes were extracted within the same large-scale shell-model calculation performed for the first one-nucleon transfer step as previously described. The overlaps between intermediate and final partition states were constructed using the same wave functions of the intermediate partition guaranteeing the coherence of structure calculations in the two steps.

The p-sd-mod interaction was used for both projectile and target nuclei. The spectroscopic amplitudes for the first step one-nucleon transfer calculations have been already introduced. The SA related to the $\langle ^{17}O|^{18}F\rangle$ and $\langle ^{13}C|^{12}B\rangle$ second-step overlaps, for np-sce path, are listed in Tables B.9 and B.8, respectively. Those related to the second step $\langle ^{19}F|^{18}F\rangle$ and $\langle ^{11}B|^{12}B\rangle$ overlaps, for the pn-sce path, are listed in Tables B.7 and B.6, respectively. In order to achieve a compromise between an acceptable computing time and reliability of the calculation, not all of the listed spectroscopic amplitudes were included in the reaction calculations. Only the intermediate states characterized by the larger cross section in the first step and the larger spectroscopic amplitude (SA > 0.5) to the final states were included in the calculation.

The coupling schemes for the pn-sce and np-sce paths are shown in Figures 5.15 and 5.16, respectively. In the 2-step DWBA calculations only the transitions from the

ground state of the initial partition are taken into account (green arrows) for the first step and the blue ones for the second step, using in both cases the one-way couplings. The CCBA calculations also include the inelastic couplings among the initial and intermediate partitions (orange arrows) thus allowing to also treat the transitions from these states of the initial partition (blue arrows), but again in one-way coupling mode. When the CRC calculations are performed, two-way couplings are introduced, which corresponds to take into account couplings among different partitions to infinite order. Provided that the two-way couplings are introduced up to a very high order, the CRC coupling schemes are the same as the CCBA ones. The grey arrows connecting the intermediate to the final partitions correspond to the spectroscopic amplitudes smaller than 0.5 listed in Tables B.9 B.7 B.6 B.8 neglected in the present calculations.

5.2.3.2 Reaction calculations

The FSI for the ^{18}F + ^{12}B partition uses again the SPP for the real and imaginary parts of the OPs. The radii and diffusenesses of the matter densities nuclei were taken from the SPP systematic [62] while the normalization factors were set as $N_I = 0.78$, since no inelastic coupling was defined.

In analogy with the one-nucleon transfer case, the mentioned ingredients were introduced in a unique exact finite range, prior-post, full complex remnant calculation including elastic and inelastic scattering, one-neutron and one-proton transfer as initial and intermediate partitions, respectively.

The prior-post representation was used since, as evidenced in Ref. [148], the non-orthogonality terms disappear in second-order DWBA if the first and second steps use the prior and post representations, respectively. In a recent paper (see Ref. [48]) the comparison between the prior-post, prior-prior and post-post approaches was performed for the ^{116}Cd(^{20}Ne,^{20}F$^{2+}_{gs}$)^{116}In$^{4+}_{0.223}$ charge exchange reaction at 15.3 AMeV incident energy. This comparison is reported in Figure 5.17, where the angular distribution of R is shown. R is defined as the ratio between differential cross-sections obtained under the prior-prior or the post-post approaches with respect to the prior-post one.

The agreement among the three curves proves the good numerical convergence while the discrepancies beyond 15° confirm the relevance of a proper treatment of the non-orthogonality terms. The resulting theoretical calculations are compared with the experimental angular distributions in Figures 5.18 and 5.19 for the structures competing to the bound and unbound states regions, respectively.

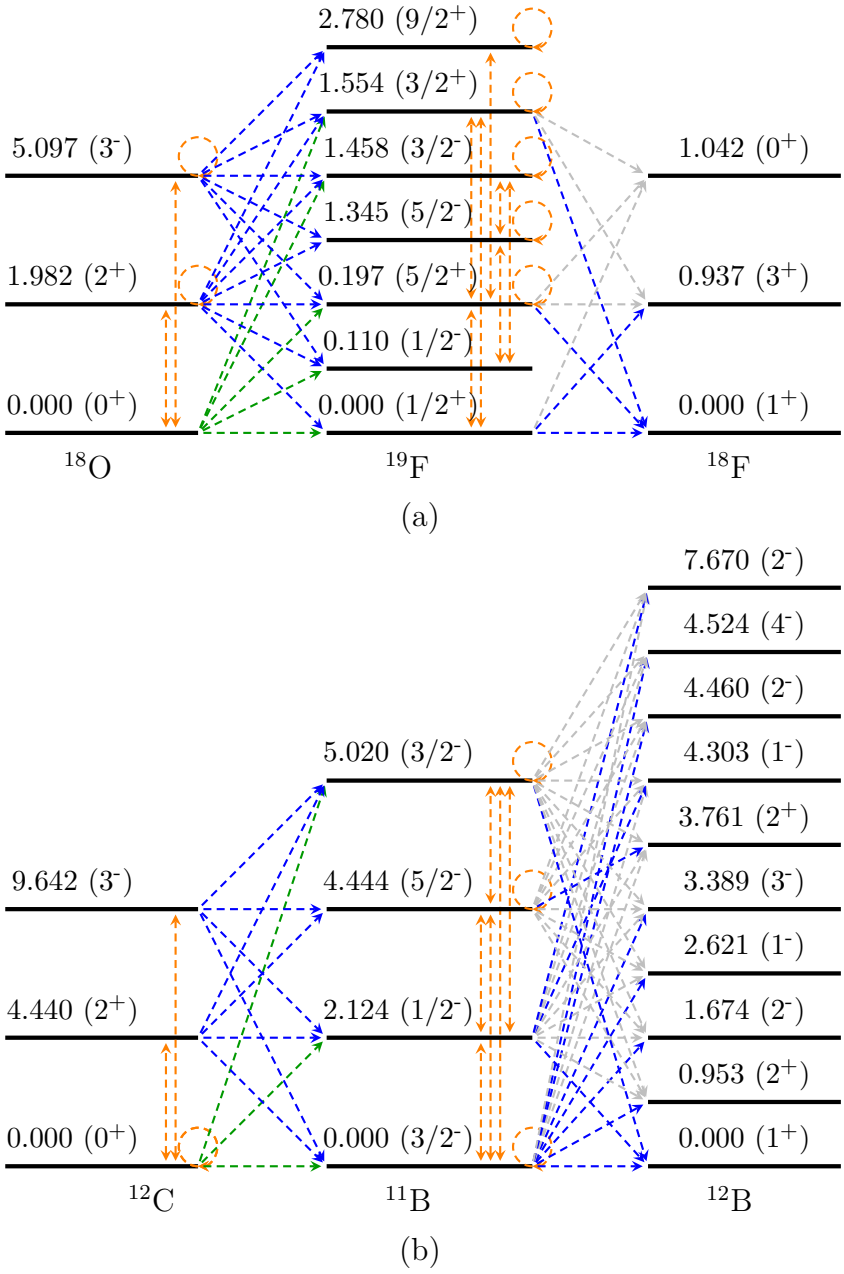

Figure 5.15: Coupling scheme adopted for the proton-neutron sequential transfer path in the ^{12}C(^{18}O,^{18}F)^{12}B SCE reaction calculation for the projectile- and target-like nuclei in (a) and (b), respectively. Couplings considered in the DWBA, CCBA and CRC calculations are indicated by the dotted green, blue and orange arrows (see text for more information). Excitation energies (in MeV) and J^{π} of each of the involved states are indicated.

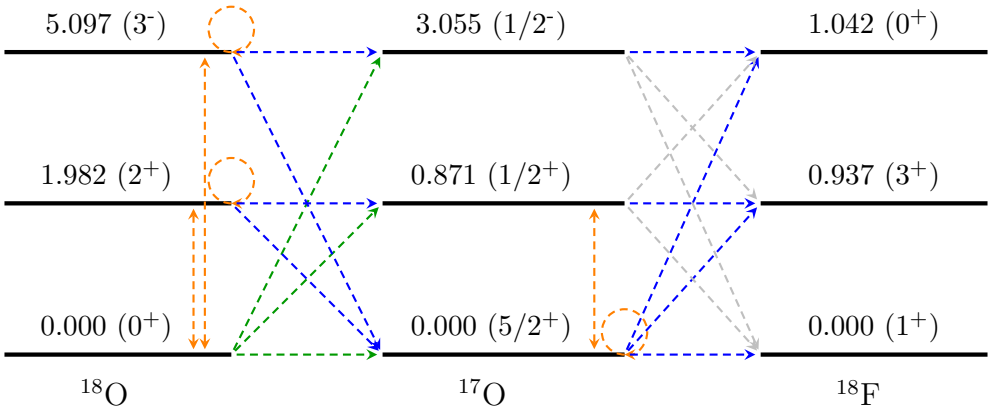

(a)

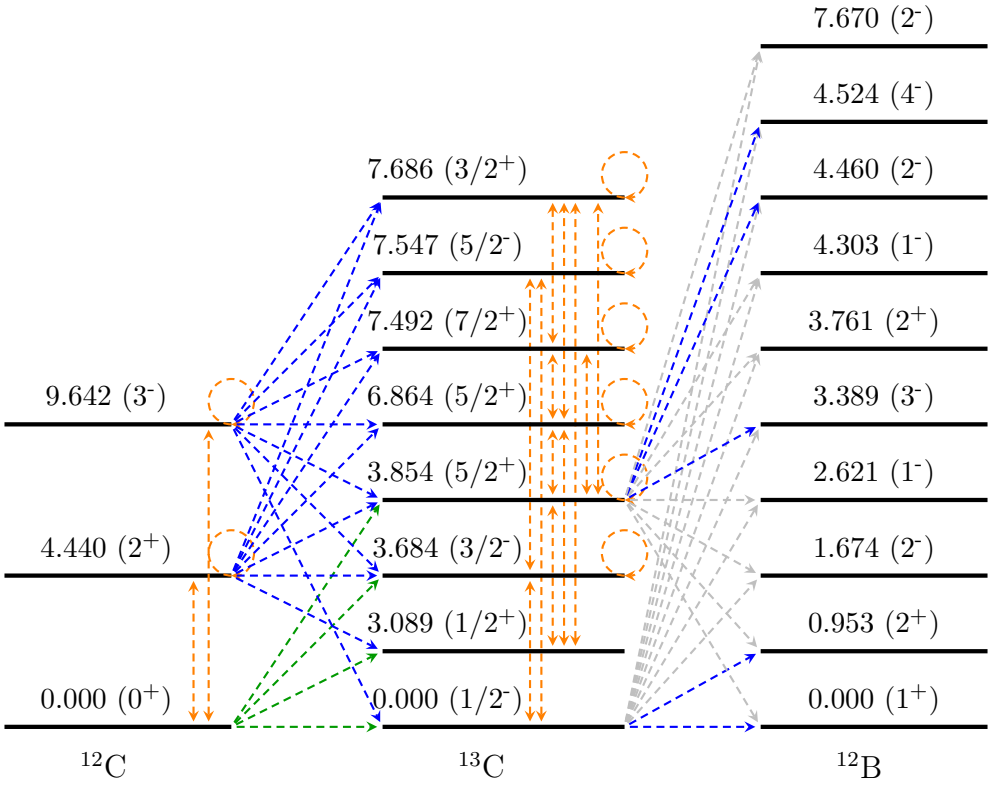

(b)

Figure 5.16: Same as Figure 5.15 but for the neutron-proton sequential transfer path in the ^{12}C(^{18}O,^{18}F)^{12}B SCE reaction.

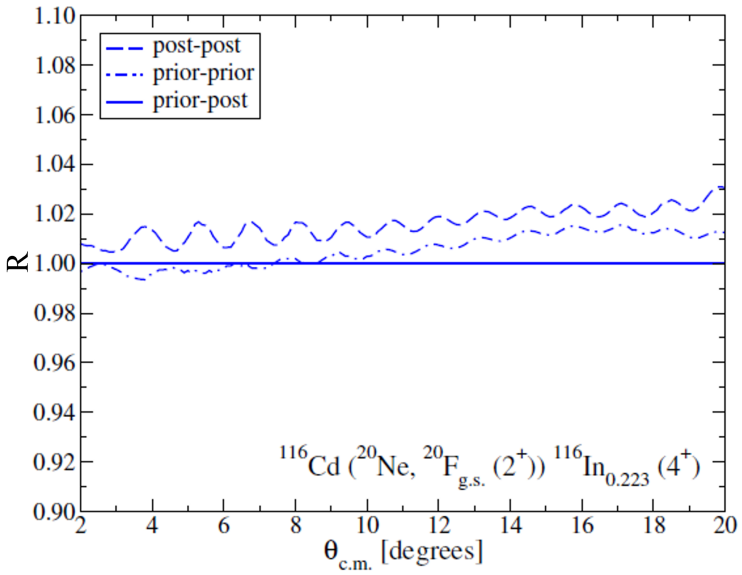

Figure 5.17: Ratio R (see text) for the SCE reaction ^{116}Cd(^{20}Ne,^{20}F$^{2+}_{gs}$)^{116}In$^{4+}_{0.223}$ differential cross-section obtained through different prior/post combinations even including, whenever non-vanishing, the corresponding non-orthogonality terms. The SCE reaction is described in terms of a two-step transfer mechanism, by assuming the DWBA approximation.

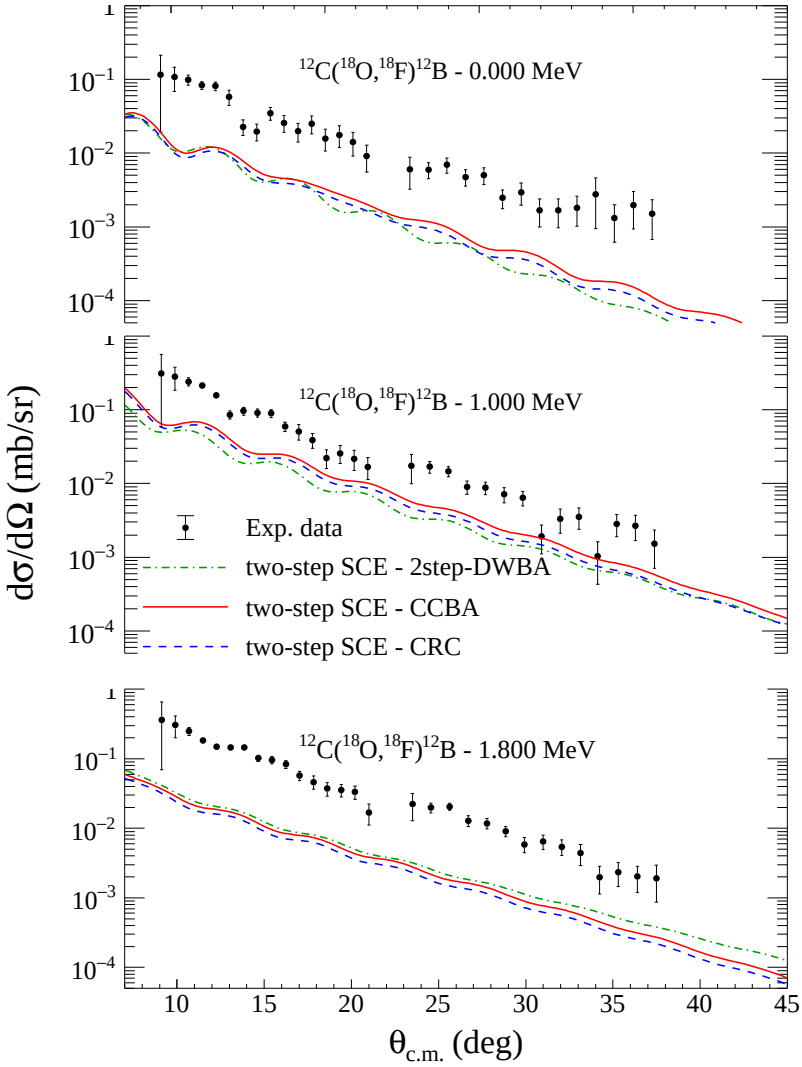

Figure 5.18: Experimental cross-section angular distribution of the ^{12}C(^{18}O,^{18}F)^{12}B single-charge exchange at 275 MeV of incident energy associated with the three peaks in the bound state region indicated in Figure 5.11 and Table 5.6. Theoretical calculations of the sequential single-charge exchange nuclear reaction for the DWBA, CCBA and CRC approaches are shown with the green dot-dashed, continuous red and blue dashed line, respectively.

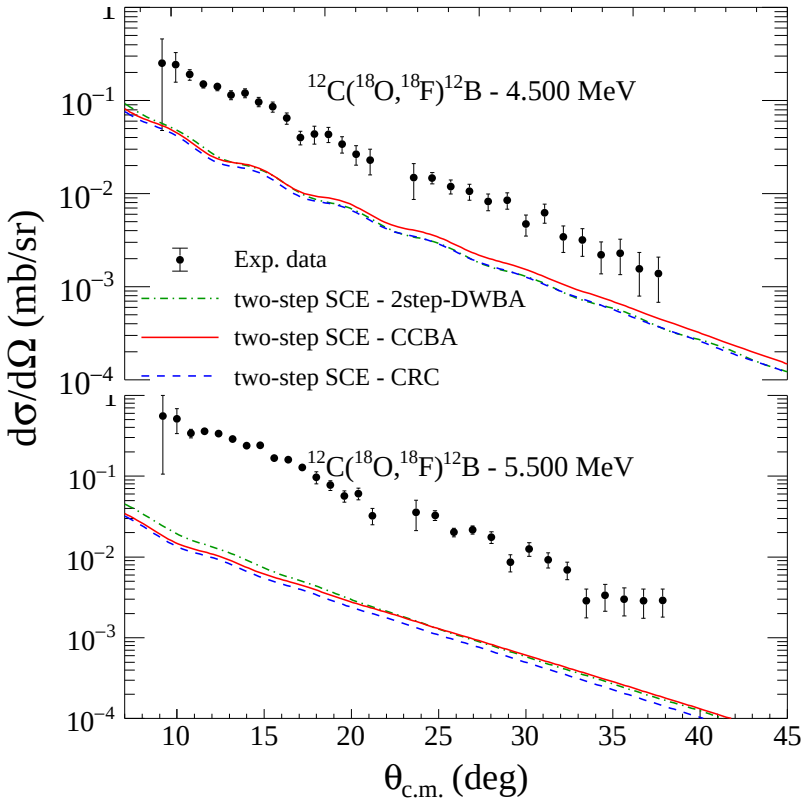

Figure 5.19: Experimental cross-section angular distribution of the ^{12}C(^{18}O,^{18}F)^{12}B single-charge exchange at 275 MeV of incident energy associated with the two peaks in the unbound states region indicated in Figure 5.11 and Table 5.6. Theoretical calculations of the sequential single-charge exchange nuclear reaction for the DWBA, CCBA and CRC approaches are shown with the green dot-dashed, continuous red and blue dashed line, respectively.

5.2.4 One-step single charge exchange: numerical calculations

The one-step reaction mechanism for the ^{12}C(^{18}O,^{18}F)^{12}B single charge exchange nuclear reaction at 275 MeV bombarding energy was analysed within the microscopic one-step direct-charge exchange theoretical formalism described in Sec. 2.2. The code `fofa` [149], developed by H. Lenske, was used to calculate the radial form factors defined in Eq. 2.22, using the microscopic QRPA response functions. Details of the nuclear structure and reaction calculations for the g.s. to g.s transition will be shown in the following.

5.2.4.1 QRPA response functions

The description of direct (meson exchange) charge exchange nuclear excitations is based on HFB calculations for nuclear ground states of the initial partition nuclei and QRPA calculation for response functions and transition densities. The shell-model approach, although being a powerful tool for high precision studies of low-energy spectra, is not the best candidate to describe collective effects over large ranges of excitation energies and for those purposes, HFB and QRPA theories are better suited. In combination, HFB and QRPA theories provide a versatile toolbox with appropriate instruments for the proper description of nuclear ground states and nuclear spectroscopy over most of the nuclear mass table, except for the lightest nuclei[6].

Single proton and neutron orbitals of ^{12}C and ^{18}O nuclei enter into the QRPA calculations and they were calculated up to 100 MeV excitation energy and L= 6 taking the nuclear systems inside a box with a radius of 60 fm. They are obtained by using the self-consistent HFB mean-field potentials, thus avoiding artificial, non-physical non-orthogonality effects [6]. The single particle continua are described by a dense spectrum of discrete states.

According to the formalism described in Sec. 2.2, the nuclear response functions to the charge-exchange operator were calculated for ^{18}O $\rightarrow$ ^{18}F and ^{12}C $\rightarrow$ ^{12}B. The results are shown in Figures 5.20 and 5.21. The curves represent different charge-exchange transitions characterized by the total angular momentum J and parity π. Such transitions can be natural ($\pi = (-1)^J$) or unnatural ($\pi = (-1)^{J+1}$). For both processes the condition $\pi = (-1)^L$ must be satisfied and, for that reason, the natural parity transitions are characterized by $J = L$ and can be both for spin-flip ($S = 1$) and non-spin-flip ($S = 0$) while the unnatural parity transitions are characterized by two different values of the transferred total angular momentum L. For unnatural parities L=

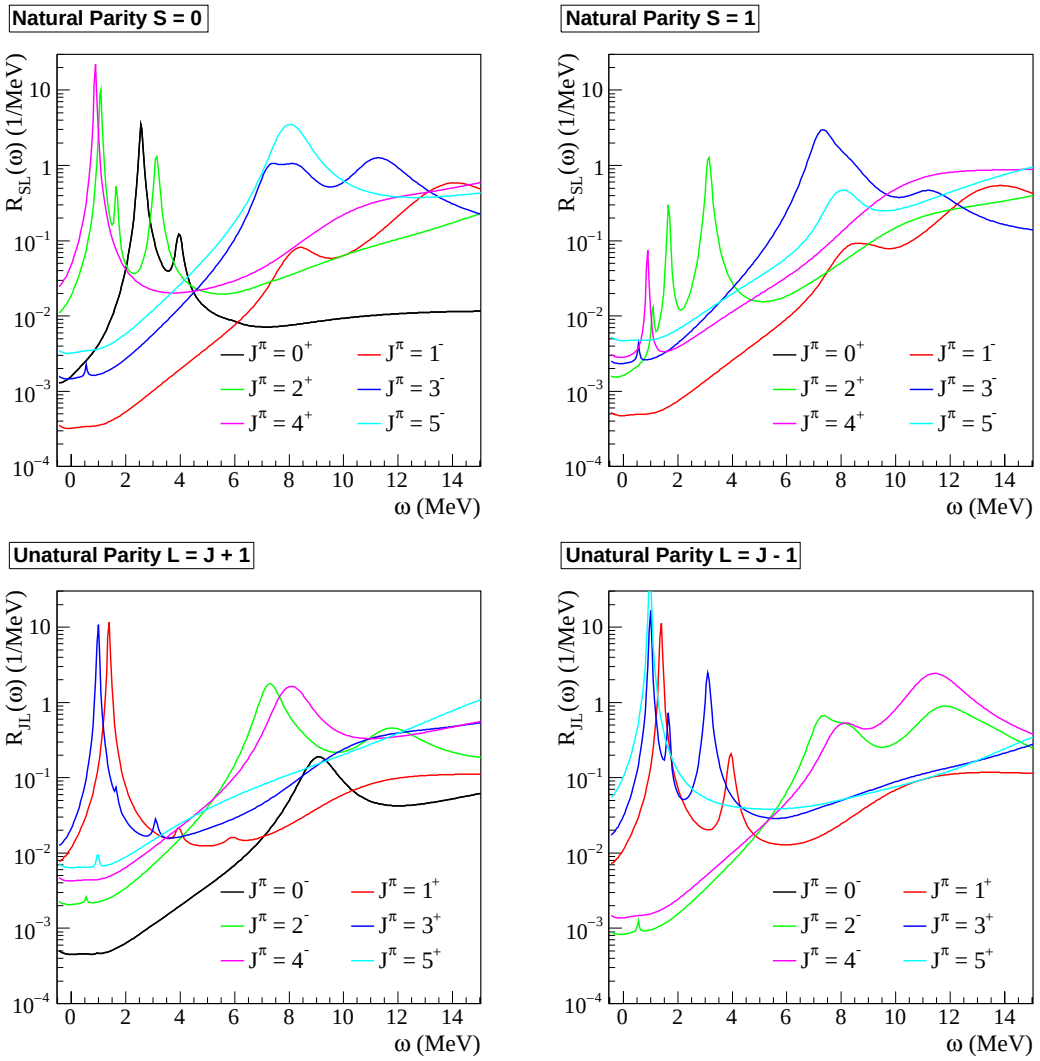

Figure 5.20: QRPA response functions of the ^{12}C to the (p→n) single charge exchange operator accounting for the ^{12}C → ^{12}B transitions competing to the J^π in the legends. Natural and unnatural parities up to $J = 5$ are shown.

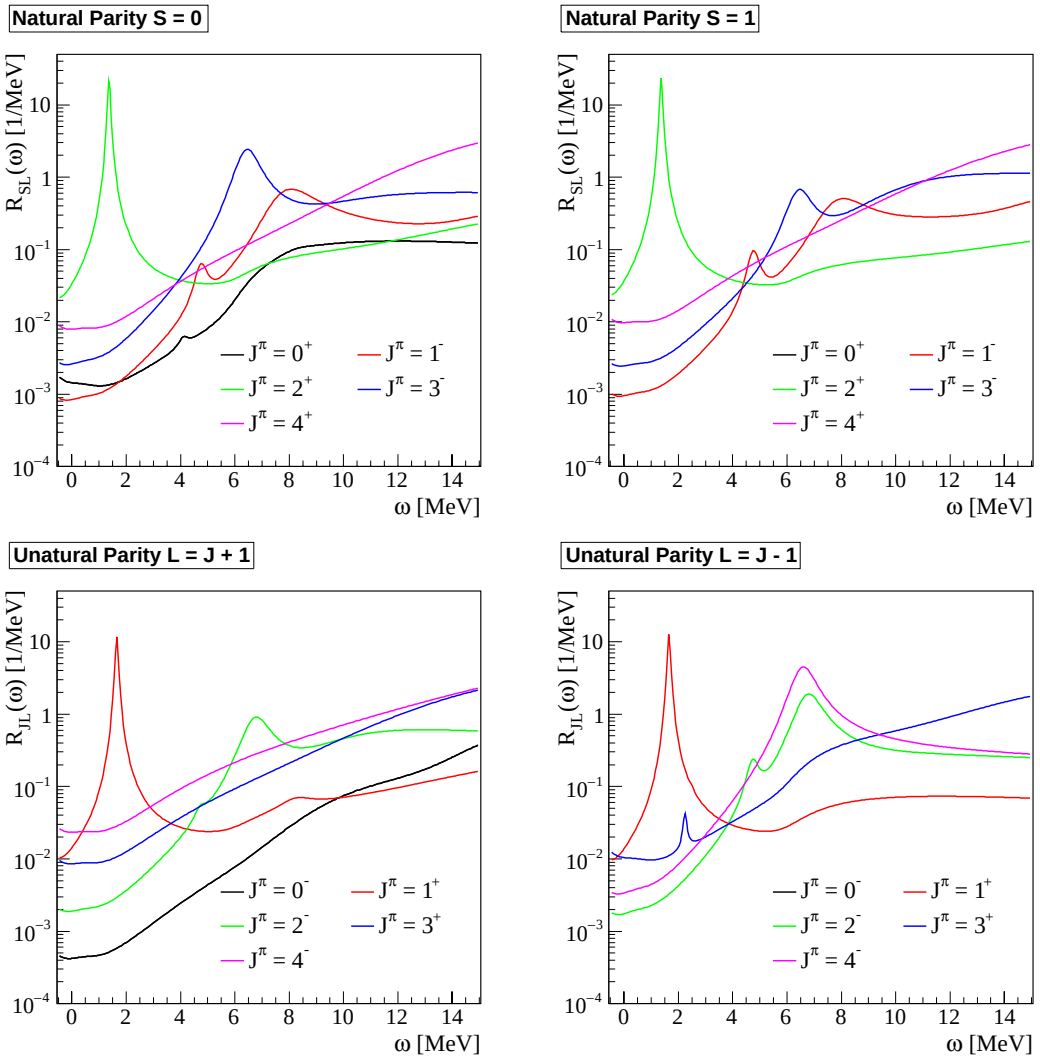

Figure 5.21: QRPA response functions of the ^{18}O to the (n→p) single charge exchange operator accounting for the $^{18}\mathrm{O} \rightarrow {}^{18}\mathrm{F}$ transitions competing to the J^π in the legends. Natural and unnatural parities up to $J = 5$ are shown.

Table 5.9: Gamow-Teller transition strengths from experiments and from the QRPA calculations described in the present work for the nuclear single-charge exchange transitions indicated in the first column.

SCE transition	B(GT)	
	QRPA	Exp. value
$^{18}O^{0^+}_{gs} \leftrightarrow ^{18}F^{1^+}_{gs}$	2.86 [41]	3.27† [150]
$^{12}C^{0^+}_{gs} \leftrightarrow ^{12}B^{1^+}_{gs}$	1.01 [129]	0.99 ± 0.01 [151]

†Error not reported in the publication.

$J \pm 1$ and S must be 1 (spin-flip). Response functions in Figures 5.21 and 5.20 shows the spectrum of natural and unnatural parity transitions populated by the single-charge-exchange operator. Peaks represents the predicted excited states of the final nucleus and the integral of each peak is related to the probability to populate it. Response functions for both ^{12}C and ^{18}O were used in previously published works [6, 9, 129]. As already there underlined, the performed QRPA calculations pretty well describe the nuclear geometry and spectra, despite some shift in the excitation energy and some intruder peak. The overall agreement was judged to be satisfactory, although the restriction to the 2QP-configuration space [6].

A general check applied to the nuclear structure models consists in the comparison of the B(GT) experimentally known and theoretically evaluated. In Table 5.9 is shown the comparison of the B(GT) strength values deduced from experimental measurements [150, 151] and the theoretical ones obtained from the QRPA [41, 129].

5.2.4.2 Choice of the t_{NN} interaction

Once the QRPA transition densities were provided and tested, the last step needed to calculate the reaction form factors of Eq. 2.22 is to provide a proper nucleon-nucleon (NN) interaction.

A realistic NN interaction, including the tensor contribution, was consistently used in both structure and reaction calculations. The central part (scalar and vector) is shown in Figure 5.22. It is the full complex local nucleon-nucleon effective interaction of Ref. [152] consisting of direct and exchange terms. It was constructed at several bombarding energies and interpolated with the low-energy G-matrix one [129] at 15.3 AMeV incident

energy, of interest in the present case. The rank-2 tensor part, much more important at smaller bombarding energies, is the full real D3Y G-matrix interaction from Ref. [61] and it is shown in Figure 5.23.

5.2.4.3 Form factors

The radial wave-functions, used to construct the form factors, were generated considering the single-particles (or single-holes) bound to the core by means of a Woods-Saxon potential. For the ^{18}O + (π_{nlj}) and ^{18}F + $(\nu_{nlj})^{-1}$ the 1.26 fm reduced radius and 0.7 fm diffuseness were used. For the ^{12}C + (ν_{nlj}) and ^{12}B + $(\pi_{nlj})^{-1}$ the 1.25 fm reduced radius and 0.65 fm diffuseness were used. The depth of the central potential was adjusted to reproduce the respective neutrons and protons experimental separation energies.The NN-interaction described in the previous paragraph was used to provide both the QRPA transition densities and form factors.

The $\Delta J^{\pi} = 1^{+}$ form factors for the ^{12}C(^{18}O,^{18}F)^{12}B ground-to-ground reaction are shown in Figure 5.24. For each L component, the real and imaginary parts of the form factors are calculated and shown for the QRPA approach.

5.2.4.4 Coupled-channels effective potential

The ISI, introduced and tested in Sec. 5.2.1, is shown in Figure 5.25 where nuclear real and imaginary parts of the SPP are shown for values of the nucleus-nucleus distance r around the surface region. The latest is most relevant for direct nuclear reactions and can be indicated by the Coulombic radius of the system $R_c = 1.2(\mathrm{A}_{tar}^{1/3} + \mathrm{A}_{proj}^{1/3})$ fm, also shown in the Figure.

In Sec. 5.2.1 we compared the theoretical OM, CC and CRC calculations performed with the SPP double-folding potential to the experimental data of elastic and inelastic scattering, obtaining a better agreement if the effects due to the inelastic couplings are explicitly taken into account. The same effect was observed also for the one-nucleon transfer case confirming not only, in some cases, the relevance of more sophisticated configurations in the one-nucleon transfer reactions but also that the proper description of the incoming and outgoing distorted wave-functions is of primary importance for all the direct nuclear reactions, therefore also for SCE.

The explicit inclusion of the couplings with relevant excited states of the initial partition is nowadays not feasible in the case of SCE reactions, as well as for DCE. In these cases, state-of-art nuclear reaction theories are presently not able to provide the

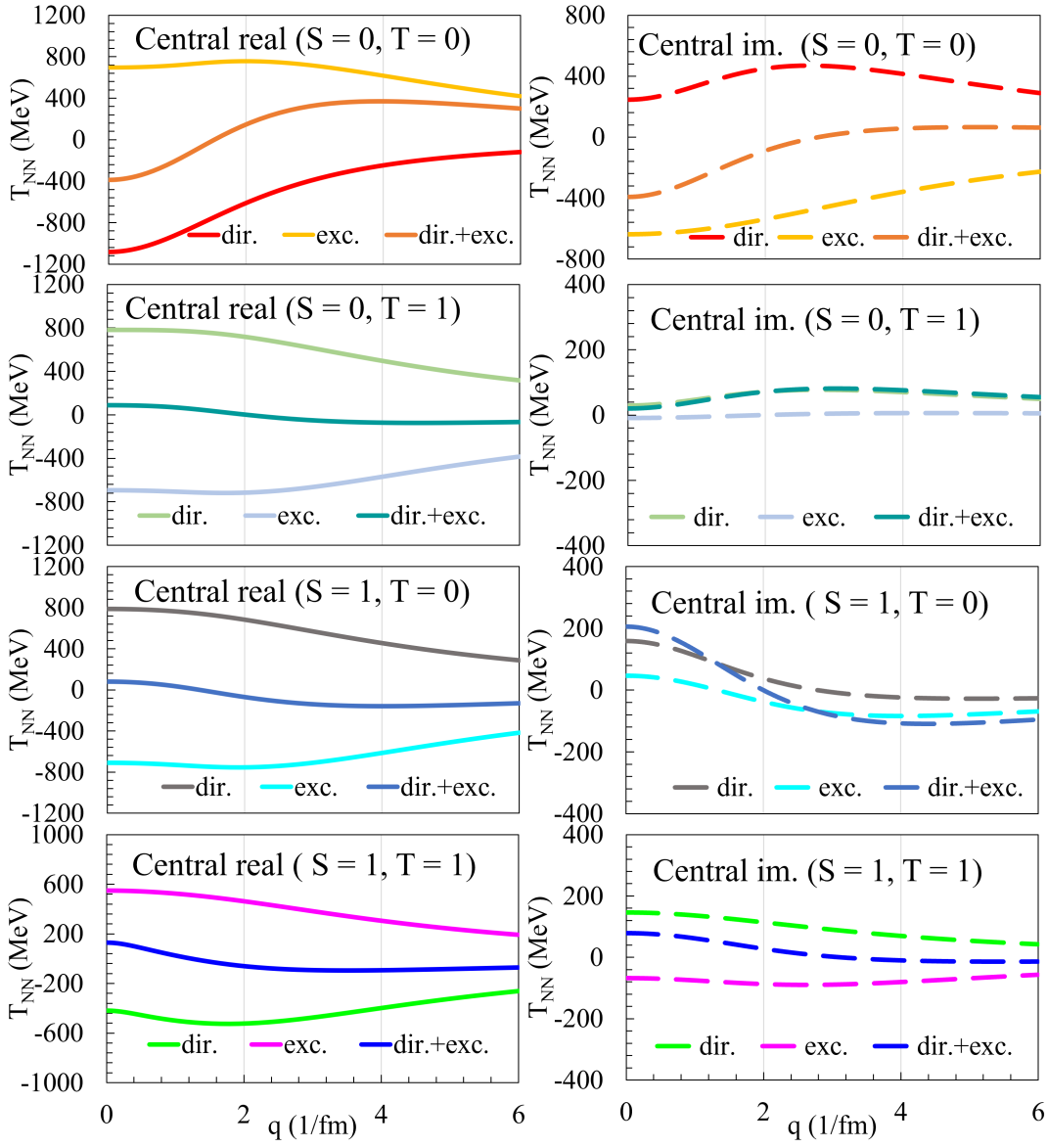

Figure 5.22: Real and imaginary central (S,T) components of the NN-interaction in the momentum space. Exchange terms were considered at zero excitation energy.

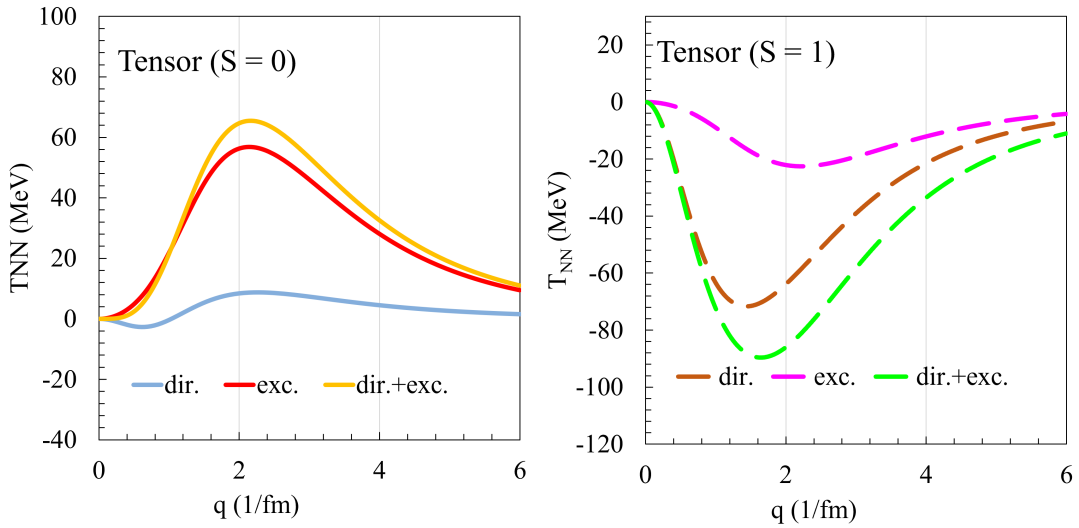

Figure 5.23: Scalar (S = 0) and vector (S = 1) rank-2 tensor components of the NN-interaction in the momentum space. Exchange terms were considered at zero excitation energy.

response functions to the isospin charge exchange operator acting on the excited states of the initial partition and DWBA calculations are typically performed. Following the approach of Ref. [42, 46, 142], it is possible to deduce a trivially equivalent effective polarization potential (TELP) that incorporates the average effect of channel coupling in the elastic optical potential.

The TELP polarization potential can be added to the optical one, used to perform the CC or CRC calculations, to get the coupled-channel equivalent polarization potential (CCEP)[42, 46]. The ISI corresponding to the CCEP is reported in Figure 5.25. This complex polarization potential affects the nuclear potential in the vicinity of the R_C, as shown by the blue and orange curves.

The CCEP was successfully used in one-channel calculations giving a quite reasonable description of the $^{12}C(^{18}O,^{18}O)^{12}C$ elastic angular distribution of differential cross-section. The obtained results are shown in Figure 5.26 where a substantial improvement is visible from the comparison with the OM calculation. The CCEP potential, accounting for a more detailed description of the main source of distortion in the incoming and outgoing nuclear wave-functions, was used to perform the one-step single charge exchange calculations shown in the following paragraph.

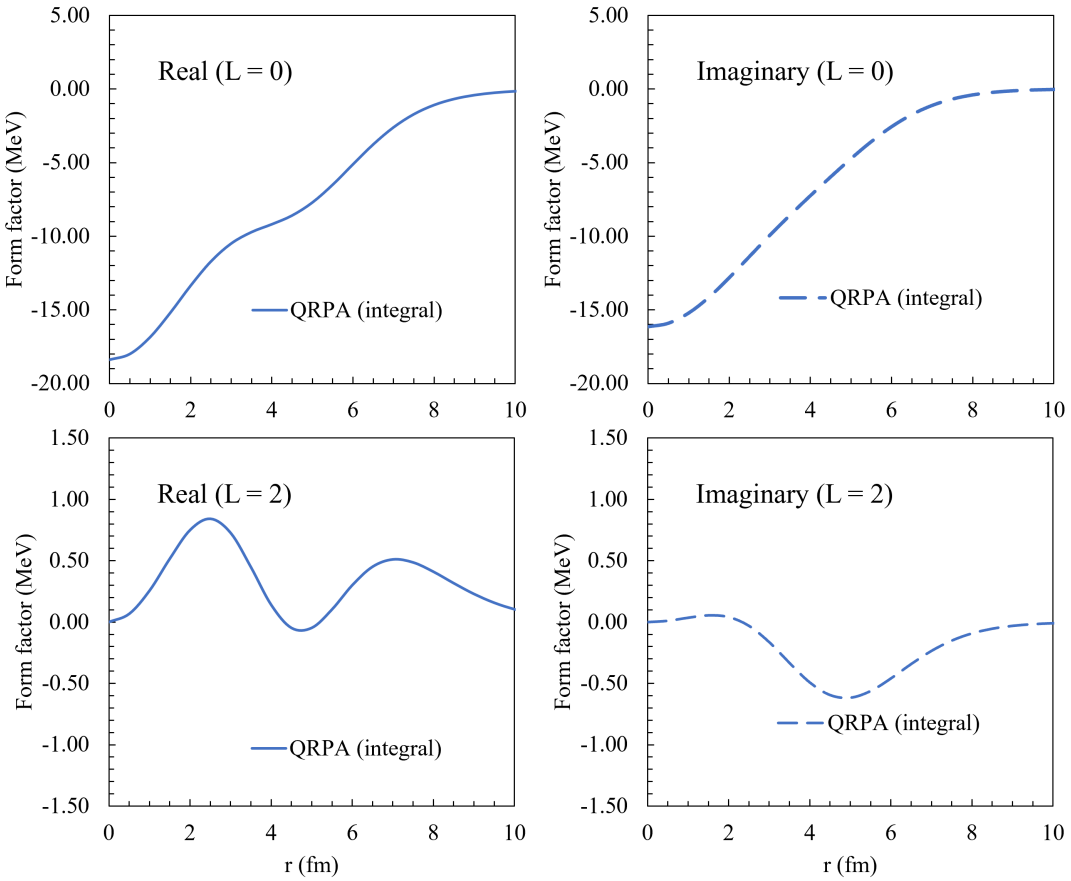

Figure 5.24: Form-factors in coordinate space as a function of the relative nucleus-nucleus distance r, for the $\Delta J^{\pi} = 1^{+}$ ground-to-ground state transition in the ^{12}C(^{18}O,^{18}F)^{12}B single charge exchange nuclear reaction. Real and imaginary parts for the L= 0 and L= 2 components are shown, as labelled in the legend.

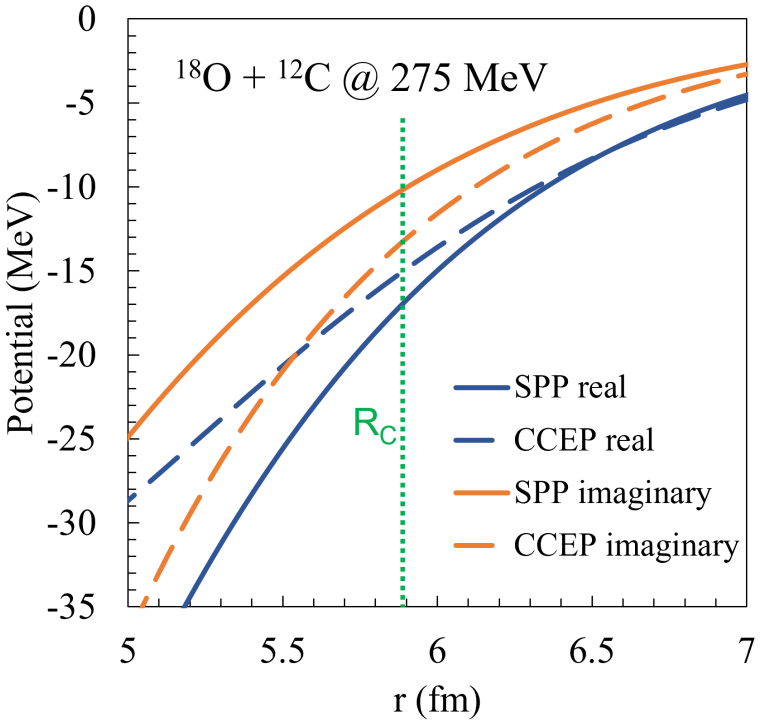

Figure 5.25: SPP and CCEP initial state interactions for the ^{18}O + ^{12}C system at 275 MeV incident energy. The nuclear real and imaginary parts of the SPP double-folding optical potential are shown as the blue continuous and dashed lines, respectively. The real and imaginary parts of the coupled-channel equivalent polarization potential (CCEP), obtained from the sum of the SPP and the polarization potential, are shown as the orange continuous and dashed lines, respectively. The coulomb radius (R_C) is also indicated as the green dotted line.

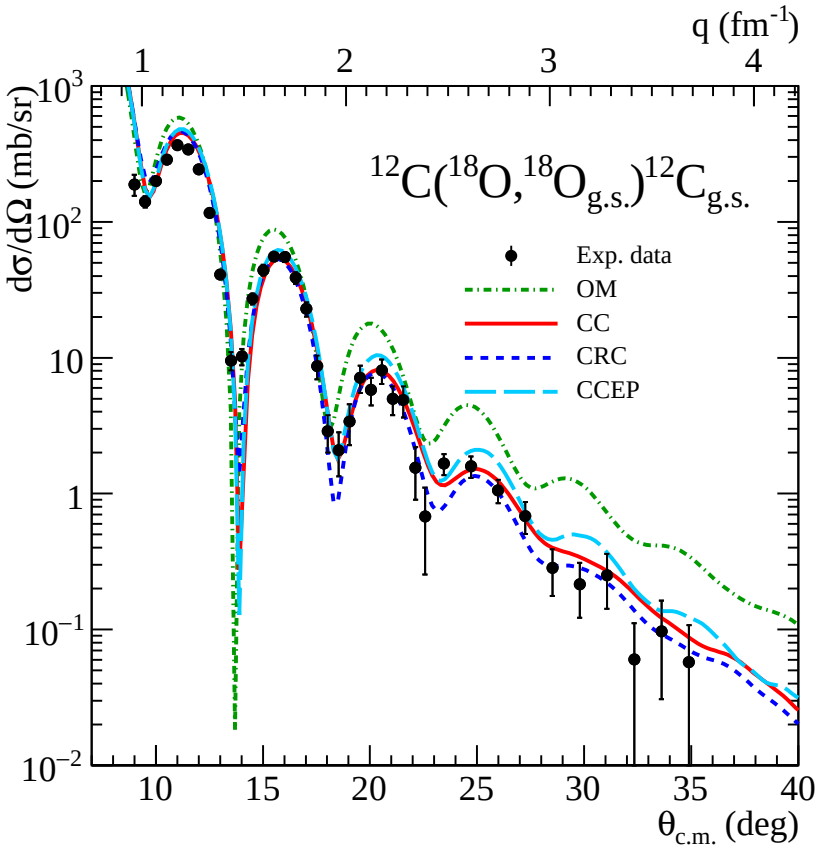

Figure 5.26: Experimental cross-section angular distribution of the ^{12}C(^{18}O,^{18}O)^{12}C elastic scattering at 275 MeV incident energy (same as Figure 5.3). Theoretical calculations for the elastic transition in OM, CC, CRC and CCEP approaches are shown with the green dot-dashed, continuous red, blue dashed and light-blue long-dashed lines, respectively.

5.2.4.5 Reaction calculations

One-step DWBA direct charge exchange calculations were performed in terms of partial wave decomposition of the CCEP distorted wave-functions and the multipole expansion of the form factor [60], as implemented in the FRESCO code [142]. The complete calculations were performed only for the ground-to-ground state peak in Figure 5.11 while the analysis of other peaks is still in progress.

The ground-to-ground state peak only includes the $\Delta J^{\pi} = 1^{+}$ transition both for the target and projectile due to high energy resolution achieved during the experiment and the relatively low level densities of the final nuclei presenting the first excited states at excitation energies larger than 0.9 MeV. The angular distribution of differential cross-section for the ^{12}C(^{18}O,^{18}F$_{gs}$)^{12}B$_{gs}$ single charge exchange reactions is shown in Figure 5.27, in comparison with the DWBA calculations performed using both the SPP standard optical potential and the CCEP one, effectively including the effects due to the channel coupling, and adopting the QRPA form factors described in the previous sections.

5.2.5 One- and two-step processes interference in SCE reaction

The theoretical calculations of the ^{12}C(^{18}O,^{18}F)^{12}B SCE nuclear reaction shown in Figures 5.18, 5.19 and 5.26 underestimate the experimental data both in the sequential 2-step approach and in the direct meson-exchange one. In the former case, the exploration of larger coupling schemes is not expected to influence the already obtained results; in the latter one, the use of a more realistic ISI, albeit have been changed the overall behaviour of the calculated angular distribution, was useless in the purpose to reach a satisfactory description of the experimental data.

The coherent sum of the calculations resulted from the two studied reaction mechanism has been performed using the following formula:

$$\frac{d\sigma}{d\Omega}(\theta_{cm}) = \frac{d\sigma_{direct}}{d\Omega}(\theta_{cm}) + \frac{d\sigma_{sequential}}{d\Omega}(\theta_{cm}) + cos(\xi)\sqrt{\frac{d\sigma_{direct}}{d\Omega}(\theta_{cm}) \cdot \frac{d\sigma_{sequential}}{d\Omega}(\theta_{cm})} \tag{5.7}$$

where the ξ is an overall phase factor. This coherent sum of the sequential and direct components has been calculated for the ^{12}C(^{18}O,^{18}F$_{g.s.}$)^{12}B$_{g.s.}$ transition and is shown in Figure 5.28 in the case of $\xi = 0$, corresponding to the constructing interference condition. The comparison of this sum and the data results in an excellent agreement confirming the relevance of a proper treatment of the competition between the two mechanisms.

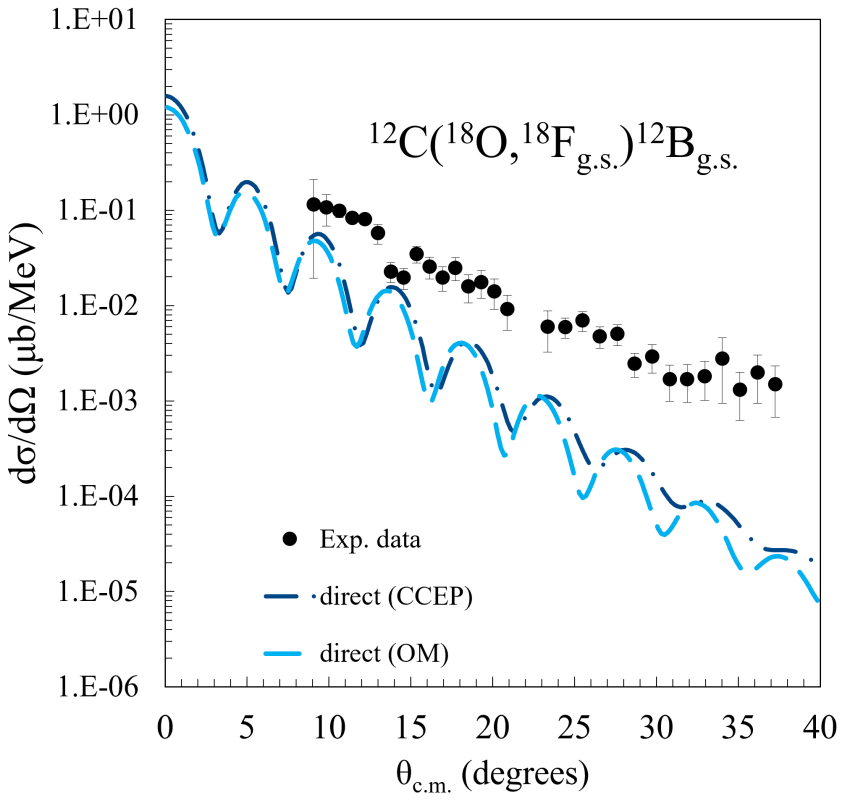

Figure 5.27: Experimental cross-section angular distribution of the ^{12}C(^{18}O,^{18}F$_{g.s.}$)^{12}B$_{g.s.}$ single-charge exchange reaction at 275 MeV incident energy. Theoretical calculations for the direct component in OM, and CCEP approaches are shown with the light-blue dashed and blue dot-dashed lines, respectively.

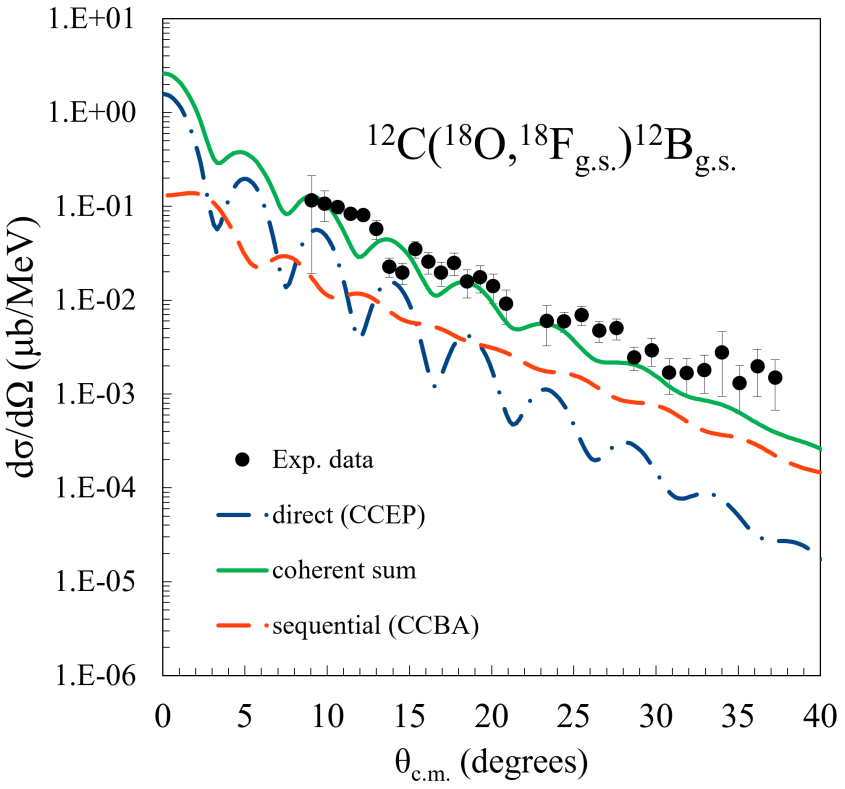

Figure 5.28: Experimental cross-section angular distribution of the ^{12}C(^{18}O,^{18}F$_{g.s.}$)^{12}B$_{g.s.}$ single-charge exchange reaction at 275 MeV incident energy. Theoretical calculations for the direct and sequential components are shown with the light-blue dashed and blue dot-dashed lines, respectively.

Further studies are in progress to consistently access the value of the ξ phase factor. Recent developments in the FRESCO code from J. A. Lay et al. [56] are highlighting the possibility to coherently perform the direct and the sequential reaction calculations simultaneously, in order to consistently treat the interference between the two reaction mechanisms inside the same (unique) calculation. Furthermore, a full-coherent study of the complete reaction mechanism implies to treat also the structure part in the same nuclear structure framework. This means that new spectroscopic amplitude calculations are needed from QRPA to re-calculate the 2-step SCE otherwise new one-body transition densities have to be provided by large-scale shell-model calculations. Both these possibilities are practicable [7, 153] and under study, constituting the main promising perspective for this research field.

Chapter References

[6] H. Lenske et al. "Heavy ion charge exchange reactions as probes for nuclear β-decay". In: *Progress in Particle and Nuclear Physics* 109 (2019), p. 103716. ISSN: 0146-6410. DOI: 10.1016/j.ppnp.2019.103716.

[7] D. Carbone et al. "Analysis of two-nucleon transfer reactions in the ^{20}Ne + ^{116}Cd system at 306 MeV". In: *Physical Review C* 102.4 (2020). cited By 6. DOI: 10.1103/PhysRevC.102.044606.

[8] J. L. Ferreira et al. "Multinucleon transfer in the ^{116}Cd(^{20}Ne,^{20} O)^{116}Sn double charge exchange reaction at 306 MeV incident energy". In: *Phys. Rev. C* 105 (1 Jan. 2022), p. 014630. DOI: 10.1103/PhysRevC.105.014630.

[9] J. I. Bellone et al. "Two-step description of heavy ion double charge exchange reactions". In: *Physics Letters B* 807 (2020), p. 135528. ISSN: 0370-2693. DOI: 10.1016/j.physletb.2020.135528.

[41] F. Cappuzzello et al. "Heavy-ion double charge exchange reactions: A tool toward $0\nu\beta\beta$ nuclear matrix elements". In: *Eur. Phys. J.* A51.11 (2015), p. 145. DOI: 10.1140/epja/i2015-15145-5.

[42] M. Cavallaro et al. "A Constrained Analysis of the ^{40}Ca(^{18}O,^{18}F)^{40}K Direct Charge Exchange Reaction Mechanism at 275 MeV". In: *Frontiers in Astronomy and Space Sciences* 8 (2021), p. 61. DOI: 10.3389/fspas.2021.659815.

[43] J.L. Ferreira et al. "Analysis of two-proton transfer in the ^{40}Ca (^{18}O, ^{20}Ne) ^{38}Ar reaction at 270 MeV incident energy". In: *Physical Review C* 103.5 (2021). cited By 0. DOI: 10.1103/PhysRevC.103.054604.

[44] S. Calabrese et al. "^{18}O-induced single-nucleon transfer reactions on ^{40}Ca at 15.3A MeV within a multichannel analysis". In: *Phys. Rev. C* 104 (6 Dec. 2021), p. 064609. DOI: 10.1103/PhysRevC.104.064609.

[46] D. Carbone et al. "Initial state interaction for the ^{20}Ne + ^{130}Te and ^{18}O + ^{116}Sn systems at 15.3 AMeV from elastic and inelastic scattering measurements". In: *Universe* 7.3 (2021). cited By 1. DOI: 10.3390/universe7030058.

[48] S. Burrello et al. "Multichannel experimental and theoretical constraints for the ^{116}Cd(^{20}Ne,^{20} F)^{116}In charge exchange reaction at 306 MeV". In: *Phys. Rev. C* 105 (2 Feb. 2022), p. 024616. DOI: 10.1103/PhysRevC.105.024616.

[50] A. Spatafora et al. "^{20}Ne+^{76}Ge elastic and inelastic scattering at 306 MeV". In: *Phys. Rev. C* 100 (3 Sept. 2019), p. 034620. DOI: 10.1103/PhysRevC.100.034620.

[51] L. La Fauci et al. "^{18}O +^{76} Se elastic and inelastic scattering at 275 MeV". In: *Phys. Rev. C* 104 (5 Nov. 2021), p. 054610. DOI: 10.1103/PhysRevC.104.054610.

[52] F. Cappuzzello et al. "Confirmation of Giant Pairing Vibration evidence in ^{12,13}C(^{18}O,^{16}O) ^{14,15}C reactions at 275 MeV". In: *European Physical Journal A* 57.1 (2021). cited By 1. DOI: 10.1140/epja/s10050-021-00345-7.

[53] O. Sgouros et al. "One-proton transfer reaction for the ^{18}O +^{48} Ti system at 275 MeV". In: *Phys. Rev. C* 104 (3 Sept. 2021), p. 034617. DOI: 10.1103/PhysRevC.104.034617.

[56] J. A. Lay et al. "Double charge-exchange reactions and the effect of transfer". In: *Journal of Physics: Conference Series* 1056 (July 2018), p. 012029. DOI: 10.1088/1742-6596/1056/1/012029.

[60] G. R. Satchler. *Direct nuclear reactions*. Vol. 68. Int. series of monographs on physics. Oxford, UK: Clarendon Press, 1983. ISBN: 9780198512691.

[61] F. Hofmann and H. Lenske. "Hartree-Fock calculations in the density matrix expansion approach". In: *Phys. Rev. C* 57 (5 May 1998), pp. 2281–2293. DOI: 10.1103/PhysRevC.57.2281.

[62] L. C. Chamon et al. “Toward a global description of the nucleus-nucleus interaction”. In: *Phys. Rev.* C66 (2002), p. 014610. DOI: 10.1103/PhysRevC.66.014610.

[84] M. Cavallaro et al. “Transport efficiency in large acceptance spectrometers”. In: *Nucl. Instrum. Meth. A* 637 (May 2011), pp. 77–87. DOI: 10.1016/j.nima.2011.01.078.

[110] D.R. Tilley et al. “Energy levels of light nuclei A = 18–19”. In: *Nuclear Physics A* 595.1 (1995), pp. 1–170. ISSN: 0375-9474. DOI: https://doi.org/10.1016/0375-9474(95)00338-1.

[111] J.H. Kelley, J.E. Purcell, and C.G. Sheu. “Energy levels of light nuclei A=12”. In: *Nuclear Physics A* 968 (2017), pp. 71–253. ISSN: 0375-9474. DOI: https://doi.org/10.1016/j.nuclphysa.2017.07.015.

[112] M. Freer et al. “2^+ excitation of the ^{12}C Hoyle state”. In: *Phys. Rev. C* 80 (4 Oct. 2009), p. 041303. DOI: 10.1103/PhysRevC.80.041303.

[113] M. Itoh et al. “Candidate for the 2^+ excited Hoyle state at $E_x \sim 10$ MeV in ^{12}C”. In: *Phys. Rev. C* 84 (5 Nov. 2011), p. 054308. DOI: 10.1103/PhysRevC.84.054308.

[114] M. Cavallaro et al. “Quantitative analysis of two-neutron correlations in the ^{12}C(^{18}O,^{16}O)^{14}C reaction”. In: *Phys. Rev. C* 88 (5 Nov. 2013), p. 054601. DOI: 10.1103/PhysRevC.88.054601.

[115] D.M. Brink. “Kinematical effects in heavy-ion reactions”. In: *Physics Letters B* 40.1 (1972), pp. 37–40. ISSN: 0370-2693. DOI: https://doi.org/10.1016/0370-2693(72)90274-2.

[116] H. Ohnuma et al. “The ^{12}C(d, p)^{12}C reaction at E_d = 30 MeV and positive-parity states in $_{13}$C”. In: *Nuclear Physics A* 448.2 (1986), pp. 205–220. ISSN: 0375-9474. DOI: https://doi.org/10.1016/0375-9474(86)90087-4.

[117] D.R. Tilley, H.R. Weller, and C.M. Cheves. “Energy levels of light nuclei A = 16–17”. In: *Nuclear Physics A* 564.1 (1993), pp. 1–183. ISSN: 0375-9474. DOI: https://doi.org/10.1016/0375-9474(93)90073-7.

[118] F. Ajzenberg-Selove. "Energy levels of light nuclei A = 13–15". In: *Nuclear Physics A* 523.1 (1991), pp. 1–196. ISSN: 0375-9474. DOI: https://doi.org/10.1016/0375-9474(91)90446-D.

[119] F. Cappuzzello et al. "Signatures of the giant pairing vibration in the ^{14}C and ^{15}C atomic nuclei". In: *Nature Communications* 6 (2015). cited By 75. DOI: 10.1038/ncomms7743.

[120] G. G. Ohlsen. "Kinematic relations in reactions of the form A+B→C+D+E". In: *Nuclear Instruments and Methods* 37 (1965), pp. 240–248. ISSN: 0029-554X. DOI: https://doi.org/10.1016/0029-554X(65)90368-X.

[121] S. Kahana and A. J. Baltz. "One- and Two-Nucleon Transfer Reactions with Heavy Ions". In: *Advances in Nuclear Physics*. Ed. by Michel Baranger and Erich Vogt. Boston, MA: Springer US, 1977, pp. 1–122. ISBN: 978-1-4615-8234-2. DOI: 10.1007/978-1-4615-8234-2_1.

[122] G. Van Der Steenhoven et al. "Weak transitions in the quasi-elastic reaction ^{12}C(e, e'p)^{11}B". In: *Nuclear Physics A* 484.3 (1988), pp. 445–475. ISSN: 0375-9474. DOI: https://doi.org/10.1016/0375-9474(88)90304-1.

[123] P. L. Kerr et al. "Analyzing powers for mirror states in ^{12}C(^{6}Li,^{7}Li/^{7}Be) at $E_{^{6}\mathrm{Li}} = 50$ MeV: Evaluation of channel coupling". In: *Phys. Rev. C* 55 (5 May 1997), pp. 2441–2447. DOI: 10.1103/PhysRevC.55.2441.

[124] H. G. Pugh et al. "High-Resolution Study of the Reaction ^{12}C$(p, 2p)^{11}$B at 50 MeV". In: *Phys. Rev. Lett.* 14 (12 Mar. 1965), pp. 434–436. DOI: 10.1103/PhysRevLett.14.434.

[125] J.H. Kelley et al. "Energy levels of light nuclei A=11". In: *Nuclear Physics A* 880 (2012), pp. 88–195. ISSN: 0375-9474. DOI: https://doi.org/10.1016/j.nuclphysa.2012.01.010.

[126] S. Nakayama et al. "Relative strength (ΔS=1)/[(ΔS=0)+(ΔS=1)] of isovector spin excitations in the high-lying resonance region of ^{12}C". In: *Phys. Rev. Lett.* 67 (9 Aug. 1991), pp. 1082–1085. DOI: 10.1103/PhysRevLett.67.1082.

[127] S. Nakayama et al. “Excitation of isovector states by the (^{7}Li,^{7}Be) reaction on ^{12}C and ^{13}C”. In: *Nuclear Physics A* 507.2 (1990), pp. 515–530. ISSN: 0375-9474. DOI: https://doi.org/10.1016/0375-9474(90)90306-7.

[128] S. Nakayama et al. “Dominance of the direct reaction process in the ^{12}C (^{7}Li, ^{7}Be) ^{12}B reaction at θ_L=0° and $E_L \geq$ 21 AMeV”. In: *Physics Letters B* 246.3 (1990), pp. 342–346. ISSN: 0370-2693. DOI: https://doi.org/10.1016/0370-2693(90)90611-9.

[129] F. Cappuzzello et al. “Analysis of the ^{11}B(^{7}Li,^{7}Be)^{7}Be reaction at 57 MeV in a microscopic approach”. In: *Nucl. Phys.* A739.1-2 (2004), pp. 30–56. DOI: 10.1016/j.nuclphysa.2004.03.221.

[130] D. Carbone et al. “Microscopic cluster model for the description of new experimental results on the ^{13}C(^{18}O,^{16}O)^{15}C two-neutron transfer at 84 MeV incident energy”. In: *Phys. Rev.* C95.3 (2017), p. 034603. DOI: 10.1103/PhysRevC.95.034603.

[131] B. Paes et al. “Long-range versus short-range correlations in the two-neutron transfer reaction ^{64}Ni(^{18}O,^{16}O)^{66}Ni”. In: *Phys. Rev.* C96.4 (2017), p. 044612. DOI: 10.1103/PhysRevC.96.044612.

[132] M.J. Ermamatov et al. “Two-neutron transfer analysis of the ^{16}O (^{18}O, ^{16}O) ^{18}O reaction”. In: *Phys. Rev.* C94.2 (2016), p. 024610. DOI: 10.1103/PhysRevC.94.024610.

[133] M. J. Ermamatov et al. “Comprehensive analysis of high-lying states in ^{18}O populated with (t,p) and (^{18}O,^{16}O) reactions”. In: *Phys. Rev.* C96.4 (2017), p. 044603. DOI: 10.1103/PhysRevC.96.044603.

[134] V.A.B. Zagatto et al. “Important role of projectile excitation in ^{16}O + ^{60}Ni and ^{16}O + ^{27}Al scattering at intermediate energies”. In: *Phys. Rev. C* 97 (May 2018), p. 054608. DOI: 10.1103/PhysRevC.97.054608.

[135] E. N. Cardozo et al. “Competition between direct and sequential two-neutron transfers in the ^{18}O +^{28} Si collision at 84 MeV”. In: *Phys. Rev. C* 97 (6 June 2018), p. 064611. DOI: 10.1103/PhysRevC.97.064611.

[136] D. Pereira et al. “An imaginary potential with universal normalization for dissipative processes in heavy-ion reactions”. In: *Phys. Lett. B* 670.4 (2009), pp. 330–335. ISSN: 0370-2693. DOI: https://doi.org/10.1016/j.physletb.2008.10.066.

[137] G.R. Satchler and W.G. Love. “Folding model potentials from realistic interactions for heavy-ion scattering”. In: *Physics Reports* 55.3 (1979), pp. 183–254. ISSN: 0370-1573. DOI: https://doi.org/10.1016/0370-1573(79)90081-4.

[138] M.E. Brandan and G.R. Satchler. “The interaction between light heavy-ions and what it tells us”. In: *Physics Reports* 285.4 (1997), pp. 143–243. ISSN: 0370-1573. DOI: https://doi.org/10.1016/S0370-1573(96)00048-8.

[139] E. Crema et al. “Near-barrier quasielastic scattering as a sensitive tool to derive nuclear matter diffuseness”. In: *Phys. Rev. C* 84 (2 Aug. 2011), p. 024601. DOI: 10.1103/PhysRevC.84.024601.

[140] E. Crema et al. “Reaction mechanisms of the ^{18}O +^{63} Cu system at near-barrier energies”. In: *Phys. Rev. C* 98 (4 Oct. 2018), p. 044614. DOI: 10.1103/PhysRevC.98.044614.

[141] L. M. Fonseca et al. “Elastic and inelastic scattering of ^{16}O on ^{27}Al and ^{28}Si at 240 MeV”. In: *Phys. Rev. C* 100 (1 July 2019), p. 014604. DOI: 10.1103/PhysRevC.100.014604.

[142] I. J. Thompson. “Coupled reaction channels calculations in nuclear physics”. In: *Comput. Phys. Rep.* 7.4 (1988), pp. 167–212. ISSN: 0167-7977. DOI: https://doi.org/10.1016/0167-7977(88)90005-6.

[143] B. Pritychenko et al. “Tables of E2 Transition Probabilities from the first 2^+ States in Even-Even Nuclei”. In: *Atom. Data Nucl. Data Tabl.* 107 (2016), pp. 1–139. DOI: 10.1016/j.adt.2015.10.001,10.1016/j.adt.2016.08.002.

[144] T. Kibedi and R. H. Spear. "Reduced electric-octupole transition probabilities, B(E3;$0^+ \rightarrow 3^-$) - an update". In: *Atomic Data and Nuclear Data Tables* 80.1 (2002), pp. 35–82. ISSN: 0092-640X. DOI: https://doi.org/10.1006/adnd.2001.0871.

[145] N. Shimizu et al. "Thick-restart block Lanczos method for large-scale shell-model calculations". In: *Computer Physics Communications* 244 (2019), pp. 372–384. ISSN: 0010-4655. DOI: https://doi.org/10.1016/j.cpc.2019.06.011.

[146] Y. Utsuno and S. Chiba. "Multiparticle-multihole states around ^{16}O and correlation-energy effect on the shell gap". In: *Phys. Rev. C* 83 (2 Feb. 2011), p. 021301. DOI: 10.1103/PhysRevC.83.021301.

[147] E. K. Warburton and B. A. Brown. "Effective interactions for the 0p1s0d nuclear shell-model space". In: *Phys. Rev. C* 46 (3 Sept. 1992), pp. 923–944. DOI: 10.1103/PhysRevC.46.923.

[148] I. J. Thompson. "Reaction Mechanisms of Pair Transfer". In: *Fifty Years of Nuclear BCS*, pp. 455–467. DOI: 10.1142/9789814412490_0034.

[149] H. Lenske, ed. *DFOL private comunication*.

[150] D. J. Mercer et al. "Multipole decomposition of the ^{16}O(p,n)^{16}F and ^{18}O(p,n)^{18}F reactions at 494 MeV". In: *Phys. Rev. C* 49 (6 June 1994), pp. 3104–3116. DOI: 10.1103/PhysRevC.49.3104.

[151] F. Ajzenberg-Selove. "Energy levels of light nuclei A = 11−12". In: *Nuclear Physics A* 506.1 (1990), pp. 1–158. ISSN: 0375-9474. DOI: https://doi.org/10.1016/0375-9474(90)90271-M.

[152] M. A. Franey and W. G. Love. "Nucleon-nucleon T-matrix interaction for scattering at intermediate energies". In: *Phys. Rev.* C31 (1985), pp. 488–498. DOI: 10.1103/PhysRevC.31.488.

[153] A. Etchegoyen et al. "A study of the ^{26}Mg(^{12}C, ^{12}B)^{26}Al charge-exchange reaction". In: *Nuclear Physics A* 397.2 (1983), pp. 343–364. ISSN: 0375-9474. DOI: https://doi.org/10.1016/0375-9474(83)90107-0.

[159] R. Linares et al. “Analysis of the one-neutron transfer to ^{16}O, ^{28}Si, and ^{64}Ni induced by the (^{18}O, ^{17}O) reaction at 84 MeV”. In: *Phys. Rev. C* 98 (5 Nov. 2018), p. 054615. DOI: 10.1103/PhysRevC.98.054615.

Potrebbe essere proficuo staccarsi dall'abitudine di star ad ascoltare soltanto quello che risulta subito chiaro.

Martin Heidegger

6

The ^{76}Ge - ^{76}Se network of nuclear reactions

Contents

The ^{76}Ge nucleus is one of the most investigated candidates in $0\nu\beta\beta$ decay experiments [2–5, 154]. The nuclear response to isospin probes were studied using the high-resolution (^{3}He,t) [155] and (d,^{2}He) [72] charge-exchange nuclear reactions at very forward angles, mainly to extract the Gamow-Teller strength distribution in the ^{76}As. These works were crucial to constraint the $2\nu\beta\beta$ decay nuclear matrix elements in which the $L = 0$ component dominates both the light-ion induced charge exchange reaction (under proper conditions) and the $2\nu\beta\beta$ decay. However, the same argument cannot be applied to the $0\nu\beta\beta$ decay, where a large linear momentum ($\approx$ 100 MeV/c) is available in the virtual intermediate channel and the $L > 0$ components could even dominate the decay.

In this chapter, the study of a wide network of nuclear reactions involving the nuclear structure of the ^{76}Ge and ^{76}Se $0\nu\beta\beta$ partners and many other nuclear systems is presented. In Figure 6.1, a cartoon shows the A = 76 region of the nuclides' chart and the arrows indicate the nuclear reactions of interest for the purposes of the NUMEN project. Two experiments were dedicated to this scope and 14 nuclear reaction channels are involved in the complete study, including the ^{76}Ge$\leftrightarrow^{76}$Se transition studied in both directions through the (^{18}O,^{18}Ne) and the (^{20}Ne,^{20}O) double charge exchange nuclear reactions. The high density of levels characterizing odd-odd and even-odd nuclei involved in the study makes the theoretical analysis more demanding than the one described in the previous Chapter for the ^{12}C case, especially from the structure calculation side.

In the following sections, the study of the initial state interactions for the ^{18}O + ^{76}Se and the ^{20}Ne + ^{76}Ge systems at 15.3 AMeV incident energy, recently published in Refs. [50] and [51], will be presented. The experimental results obtained from the study of the ^{76}Se(^{18}O,^{18}F)^{76}As and ^{76}Ge(^{20}Ne,^{20}F)^{76}As single-charge exchange and the ^{76}Se(^{18}O,^{18}Ne)^{76}Ge and ^{76}Ge(^{20}Ne,^{20}O)^{76}Se double-charge exchange reactions are here presented for the first time.

6.1 Experimental Set-up

The ^{18}O + ^{76}Se and the ^{20}Ne + ^{76}Ge collisions at 15.3 AMeV incident energy were performed at the LNS-INFN using the $^{18}O^{8+}$ and the $^{20}Ne^{10+}$ beams accelerated by the

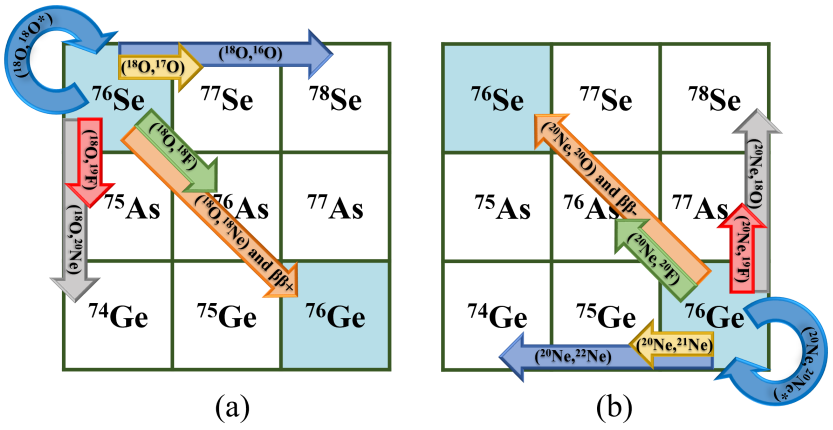

Figure 6.1: Cartoons of the nuclear reactions involved in the NUMEN experimental campaign for the ^{76}Se (a) and the ^{76}Ge (b) targets with the $^{18}O^{8+}$ and the $^{20}Ne^{10+}$ ion beams, respectively.

K800 Superconducting Cyclotron and the MAGNEX magnetic spectrometer to detect the ejectiles. The experimental set-up and data reduction techniques were described in the Chapters 3 and 4. The relevant experimental details for the reaction channels presented in this Chapter are listed in Table 6.1.

Table 6.1: Main parameters characterizing the experimental set-up of each explored reaction channel: target, carbon backing and post-stripper thicknesses, covered scattering angles $[\theta_{lab}^{min}; \theta_{lab}^{max}]$, MAGNEX central angle θ_{opt}, magnetic rigidity Bρ, quadrupole field BQ and MAGNEX solid angle acceptance are given.

	target (μg/cm^2)	C backing (μg/cm^2)	C post-stripper (μg/cm^2)	$[\theta_{lab}^{min}; \theta_{lab}^{max}]$ (deg)	θ_{opt} (deg)	Bρ (Tm)	BQ (T)	Ω (msr)
^{76}Se(^{18}O,^{18}O)^{76}Se	280 ± 15	80 ± 4	-	[3.0; 18.5]	8.0	1.1968	-0.6638	49.2
					8.0			35.0
					14.0			49.2
					18.0			49.2
^{76}Se(^{18}O,^{18}F)^{76}As	280 ± 15	80 ± 4	-	[3.0; 14.0]	8.0	1.1495	-0.6220	13.6
^{76}Se(^{18}O,^{18}Ne)^{76}Ge	280 ± 15	80 ± 4	-	[0.0; 9.0]	3.0	1.0086	-0.5482	10.4
^{76}Ge(^{20}Ne,^{20}Ne)^{76}Ge	390 ± 20	56 ± 3	300 ± 15	[3.0; 20.0]	8.0	1.1397	-0.6805	49.2
					8.0			32.0
					13.0			49.2
					16.0			49.2
					19.0			49.2
^{76}Ge(^{20}Ne,^{20}F)^{76}As	390 ± 20	56 ± 3	300 ± 15	[3.0; 14.0]	8.0	1.2270	-0.6286	1.6
^{76}Ge(^{20}Ne,^{20}O)^{76}Se	390 ± 20	56 ± 3	300 ± 15	[0.0; 9.0]	-3.0	1.3761	-0.8175	49.2

6.2 Study of the Initial State Interactions

Elastic and inelastic scattering are the most relevant processes to provide and test the Initial State Interaction (ISI) [60, 156]. Elastic scattering is the most probable process and its description is a necessary step to obtain a realistic representation of the nucleus-nucleus interaction. The comparison of the elastic scattering cross sections with the Optical Model (OM) calculations gives crucial information on the nucleus-nucleus optical potential (OP), which is the most important part of the interaction between the colliding nuclei prior to the nuclear reaction. A practical way to find a reasonable ISI is to describe the elastic scattering using an OP with a Woods-Saxon shape, adjusting its parameters to describe the measured elastic cross sections [60, 156]. However, such effective approach hides the physical insight and it is not suitable when elastic scattering data are not available, e.g. for the core-core potentials involved in the multi-nucleon transfer reactions [7]. The best models to determine the OP in heavy-ion collisions are obtained by folding the frozen densities of the colliding nuclei with a realistic nucleon-nucleon interaction. In such cases, the frozen densities approximation is justified by the strong absorption in heavy-ion collisions that bounds the reaction source near the surfaces of the colliding nuclei making the reaction mechanism insensitive to the internal regions [60].

The present section focuses on the experimental and theoretical analysis of the elastic and inelastic channels of the ^{18}O + ^{76}Se and ^{20}Ne + ^{76}Ge systems at 15.3 AMeV incident energy. The theoretical description of the DCE reaction mechanisms requires an accurate determination of the ISIs, representing a key aspect for these studies. To determine the effect of the inelastic channel on the ISI, coupling schemes that include the first excited states of the colliding nuclei are considered. In particular, the role of the first low-lying excitation of the projectile and the target is investigated. This study compares elastic scattering data and calculations performed in the OM and in the Coupled Channels (CC) formalism. For the inelastic channels, results obtained using the Distorted Wave Born Approximation (DWBA) and CC approaches are compared. These results have been recently published in Refs. [50] and [51].

6.2.1 Experimental results

The ^{18}O and ^{20}Ne ejectiles were momentum analysed in different runs in which the optical axis of MAGNEX was oriented at different angles compared to the beam direction, as listed in Table 6.1. The MAGNEX solid angle acceptance was set to the full

value ($\approx$ 50 msr) by means of the slits at the entrance of the quadrupole magnet (see Chapter 3). At $\theta_{\rm opt} = 8°$, due to the high elastic cross section at forward angles, the beam current was optimized at about 100 epA, but in this range the signal from the Faraday cup was small compared to the electronic noise. So, in order to re-normalize the cross section with a good Faraday cup measurement, in a second run at the same $\theta_{\rm opt}$ the solid angle was reduced excluding the forward angles and increasing the beam current to measurable values. The beam current was optimized at each angular setting up to 10 enA. Under these conditions, a large angular overlap ($\approx 6°$) in the laboratory reference frame was achieved between adjacent runs.

6.2.1.1 Excitation energy spectra

In both experiments the achieved energy resolutions was δE(FWHM) $\sim$ 0.5 MeV and the angular resolution was $\delta\theta_{lab}$(FWHM) $\sim 0.7°$ and $0.5°$ in the ^{18}O + ^{76}Se and ^{20}Ne + ^{76}Ge, respectively. Figure 6.2 shows the excitation energy (E_x) spectra for the ^{76}Ge and ^{76}Se nuclei populated in the ^{76}Ge(^{20}Ne,^{20}Ne)^{76}Ge and the ^{76}Se(^{18}O,^{18}O)^{76}Se elastic and inelastic scattering, respectively, measured in the angular regions indicated therein. The spectra show a similar behaviour. The first observed peak corresponds to the superposition of the ground state (g.s.) and the first 2^+ state of the target nucleus (E_x = 0.563 MeV for the ^{76}Ge and E_x = 0.559 MeV for the ^{76}Se). Although the energy resolution is not enough to fully separate them, the presence of the 2^+ state in the spectra is evident. Other structures are visible in the ^{76}Ge and the ^{76}Se spectra at E_x $\simeq$ 1.6 MeV and $E_x \simeq$ 2.0 MeV , respectively. They are due to the superposition of several states among which the dominant is expected to be the 2^+ one-phonon state of the ^{20}Ne and ^{18}O ejectiles at E_x = 1.634 MeV and E_x = 1.982 MeV, respectively. The ^{76}Se spectrum also shows a structure at $E_x \simeq$ 1.2 MeV corresponding to the 0^+ (1.122 MeV), 2^+ (1.216 MeV), 4^+ (1.330 MeV) [157] triplet, the two-phonon quadrupole excitation of the ^{76}Se nucleus. The simultaneous excitation of the first 2^+ states of both target and projectile is clearly visible both in the ^{76}Se spectrum (at $E_x \simeq$ 2.2 MeV) and in the ^{76}Ge one (at $E_x \simeq$ 2.5 MeV).

Multiple fit procedure was applied to the spectra to extract the number of counts for each peak at several angles. The width of each Gaussian function was fixed according to the achieved energy resolution and the Doppler broadening due to the in-flight γ-decay of the projectile populated states. The contributions above $\simeq$ 3 MeV in the excitation energy spectra are due to the weakly populated states of both projectile and target and

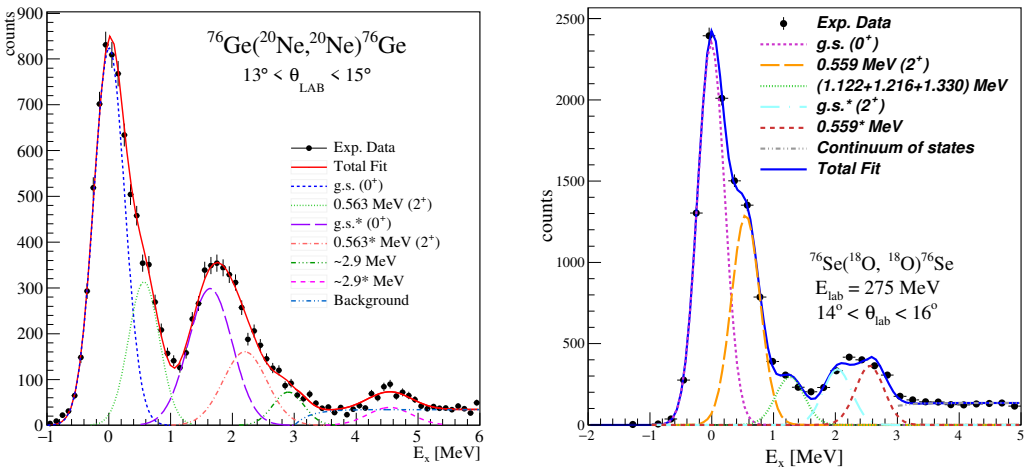

(a) (b)

Figure 6.2: Excitation energy spectra for the ^{20}Ne + ^{76}Ge ((a) panel) and the ^{18}O + ^{76}Se ((b) panel) elastic and inelastic scattering at 15.3 AMeV bombarding energy. Some peaks are identified in the figure by lines obtained fitting the experimental data. Several states are expected to be populated starting from 3 MeV and are summarized in the fit by a unique background curve. In the legend, the curves marked by an asterisk correspond to states where the ejectile (^{20}Ne and ^{18}O) is in its first 2^+ excited state. Figures from Ref. [50] and [51].

are summarized in the fit procedure as a unique background curve (see Figure 6.2).

6.2.1.2 Angular distributions of differential cross-section

Cross-sections angular distributions are presented in Figure 6.3 for the angular ranges explored at different settings of θ_{opt}, central angle of the spectrometer. The statistical error and the uncertainties coming from the fitting procedure and from the differential solid angle evaluation are included in the error bars. The systematic error, due to the uncertainty in the charge collection and in the measurement of the number of scattering centres in the target, is not explicitly included in the error bars because common to all the points and was estimated in experiments performed in similar conditions to be less than 10%. A scale factor equal to 1.11 was applied to the ^{20}Ne + ^{76}Ge elastic and inelastic scattering data to ensure a good agreement with the Rutherford cross section at very forward angles. No scale factor was applied in the ^{18}O + ^{76}Se case.

Table 6.2: Total beam energy in the laboratory reference frame E_{lab} and in the centre-of-mass E_{cm}, Sommerfeld parameter η, grazing angle θ_{cm}^{gr} and angular momentum L^{gr}, Coulomb barrier V_C and radius R_C for the ^{20}Ne + ^{76}Ge and ^{18}O + ^{76}Se scattering at 15.3 AMeV incident energy.

	E_{lab} (MeV)	E_{cm} (MeV)	η	θ_{cm}^{gr} (deg)	L^{gr} ($\hbar$)	V_C (MeV)	R_C (fm)
^{20}Ne + ^{76}Ge	306.0	242.25	12	11.0	129	42.8	10.0
^{18}O + ^{76}Se	275.4	222.34	11	10.2	118	36.5	10.0

The good agreement with the Rutherford cross-section and between the cross-sections obtained in independent measurements at different settings of the optical angle, is a clear proof that the systematic error components are small and under control. In any case, the normalization to Rutherford scattering minimizes the systematic errors in all the measured cross sections.

The representation of the elastic scattering cross-sections in terms of their ratio to the Rutherford one (σ/σ_{ruth}) in both the ^{18}O + ^{76}Se and ^{20}Ne + ^{76}Ge cases is shown in Figures 6.4 and 6.5. The σ/σ_{ruth} angular distributions are very similar in the two cases revealing a Fresnel-like scattering pattern, as expected for such heavy colliding nuclei. The Sommerfeld parameter η, the grazing angular momentum L^{gr} and angle θ_{cm}^{gr}, the Coulomb barrier strength V_C and radius R_C are defined in Ref. [158], reported in the footnote (*) for the reader convenience, and the numerical results are listed in Table 6.2. The values of such parameters are similar for the two systems. In this regime ($\eta > 10$), the Coulomb field dominates the scattering up to the grazing angle. Beyond θ_{cm}^{gr} the data are more sensitive to the nuclear component of the nucleus-nucleus potential, showing the typical fall-off associated to near-side and far-side scattering amplitudes.

Cross-section angular distributions for the 2^+ low-lying excited states of projectile and target and for the simultaneous excitation of both of them are shown in Figures 6.7 and 6.8 for the ^{18}O + ^{76}Se and ^{20}Ne + ^{76}Ge inelastic scattering, respectively.

*$\eta = Z_p Z_t e^2/\hbar\nu_{c.m.}$, where $\nu_{c.m.}$ is the relative velocity of colliding nuclei in the centre of mass (c.m.) system; L^{gr} is obtained from the $L(L+1) = 2\mu(E_{lab} - V_C)R_C^2/\hbar^2$ relation, where μ is the reduced mass of the colliding system and E_{lab} is the projectile incident energy in the laboratory reference frame; $\theta_{cm}^{gr} = 2\arcsin\left(\frac{V_C/\mu}{2E_{lab}/A_p - V_C/\mu}\right)$; $V_C = \frac{Z_p Z_t e^2}{R_C}$; $R_C = 1.44(A_t^{1/3} + A_p^{1/3})$.

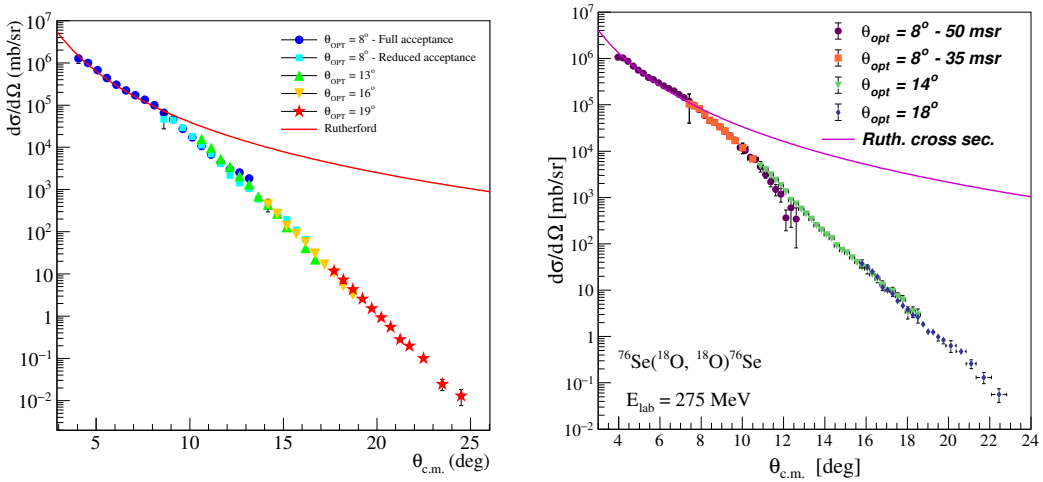

(a) ^{20}Ne + ^{76}Ge (b) ^{18}O + ^{76}Se

Figure 6.3: Angular distribution of differential cross section for ^{20}Ne + ^{76}Ge ((a) panel) and ^{18}O + ^{76}Se ((b) panel) elastic scattering at 15.3 MeV bombarding energy. Coloured points show data acquired in separate runs for different angular settings (see text). The red and purple lines represent the Rutherford cross-section. Figures from Ref. [50] and [51].

6.2.2 Theoretical analysis

The theoretical analysis calculations were performed using the FRESCO code [142]. The influence of the choice of different types of optical potentials was investigated comparing the calculations obtained in the OM elastic scattering differential cross sections. The inelastic cross sections was initially obtained from DWBA calculations. The effect and strength of the coupling are evaluated by comparing these elastic and inelastic cross sections with those obtained by the CC technique.

6.2.2.1 Choice of the Optical Potential

Following the same approach already presented in Sec. 5.2.1, the theoretical description of the elastic and inelastic scattering was performed using an optical potential:

$$U_{opt} = V(r) + iW(r) \tag{6.1}$$

where the absorptive-imaginary part accounts for all the effects on the elastic cross section due to the non explicit inclusion of states and reaction channels in the assumed reduced coupling scheme. The first theoretical approximation, known as one-channel approximation or OM, was assumed considering only the elastic channel in the coupling scheme. This was performed to clarify what are the effects of the choice of the OP used in the analysis of the two ^{76}Ge(^{20}Ne,^{20}Ne)^{76}Ge and the ^{76}Se(^{18}O,^{18}O)^{76}Se elastic and inelastic scatterings.

Two double folding optical potentials, `dfol` [149] and São Paulo Potential (SPP) [62, 136], were compared. In this approach, the heavy-ion nuclear potential depends on the nuclear densities of the colliding nuclei, since the real part of the potential is obtained by the folding of the nucleon-nucleon interaction $V_{NN}(\mathbf{r_1}, \mathbf{r_2}, E)$ with the ground state densities of the two involved nuclei $\rho_1(\mathbf{r_1})$ and $\rho_2(\mathbf{r_2})$:

$$V(r) = \int d\mathbf{r}_1 d\mathbf{r}_2 \rho_1(\mathbf{r}_1)\rho_2(\mathbf{r}_2)V_{NN}(\mathbf{r}_1, \mathbf{r}_2, E) \tag{6.2}$$

where r is the projectile-target distance and E is the energy per nucleon in the centre-of-mass reference frame. `dfol` is a double folding potential obtained by a Love-Franey-type T-matrix interaction, but extended to lower energies, as discussed in detail in Ref. [54]. In the case of the SPP, a finite-range folding-type effective nucleon-nucleon interaction, in the context of the non-local model, is adopted. This interaction is quite similar to

Table 6.3: Radius r and diffuseness a for the projectile and target nuclear matter densities adopted to construct the `dfol` and SPP double folding potentials used to analyse the ^{20}Ne + ^{76}Ge and ^{18}O + ^{76}Se elastic and inelastic scatterings.

Nucl. collision	Potential	Projectile		Target	
		r (fm)	a (fm)	r (fm)	a (fm)
^{20}Ne + ^{76}Ge	DFOL	2.85	0.48	4.74	0.48
	SPP	2.71	0.61	4.71	0.56
	DFOL(+5%)	2.99	0.48	4.97	0.48
	SPP (+5%)	2.85	0.61	4.94	0.56
^{18}O + ^{76}Se	DFOL	2.74	0.48	4.73	0.48
	SPP	2.59	0.61	4.71	0.56

the M3Y interaction [137, 138] in the surface region.

The densities $\rho_j(\mathbf{r_j})$ of projectile and target, adopted in the foldings of both SPP and `dfol`, are parametrized by two-parameter Fermi-Dirac matter distributions profiles assumed to be spherical. The adopted parameters (radius r and diffuseness a) for the two ^{20}Ne + ^{76}Ge and ^{18}O + ^{76}Se analysed systems are listed in Table 6.3 for both the `dfol` and SPP potentials. Standard parametrization of nuclear matter densities are taken from Refs. [149] and [62].

In the case of the ^{20}Ne + ^{76}Ge system, two different parametrizations were used to perform the reaction calculations. In addition to the standard set, a second one in which the radii of both ^{20}Ne and ^{76}Ge was increased by 5% with respect to the standard used parametrization. The central density parameter was renormalised in order to keep constant the volume integral of the nuclear densities and fix the correct number of nucleons. This second approach improves the agreement between the theoretical calculations and the experimental data in the grazing angle region, were the theoretical calculations depend much more on the geometrical properties of the colliding nuclei. The assumed slight increase in the radius parameter can be physically justified by the large g.s. quadrupole moments of both projectile and target nuclei as reported in Ref. [143]. Indeed, in such conditions, the hypothesis of *frozen* nuclear spherical matter densities in the reaction dynamic is too limiting and an effective way to take these arguments into account in the building of the optical potential is just a change of the density matter profiles.

In the case of the ^{18}O + ^{76}Se the standard parameter values for the nuclear matter densities were adopted, except for the ^{18}O diffuseness in the SPP case. From the study of quasi-elastic barrier distribution and direct nuclear reactions induced by ^{18}O on medium-mass targets with SPP, the authors of Refs. [42, 43, 46, 130, 131, 133, 135, 139–141, 159] concluded that an effective way to correctly describe the data is to increase the diffuseness of the density matter profiles of ^{18}O from the SPP standard value ($a = 0.56$ fm) to $0.60 - 0.62$ fm. The same assumption was adopted in the case of the ^{18}O + ^{12}C system analysed in the previous Chapter.

The imaginary part of the SPP was obtained from the real one by scaling its strength by a factor $N_W = 0.78$. This choice is the standard prescription for the SPP when calculations are performed in the DWBA [160] as confirmed by a large number of cases [42, 43, 46, 130, 131, 133, 135, 159]. For the DFOL potential, N_W was chosen in order to obtain a ratio of 0.78 between the volume integrals per nucleon of the imaginary and the real parts (J_W/J_V, see Eq. 6.3), in order to follow the same criterion also applied for SPP. The SPP includes a local-equivalent contribution, that is an energy dependence given by a strength coefficient that accounts for Pauli non locality. Both potentials assume the same nuclear densities in the folding of the real and imaginary parts. This choice is done in order to minimize the number of parameters and it was found to be successful in the description of a large set of heavy-ion elastic scattering data [7, 42, 43, 46, 130, 131, 133–135, 159].

A list of physical quantities associated to the performed calculations is given in Table 6.4. In particular, the volume integral per nucleon was calculated by the following formula:

$$J_i = \frac{\int_0^{+\infty} 4\pi r^2 V_i(r) dr}{A_p A_t} \tag{6.3}$$

in which A_p and A_t are the mass numbers of the projectile and the target, respectively, and $i = V$ or W for the real or imaginary potential, respectively.

The volume integrals of SPP and DFOL potentials, listed in Table 6.4, are close to the typical values [60]. The total reaction cross sections for the two OPs, σ_R are listed in the same table, together with the average radii calculated using the formula:

$$\langle R_i \rangle = \frac{\int 4\pi r^3 V_i(r) dr}{\int 4\pi r^2 V_i(r) dr} \tag{6.4}$$

The comparison between the σ/σ_{ruth} experimental angular distribution and the OM calculations, performed with the described optical potentials, are shown in Figures 6.4

(a) and 6.5 for the ^{18}O + ^{76}Se and ^{20}Ne + ^{76}Ge cases, respectively. The angular distributions are represented also in terms of the transferred momenta:

$$q = \frac{2\sqrt{2\mu c^2 E_{cm}}}{\hbar c} \sin(\theta_{cm}/2) \tag{6.5}$$

where μ is the reduced mass of the system.

For both the systems, the `dfol` and SPP calculations give a good description of the data at angles smaller than the grazing one ($\simeq 10°$). At larger transferred momenta the other reaction channels start to compete with elastic scattering, making channel couplings more relevant and getting worse the accuracy of OM analysis. The descriptions with the two optical potentials is almost analogous, although small differences can arise from the different systematics of mass-density used (see Table 6.3).

In the ^{20}Ne + ^{76}Ge case, the comparison between the standard results and the ones obtained increasing the matter density radius by +5% are shown in Figure 6.5 (zoomed view in the insets) by the solid blue and dot-dashed violet curves. The increase of radius appears important to correctly describe the experimental shape up to about 14°, where geometrical properties of nuclei are more relevant. However, the change of slope observed in the experimental data above 14° is still not described in the OM framework.

In the ^{18}O + ^{76}Se case, a fit with Woods-Saxon OP (WS-fit) was performed using the sFRESCO routine to describe the shape of the experimental data. The depth, radius and diffuseness of both real and imaginary parts of the optical potential were fitted in order to minimize the χ^2 of the resulting calculations shown in Figure 6.4 (a). The values of the parameters emerging from the fit procedure are: -11.2 MeV and -12.5 MeV for the depth, 0.74 fm and 0.93 fm for the diffuseness of the real and the imaginary part, respectively. The radii, the volume integral per nucleon and the total reaction cross section are listed in Table 6.4. Even if the description of the experimental data using this potential is very good, the obtained radii and the volume integrals per nucleon are far from the typical ones, such as those obtained from SPP and `dfol` OPs (see Table 6.4). Another fit was performed by fixing the values of the diffuseness to a standard value (0.644 fm) leaving the other parameters free, but also in this case the radii and the volume integrals per nucleon are not reliable.

6.2.2.2 Study of inelastic coupling contributions

The theoretical calculations for the ^{20}Ne + ^{76}Ge and the ^{18}O + ^{76}Se inelastic scattering were performed both in the DWBA and CC approaches using the `dfol` and SPP optical

Table 6.4: Mean radii $\langle R \rangle$ and volume integral per nucleon J for the real (V) and the imaginary (W) parts of the DFOL, SPP and WS-fit potentials. Coefficient N_W of the imaginary part of the potential and total reaction cross section σ_R in the case of the DWBA and the CC calculations for the different potentials.

						DWBA		CC	
Reaction	Potential	$\langle R_V \rangle$ (fm)	$\langle R_W \rangle$ (fm)	J_V (MeV fm^3)	J_W (MeV fm^3)	N_W	σ_R (mb)	N_W	σ_R (mb)
^{20}Ne + ^{76}Ge	DFOL	5.30	5.30	-438	-323	0.80	2819		
	SPP	5.32	5.32	-343	-257	0.78	2700		
^{18}O + ^{76}Se	DFOL	4.91	4.79	-437	-341	0.84	2801	0.65	2753
	SPP	5.02	5.02	-343	-268	0.78	2919	0.60	2836
	WS-fit	8.84	8.98	-19	-22		3327		

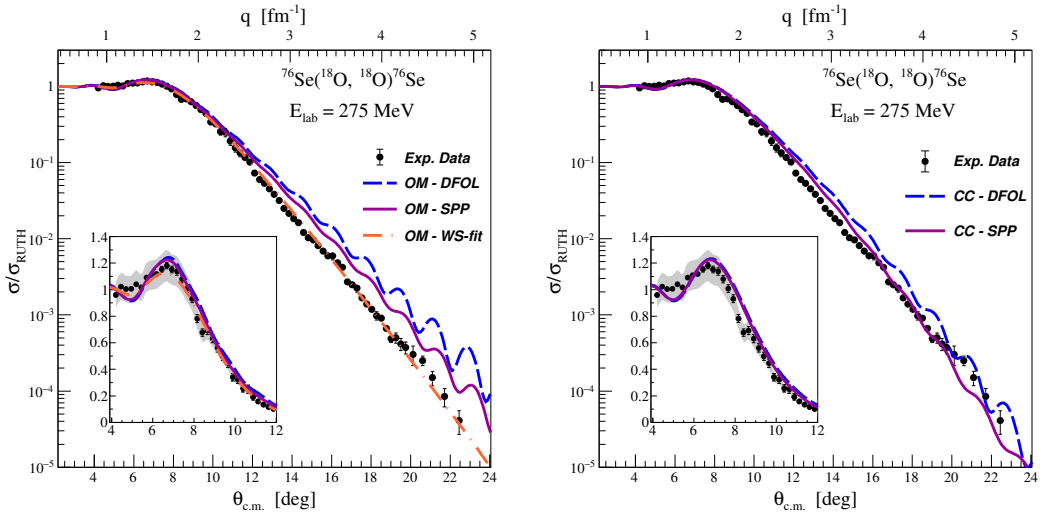

(a) Optical Model

(b) Coupled channels

Figure 6.4: Elastic scattering angular distribution in terms of the σ/σ_{ruth} ratio for the ^{18}O + ^{76}Se system at 15.3 AMeV. The (a) and (b) panels show the comparison between the experimental data and the reaction calculations obtained with the `dfol` and SPP double folding potentials in the OM and CC approaches, respectively. In both panels, the solid violet and the dashed blue curves represent the `dfol` and SPP calculations, respectively. The dot-dashed orange curve in panel (a) is the result of the Woods-Saxon fit (see text). In the insets a zoomed view of the grazing angle region in linear scale. The experimental data are shown together with a dark-grey band corresponding to the 10% uncertainty due to the charge collection and target thickness (see text).

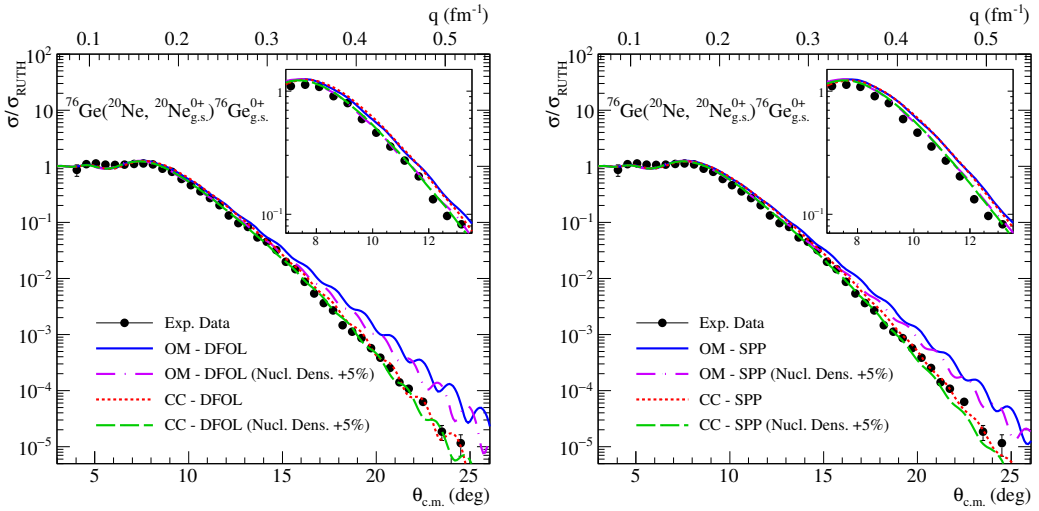

(a) `dfol` (b) SPP

Figure 6.5: Elastic scattering angular distribution in terms of the σ/σ_{ruth} ratio for the ^{20}Ne + ^{76}Ge system at 15.3 AMeV. The (a) and (b) panels show the results obtained in OM and CC approaches with the DFOL and SPP double folding potentials, respectively. In both panels, the solid blue and the dot-dashed violet curves represent the OM calculations with the standard potentials and by 5% the radius of the nuclear density distributions, respectively (see text). The red dotted and the green dashed curves are the results of the CC approach obtained with the standard and the modified potentials, respectively.

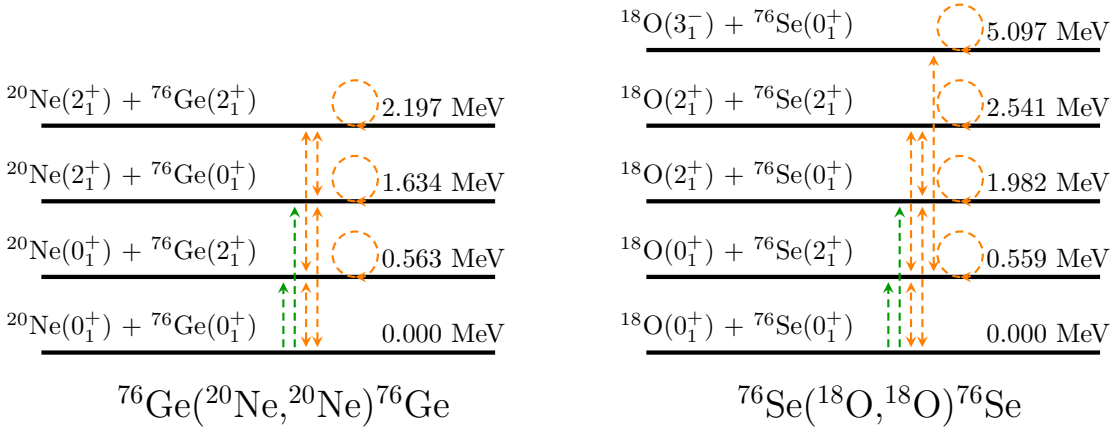

Figure 6.6: Coupling schemes the ^{76}Ge(^{20}Ne,^{20}Ne)^{76}Ge and the ^{76}Se(^{18}O,^{18}O)^{76}Se elastic and inelastic scattering adopted in the calculations. Couplings considered in the DWBA and CC calculations are indicated by the dashed green and orange arrows, respectively. Values on the right are the corresponding excitation energies.

potentials described in the previous section. The transition to the low-lying 2^+ states of the projectile and target and their combined excitation was analysed. This study also allows to evaluate the effects, due to the couplings with inelastic transitions, in the elastic scattering theoretical cross-section. The two most important aspects in this framework are related to the choice of a proper coupling scheme and to the definition of accurate coupling potentials.

The couplings to the inelastic channels were introduced through the usage of deformed *complex* coupling potentials [142]. Indeed, in Ref. [134] it was proven that, in similar transferred momenta conditions, the coupled channel calculations are compatible with the experimental data if the low-lying excited states of both target and projectile are explicitly included in the coupling scheme. Moreover, only when the deformations of the imaginary part of the nuclear OP are properly included in the coupling potentials, the description of the experimental data becomes satisfactory. The DWBA and CC coupling schemes adopted for the analysis described in the following are sketched in Figure 6.6. These include the first 2^+ excited states of projectile and target for both the ^{20}Ne + ^{76}Ge and the ^{18}O + ^{76}Se systems. In the case of the ^{18}O + ^{76}Se also the first 3^- state of the ^{18}O projectile at 5.097 MeV was also considered.

The reduced transition probabilities $B(E2)$ and $B(E3)$, listed in Table 6.5, were introduced to describe the Coulomb deformations of nuclei involved in the scattering. The nuclear coupling potentials $V_\lambda^i(r)$ for $\lambda = 2, 3$ were derived from Eq. 5.2. The radii

Table 6.5: Reduced transition probabilities $B(E\lambda;\uparrow)$ and deformation lengths δ_λ adopted in the elastic and inelastic scattering analysis of the ^{20}Ne + ^{76}Ge and the ^{18}O + ^{76}Se collisions.

Nuclei	λ	$B(E\lambda;\uparrow)$ (e^2b^λ)	δ_λ (fm)	Reference
^{18}O	2	0.0043	0.68	[143]
^{18}O	3	0.00125	0.73	[144]
^{20}Ne	2	0.0333	1.44	[143]
^{76}Ge	2	0.2735	1.29	[143]
^{76}Se	2	0.432	1.61	[143]

R_V of the two optical potentials are listed in Table 6.4. The inclusion of a deformed imaginary potential was shown to be a crucial aspect to obtain a good description of the experimental data in Refs. [134, 161]. For the imaginary coupling potentials, the same radial form factors are assumed, following the $\delta_2^{real} = \delta_2^{imag}$ convention. When the couplings are explicitly included in the CC calculations, N_W is typically reduced to 0.6 for the SPP [114, 133, 134, 136, 159, 162] and thus the same was done also for the `dfol`. The N_W coefficients adopted in the CC calculations are listed in Table 6.4.

The theoretical results are compared to the inelastic cross-section experimental angular distributions for the transitions to the first 2^+ excited states of either the projectile or target, or the mutual combination of them in Figures 6.7 and 6.8 for the ^{18}O + ^{76}Se and the ^{20}Ne + ^{76}Ge collisions, respectively. For the transition to the first 2^+ state, the agreement between theoretical and experimental first low-lying excited states results is satisfactory in both the studied systems. The similarity between the CC and DWBA calculations proves that the channel coupling does not influence much the angular distributions and the main effect is an attenuation of the oscillatory pattern, consistent with the experimental behaviour. In the case of the combined $2^+ \oplus 2^+$ transition in the projectiles and targets, the agreement between the experimental data and the CC results is good in the case of the ^{20}Ne + ^{76}Ge and not enough satisfactory in the ^{18}O + ^{76}Se case. A possible reason is that in the 2.5 MeV excitation energy region there are many excited states of the ^{76}Se nucleus, which are not experimentally resolved. The contributions of such states, which were not calculated, could be not negligible at small angles, where the agreement with the data seems to be worst.

In Figures 6.4 (b) and 6.5 the CC theoretical results for the two OPs are compared with the elastic scattering experimental data for the ^{18}O + ^{76}Se and the ^{20}Ne + ^{76}Ge collisions, respectively. In the case of the ^{20}Ne + ^{76}Ge elastic scattering, the inclusion of couplings with the first low-lying excited states of projectile and target starts to be important above about 15° where the absolute cross sections for the elastic and the inelastic scattering channels become comparable. The inclusion of couplings improves the agreement between experimental and theoretical angular distributions with both the `dfol` and the SPP optical potentials.

The small differences between OM and CC calculations in the Coulomb-nuclear interference region are within the already discussed 10% sensitivity (see Figure 6.4). The data beyond the grazing angle ($\sim 10°$) show a steeper slope than in the OM calculations. The couplings with the low-lying excited states start to be important in the description of the elastic scattering beyond about 12°, corresponding to almost 2.5 fm^{-1}, where the cross sections for the elastic and inelastic scattering channels become comparable. The couplings with the excited states produce sizeable effects in this region and allow a very good description of the data. Regarding the ^{18}O + ^{76}Se elastic scattering, in the insets of Figure 6.4, a zoomed view of the Coulomb-nuclear interference region is shown in linear scale to better determine the sensitivity to the potential [163, 164].

In both systems, it was found that at large transferred momenta the effect of couplings with first low-lying excited states is crucial to correctly describe the differential cross sections. To determine the inelastic flux and its effect on the elastic channel, DWBA and CC calculations were performed. The first collective states of the colliding nuclei were included. Inclusion of only the first 2^+ of the projectile and target and the first 3^- of the ^{18}O collective low-lying excited states turned out to be enough to well describe almost all the angular distributions over the full range of transferred momenta explored.

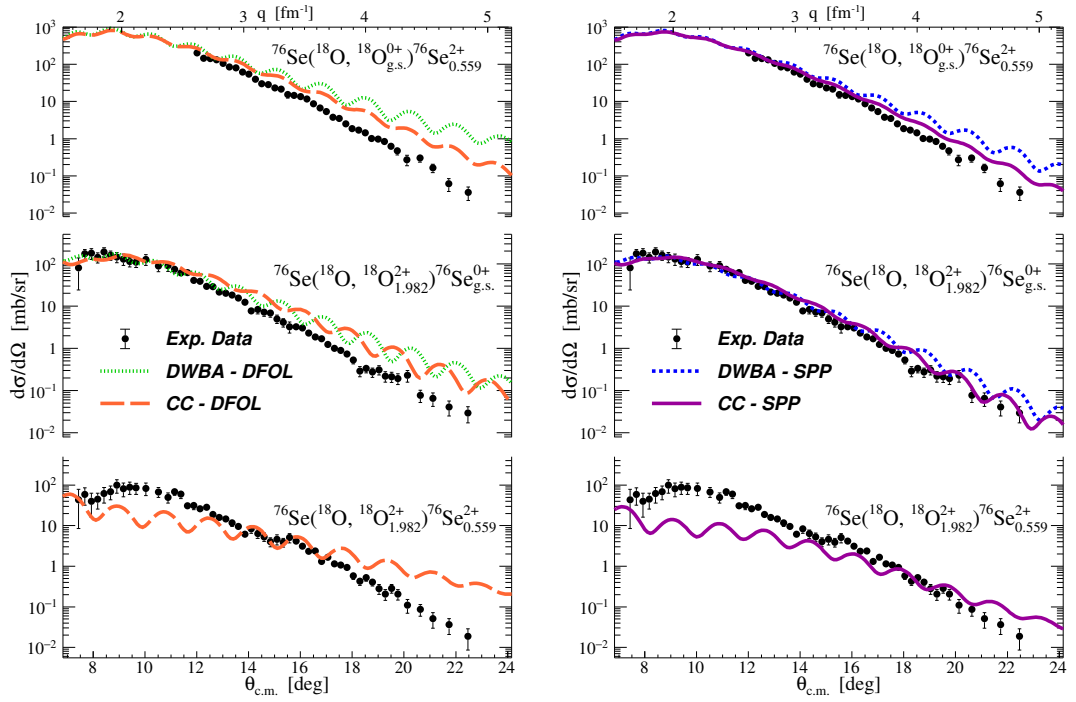

(a) DFOL Potential (b) SPP Potential

Figure 6.7: Angular distribution of differential cross section for the low-lying states of projectile and target populated in the ^{18}O + ^{76}Se inelastic scattering at 15.3 AMeV bombarding energy. (a) `dfol` potential (b) SPP potential. In the top, the 2^+ state of ^{76}Se at 0.559 MeV; in the middle, the 2^+ state of the ^{18}O at 1.982 MeV; in the bottom, the 2.541 MeV state that corresponds to the excitation of both projectile and target $2^+ \oplus 2^+$. The lines are obtained from reaction calculations in the DWBA and CC approaches as described in the therein legend. Figure from Ref. [51]

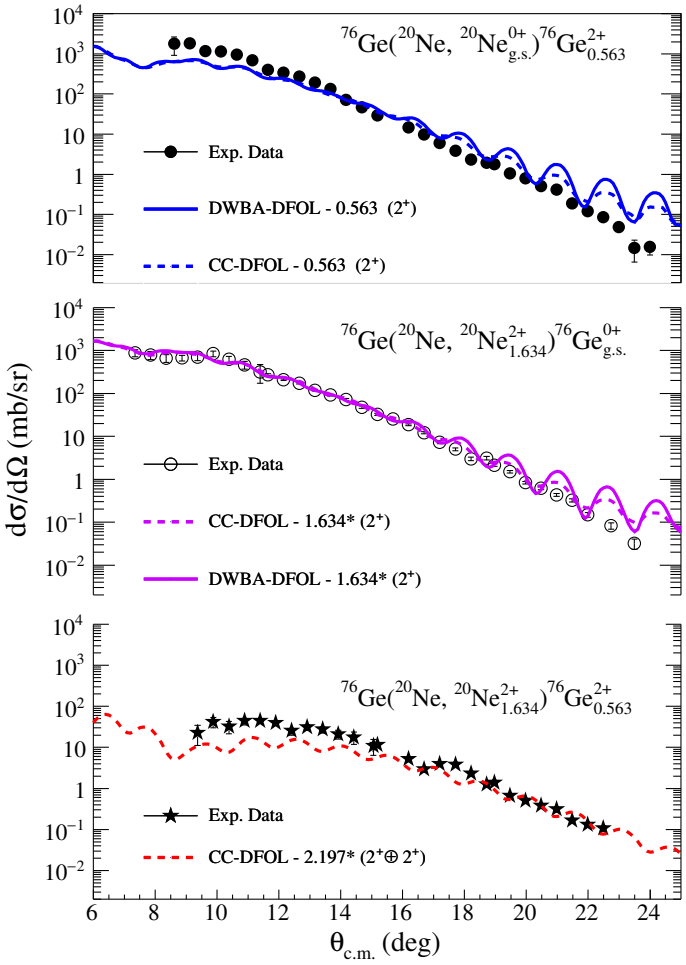

Figure 6.8: Angular distribution of differential cross section for the low-lying states of projectile and target populated in the ^{20}Ne + ^{76}Ge inelastic scattering at 15.3 AMeV bombarding energy: in the top, the 2^+ state of ^{76}Ge at 0.563 MeV; in the middle, the 2^+ state of the ^{20}Ne at 1.634 MeV; in the bottom, the 2.197 MeV state that corresponds to the excitation of both projectile and target $2^+ \oplus 2^+$. Solid lines are obtained in DWBA approach; dashed lines are CC calculations.

6.3 Single-charge exchange spectrum of ^{76}As from (^{18}O,^{18}F) and (^{20}Ne,^{20}F) nuclear reactions

Single charge exchange reactions are the best probe to explore the isospin and spin-isospin nuclear response to the strong interaction. In this section, the population of the ^{76}As nucleus using the (^{20}Ne,^{20}F) and the (^{18}O,^{18}F) SCE reactions at 15.3 AMeV incident energy is described. Two independent measurements were performed at INFN-LNS using the beams provided by the K800 Superconducting Cyclotron and the MAGNEX spectrometer. The experimental set-up and the data reduction have been already described and the same were used to study the ^{18}O + ^{12}C network of nuclear reactions described in the previous Chapter. The experimental set-up details of the ^{76}Ge(^{20}Ne,^{20}F)^{76}As and the ^{76}Se(^{18}O,^{18}F)^{76}As reaction measurements are summarized in Table 6.1.

The ^{76}As excitation energy (E_x) spectra extracted up to E_x = 10 MeV from the ^{76}Se(^{18}O,^{18}F)^{76}As and ^{76}Ge(^{20}Ne,^{20}F)^{76}As SCE measurements, performed in the angular region $4° < \theta_{lab} < 11.5°$, are shown in Figure 6.9 and 6.10, respectively. The error bars reported in Figure 6.9 and 6.10 include the statistical contribution and the uncertainties coming from the determination of the solid angle intervals. The overall uncertainty of about 10%, due to the determination of the charge collection and target thickness, is common to all the data points and, for such reason, is not explicitly included in the error bars.

The ^{76}As spectrum measured in the ^{76}Se(^{18}O,^{18}F)^{76}As reaction (Q_0 = -4.618 MeV) is expected to be contaminated by the events coming from the ^{12}C(^{18}O,^{18}F)^{12}B reaction (Q_0 = -15.024 MeV) due to the presence of Carbon in the target backing. Analogously, the ^{76}As spectrum measured in the ^{76}Ge(^{20}Ne,^{20}F)^{76}As reaction (Q_0 = -7.948 MeV) is expected to be contaminated by the events coming from the ^{12}C(^{20}Ne,^{20}F)^{12}N reaction (Q_0 = -24.363 MeV) due to the presence of Carbon in the target backing and in the post-stripper foil. Due to the different kinematics, such contributions are expected to appear at E_x = 10.406 MeV and 16.415 MeV (at 0° scattering angle) of the ^{76}Se(^{18}O,^{18}F)^{76}As and ^{76}Ge(^{20}Ne,^{20}F)^{76}As nuclear reactions, respectively. Carbon contaminations are therefore expected to be above the low-lying excited states region of interest for the present analysis and, in any case, above the excitation energy shown in Figures 6.9 and 6.10.

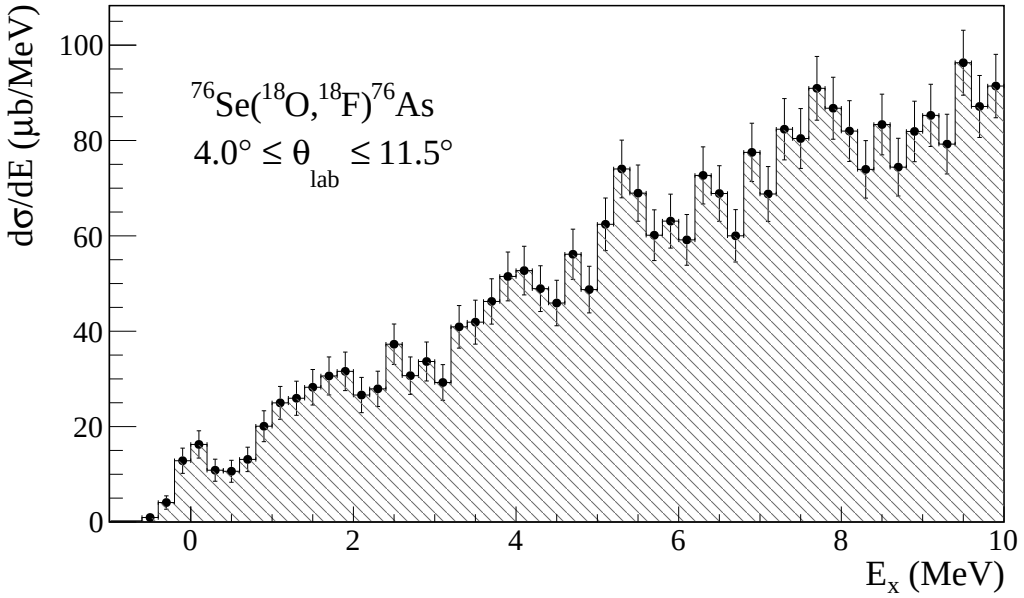

Figure 6.9: Excitation energy spectrum of the ^{76}Se(^{18}O,^{18}F)^{76}As SCE reaction at 15.3 AMeV incident energy and $4° < \theta_{lab} < 11.5°$.

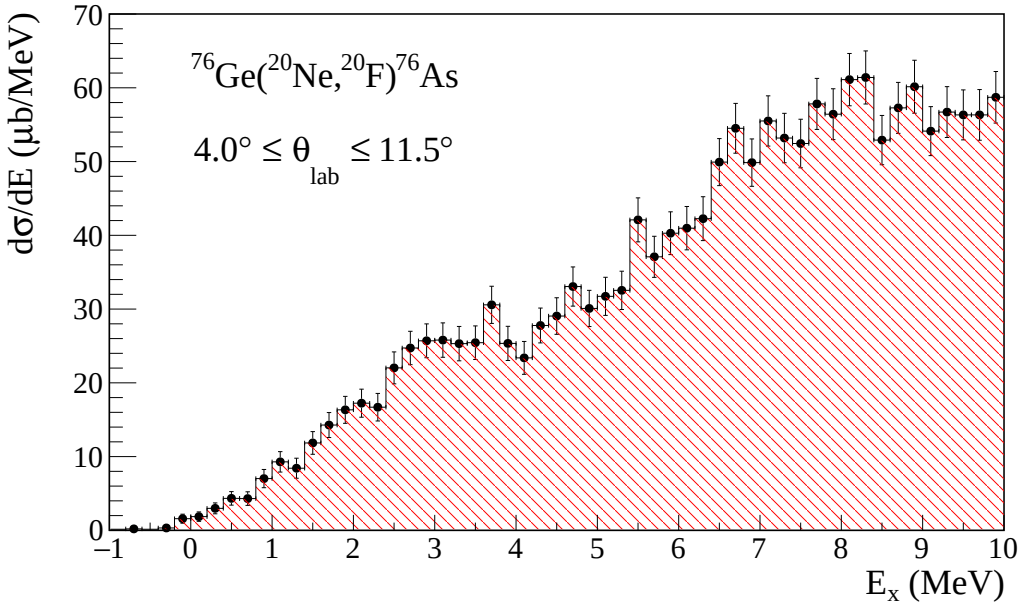

Figure 6.10: Excitation energy spectrum of the ^{76}Ge(^{20}Ne,^{20}F)^{76}As SCE reaction at 15.3 AMeV incident energy and $4° < \theta_{lab} < 11.5°$.

6.3.1 The ^{76}Se(^{18}O,^{18}F)^{76}As SCE reaction

The ^{76}Se(^{18}O,^{18}F)^{76}As spectrum in Figure 6.9 appears to be very different from the one of the ^{12}C(^{18}O,^{18}F)^{12}B SCE reaction discussed in the previous Chapter (see Figure 5.11). The difference between the ^{76}As and the ^{12}B spectra populated through the (^{18}O,^{18}F) SCE reaction are mainly due to very different level density characterizing the residual nuclei. The ^{76}As is an odd-odd medium-mass nucleus and, as a consequence of the huge number of single particle configurations available for this mid-shell nucleus, about 27 states (see Ref. [157]) are expected, for example, within 500 keV of excitation energy. The ^{76}As excitation energy (E_x) spectrum extracted from the ^{76}Se(^{18}O,^{18}F)^{76}As is characterized by a structure in the ground-state region with a width of $\approx$ 500 keV in FWHM, compatible with the achieved energy resolution, so that we can suppose that the mentioned peak corresponds to the transition toward a single or a limited number of states of the residual nucleus.

A similar spectrum was observed in the case of the ^{76}Se(d,^{2}He)^{76}As SCE reaction described in Ref. [72] where the (d,^{2}He) charge-exchange reaction on ^{76}Se was studied at an incident energy of 183 MeV. The experiment was performed at Kernfysisch Versneller Instituut (KVI), Groningen, using the Big-bite magnetic spectrometer at three angular positions (0°, 2.5° and 5°). The $E_x$spectra of the residual nucleus ^{76}As were obtained with an energy resolution of about 120 keV (FWHM) as shown in the top panel of Figure 6.12. The measured excitation-energy spectrum is dominated by five strong transitions below 3 MeV while above 3 MeV no isolated level could be identified. These peaks are located at 0.04, 1.03, 1.63, 1.86 and 2.22 MeV and share a substantial fraction of the total GT strength.

Although the (^{18}O,^{18}F) and (d,^{2}He) appear to be compatible in the first MeVs of ^{76}As excitation energy spectrum, the differences in terms of incident beam energy and explored angular range are important and need to be properly taken into account when the two spectra are compared. In the case of (^{18}O,^{18}F) measurement, performed at $4° < \theta_{lab} < 11.5°$ and 15.3 AMeV incident energy, the $L > 0$ multipolarities are expected to largely contribute or even to dominate the spectrum with respect to the (d,^{2}He) zero degrees measurement mainly characterized by the L = 0 strength. Furthermore, in heavy-ion case, the charge-exchange transition occurring in the target-residual nuclei also occurs in opposite direction in the projectile-ejectile nuclei. This implies a further fragmentation of the many ^{76}As structures, already present in the light-ion induced SCE spectrum, due to the populated (bound) states of the ^{18}F ejectile.

6.3.2 The ^{76}Ge(^{20}Ne,^{20}F)^{76}As SCE reaction

The ^{76}As excitation energy (E_x) spectrum extracted from the ^{76}Ge(^{20}Ne,^{20}F)^{76}As SCE measurement appears (see Figure 6.10) to be practically structureless. The very high-level density and the limited energy resolution do not allow to isolate transitions to individual states.

Measurements of the same transition occurring in the target was performed using the ^{76}Ge(^{3}H,t)^{76}As[155] and the ^{76}Ge(p,n)^{76}As [165] SCE reactions at very forward angles and at incident energies of 420 MeV and 134.4 MeV, with an energy resolutions of 30 keV and 338 keV, respectively. The ^{76}Ge(^{3}H,t)^{76}As single-charge exchange reaction was performed at the Research Center of Nuclear Physics (RCNP), Osaka University using a 420 MeV ^{3}He^{++} beam accelerated by the Azimuthally Varying Field Cyclotron in combination with the Ring Cyclotron and transported to the scattering chamber of the Grand Raiden Spectrometer. The beam line provided the necessary beam dispersion thanks to the several tuning techniques employed to guarantee the dispersion matching between beam-line and spectrometer and to optimize the energy and angular resolutions [68, 69]. The high-resolution measured spectra (see bottom panel in Figure 6.12) show an extraordinary large number of peaks and above $E_x \approx 2$ MeV the level density increases rapidly. The strongly excited $S = 0$, T = 1, L = 0 isobaric-analog state (IAS) of ^{76}Ge dominates the spectrum at $E_x = 8.308$ MeV with a shoulder from the IAS of ^{74}Ge ground state at $E_x = 8.360$ MeV (also present in the target material). Around $E_x = 11$ MeV the broad Gamow-Teller resonance is present and at about 18.5 MeV the rather broad ($\approx$ 10 MeV) spin-dipole resonance is also present. The spectra are qualitatively similar to the ones in the (p,n) measurement although those were generated at a much reduced resolution.

The spectrum measured in the case of the ^{76}Ge(^{20}Ne,^{20}F)^{76}As single charge exchange reaction is very different from the light-ions induced ones. It is in fact structureless and the huge ^{76}Ge IAS is completely missed in the heavy-ion case. One reason can be related to the fact that the L = 0 transition toward the ^{76}Ge IAS is strongly peaked at $\theta_{lab} = 0°$ and rapidly decreases as the scattering angle increases. Our (^{20}Ne,^{20}F) measurement was performed at $4° < \theta_{lab} < 11.5°$ where the $L > 0$ are expected to dominate. Furthermore, in the heavy-ion case, the same charge-exchange transition also occurs in the projectile-ejectile nuclei. This implies the fragmentation of the IAS strength in many different states of the ^{20}F ejectile and consequently the missing of the IAS peak. The same arguments can be also applied to large number of $J^{\pi} = 1^{+}$

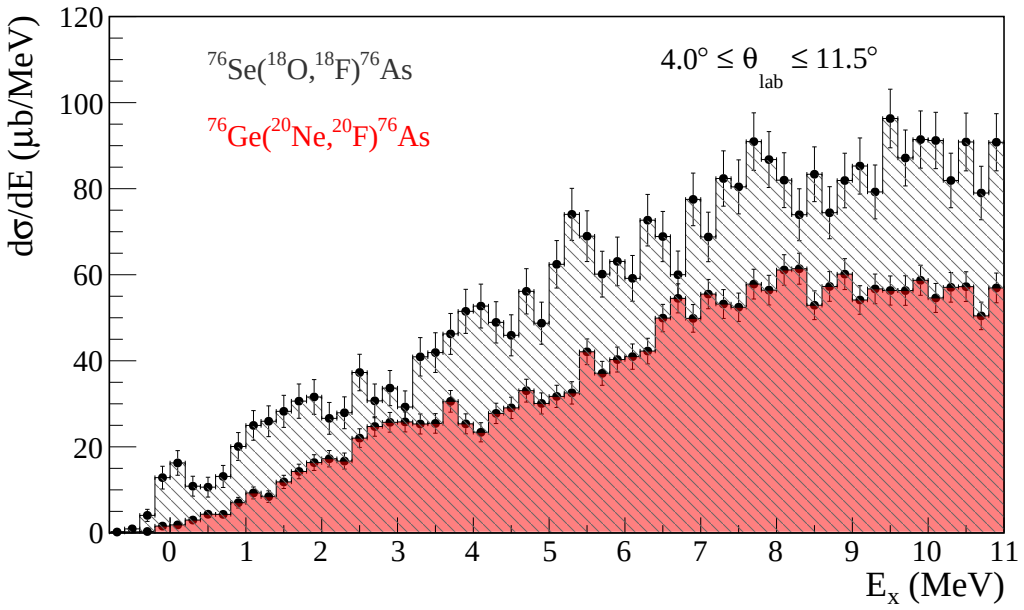

Figure 6.11: Superposition of the ^{76}As excitation energy spectra obtained from the ^{76}Se(^{18}O,^{18}F)^{76}As (black hatched) and ^{76}Ge(^{20}Ne,^{20}F)^{76}As (red filled) single charge-exchange nuclear reactions at 15.3 AMeV incident energy and $4° < \theta_{lab} < 11.5°$.

states in the first few MeVs of the spectrum in Ref. [155], completely drowned in the continuum of unresolved states.

6.3.3 Comparison of the ^{76}As SCE spectra

The measured energy spectra in the ^{76}Se(^{18}O,^{18}F)^{76}A and the ^{76}Ge(^{20}Ne,^{20}F)^{76}As SCE nuclear reactions are superimposed in Figure 6.11. The ^{76}Ge(^{20}Ne,^{20}F)^{76}As spectrum, in red, is flatter than the ^{76}Se(^{18}O,^{18}F)^{76}A one. The cross-sections measured in the ^{76}Se(^{18}O,^{18}F)^{76}As and the ^{76}Ge(^{20}Ne,^{20}F)^{76}As SCE nuclear reactions were integrated in the full angular range ($4° < \theta_{lab} < 11.5°$) and in the excitation energy ranges 0 MeV $< E_x <$ 3 MeV, 0 MeV $< E_x <$ 5 MeV and 0 MeV $< E_x <$ 10 MeV in order to perform a quantitative comparison between the two SCE reactions. The obtained values are reported in Table 6.6.

A similar comparison of the ^{76}As spectra populated in the ^{76}Se(d,^{2}He)^{76}As and the ^{76}Ge(^{3}He,t)^{76}As was also performed by the authors of Ref. [155]. The comparison between the two measured spectra, shown in Figure 6.12, suggests a remarkable lack

Table 6.6: Cross-sections integrated in the full angular range $4° < \theta_{lab} < 11.5°$ and in three different excitation energy ranges measured in the ^{76}Se(^{18}O,^{18}F)^{76}As and ^{76}Ge(^{20}Ne,^{20}F)^{76}As single-charge exchange reactions at 15.3 AMeV incident energy. Their ratio is also reported.

Energy range (MeV)	^{76}Se(^{18}O,^{18}F)^{76}As (μb)	^{76}Ge(^{20}Ne,^{20}F)^{76}As (μb)	Ratio
$[0-3]$	77 ± 2	37 ± 1	2.08
$[0-5]$	170 ± 3	93 ± 2	1.83
$[0-10]$	552 ± 6	347 ± 4	1.59

of correlation already noticed by the authors of Ref. [72] comparing their results with the (p,n) data [165]. While from the ^{76}Se $\rightarrow$ ^{76}As side the GT strength is almost concentrated in few states, from the ^{76}Ge $\rightarrow$ ^{76}As one it is fragmented in large number of different states. Furthermore, strong transitions from one direction do not seems to have a strong partner from the other direction and vice-versa. The same was also observed in the $A = 48$ case [166].

The same lack of correlation may be deduced also in the case of the ^{76}As spectra populated in the (^{18}O,^{18}F) and (^{20}Ne,^{20}F) SCE reactions. The ^{76}Se(^{18}O,^{18}F)^{76}As is more structured than the ^{76}Ge(^{20}Ne,^{20}F)^{76}As one suggesting the possible dominance of only few states in the former case with respect to the latter. Once available, theoretical calculations, constrained by the new experimental data, will help to verify such hypothesis.

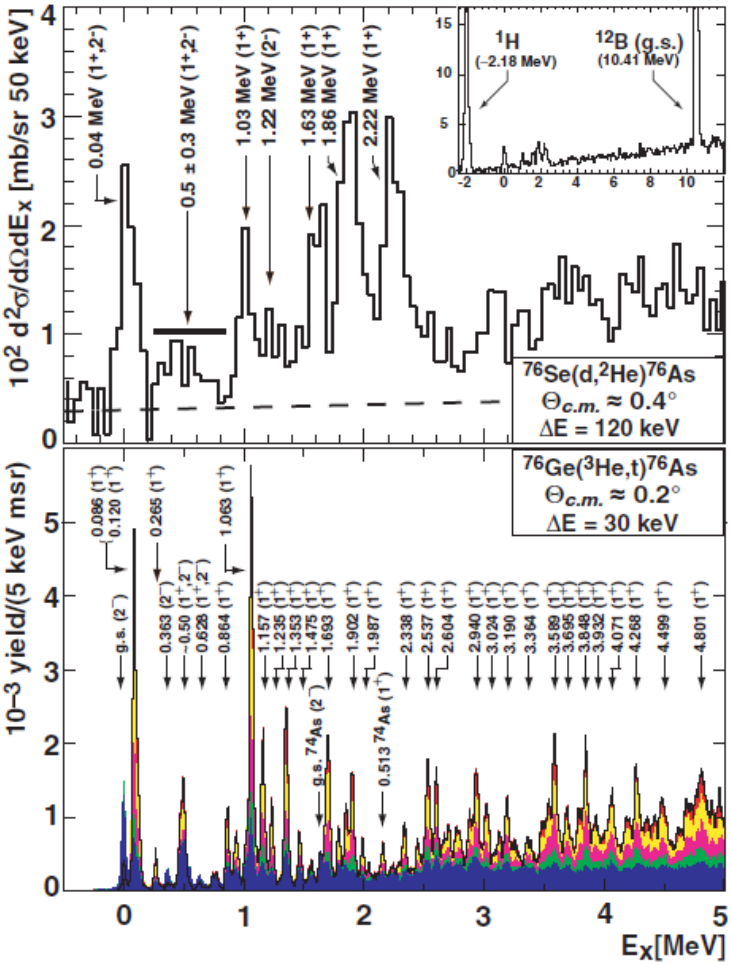

Figure 6.12: Comparison of the ^{76}Se(d,^{2}He)^{76}As spectrum (from Ref. [72]) with the one from the ^{76}Ge(^{3}He,t)^{76}As reaction. Top panel: ^{76}Se(d,^{2}He)^{76}As spectrum indicates the level of instrumental background. The inset shows the excitation spectrum up to 12 MeV and the ^{12}C(d,^{2}He)^{76}B (g.s.) reaction from the carbon backing of the target. The hydrogen line is an ever present background line in metallic targets. Bottom panel: The spectra were generated from different angle cuts (as indicated by the colors) and stacked on top of each other to indicate the effect of the angular dependence. Transitions with $\Delta L = 0$ are forward peaked and appear in red at the most forward angle. The various states with their spin assignments are indicated. Figure from Ref. [155]

6.4 Study of the ^{76}Ge $\leftrightarrow$ ^{76}Se transition via double-charge exchange reaction measurements

Double charge exchange reactions are the best tools to explore the response of nuclei to the double-isospin component of nuclear interaction. In this section the experimental results obtained in the study of the ^{76}Ge(^{20}Ne,^{20}O)^{76}Se and the ^{76}Se(^{18}O,^{18}Ne)^{76}Ge DCE reactions at 15.3 AMeV incident energy are described. Two independent measurements were performed at the INFN-LNS using the beams provided by the K800 Superconducting Cyclotron and the MAGNEX spectrometer. The experimental set-up and the data reduction have been already described in this volume. The experimental details are summarized in Table 6.1.

The ^{76}Ge and the ^{76}Se excitation energy were measured for the ^{76}Se(^{18}O,^{18}Ne)^{76}Se and ^{76}Ge(^{20}Ne,^{20}O)^{76}Se DCE reactions at forward angles including zero-degrees ($0° < \theta_{lab} < 8°$) shown in Figures 6.13 and 6.14, respectively, up to $E_x = 30$ MeV. Both counts and energy differential cross-section are indicated in the two vertical scales. The error bars reported in the Figures include the statistical contribution and the uncertainties coming from the determination of the solid angle intervals. The overall uncertainty of about 10%, due to the determination of the charge collection and target thickness, is common to all the data points and, for such reason, is not explicitly included in the error bars.

The ^{76}Ge spectrum measured in the ^{76}Se(^{18}O,^{18}Ne)^{76}Ge reaction (Q_0 = -8.138 MeV) is expected to be contaminated by the events coming from the ^{12}C(^{18}O,^{18}Ne)^{12}Be reaction (Q_0 = -31.175 MeV) due to the presence of Carbon in the target backing. Analogously, the ^{76}Se spectrum measured in the ^{76}Ge(^{20}Ne,^{20}O)^{76}Se reaction (Q_0 = -8.800 MeV) is expected to be contaminated by the events coming from the ^{12}C(^{20}Ne,^{20}O)^{12}O reaction (Q_0 = -42.887 MeV) due to the presence of Carbon in the target backing and in the post-stripper foil. Such contributions are expected to appear at E_x = 23.037 MeV in the ^{76}Ge spectrum of Figure 6.13 (as therein indicated) and at 33.2 MeV in the ^{76}Se spectrum of Figure 6.14. In the second case, Carbon contaminations are expected above the excitation energy regime in which the measurement was performed, as shown in Figure 6.14.

The DCE ^{76}Ge and ^{76}Se measured spectra show similar features. Most of the strength is concentrated at high excitation energy where the spectra are dominated by the break-up continuum components. The nucleon separation energies S_p and S_n and the α-emission Q-value (Q_α) are reported in Table 6.7 for each of the ejectiles and residual

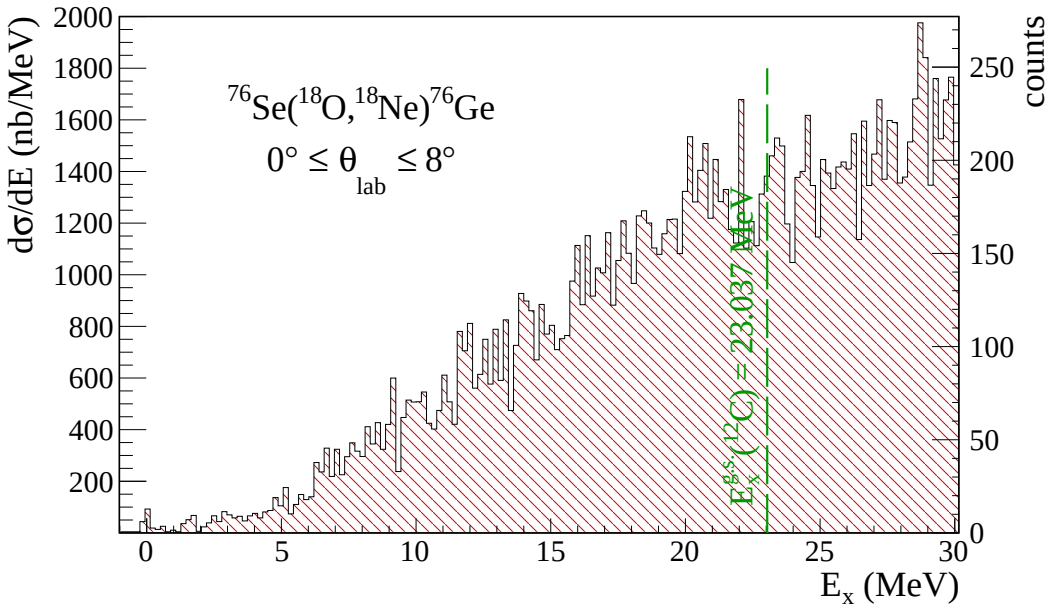

Figure 6.13: ^{76}Ge excitation energy spectrum obtained from the ^{76}Se(^{18}O,^{18}Ne)^{76}Ge double charge-exchange nuclear reactions at 15.3 AMeV incident energy and $0° < \theta_{lab} < 8°$.

nuclei involved in the DCE measurements. Despite the dominant and structureless behaviour in the continuum region, the ground states and the first excited bound states are clearly visible in the zoomed views of the DCE ^{76}Ge and ^{76}Se spectra shown in Figures 6.15 and 6.16, respectively. A detailed analysis of the structures observed in both spectra is discussed in the following paragraphs.

6.4.1 The ^{76}Se(^{18}O,^{18}Ne)^{76}Ge DCE reaction

The energy resolution δE_x(FWHM) achieved in the ^{76}Se(^{18}O,^{18}Ne)^{76}Ge DCE measurement is $\approx$ 0.3 MeV. This value should be compared to δE_{TARGET} representing the upper physical limit and coming from the projectile/ejectile-target interaction (see Section 3.2.1.1). The δE_{TARGET} contribution to the overall energy resolution can be estimated considering the differences in the kinetic energies of the ejectiles emerging from the target when the reaction occurs at the beginning or at the end of it. In the case of the ^{76}Se(^{18}O,^{18}Ne)^{76}Ge reaction, the obtained value is $\delta E_{TARGET} = 0.2$ MeV. This represents the upper limit for the achievable energy resolution. In the DCE reaction channel, such as in the two-proton transfer, this effect is more enhanced being larger

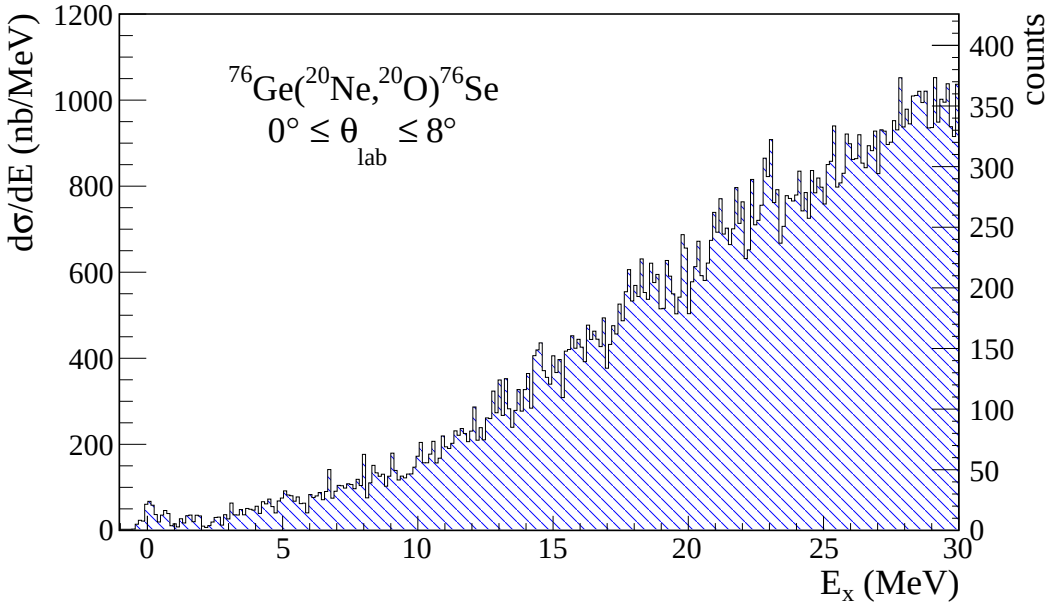

Figure 6.14: ^{76}Se excitation energy spectrum obtained from the ^{76}Ge(^{20}Ne,^{20}O)^{76}Se double charge-exchange nuclear reactions at 15.3 AMeV incident energy and $0° < \theta_{lab} < 8°$.

Table 6.7: Neutron and proton separation energies and α-emission Q-value for the ejectiles and residual nuclei of the studied double-charge exchange reactions. Values are from Refs. [110, 157, 167]

Nucleus	S_n (MeV)	S_p (MeV)	Q_α (MeV)
^{18}Ne	19.254	3.923	-5.114
^{20}O	7.608	19.348	-12.323
^{76}Ge	9.427	12.037	-7.492
^{76}Se	11.153	9.507	-5.090

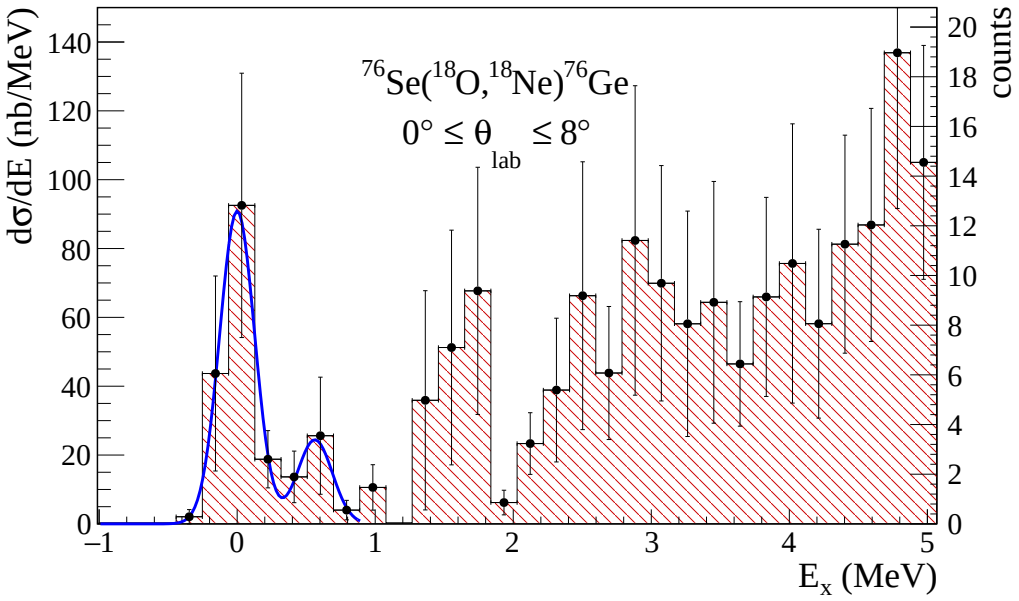

Figure 6.15: ^{76}Ge excitation energy spectrum obtained from the ^{76}Se(^{18}O,^{18}Ne)^{76}Ge double charge-exchange nuclear reactions at 15.3 AMeV incident energy and $0° < \theta_{lab} < 8°$.

increasing the atomic number difference between the beam and the ejectile ions. The achieved $\delta E_x \approx 0.3$ MeV demonstrates that the effect of the δE_{CS} and δE_{MAGNEX} on the overall resolution is small and minimized thanks to the accurate tuning of the experimental set-up and the advanced data-reduction.

The δE_x is enough to clearly separate the 0^+ ground state from the first 2^+ excited state of ^{76}Ge at 0.563 MeV. The energy resolution was evaluated from the FWHM of the Gauss function (see Figure 6.15) used to fit the ground-state peak. A third structure, at ≈ 1.5 MeV, is due to the superposition of the 4^+ and (3^+) ^{76}Ge states at 1.410 MeV and 1.539 MeV, respectively, and to the first 2^+ excited state of the ^{18}Ne at 1.887 MeV. Above $E_x \approx 2$ MeV, the ^{76}Se density of states starts to increase and no peak is clearly visible in the spectrum.

In the experimental run, about 350 hours long with a beam current of 1.8 nA, the total number of incident beam ions was $\approx 1.3{\cdot}10^{15}$. Despite that, a limited yield was collected in the ground-state region, which we are interested in. Only 21 counts compete to the 0^+ ground-state and only 9 to the first 2^+ excited state. In such conditions no accurate angular distribution can be extracted for the identified peaks.

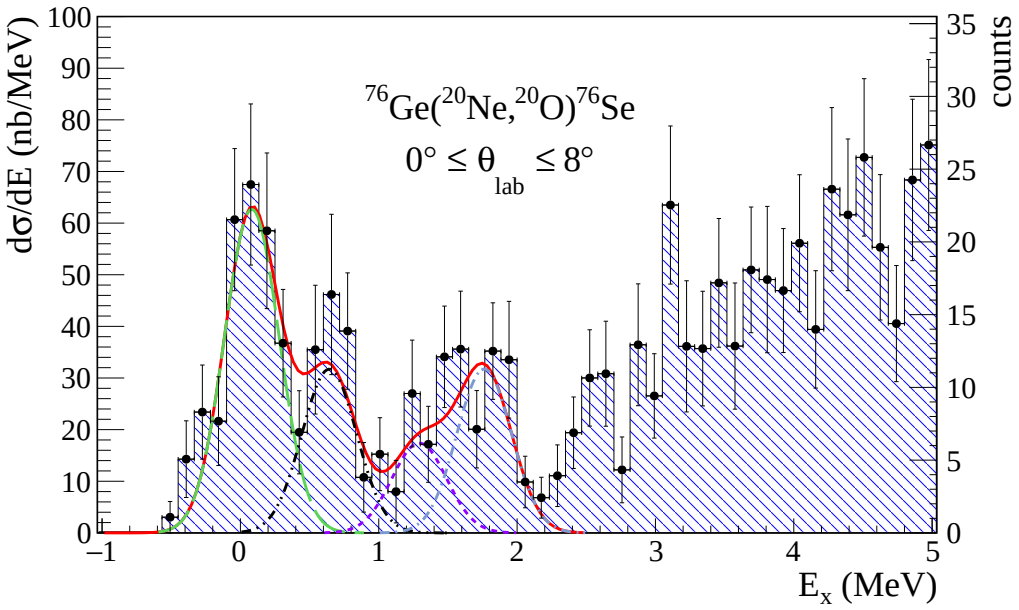

Figure 6.16: ^{76}Se excitation energy spectrum obtained from the ^{76}Ge(^{20}Ne,^{20}O)^{76}Se double charge-exchange nuclear reactions at 15.3 AMeV incident energy and $0° < \theta_{lab} < 8°$.

6.4.2 The ^{76}Ge(^{20}Ne,^{20}O)^{76}Se DCE reaction

The energy resolution was evaluated from the FWHM ground-state peak Gaussian fit shown in Figure 6.16. In the case of the ^{76}Ge(^{20}Ne,^{20}O)^{76}Se DCE reaction the achieved energy resolution was δE_x(FWHM) $\approx$ 0.4 MeV, evaluated from the FWHM of the Gauss function used to fit the ground-state peak shown in Figure 6.16. The high resolution achieved is very close to the best achievable one, determined by the inevitable effect due to the projectile/ejectile-target interaction ($\delta E_{TARGET} \approx 0.25$ MeV). This energy resolution was enough to separate the 0^+ ground state from the first excited 2^+ state of ^{76}Se at 0.559 MeV. A third structure is made of two different peaks. The first one at $\approx$ 1.25 MeV is due to the superposition of the 0^+, 2^+ and 4^+ states of ^{76}Se at 1.122, 1.216 and 1.331 MeV, respectively; the second one at $\approx$ 1.8 MeV is due to the sum of the 3^+ and 2^+ states of ^{76}Se at 1.689 MeV and 1.789 MeV, respectively but more likely it may be dominated by the 2^+ first excited state of ^{20}O at 1.673 MeV. Similarly as in the DCE ^{76}Ge spectrum, above $\approx$ 2 MeV the ^{76}Se density of states starts to increase and no structure is clearly visible in the spectrum.

In the measurement, about 100 hours long with a beam current of 7.0 nA, the total

number of incident beam ions was $1.7{\cdot}10^{15}$. Only 117 counts compete to the 0^+ ground state and, in such conditions, the possibility to extract a statistically significant angular distribution for the ground-to-ground state transition is a demanding task.

6.4.3 Comparison of the ^{76}Ge and ^{76}Se DCE spectra

The experimental results obtained from the DCE nuclear reaction measurements are particularly relevant and advanced, especially for the achieved energy resolution allowing to separate the ground-to-ground state transition from the one toward the first 2^+ excited state of the involved residual nuclei. The measured cross-sections integrated in the full angular range ($0° < \theta_{lab} < 8°$) for both the ground-state and the 2^+ first excited state of the residual nucleus are listed in Table 6.8.

Statistically relevant angular distributions of differential cross-sections cannot be extracted from the experimental data here presented for the ground-to-ground state transition, limiting the possibility to compare the experimental and theoretical results only in terms of the integrated cross-sections. Albeit with significant error bars, these first measurements of DCE absolute cross-sections are particularly relevant to design the next-generation NUMEN experiments.

Despite that, some relevant deductions can be made looking at the spectra of Figures 6.13 and 6.14 and at the integrated cross-sections of Table 6.8. The double-isospin strong operator strength distribution follows in both spectra the level density of the ^{76}Ge and ^{76}Se residual nuclei. However, a relevant amount of the strength compared to the level density in that region seems to be concentrated, in both nuclear reactions, in the ground-state and in the first low-lying states of both projectile and target, suggesting the possible collectivity of the ground-to-ground state transition.

The symmetry characterizing the overall behaviour of the two spectra is also a feature of the ground-to-ground state integrated cross-sections (see Table 6.8). The 29 ± 6 nb value for the ^{76}Se(^{18}O,^{18}Ne$_{\text{g.s.}}$)^{76}Ge$_{\text{g.s.}}$ DCE reaction and the 30 ± 4 nb value for the ^{76}Ge(^{20}Ne,^{20}O$_{\text{g.s.}}$)^{76}Se$_{\text{g.s.}}$ one perfectly match. This outcome, that could suggest the time-reversal symmetry of the nuclear matrix element of double-charge exchange operator, needs a further theoretical investigation in order to completely disentangle the nuclear reaction from the nuclear structure aspects.

A stronger consequence of the achieved results regards the role of the projectile/ejectile nuclei in the overall reaction. In Ref. [1] the authors discussed about the differences between the (^{18}O,^{18}Ne) and the (^{20}Ne, ^{20}O) reactions. It was therein under-

Table 6.8: Cross-sections integrated in the full angular range ($0° < \theta_{lab} < 8°$) for both the ground-state and the 2^+ first excited state of the residual nucleus measured in the ^{76}Se(^{18}O,^{18}Ne)^{76}Ge and ^{76}Ge(^{20}Ne,^{20}O)^{76}Se double-charge exchange nuclear reactions.

	^{76}Se(^{18}O,^{18}Ne)^{76}Ge (nb)	^{76}Ge(^{20}Ne,^{20}O)^{76}Se (nb)
$0^+ \rightarrow 0^+$	29 ± 6	30 ± 4
$0^+ \rightarrow 2^+$	8 ± 3	17 ± 5

lined that the (^{18}O,^{18}Ne), used to investigate the $\beta^+\beta^+$ direction, could be particularly advantageous, due to the large value of both the $B[GT; {}^{18}O_{\text{g.s.}}(0^+) \rightarrow {}^{18}F_{\text{g.s.}}(1^+)]$ and $B[GT; {}^{18}F_{\text{g.s.}}(1^+) \rightarrow {}^{18}Ne_{\text{g.s.}}(0^+)]$ strengths and to the concentration of the GT strength in the ^{18}F(1^+) ground state. To investigate the $\beta^-\beta^-$ direction, the authors proposes the (^{20}Ne,^{20}O) reaction, which has smaller $B(GT)$, so that a reduction of the yield could be foreseen in these cases. This early hypothesis is overturned by the experimental results presented in this thesis from which the role of the projectile/ejectile $B(GT)$ toward the nuclei of the intermediate partition appears to be scaled down when the complete DCE reaction is considered. This result needs to be further investigated by next generation high-intensity NUMEN experiment also in other systems of interest for the project.

To date, several steps forward have been made also from the theoretical side. It has to be noticed that an even approximate approach to the full DCE reaction mechanism did not exist before the start of the NUMEN experimental activity, which allowed to verify for the first time the experimental feasibility of the absolute cross section measurement of DCE reaction induced by heavy-ions, at zero-degrees, with a sufficient energy resolution to separate the ground-state from the first excited state of the residual nucleus [41, 45]. Today this theoretical study is in progress [6, 8, 9, 55, 82]. In particular, the development of the formalism is still underway for the Majorana-DCE analogous to the Majorana $0\nu\beta\beta$ decay process.

Chapter References

[1] F. Cappuzzello et al. “The NUMEN project: NUclear Matrix Elements for Neutrinoless double beta decay”. In: *European Physical Journal A* 54.5 (2018). cited By 106. DOI: 10.1140/epja/i2018-12509-3.

[2] H. Ejiri, J. Suhonen, and K. Zuber. “Neutrino–nuclear responses for astro-neutrinos, single beta decays and double beta decays”. In: *Physics Reports* 797 (2019). Neutrino-nuclear responses for astro-neutrinos, single beta decays and double beta decays, pp. 1–102. DOI: 10.1016/j.physrep.2018.12.001.

[3] S. Dell’Oro et al. “Neutrinoless Double Beta Decay: 2015 Review”. In: *Advances in High Energy Physics* 2016.2162659 (2016), p. 37. DOI: 10.1155/2016/2162659.

[4] M. J. Dolinski, A. W.P. Poon, and W. Rodejohann. “Neutrinoless Double-Beta Decay: Status and Prospects”. In: *Annual Review of Nuclear and Particle Science* 69.1 (2019), pp. 219–251. DOI: 10.1146/annurev-nucl-101918-023407.

[5] J. Engel and J. Menéndez. “Status and future of nuclear matrix elements for neutrinoless double-beta decay: a review”. In: *Reports on Progress in Physics* 80.4 (2017), p. 046301.

[6] H. Lenske et al. “Heavy ion charge exchange reactions as probes for nuclear β-decay”. In: *Progress in Particle and Nuclear Physics* 109 (2019), p. 103716. ISSN: 0146-6410. DOI: 10.1016/j.ppnp.2019.103716.

[7] D. Carbone et al. “Analysis of two-nucleon transfer reactions in the ^{20}Ne + ^{116}Cd system at 306 MeV”. In: *Physical Review C* 102.4 (2020). cited By 6. DOI: 10.1103/PhysRevC.102.044606.

[8] J. L. Ferreira et al. “Multinucleon transfer in the ^{116}Cd(^{20}Ne,^{20} O)^{116}Sn double charge exchange reaction at 306 MeV incident energy”. In: *Phys. Rev. C* 105 (1 Jan. 2022), p. 014630. DOI: 10.1103/PhysRevC.105.014630.

[9] J. I. Bellone et al. “Two-step description of heavy ion double charge exchange reactions”. In: *Physics Letters B* 807 (2020), p. 135528. ISSN: 0370-2693. DOI: 10.1016/j.physletb.2020.135528.

[41] F. Cappuzzello et al. “Heavy-ion double charge exchange reactions: A tool toward $0\nu\beta\beta$ nuclear matrix elements”. In: *Eur. Phys. J.* A51.11 (2015), p. 145. DOI: 10.1140/epja/i2015-15145-5.

[42] M. Cavallaro et al. “A Constrained Analysis of the ^{40}Ca(^{18}O,^{18}F)^{40}K Direct Charge Exchange Reaction Mechanism at 275 MeV”. In: *Frontiers in Astronomy and Space Sciences* 8 (2021), p. 61. DOI: 10.3389/fspas.2021.659815.

[43] J.L. Ferreira et al. “Analysis of two-proton transfer in the ^{40}Ca (^{18}O, ^{20}Ne) ^{38}Ar reaction at 270 MeV incident energy”. In: *Physical Review C* 103.5 (2021). cited By 0. DOI: 10.1103/PhysRevC.103.054604.

[45] V. Soukeras et al. “Measurement of the double charge exchange reaction for the ^{20}Ne + ^{130}Te system at 306 MeV”. In: *Results in Physics* 28 (2021), p. 104691. ISSN: 2211-3797. DOI: https://doi.org/10.1016/j.rinp.2021.104691.

[46] D. Carbone et al. “Initial state interaction for the ^{20}Ne + ^{130}Te and ^{18}O + ^{116}Sn systems at 15.3 AMeV from elastic and inelastic scattering measurements”. In: *Universe* 7.3 (2021). cited By 1. DOI: 10.3390/universe7030058.

[50] A. Spatafora et al. “^{20}Ne+^{76}Ge elastic and inelastic scattering at 306 MeV”. In: *Phys. Rev. C* 100 (3 Sept. 2019), p. 034620. DOI: 10.1103/PhysRevC.100.034620.

[51] L. La Fauci et al. "^{18}O + ^{76} Se elastic and inelastic scattering at 275 MeV". In: *Phys. Rev. C* 104 (5 Nov. 2021), p. 054610. DOI: 10.1103/PhysRevC.104.054610.

[54] H. Lenske et al. "Theory of Single Charge Exchange Heavy Ion Reactions". In: *Phys. Rev.* C98.4 (2018), p. 044620. DOI: 10.1103/PhysRevC.98.044620.

[55] H. Lenske. "Probing Double Beta-Decay by Heavy Ion Charge Exchange Reactions". In: *J. Phys.: Conf. Ser.* 1056 (July 2018), p. 012030. DOI: 10.1088/1742-6596/1056/1/012030.

[60] G. R. Satchler. *Direct nuclear reactions*. Vol. 68. Int. series of monographs on physics. Oxford, UK: Clarendon Press, 1983. ISBN: 9780198512691.

[62] L. C. Chamon et al. "Toward a global description of the nucleus-nucleus interaction". In: *Phys. Rev.* C66 (2002), p. 014610. DOI: 10.1103/PhysRevC.66.014610.

[68] Y. Fujita, B. Rubio, and W. Gelletly. "Spin–isospin excitations probed by strong, weak and electro-magnetic interactions". In: *Progress in Particle and Nuclear Physics* 66.3 (2011), pp. 549–606. ISSN: 0146-6410. DOI: https://doi.org/10.1016/j.ppnp.2011.01.056.

[69] Y. Fujita et al. "Matching of a beam line and a spectrometer New beam line project at RCNP". In: *Nuclear Instruments and Methods in Physics Research Section B: Beam Interactions with Materials and Atoms* 126.1 (1997). International Conference on Electromagnetic Isotope Separators and Techniques Related to Their Applications, pp. 274–278. ISSN: 0168-583X. DOI: https://doi.org/10.1016/S0168-583X(96)01008-7.

[72] E. W. Grewe et al. "The $(d, {}^2\mathrm{He})$ reaction on ^{76}Se and the double-β-decay matrix elements for $A = 76$". In: *Phys. Rev. C* 78 (4 Oct. 2008), p. 044301. DOI: 10.1103/PhysRevC.78.044301.

[82] H. Lenske et al. "Nuclear Matrix Elements for Heavy Ion Sequential Double Charge Exchange Reactions". In: *Universe* 7.4 (2021). ISSN: 2218-1997. DOI: 10.3390/universe7040098.

[99] M. Bordessoule et al. “A simplified read out for high-resolution linear gas detector”. In: *Nuclear Instruments and Methods in Physics Research Section A: Accelerators, Spectrometers, Detectors and Associated Equipment* 390.1 (1997), pp. 79–85. ISSN: 0168-9002. DOI: https://doi.org/10.1016/S0168-9002(97)00352-5.

[110] D.R. Tilley et al. “Energy levels of light nuclei A = 18–19”. In: *Nuclear Physics A* 595.1 (1995), pp. 1–170. ISSN: 0375-9474. DOI: https://doi.org/10.1016/0375-9474(95)00338-1.

[114] M. Cavallaro et al. “Quantitative analysis of two-neutron correlations in the ^{12}C(^{18}O,^{16}O)^{14}C reaction”. In: *Phys. Rev. C* 88 (5 Nov. 2013), p. 054601. DOI: 10.1103/PhysRevC.88.054601.

[119] F. Cappuzzello et al. “Signatures of the giant pairing vibration in the ^{14}C and ^{15}C atomic nuclei”. In: *Nature Communications* 6 (2015). cited By 75. DOI: 10.1038/ncomms7743.

[130] D. Carbone et al. “Microscopic cluster model for the description of new experimental results on the ^{13}C(^{18}O,^{16}O)^{15}C two-neutron transfer at 84 MeV incident energy”. In: *Phys. Rev.* C95.3 (2017), p. 034603. DOI: 10.1103/PhysRevC.95.034603.

[131] B. Paes et al. “Long-range versus short-range correlations in the two-neutron transfer reaction ^{64}Ni(^{18}O,^{16}O)^{66}Ni”. In: *Phys. Rev.* C96.4 (2017), p. 044612. DOI: 10.1103/PhysRevC.96.044612.

[133] M. J. Ermamatov et al. “Comprehensive analysis of high-lying states in ^{18}O populated with (t,p) and (^{18}O,^{16}O) reactions”. In: *Phys. Rev.* C96.4 (2017), p. 044603. DOI: 10.1103/PhysRevC.96.044603.

[134] V.A.B. Zagatto et al. “Important role of projectile excitation in ^{16}O + ^{60}Ni and ^{16}O + ^{27}Al scattering at intermediate energies”. In: *Phys. Rev. C* 97 (May 2018), p. 054608. DOI: 10.1103/PhysRevC.97.054608.

[135] E. N. Cardozo et al. “Competition between direct and sequential two-neutron transfers in the ^{18}O +^{28} Si collision at 84 MeV”. In: *Phys. Rev. C* 97 (6 June 2018), p. 064611. DOI: 10.1103/PhysRevC.97.064611.

[136] D. Pereira et al. “An imaginary potential with universal normalization for dissipative processes in heavy-ion reactions”. In: *Phys. Lett. B* 670.4 (2009), pp. 330–335. ISSN: 0370-2693. DOI: https://doi.org/10.1016/j.physletb.2008.10.066.

[137] G.R. Satchler and W.G. Love. “Folding model potentials from realistic interactions for heavy-ion scattering”. In: *Physics Reports* 55.3 (1979), pp. 183–254. ISSN: 0370-1573. DOI: https://doi.org/10.1016/0370-1573(79)90081-4.

[138] M.E. Brandan and G.R. Satchler. “The interaction between light heavy-ions and what it tells us”. In: *Physics Reports* 285.4 (1997), pp. 143–243. ISSN: 0370-1573. DOI: https://doi.org/10.1016/S0370-1573(96)00048-8.

[139] E. Crema et al. “Near-barrier quasielastic scattering as a sensitive tool to derive nuclear matter diffuseness”. In: *Phys. Rev. C* 84 (2 Aug. 2011), p. 024601. DOI: 10.1103/PhysRevC.84.024601.

[140] E. Crema et al. “Reaction mechanisms of the ^{18}O +^{63} Cu system at near-barrier energies”. In: *Phys. Rev. C* 98 (4 Oct. 2018), p. 044614. DOI: 10.1103/PhysRevC.98.044614.

[141] L. M. Fonseca et al. “Elastic and inelastic scattering of ^{16}O on ^{27}Al and ^{28}Si at 240 MeV”. In: *Phys. Rev. C* 100 (1 July 2019), p. 014604. DOI: 10.1103/PhysRevC.100.014604.

[142] I. J. Thompson. “Coupled reaction channels calculations in nuclear physics”. In: *Comput. Phys. Rep.* 7.4 (1988), pp. 167–212. ISSN: 0167-7977. DOI: https://doi.org/10.1016/0167-7977(88)90005-6.

[143] B. Pritychenko et al. “Tables of E2 Transition Probabilities from the first 2^+ States in Even-Even Nuclei”. In: *Atom. Data Nucl. Data Tabl.* 107 (2016), pp. 1–139. DOI: 10.1016/j.adt.2015.10.001,10.1016/j.adt.2016.08.002.

[144] T. Kibedi and R. H. Spear. "Reduced electric-octupole transition probabilities, B(E3;$0^+ \rightarrow 3^-$) - an update". In: *Atomic Data and Nuclear Data Tables* 80.1 (2002), pp. 35–82. ISSN: 0092-640X. DOI: https://doi.org/10.1006/adnd.2001.0871.

[145] N. Shimizu et al. "Thick-restart block Lanczos method for large-scale shell-model calculations". In: *Computer Physics Communications* 244 (2019), pp. 372–384. ISSN: 0010-4655. DOI: https://doi.org/10.1016/j.cpc.2019.06.011.

[146] Y. Utsuno and S. Chiba. "Multiparticle-multihole states around ^{16}O and correlation-energy effect on the shell gap". In: *Phys. Rev. C* 83 (2 Feb. 2011), p. 021301. DOI: 10.1103/PhysRevC.83.021301.

[149] H. Lenske, ed. *DFOL private comunication.*

[154] M. Agostini and et al. "Improved Limit on Neutrinoless Double-β Decay of ^{76}Ge from GERDA Phase II". In: *Phys. Rev. Lett.* 120 (13 Mar. 2018), p. 132503. DOI: 10.1103/PhysRevLett.120.132503.

[155] J. H. Thies et al. "The (^{3}He,t) reaction on ^{76}Ge, and the double-β-decay matrix element". In: *Phys. Rev. C* 86 (1 July 2012), p. 014304. DOI: 10.1103/PhysRevC.86.014304.

[156] N. K. Glendenning. "Chapter 4 - The Phenomenological Optical Potential". In: *Direct Nuclear Reactions*. Ed. by N. K. Glendenning. Academic Press, 1983, pp. 24–44. ISBN: 978-0-12-286320-2. DOI: https://doi.org/10.1016/B978-0-12-286320-2.50010-3.

[157] B. Singh. "Nuclear Data Sheets Update for A = 76". In: *Nuclear Data Sheets* 74.1 (1995), pp. 63–164. ISSN: 0090-3752. DOI: https://doi.org/10.1006/ndsh.1995.1005.

[158] R. Bass. *Nuclear Reactions with Heavy Ions*. Theoretical and Mathematical Physics. Springer Berlin Heidelberg, 1980. ISBN: 978-3-540-09611-5.

[159] R. Linares et al. "Analysis of the one-neutron transfer to ^{16}O, ^{28}Si, and ^{64}Ni induced by the (^{18}O, ^{17}O) reaction at 84 MeV". In: *Phys. Rev. C* 98 (5 Nov. 2018), p. 054615. DOI: 10.1103/PhysRevC.98.054615.

[160] M.A.G. Alvarez et al. “A parameter-free optical potential for the heavy-ion elastic scattering process”. In: *Nuclear Physics A* 723.1 (2003), pp. 93–103. ISSN: 0375-9474. DOI: https://doi.org/10.1016/S0375-9474(03)01158-8.

[161] G. R. Satchler. “Observation of the phase of the effective interaction for inelastic scattering of complex particles”. In: *Physics Letters B* 33.6 (1970), pp. 385–387. ISSN: 0370-2693. DOI: https://doi.org/10.1016/0370-2693(70)90610-6.

[162] F. Cappuzzello et al. “Interplay of the elastic and inelastic channels in the ^{16}O + ^{27}Al scattering at E_{lab} = 280 MeV”. In: *Eur. Phys. J. A* 52 (June 2016), p. 169.

[163] J.B. Ball et al. “Heavy ion elastic scattering survey: (I). ^{208}Pb target”. In: *Nuclear Physics A* 252.1 (1975), pp. 208–236. ISSN: 0375-9474. DOI: https://doi.org/10.1016/0375-9474(75)90613-2.

[164] G. R. Satchler. “A simple effective interaction for peripheral heavy-ion collisions at intermediate energies”. In: *Nuclear Physics A* 579.1 (1994), pp. 241–255. ISSN: 0375-9474. DOI: https://doi.org/10.1016/0375-9474(94)90804-4.

[165] R. Madey et al. “Low-lying structures in the Gamow-Teller strength functions for the double-beta-decaying nuclei ^{76}Ge, ^{82}Se, ^{128}Te, and ^{130}Te”. In: *Phys. Rev. C* 40 (2 Aug. 1989), pp. 540–552. DOI: 10.1103/PhysRevC.40.540.

[166] E.-W. Grewe et al. “(^{3}He,t) reaction on the double β decay nucleus ^{48}Ca and the importance of nuclear matrix elements”. In: *Phys. Rev. C* 76 (5 Nov. 2007), p. 054307. DOI: 10.1103/PhysRevC.76.054307.

[167] D.R. Tilley et al. “Energy levels of light nuclei, A = 20”. In: *Nuclear Physics A* 636.3 (1998), pp. 249–364. ISSN: 0375-9474. DOI: https://doi.org/10.1016/S0375-9474(98)00129-8.

Conclusions

The experimental data presented for the first time in this work are the results of three experiments performed at the INFN-Laboratori Nazionali del Sud in Catania. The ^{18}O and ^{20}Ne ion beams were accelerated up to 15.3 AMeV by the K800 Superconducting Cyclotron and, from the nuclear collisions with three different targets, several reaction channels were analysed. The ^{18}O beam was used to explore the networks of nuclear reactions populated in the collisions with the ^{12}C and the ^{76}Se targets while the ^{20}Ne beam was used in combination with a ^{76}Ge target. The studies on ^{76}Se and ^{76}Ge are highly complementary allowing a detailed characterization of the parent and daughter system of ^{76}Ge $\beta\beta$-emitter. The ejectiles, emerging from the nuclear reactions, were momentum analysed by the MAGNEX spectrometer. The high resolution beams, the thin targets manufacturing, the accurate tunings of the experimental set-up and the advanced data-reduction technique guaranteed high resolutions both in excitation energy (δ E_{x}(FWHM) $\approx$ 0.5 MeV) and scattering angle ($\delta\theta_{lab}$(FWHM) $\approx$ 0.5°) in all the explored reaction channels, including the challenging zero-degrees double charge-exchange (DCE) measurements. Excitation energy spectra were obtained for all the reaction channels analysed and, in the cases of a reasonable amount of the collected events, cross-section angular distributions were extracted for several structures visible in the spectra. In the available angular distributions, broad ranges of cross sections were explored, covering several orders of magnitude always keeping a high significance level. The small error bars and the overall quality of the experimental data justify the use of sophisticated microscopic analysis.

The ^{18}O + ^{12}C elastic and inelastic scattering, one-neutron and two-neutron addition, one proton removal and single charge-exchange nuclear reaction experimental data were collected under the same experimental conditions and the data reduction was performed consistently. This allowed to constrain the experimental results limiting the overall systematic uncertainty. All the measurements were performed in three different settings

of the spectrometer optical angle (θ_{opt} = 7.5°, 8° and 13.5°) allowing to access the angular distributions of differential cross-section at forward angles and in a broad range of transferred momentum.

From the ^{12}C(^{18}O,^{18}O)^{12}C elastic and inelastic scattering data reduction, angular distributions were extracted for the transitions to the ground-state and the first 2^+ and 3^- low-lying excited states of both projectile and target. From the ^{12}C(^{18}O,^{17}O)^{13}C one-neutron addition and the ^{12}C(^{18}O,^{19}F)^{11}B one-proton removal reactions, the excitation energy spectra and several cross-section angular distributions were extracted. In the one-neutron addition case, they correspond to transitions towards single-isolated and groups of unresolved states of the residual nuclei, whereas the ^{19}F high density of states did not allow to isolate transitions to single states of the ^{19}F + ^{11}B partition.

The ^{12}C(^{18}O,^{18}F)^{12}B SCE nuclear reaction was also analysed. The energy spectrum, extracted up to 12 MeV excitation energy, is characterized by different structures attributed to well known bound states and resonances of ^{18}F and ^{12}B nuclei for which angular distributions were extracted. Thanks to the high energy resolution, it was possible to isolate the transition to the ground-state of the final partition. This outcome turns out as a very powerful tool to better constrain the theoretical results, especially to bring light in the much debated aspect of the competition between the direct and the sequential reaction mechanism in SCE nuclear reactions.

The theoretical analysis of the elastic and inelastic scattering, one-neutron addition and one-proton removal nuclear reaction channels was performed in a full-consistent multi-channel approach, including also the description of the SCE reaction as a two-step one-nucleon transfer process. The double folding São Paulo optical potential (SPP) was adopted as the optical potential and the couplings with the inelastic states were introduced in terms of deformed Coulomb and nuclear potentials. Couplings between different partitions were treated in the exact finite range full complex remnant approach developed in the FRESCO code. Several coupling schemes were tested at progressively higher level of sophistication, performing the calculations in optical-model (OM), distorted-wave Born approximation (DWBA), coupled channels (CC), coupled channels Born approximation (CCBA) and coupled reaction channels (CRC). Spectroscopic amplitudes were calculated in the large-scale shell-model nuclear structure approach using the psd-mod interaction both for projectile-like and target-like nuclei.

Regarding the initial partition and its mean field potential interaction, the results highlight the importance to perform CC calculations explicitly including the couplings with the mentioned 2^+ and 3^- low-lying excited states of ^{12}C and ^{18}O in the description of

both the elastic and inelastic scattering cross-section angular distributions. The explicit inclusion of couplings with states of different partitions (CRC) proves to be less relevant than the one coming from the inelastic states of the same partition. This analysis allowed to access initial state interaction (ISI) adopted for the theoretical analysis of the complete network of nuclear reactions.

The newly defined *quality factor* helps to establish that the best theoretical description of the complete network of nuclear reaction channels here discussed is achieved using the CCBA approach in which also the couplings between different states of the intermediate partitions are properly taken into account. The two-step sequential single charge-exchange reaction calculations underestimates the experimental cross-section angular distributions suggesting the presence of missing reaction mechanisms feeding the SCE channel, such as the direct meson-exchange contribution.

The direct meson-exchange SCE calculations were also performed to describe the ground-to-ground state transition. Quasi-particle random phase approximation (QRPA) calculations provided the one-body response functions. The coupled-channels equivalent potential (CCEP) was introduced to effectively take into account the relevant couplings with the inelastic states of the initial partition in the adopted ISI. Also, these calculations underestimate the ground-to-ground state experimental cross-section suggesting that either mechanisms are indeed coherently contributing. This, in turn, demands for additional developments to properly treat the interference between the two reaction mechanisms. Preliminary results in this last subject, obtained considering the constructive interference of the two reaction mechanisms in a simplified approach, successfully describe the ground-to-ground state experimental cross-section. The interference among the two paths turns out as the most relevant and the intriguing aspect of the present study, requiring to be coherently treated both from the reaction and nuclear structure calculations side.

The study of the ^{12}C(^{18}O,^{16}O)^{14}C two-neutron transfer reaction allowed to access the energy spectra and cross-section angular distributions of several isolated states and more complex structures in both the bound an unbound states region of the residual nuclei. The energy spectra give unambiguous confirmation of the Giant Pairing Vibration mode in the ^{14}C nucleus, whose signature was previously reported from the analysis of the same reaction at 84 MeV incident energy [119]. Suggested values for the excitation energy and widths (FWHM) are extracted by matching the results of the experiments at both energies, obtaining a pairing energy of 19.94 $\pm$ 0.09 MeV and a width of 1.1 $\pm$ 0.2 MeV for the ^{12}C GPV. The $L = 0$ character of the transition feeding the GPV is

confirmed from the shape of the measured angular distribution, common to the ground-to-ground state transition which was also extracted.

Further theoretical calculations are desirable in the larger multi-channel full-comprehensive framework, to better analyse the role of the ^{12}C(^{18}O,^{16}O)^{14}C two-neutron transfer reaction channel in the complete network of nuclear reactions. Indeed, the present result gives a robust confirmation of the GPV as a relevant aspect of the nuclear response to an external particle-particle addition operator. The nuclear response shows in the particle-particle sector a behaviour symmetric to the particle-hole one, where Giant Resonances represent the dominant features of the nuclear excitations. Pairing correlations play an important role not only in lowering the binding energy of 0^+ ground states in even-even nuclei, but also in the continuum. It is thus essential to further develop the theories in both nuclear structure and reactions in order to cast the subtle coupling of the GPV degrees of freedom with the underlying non resonant states.

The new multi-channel experimental and theoretical approach was further applied to a wide network of nuclear reactions involving the ^{76}Ge and ^{76}Se $\beta\beta$ decay partners. Two experiments were dedicated to this scope and many nuclear reaction channels were studied, including the ^{76}Ge $\leftrightarrow$ ^{76}Se transition populated in both directions through the (^{18}O,^{18}Ne) and the (^{20}Ne,^{20}O) double charge exchange reactions. In this thesis, the results obtained from the elastic and inelastic scattering, the single and double charge exchange reactions were presented.

The ^{20}Ne + ^{76}Ge and the ^{18}O + ^{76}Se elastic and inelastic scatterings at 15.3 AMeV incident energy were studied both from the experimental and theoretical points of view. The experimental results were compared with cross section calculations performed with the FRESCO code. The `dfol` and SPP double-folding optical potentials were scrutinized to test their capability in describing the measured elastic scattering cross sections. The description of the data is not fully satisfactory beyond the grazing angle if such calculations are performed in the OM formalism. In both systems, it was found that at large transferred momenta the effect of couplings with first low-lying excited states is crucial. To determine the inelastic flux and its effect on the elastic channel, DWBA and CC calculations were performed. The inclusion of only the first 2^+ of the projectile and target and the first 3^- of the ^{18}O collective low-lying excited states turns out to be enough to well describe almost all the angular distributions over the full range of explored transferred momenta.

The ^{76}As excitation energy spectra were extracted from the ^{76}Se(^{18}O,^{18}F)^{76}As and ^{76}Ge(^{20}Ne,^{20}F)^{76}As SCE reactions. The ^{76}Se(^{18}O,^{18}F)^{76}As spectrum is more structured

than the ^{76}Ge(^{20}Ne,^{20}F)^{76}As one, suggesting the possible dominance of only few states in the former with respect to the latter. The same behaviour was discussed in previous works concerning the study of the ^{76}Se(d,^{2}He)^{76}As and the ^{76}Ge(^{3}He,t)^{76}As SCE reactions. Furthermore, they observed that strong transitions feeding ^{76}As from one direction do not seem to have a strong partner from the other direction and vice-versa resulting in a sort of anti-correlation. Once available, theoretical calculations constrained by the present new experimental data will help to verify the non-correlation or the anti-correlation hypothesis.

Finally, the ^{76}Ge and the ^{76}Se excitation energy spectra were measured for the first time in the ^{76}Se(^{18}O,^{18}Ne)^{76}Se and ^{76}Ge(^{20}Ne,^{20}O)^{76}Se DCE reactions in a large momentum transfer domain at forward angles including zero-degrees ($0° < \theta_{lab} < 8°$) and up to 30 MeV excitation energy. These results are particularly relevant and advanced, especially for the achieved energy resolution ($\approx$ 350 keV FWHM) allowing to separate the ground-to-ground state transition from that to the first 2^+ excited state of the involved residual nuclei. The DCE ^{76}Ge and ^{76}Se measured spectra show similar features. The double-isospin operator strength distribution follows in both spectra the level density of the ^{76}Ge and ^{76}Se residual nuclei. In both cases, most of the strength is concentrated at high excitation energy, where the spectra are dominated by the break-up continuum components. However, a relevant amount of the strength compared to the level density in that region seems to be concentrated in the ground-state and in the first low-lying states of both projectiles and targets, suggesting the hint for a possible collectivity of the ground-to-ground state transitions. Statistically relevant angular distributions of differential cross-sections cannot be extracted for the ground-to-ground state transitions, limiting the possibility to compare the experimental and theoretical results only in terms of integrated cross-sections, which are also symmetric in the two cases. Indeed, the 29 $\pm$ 6 nb value for the ^{76}Se(^{18}O,^{18}Ne$_{\text{g.s.}}$)^{76}Ge$_{\text{g.s.}}$ DCE reaction and the 30 $\pm$ 4 nb value for the ^{76}Ge(^{20}Ne,^{20}O$_{\text{g.s.}}$)^{76}Se$_{\text{g.s.}}$ one perfectly match. This outcome, that could suggest the time-reversal symmetry of the nuclear matrix element of DCE operator, needs a further theoretical investigation to completely disentangle the nuclear reaction from the nuclear structure aspects. A stronger consequence of the achieved results regards the role of the projectile/ejectile nuclei in the overall reaction. The early hypothesis of their relevant role in the reaction mechanisms has been overturned by the experimental results shown in this thesis. Indeed, the role of the projectile/ejectile B(GT) towards the nuclei of the intermediate partition appears to be scaled down. These first measurements of DCE absolute cross-sections are particularly relevant and

will be further investigated by next generation high-intensity NUMEN experiments also in other systems of interest.

To date, several steps forward have been made also from the theoretical side. It has to be noticed that even a schematic approach to the full DCE reaction mechanism did was missing before the start of the NUMEN experimental activity, which demonstrated the feasibility of DCE absolute cross-section measurements. Today this theoretical study is in progress. In particular, the development of the formalism is underway for the Majorana-DCE analogous to the Majorana $0\nu\beta\beta$-decay process.

A

Electronics schemes: detector signal processing

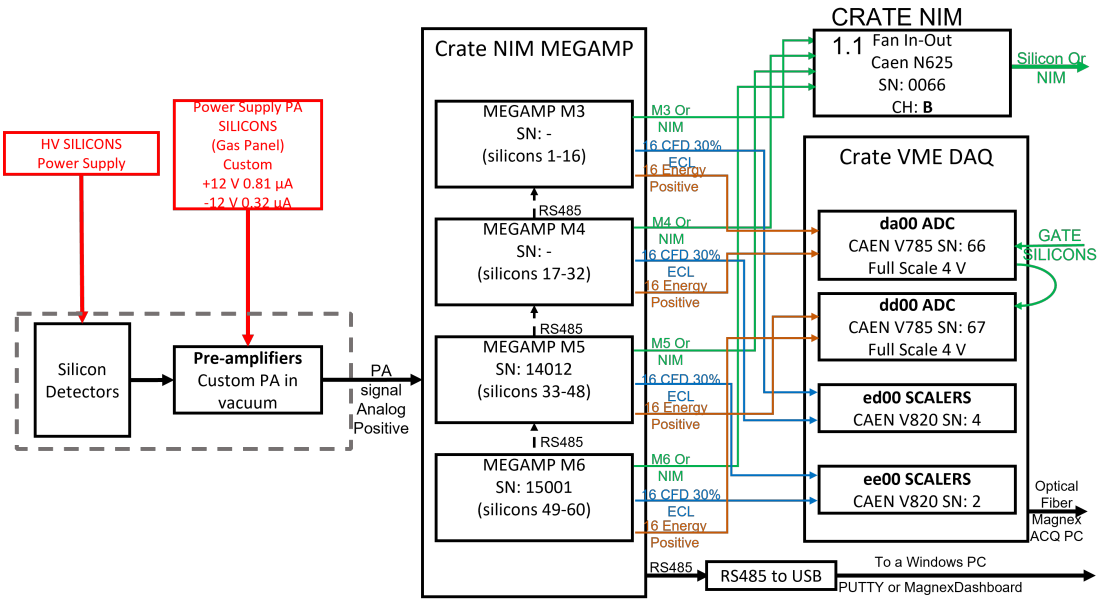

Figure A.1: Pid wall silicon detectors electronics chain.

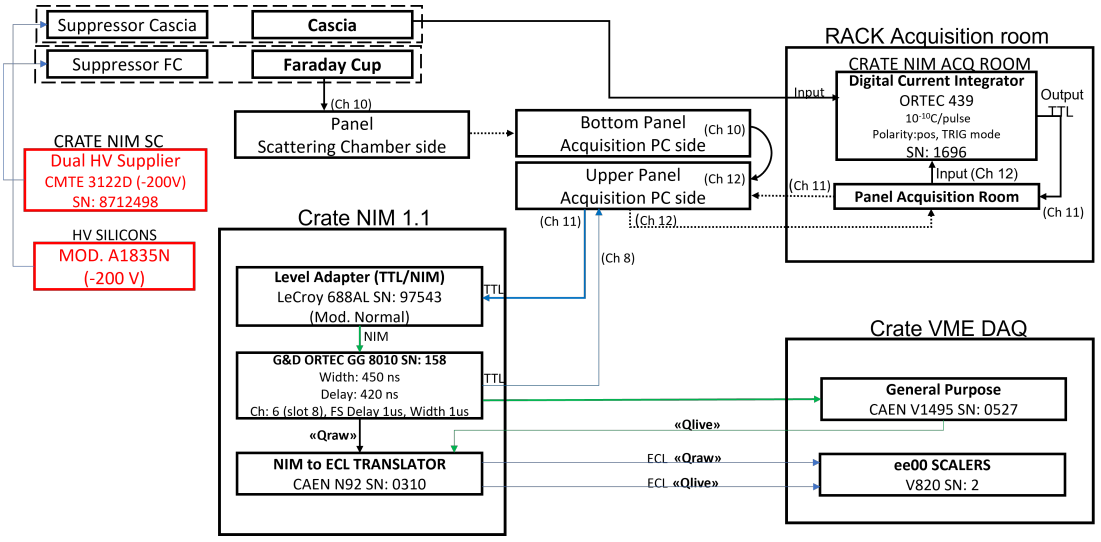

Figure A.2: Faraday cups electronics chain.

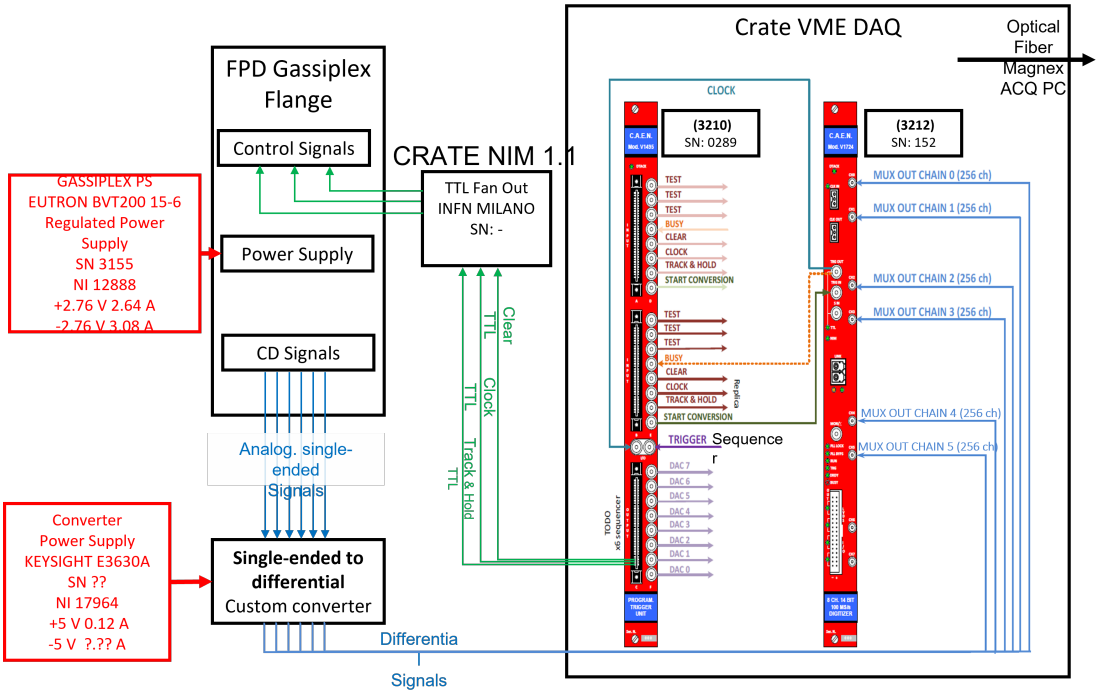

Figure A.3: GASSIPLEX [99] electronics chain.

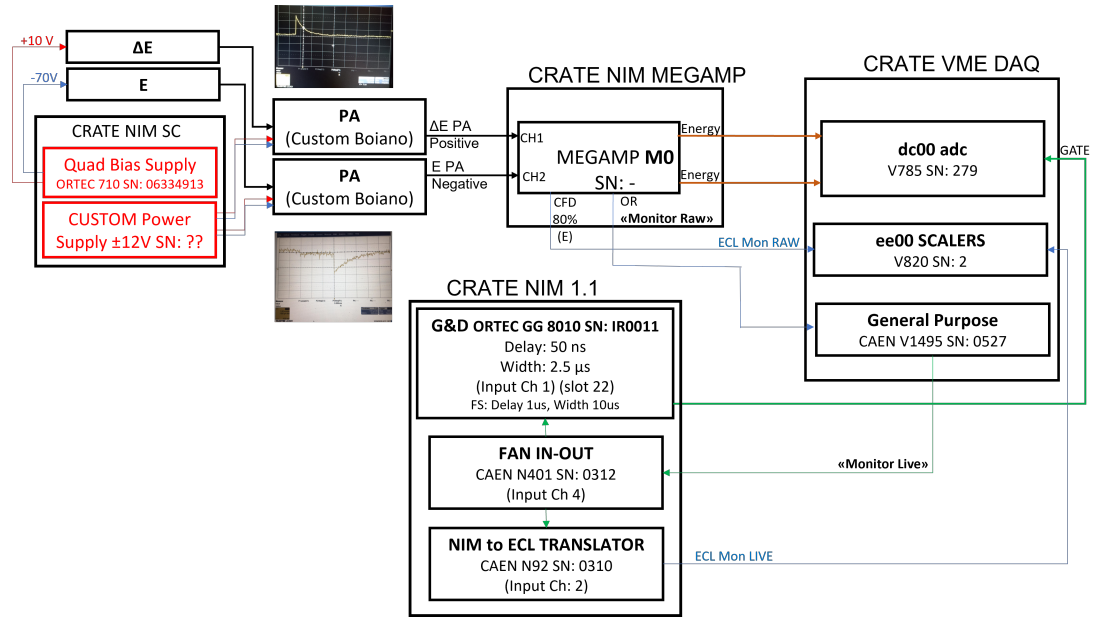

Figure A.4: Monitor detector electronics chain.

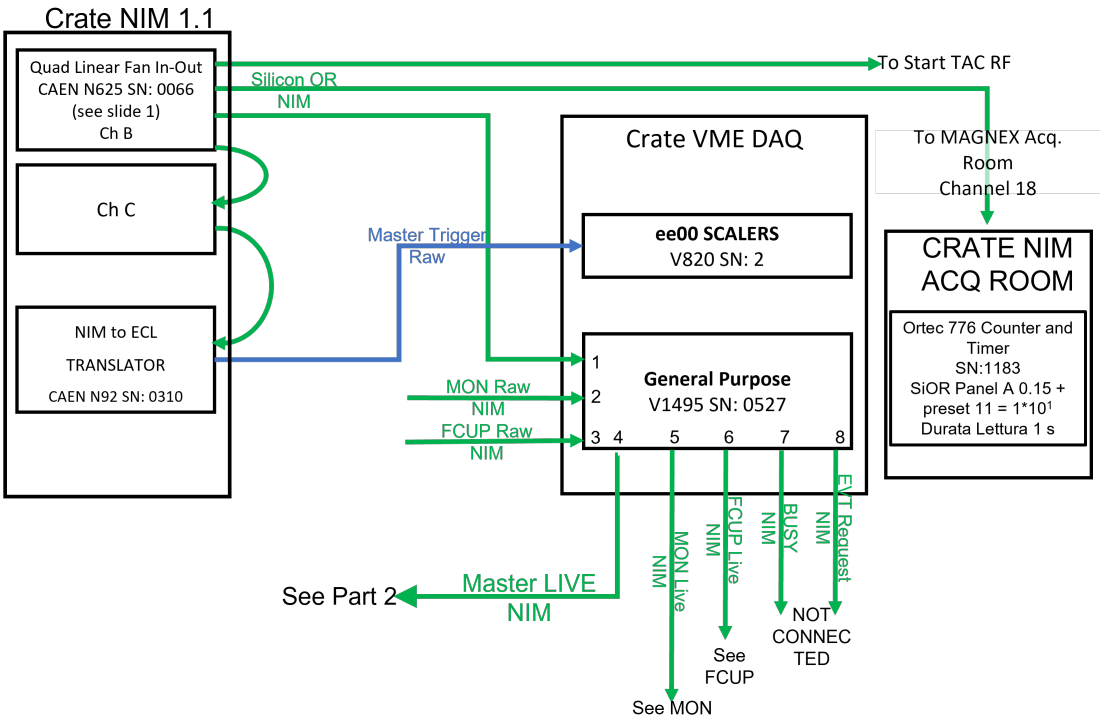

Figure A.5: First part of the MAGNEX logic chain.

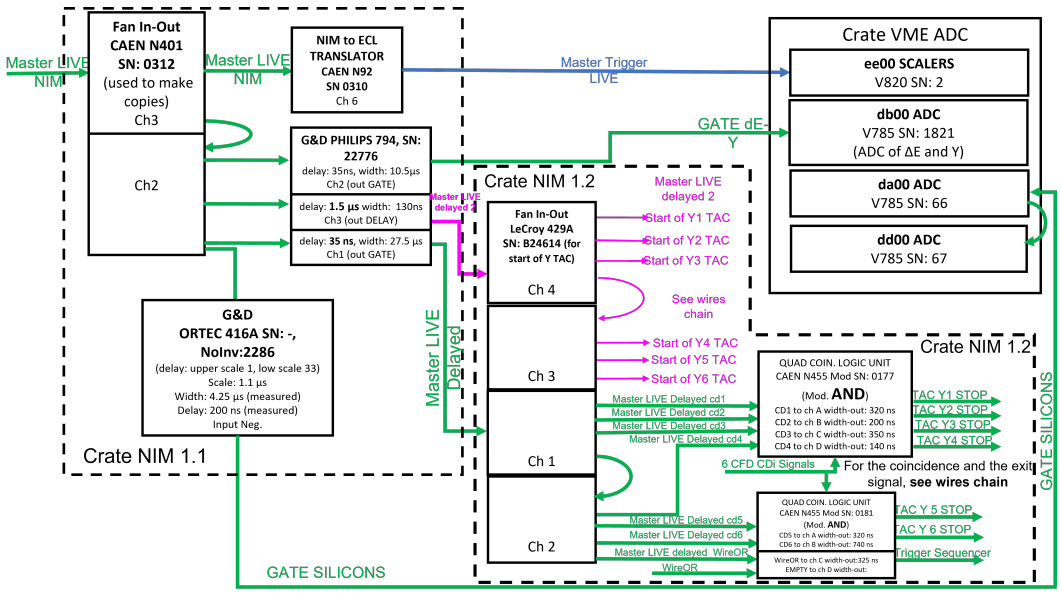

Figure A.6: Second part of the MAGNEX logic chain.

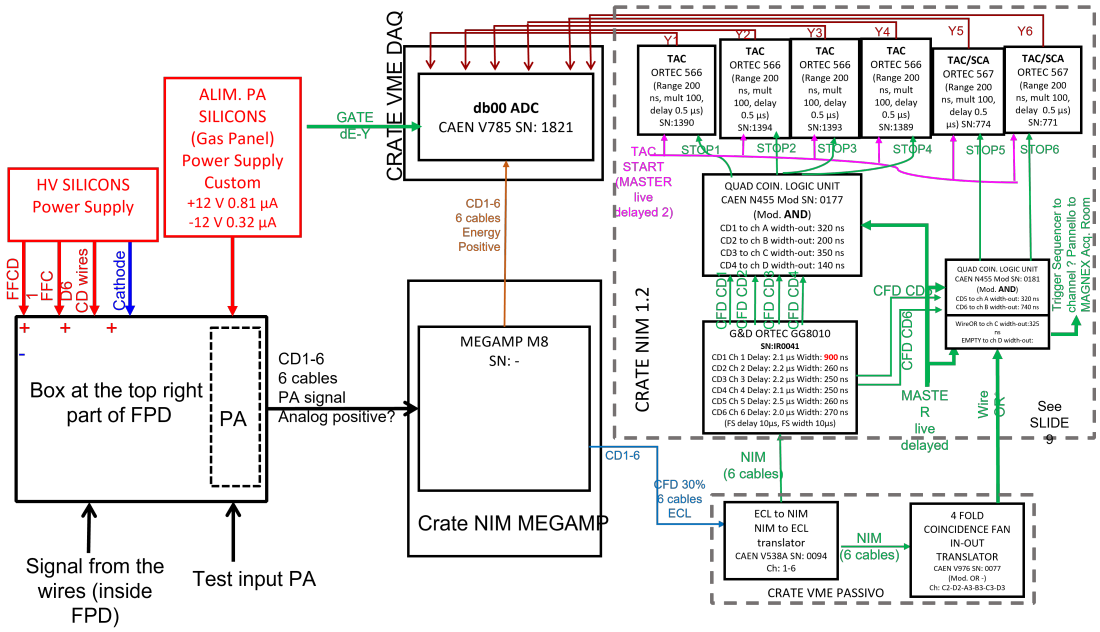

Figure A.7: Wires electronics chain.

B

Shell-model spectroscopic amplitudes

In the following, the comparison between the experimental and theoretical spectra obtained by the large scale shell-model calculations are reported. The spectroscopic amplitudes used in the performed reaction calculations for the involved nuclei are also listed. The values of the theoretical excitation energies and the spectroscopic amplitudes are obtained by the KSHELL [145] software using the ps-d-mod interaction [146] (see subsection 5.2.2.1).

Table B.1: Comparison between the experimental and theoretical low-lying spectra obtained by large scale shell-model calculations for the involved nuclei. using the p-sd-mod interaction [146] Energies are in MeV.

	J^π	Exp.	Theo.
^{18}O	0_1^+	0.000	0.000
	2_1^+	1.982	2.264
	4_1^+	3.554	3.620
	0_2^+	3.633	4.249
	3_1^-	5.097	4.929
^{12}C	0_1^+	0.000	0.000
	2_1^+	4.440	4.950
	3_1^-	9.641	8.127
^{17}O	$\frac{5}{2}^+_1$	0.000	0.000
	$\frac{1}{2}^+_1$	0.871	0.871
	$\frac{1}{2}^-_1$	3.055	3.538
^{13}C	$\frac{1}{2}^-_1$	0.000	0.000
	$\frac{1}{2}^+_1$	3.089	1.830
	$\frac{3}{2}^-_1$	3.684	3.509
	$\frac{5}{2}^+_1$	3.854	2.418
	$\frac{5}{2}^+_2$	6.864	6.164
	$\frac{7}{2}^+_1$	7.492	6.535
	$\frac{5}{2}^-_1$	7.547	7.537
	$\frac{3}{2}^+_1$	7.686	6.706
^{19}F	$\frac{1}{2}^+_1$	0.000	0.107
	$\frac{1}{2}^-_1$	0.110	0.744
	$\frac{5}{2}^+_1$	0.197	0.000
	$\frac{5}{2}^-_1$	1.345	2.422
	$\frac{3}{2}^-_1$	1.458	2.615
	$\frac{3}{2}^+_1$	1.554	1.080
	$\frac{9}{2}^+_1$	2.780	3.104

Table B.1: continued on the next page.

Table B.1: continued from the previous page.

	J^π	Exp.	Theo.
^{11}B	$\frac{3}{2}^-_1$	0.000	0.000
	$\frac{1}{2}^-_1$	2.124	1.689
	$\frac{5}{2}^-_1$	4.444	4.666
	$\frac{3}{2}^-_2$	5.020	4.654

Table B.2: Spectroscopic amplitudes for the target like $\langle^{12}C|^{13}C\rangle$ overlaps used in the DWBA, CCBA and CRC calculations for the ^{12}C(^{18}O,^{17}O)^{13}C one-neutron addition and for the sequential components of the ^{12}C(^{18}O,^{18}F)^{12}B single-charge exchange nuclear reactions. The symbols n, l, and j correspond to the principal quantum number, the orbital, and the total angular momentum of the transferred neutron orbitals, respectively.

^{12}C		^{13}C		nl_j	SA
E_X (MeV)	J^π	E_X (MeV)	J^π		
0.000	0^+	0.000	$\frac{1}{2}^-$	$1p_{\frac{1}{2}}$	0.8025
		3.089	$\frac{1}{2}^+$	$2s_{\frac{1}{2}}$	0.8962
		3.684	$\frac{3}{2}^-$	$1p_{\frac{3}{2}}$	-0.3601
		3.854	$\frac{5}{2}^+$	$1d_{\frac{5}{2}}$	-0.9099
		6.864	$\frac{5}{2}^+$	$1d_{\frac{5}{2}}$	0.0934
		7.492	$\frac{7}{2}^+$		
		7.547	$\frac{5}{2}^-$		
		7.686	$\frac{3}{2}^+$	$1d_{\frac{3}{2}}$	-0.7481

Table B.2: continued on the next page.

Table B.2: continued from the previous page.

^{12}C		^{13}C		nl_j	SA
E_X (MeV)	J^π	E_X (MeV)	J^π		
		0.000	$\frac{1}{2}^-$	$1p_{\frac{3}{2}}$	0.9948
		3.089	$\frac{1}{2}^+$	$1d_{\frac{3}{2}}$	0.0393
		3.089	$\frac{1}{2}^+$	$1d_{\frac{5}{2}}$	-0.3112
		3.684	$\frac{3}{2}^-$	$1p_{\frac{1}{2}}$	0.8205
		3.684	$\frac{3}{2}^-$	$1p_{\frac{3}{2}}$	-0.5404
		3.854	$\frac{5}{2}^+$	$1d_{\frac{3}{2}}$	-0.0588
		3.854	$\frac{5}{2}^+$	$1d_{\frac{5}{2}}$	0.1982
		3.854	$\frac{5}{2}^+$	$2s_{\frac{1}{2}}$	0.1105
4.443	2^+	6.864	$\frac{5}{2}^+$	$1d_{\frac{3}{2}}$	0.0414
		6.864	$\frac{5}{2}^+$	$1d_{\frac{5}{2}}$	0.631
		6.864	$\frac{5}{2}^+$	$2s_{\frac{1}{2}}$	-0.7015
		7.492	$\frac{7}{2}^+$	$1d_{\frac{3}{2}}$	0.004
		7.492	$\frac{7}{2}^+$	$1d_{\frac{5}{2}}$	0.857
		7.547	$\frac{5}{2}^-$	$1p_{\frac{1}{2}}$	0.5441
		7.547	$\frac{5}{2}^-$	$1p_{\frac{3}{2}}$	0.2146
		7.686	$\frac{3}{2}^+$	$1d_{\frac{3}{2}}$	0.2283
		7.686	$\frac{3}{2}^+$	$1d_{\frac{5}{2}}$	0.5145
		7.686	$\frac{3}{2}^+$	$2s_{\frac{1}{2}}$	-0.1059

Table B.2: continued on the next page.

Table B.2: continued from the previous page.

^{12}C		^{13}C		nl$_j$	SA
E_X (MeV)	J^π	E_X (MeV)	J^π		
		0.000	$\frac{1}{2}^-$	$1d_{\frac{5}{2}}$	0.1371
		3.089	$\frac{1}{2}^+$		
		3.684	$\frac{3}{2}^-$	$1d_{\frac{3}{2}}$	-0.0085
		3.684	$\frac{3}{2}^-$	$1d_{\frac{5}{2}}$	0.2771
		3.854	$\frac{5}{2}^+$	$1p_{\frac{1}{2}}$	0.0222
		3.854	$\frac{5}{2}^+$	$1p_{\frac{3}{2}}$	-0.5466
9.64	3$^-$	6.864	$\frac{5}{2}^+$	$1p_{\frac{1}{2}}$	0.0718
		6.864	$\frac{5}{2}^+$	$1p_{\frac{3}{2}}$	-0.123
		7.492	$\frac{7}{2}^+$	$1p_{\frac{1}{2}}$	-0.4395
		7.492	$\frac{7}{2}^+$	$1p_{\frac{3}{2}}$	0.5076
		7.547	$\frac{5}{2}^-$	$1d_{\frac{3}{2}}$	0.0284
		7.547	$\frac{5}{2}^-$	$1d_{\frac{5}{2}}$	-0.1507
		7.547	$\frac{5}{2}^-$	$2s_{\frac{1}{2}}$	0.0288
		7.686	$\frac{3}{2}^+$	$1p_{\frac{3}{2}}$	-0.4286

Table B.3: Spectroscopic amplitudes for the projectile-like $\langle^{18}O|^{17}O\rangle$ overlaps used in the DWBA, CCBA and CRC calculations for the ^{12}C(^{18}O,^{17}O)^{13}C one-neutron addition and for the sequential components of the ^{12}C(^{18}O,^{18}F)^{12}B single-charge exchange nuclear reactions. The symbols n, l, and j correspond to the principal quantum number, the orbital, and the total angular momentum of the transferred neutron orbitals, respectively.

^{18}O		^{17}O		nl$_j$	SA
E_X (MeV)	J^π	E_X (MeV)	J^π		
		0.000	$\frac{5}{2}^+$	$1d_{\frac{5}{2}}$	1.2780
0.000	0^+	0.871	$\frac{1}{2}^+$	$2s_{\frac{1}{2}}$	-0.4345
		3.055	$\frac{1}{2}^-$	$1p_{\frac{1}{2}}$	-0.2810

Table B.3: continued on the next page.

Table B.3: continued from the previous page.

^{18}O		^{17}O		nl$_j$	SA
E_X (MeV)	J^π	E_X (MeV)	J^π		
1.982	2^+	0.000	$\frac{5}{2}^+$	$1d_{\frac{5}{2}}$	1.0734
		0.000	$\frac{5}{2}^+$	$2s_{\frac{1}{2}}$	0.5093
		0.000	$\frac{5}{2}^+$	$1d_{\frac{3}{2}}$	0.0799
		0.871	$\frac{1}{2}^+$	$1d_{\frac{5}{2}}$	-0.4994
		0.871	$\frac{1}{2}^+$	$1d_{\frac{3}{2}}$	-0.1737
5.097	3^-	0.000	$\frac{5}{2}^+$	$1p_{\frac{1}{2}}$	-0.1135
		0.000	$\frac{5}{2}^+$	$1p_{\frac{3}{2}}$	0.0988
		0.871	$\frac{1}{2}^+$		
		3.055	$\frac{1}{2}^+$	$1d_{\frac{5}{2}}$	-0.2430

Table B.4: Spectroscopic amplitudes for the target-like $\langle^{12}C|^{11}B\rangle$ overlaps used in the DWBA, CCBA and CRC calculations for the ^{12}C(^{18}O,^{19}F)^{11}B one-proton addition and for the sequential components of the ^{12}C(^{18}O,^{18}F)^{12}B single-charge exchange nuclear reactions. The symbols n, l, and j correspond to the principal quantum number, the orbital, and the total angular momentum of the transferred proton orbitals, respectively.

^{12}C		^{11}B		nl$_j$	SA
E_X (MeV)	J^π	E_X (MeV)	J^π		
0.000	0^+	0.000	$\frac{3}{2}^-$	$1p_{\frac{3}{2}}$	1.7239
		2.124	$\frac{1}{2}^-$	$1p_{\frac{1}{2}}$	0.6520
		4.444	$\frac{5}{2}^-$		
		5.020	$\frac{3}{2}^-$	$1p_{\frac{3}{2}}$	0.5131

Table B.4: continued on the next page.

Table B.4: continued from the previous page.

^{12}C		^{11}B		nl_j	SA
E_X (MeV)	J^π	E_X (MeV)	J^π		
		0.000	$\frac{3}{2}^-$	$1p_{\frac{1}{2}}$	-0.6607
		0.000	$\frac{3}{2}^-$	$1p_{\frac{3}{2}}$	0.0733
		2.124	$\frac{1}{2}^-$	$1p_{\frac{3}{2}}$	0.5802
4.443	2^+	4.444	$\frac{5}{2}^-$	$1p_{\frac{1}{2}}$	-0.3768
		4.444	$\frac{5}{2}^-$	$1p_{\frac{3}{2}}$	-1.0979
		5.020	$\frac{3}{2}^-$	$1p_{\frac{1}{2}}$	0.2434
		5.020	$\frac{3}{2}^-$	$1p_{\frac{3}{2}}$	-0.7902
		0.000	$\frac{3}{2}^-$	$1d_{\frac{3}{2}}$	-0.2374
		0.000	$\frac{3}{2}^-$	$1d_{\frac{5}{2}}$	-0.4559
		2.124	$\frac{1}{2}^-$	$1d_{\frac{5}{2}}$	0.2820
9.64	3^-	4.444	$\frac{5}{2}^-$	$1d_{\frac{3}{2}}$	0.1858
		4.444	$\frac{5}{2}^-$	$1d_{\frac{5}{2}}$	0.2286
		4.444	$\frac{5}{2}^-$	$2s_{\frac{1}{2}}$	0.0022
		5.020	$\frac{3}{2}^-$	$1d_{\frac{3}{2}}$	-0.2697
		5.020	$\frac{3}{2}^-$	$1d_{\frac{5}{2}}$	0.0500

Table B.5: Spectroscopic amplitudes for the projectile-like $\langle^{18}O|^{19}F\rangle$ overlaps used in the DWBA, CCBA and CRC calculations for the ^{12}C(^{18}O,^{19}F)^{11}B one-proton removal and for the sequential components of the ^{12}C(^{18}O,^{18}F)^{12}B single-charge exchange nuclear reactions. The symbols n, l, and j correspond to the principal quantum number, the orbital, and the total angular momentum of the transferred proton orbitals, respectively.

^{18}O		^{19}F		nl_j	SA
E_X (MeV)	J^π	E_X (MeV)	J^π		
		0.000	$\frac{1}{2}^+$	$2s_{\frac{1}{2}}$	-0.5539
		0.110	$\frac{1}{2}^-$	$1p_{\frac{1}{2}}$	-0.2444
		0.197	$\frac{5}{2}^+$	$1d_{\frac{5}{2}}$	0.6644
0.000	0^+	1.345	$\frac{5}{2}^-$		
		1.458	$\frac{3}{2}^-$	$1p_{\frac{3}{2}}$	-0.0106
		1.554	$\frac{3}{2}^+$	$1d_{\frac{3}{2}}$	-0.4238
		2.780	$\frac{9}{2}^+$		
		0.000	$\frac{1}{2}^+$	$1d_{\frac{5}{2}}$	-0.5864
		0.000	$\frac{1}{2}^+$	$1d_{\frac{3}{2}}$	0.2806
		0.110	$\frac{1}{2}^-$	$1p_{\frac{3}{2}}$	0.0301
		0.197	$\frac{5}{2}^+$	$1d_{\frac{5}{2}}$	0.4265
		0.197	$\frac{5}{2}^+$	$2s_{\frac{1}{2}}$	0.3113
		0.197	$\frac{5}{2}^+$	$1d_{\frac{3}{2}}$	-0.1563
1.982	2^+	1.345	$\frac{5}{2}^-$	$1p_{\frac{3}{2}}$	-0.0186
		1.345	$\frac{5}{2}^-$	$1p_{\frac{1}{2}}$	-0.1366
		1.458	$\frac{3}{2}^-$	$1p_{\frac{3}{2}}$	0.0022
		1.458	$\frac{3}{2}^-$	$1d_{\frac{1}{2}}$	-0.1639
		1.554	$\frac{3}{2}^+$	$1s_{\frac{5}{2}}$	-0.3146
		1.554	$\frac{3}{2}^+$	$2s_{\frac{1}{2}}$	-0.3539
		1.554	$\frac{3}{2}^+$	$1d_{\frac{3}{2}}$	-0.3185
		2.780	$\frac{9}{2}^+$	$1d_{\frac{5}{2}}$	-0.7872

Table B.5: continued on the next page.

Table B.5: continued from the previous page.

^{18}O		^{19}F		nl$_j$	SA
E_X (MeV)	J^π	E_X (MeV)	J^π		
		0.000	$\frac{1}{2}^+$		
		3.089	$\frac{1}{2}^-$	$1d_{\frac{5}{2}}$	-0.4906
		3.684	$\frac{5}{2}^+$	$1p_{\frac{1}{2}}$	0.5849
		3.684	$\frac{5}{2}^+$	$1p_{\frac{3}{2}}$	-0.0900
		3.854	$\frac{5}{2}^+$	$1d_{\frac{3}{2}}$	-0.0268
5.097	3^-	3.854	$\frac{5}{2}^-$	$1d_{\frac{5}{2}}$	-0.4864
		6.864	$\frac{5}{2}^-$	$2s_{\frac{1}{2}}$	-0.3768
		6.864	$\frac{3}{2}^-$	$1d_{\frac{3}{2}}$	0.0486
		7.492	$\frac{3}{2}^-$	$1d_{\frac{5}{2}}$	0.2614
		7.492	$\frac{3}{2}^+$	$1p_{\frac{3}{2}}$	0.1675
		7.547	$\frac{9}{2}^+$	$1p_{\frac{3}{2}}$	-0.0787

Table B.6: Spectroscopic amplitudes for the target-like $\langle {}^{11}B|{}^{12}B\rangle$ overlaps used in the DWBA, CCBA and CRC calculations for the sequential components of the ^{12}C(^{18}O,^{18}F)^{12}B single-charge exchange nuclear reactions. The symbols n, l, and j correspond to the principal quantum number, the orbital, and the total angular momentum of the transferred neutron orbitals, respectively.

^{11}B		^{12}B		nl_j	SA
E_X (MeV)	J^π	E_X (MeV)	J^π		
		0.000	1^+	$1p\frac{1}{2}$	0.8138
		0.000	1^+	$1p\frac{3}{2}$	-0.3101
		0.953	2^+	$1p\frac{1}{2}$	0.8142
		0.953	2^+	$1p\frac{3}{2}$	0.1069
		1.674	2^-	$1d\frac{3}{2}$	-0.1
		1.674	2^-	$1d\frac{5}{2}$	-0.5646
		1.674	2^-	$2s\frac{1}{2}$	0.7288
		2.621	1^-	$1d\frac{3}{2}$	0.1402
		2.621	1^-	$1d\frac{5}{2}$	0.3411
		2.621	1^-	$2s\frac{1}{2}$	-0.8196
		3.389	3^-	$1d\frac{3}{2}$	-0.0185
0.000	$\frac{3}{2}^-$	3.389	3^-	$1d\frac{5}{2}$	0.9317
		3.761	2^+	$1p\frac{1}{2}$	-0.0361
		3.761	2^+	$1p\frac{3}{2}$	-0.2845
		4.303	1^-	$1d\frac{3}{2}$	0.0066
		4.303	1^-	$1d\frac{5}{2}$	-0.1422
		4.303	1^-	$2s\frac{1}{2}$	-0.0632
		4.460	2^-	$1d\frac{3}{2}$	0.1054
		4.460	2^-	$1d\frac{5}{2}$	0.6025
		4.460	2^-	$2s\frac{1}{2}$	0.4809
		4.524	4^-	$1d\frac{5}{2}$	-0.9325
		7.670	2^-	$1d\frac{3}{2}$	-0.1756
		7.670	2^-	$1d\frac{5}{2}$	-0.3262
		7.670	2^-	$2s\frac{1}{2}$	-0.2284

Table B.6: continued on the next page.

Table B.6: continued from the previous page.

^{11}B		^{12}B		nl_j	SA
E_X (MeV)	J^π	E_X (MeV)	J^π		
		0.000	1^+	$1p\frac{1}{2}$	-0.1785
		0.000	1^+	$1p\frac{3}{2}$	0.5635
		0.953	2^+	$1p\frac{3}{2}$	-0.1089
		1.674	2^-	$1d\frac{3}{2}$	0.0103
		1.674	2^-	$1d\frac{5}{2}$	0.0562
		2.621	1^-	$1d\frac{3}{2}$	0.0290
		2.621	1^-	$2s\frac{1}{2}$	-0.0735
		3.389	3^-	$1d\frac{5}{2}$	0.0229
2.124	$\frac{1}{2}^-$	3.761	2^+	$1p\frac{3}{2}$	-0.2702
		4.303	1^-	$1d\frac{3}{2}$	0.0076
		4.303	1^-	$2s\frac{1}{2}$	0.8113
		4.460	2^-	$1d\frac{3}{2}$	-0.0480
		4.460	2^-	$1d\frac{5}{2}$	0.4698
		4.524	4^-		
		7.670	2^-	$1d\frac{3}{2}$	-0.0682
		7.670	2^-	$1d\frac{5}{2}$	0.6032

Table B.6: continued on the next page.

Table B.6: continued from the previous page.

^{11}B		^{12}B		nl_j	SA
E_X (MeV)	J^π	E_X (MeV)	J^π		
		0.000	1^+	$1p\frac{3}{2}$	-0.4077
		0.953	2^+	$1p\frac{1}{2}$	-0.0257
		0.953	2^+	$1p\frac{3}{2}$	0.4590
		1.674	2^-	$1d\frac{3}{2}$	0.0507
		1.674	2^-	$1d\frac{5}{2}$	-0.2204
		1.674	2^-	$2s\frac{1}{2}$	-0.0184
		2.621	1^-	$1d\frac{3}{2}$	0.0433
		2.621	1^-	$1d\frac{5}{2}$	0.2354
		3.389	3^-	$1d\frac{3}{2}$	-0.0578
		3.389	3^-	$1d\frac{5}{2}$	0.0706
		3.389	3^-	$2s\frac{1}{2}$	0.1657
4.444	$\frac{5}{2}^-$	3.761	2^+	$1p\frac{1}{2}$	-0.7892
		3.761	2^+	$1p\frac{3}{2}$	0.2339
		4.303	1^-	$1d\frac{3}{2}$	-0.0170
		4.303	1^-	$1d\frac{5}{2}$	0.2673
		4.460	2^-	$1d\frac{3}{2}$	-0.0287
		4.460	2^-	$1d\frac{5}{2}$	0.0245
		4.460	2^-	$2s\frac{1}{2}$	0.0891
		4.524	4^-	$1d\frac{3}{2}$	-0.0082
		4.524	4^-	$1d\frac{5}{2}$	0.1918
		7.670	2^-	$1d\frac{3}{2}$	-0.0519
		7.670	2^-	$1d\frac{5}{2}$	0.1230
		7.670	2^-	$2s\frac{1}{2}$	-0.0638

Table B.6: continued on the next page.

Table B.6: continued from the previous page.

^{11}B		^{12}B		nl_j	SA
E_X (MeV)	J^π	E_X (MeV)	J^π		
		0.000	1^+	$1p\frac{1}{2}$	-0.0985
		0.000	1^+	$1p\frac{3}{2}$	0.5747
		0.953	2^+	$1p\frac{1}{2}$	0.0561
		0.953	2^+	$1p\frac{3}{2}$	-0.2443
		1.674	2^-	$1d\frac{3}{2}$	0.0027
		1.674	2^-	$1d\frac{5}{2}$	0.0810
		1.674	2^-	$2s\frac{1}{2}$	-0.0098
		2.621	1^-	$1d\frac{3}{2}$	-0.0305
		2.621	1^-	$1d\frac{5}{2}$	-0.0328
		2.621	1^-	$2s\frac{1}{2}$	0.0133
		3.389	3^-	$1d\frac{3}{2}$	0.0350
		3.389	3^-	$1d\frac{5}{2}$	-0.0052
5.020	$\frac{3}{2}^-$	3.761	2^+	$1p\frac{1}{2}$	0.1702
		3.761	2^+	$1p\frac{3}{2}$	-0.4338
		4.303	1^-	$1d\frac{3}{2}$	-0.0449
		4.303	1^-	$1d\frac{5}{2}$	0.3713
		4.303	1^-	$2s\frac{1}{2}$	-0.0098
		4.460	2^-	$1d\frac{3}{2}$	0.0295
		4.460	2^-	$1d\frac{5}{2}$	-0.0493
		4.460	2^-	$2s\frac{1}{2}$	-0.0940
		4.524	4^-	$1d\frac{5}{2}$	-0.0973
		7.670	2^-	$1d\frac{3}{2}$	0.0566
		7.670	2^-	$1d\frac{5}{2}$	-0.3710
		7.670	2^-	$2s\frac{1}{2}$	-0.4072

Table B.7: Spectroscopic amplitudes for the target-like $\langle^{19}F|^{18}F\rangle$ overlaps used in the DWBA, CCBA and CRC calculations for the sequential components of the ^{12}C(^{18}O,^{18}F)^{12}B single-charge exchange nuclear reactions. The symbols n, l, and j correspond to the principal quantum number, the orbital, and the total angular momentum of the transferred neutron orbitals, respectively.

^{19}F		^{18}F		nl_j	SA
E_X (MeV)	J^π	E_X (MeV)	J^π		
0.000	$\frac{1}{2}^+$	0.000	1^+	$1d\frac{3}{2}$	0.0226
		0.000	1^+	$2s\frac{1}{2}$	-0.7042
		0.937	3^+	$1d\frac{5}{2}$	0.7567
		1.042	0^+	$2s\frac{1}{2}$	-0.3917
0.197	$\frac{5}{2}^+$	0.000	1^+	$1d\frac{3}{2}$	0.2720
		0.000	1^+	$1d\frac{5}{2}$	0.5641
		0.937	3^+	$1d\frac{5}{2}$	-0.4414
		1.042	0^+	$1d\frac{5}{2}$	0.4698
1.554	$\frac{1}{2}^-$	0.000	1^+	$1d\frac{3}{2}$	0.2254
		0.000	1^+	$1d\frac{5}{2}$	0.8486
		0.000	1^+	$2s\frac{1}{2}$	-0.0319
		0.937	3^+	$1d\frac{5}{2}$	-0.3037
		1.042	0^+	$1d\frac{3}{2}$	-0.2997

Table B.8: Spectroscopic amplitudes for the target-like $\langle {}^{13}C|{}^{12}B\rangle$ overlaps used in the DWBA, CCBA and CRC calculations for the sequential components of the ^{12}C(^{18}O,^{18}F)^{12}B single-charge exchange nuclear reactions. The symbols n, l, and j correspond to the principal quantum number, the orbital, and the total angular momentum of the transferred proton orbitals, respectively.

^{13}C		^{12}B		nl_j	SA
E_X (MeV)	J^π	E_X (MeV)	J^π		
		0.000	1^+	$1p\frac{1}{2}$	-0.0393
		0.000	1^+	$1p\frac{3}{2}$	1.0795
		0.953	2^+	$1p\frac{3}{2}$	1.4409
		1.674	2^-	$1d\frac{3}{2}$	-0.0081
		1.674	2^-	$1d\frac{5}{2}$	-0.1039
		2.621	1^-	$1d\frac{3}{2}$	-0.0668
		2.621	1^-	$2s\frac{1}{2}$	0.0528
		3.389	3^-	$1d\frac{5}{2}$	-0.0663
0.000	$\frac{1}{2}^-$	3.761	2^+	$1p\frac{3}{2}$	0.0588
		4.303	1^-	$1d\frac{3}{2}$	0.0053
		4.303	1^-	$2s\frac{1}{2}$	-0.0114
		4.460	2^-	$1d\frac{3}{2}$	0.0901
		4.460	2^-	$1d\frac{5}{2}$	0.1021
		4.524	2^-		
		7.670	2^-	$1d\frac{3}{2}$	0.0099
		7.670	2^-	$1d\frac{5}{2}$	-0.0193

Table B.8: continued on the next page.

Table B.8: continued from the previous page.

^{13}C		^{12}B		nl_j	SA
E_X (MeV)	J^π	E_X (MeV)	J^π		
		0.000	1^+	$1d\frac{3}{2}$	0.1087
		0.000	1^+	$1d\frac{5}{2}$	0.0924
		0.953	2^+	$1d\frac{3}{2}$	-0.0178
		0.953	2^+	$1d\frac{5}{2}$	-0.0774
		0.953	2^+	$2s\frac{1}{2}$	-0.0107
		1.674	2^-	$1p\frac{1}{2}$	0.0188
		1.674	2^-	$1p\frac{3}{2}$	0.4668
		2.621	1^-	$1p\frac{3}{2}$	-0.2263
		3.389	3^-	$1p\frac{1}{2}$	0.0939
3.854	$\frac{5}{2}^+$	3.389	3^-	$1p\frac{3}{2}$	-0.9250
		3.761	2^+	$1d\frac{3}{2}$	0.0281
		3.761	2^+	$1d\frac{5}{2}$	0.0421
		3.761	2^+	$2s\frac{1}{2}$	0.0005
		4.303	1^-	$1p\frac{3}{2}$	-0.0034
		4.460	2^-	$1p\frac{1}{2}$	-0.3400
		4.460	2^-	$1p\frac{3}{2}$	-0.5680
		4.524	4^-	$1p\frac{3}{2}$	1.0659
		7.670	2^-	$1p\frac{1}{2}$	-0.2132
		7.670	2^-	$1p\frac{3}{2}$	0.2938

Table B.9: Spectroscopic amplitudes for the target-like $\langle^{17}O|^{18}F\rangle$ overlaps used in the DWBA, CCBA and CRC calculations for the sequential components of the ^{12}C(^{18}O,^{18}F)^{12}B single-charge exchange nuclear reactions. The symbols n, l, and j correspond to the principal quantum number, the orbital, and the total angular momentum of the transferred proton orbitals, respectively.

^{17}O		^{18}F		nl_j	SA
E_X (MeV)	J^π	E_X (MeV)	J^π		
0.000	$\frac{5}{2}$+	0.000	1^+	$1d\frac{3}{2}$	-0.4633
		0.000	1^+	$1d\frac{5}{2}$	0.5559
		0.937	3^+	$1d\frac{5}{2}$	-0.5574
		1.042	0^+	$1d\frac{5}{2}$	0.8986
0.871	$\frac{1}{2}$+	0.000	1^+	$1d\frac{3}{2}$	0.1231
		0.000	1^+	$2s\frac{1}{2}$	-0.4524
		0.937	3^+	$1d\frac{5}{2}$	0.5103
		1.042	0^+	$2s\frac{1}{2}$	-0.3073
3.055	$\frac{1}{2}$-	0.000	1^+	$1p\frac{1}{2}$	-0.2545
		0.000	1^+	$1p\frac{3}{2}$	0.1684
		0.937	3^+		
		1.042	0^+	$1p\frac{1}{2}$	0.5766